

## Experiments on free-surface turbulence

**Citation for published version (APA):**

Savelsberg, R. (2006). *Experiments on free-surface turbulence*. [Phd Thesis 1 (Research TU/e / Graduation TU/e), Applied Physics]. Technische Universiteit Eindhoven. <https://doi.org/10.6100/IR609526>

**DOI:**

[10.6100/IR609526](https://doi.org/10.6100/IR609526)

**Document status and date:**

Published: 01/01/2006

**Document Version:**

Publisher's PDF, also known as Version of Record (includes final page, issue and volume numbers)

**Please check the document version of this publication:**

- A submitted manuscript is the version of the article upon submission and before peer-review. There can be important differences between the submitted version and the official published version of record. People interested in the research are advised to contact the author for the final version of the publication, or visit the DOI to the publisher's website.
- The final author version and the galley proof are versions of the publication after peer review.
- The final published version features the final layout of the paper including the volume, issue and page numbers.

[Link to publication](#)

**General rights**

Copyright and moral rights for the publications made accessible in the public portal are retained by the authors and/or other copyright owners and it is a condition of accessing publications that users recognise and abide by the legal requirements associated with these rights.

- Users may download and print one copy of any publication from the public portal for the purpose of private study or research.
- You may not further distribute the material or use it for any profit-making activity or commercial gain
- You may freely distribute the URL identifying the publication in the public portal.

If the publication is distributed under the terms of Article 25fa of the Dutch Copyright Act, indicated by the "Taverne" license above, please follow below link for the End User Agreement:

[www.tue.nl/taverne](http://www.tue.nl/taverne)

**Take down policy**

If you believe that this document breaches copyright please contact us at:

[openaccess@tue.nl](mailto:openaccess@tue.nl)

providing details and we will investigate your claim.

# Experiments on Free-Surface Turbulence

PROEFSCHRIFT

ter verkrijging van de graad van doctor aan de  
Technische Universiteit Eindhoven, op gezag van  
de Rector Magnificus, prof.dr.ir C.J. van Duijn,  
voor een commissie aangewezen door het College  
voor Promoties in het openbaar te verdedigen op  
donderdag 8 juni 2006 om 16.00 uur

door

Ralph Savelsberg

geboren te Kerkrade

Dit proefschrift is goedgekeurd door de promotoren :

prof.dr.ir. W. van de Water

en

prof.dr.ir. G.J.F. van Heijst

Dit werk maakt deel uit van het onderzoeksprogramma van de Stichting voor Fundamenteel Onderzoek der Materie (FOM), die financieel wordt gesteund door de Nederlandse Organisatie voor Wetenschappelijk Onderzoek (NWO).

Omslag / Cover: Yellowstone Lake, Yellowstone National Park, Wyoming, USA. Foto met dank aan / Photograph courtesy of Maikel van Hest.

Omslag ontwerp / Cover design: Paul Verspaget & Carin Bruinink Grafische vormgeving.

Druk / Printed by: Universiteitsdrukkerij Technische Universiteit Eindhoven.

CIP-DATA LIBRARY TECHNISCHE UNIVERSITEIT EINDHOVEN

Savelsberg, Ralph

Experiments on Free-Surface Turbulence / by Ralph Savelsberg. –  
Eindhoven: Technische Universiteit Eindhoven, 2006. –

Proefschrift.

ISBN-10: 90-386-2501-4

ISBN-13: 978-90-386-2501-0

NUR 926

Trefwoorden: turbulentie / turbulente stroming / lasersnelheidsmetingen /  
optische meetmethoden /hydrodynamische golven

Subject headings: turbulence / turbulent flow / water waves / laser  
velocimetry / shape measurement

# CONTENTS

<b>1</b>	<b>Introduction</b>	<b>1</b>
1.1	Turbulence . . . . .	1
1.2	Free-surface deformations . . . . .	3
1.3	Experiments . . . . .	4
1.4	Overview of this thesis . . . . .	7
<b>2</b>	<b>Free-surface turbulence</b>	<b>9</b>
2.1	Boundary conditions at a free surface . . . . .	9
2.1.1	Linear gravity-capillary waves . . . . .	12
2.1.2	Sub-surface structures . . . . .	15
2.2	Phenomenology of free-surface turbulence . . . . .	19
2.2.1	Turbulence statistics under a free surface. . . . .	19
2.2.2	Free-surface deformations . . . . .	22
2.2.3	The generation of waves by turbulence . . . . .	25
<b>3</b>	<b>Basic properties of the turbulence</b>	<b>27</b>
3.1	Active-grid-generated turbulence . . . . .	27
3.1.1	Grid geometry . . . . .	29
3.1.2	Forcing protocols . . . . .	31
3.2	Laser Doppler Velocimetry . . . . .	33
3.2.1	Principle of LDV . . . . .	33
3.2.2	The set-up for Laser-Doppler measurements . . . . .	36
3.3	Properties of the turbulence . . . . .	39
3.3.1	Homogeneity . . . . .	39
3.3.2	Turbulent scales . . . . .	42
3.3.3	Isotropy . . . . .	46
3.4	Conclusions . . . . .	49
<b>4</b>	<b>Measuring turbulence properties with PIV</b>	<b>51</b>
4.1	Introduction . . . . .	51
4.2	The principle of PIV . . . . .	53
4.3	Inherent filtering by PIV . . . . .	58

4.3.1	A description of the filter . . . . .	58
4.3.2	The effect of spatial averaging on turbulence statistics. . .	59
4.4	Applying PIV to simulated velocity fields . . . . .	66
4.4.1	Kinematic simulations . . . . .	66
4.4.2	Generating realistic particle images . . . . .	69
4.4.3	Comparison of turbulence statistics . . . . .	72
4.4.4	The influence of particle loss . . . . .	76
4.5	Experiments . . . . .	79
4.5.1	A comparison of PIV and LDV measurements . . . . .	80
4.5.2	Isotropy in horizontal planes . . . . .	84
4.6	Conclusions . . . . .	87
<b>5</b>	<b>A statistical description of the surface shape</b>	<b>89</b>
5.1	Basic definitions . . . . .	89
5.2	Statistics of the slope at a point . . . . .	91
5.3	Slope statistics in time and space . . . . .	93
5.3.1	Dispersive surface waves . . . . .	94
5.3.2	Spectra in time and space . . . . .	96
5.3.3	Isotropy in the surface slopes . . . . .	98
<b>6</b>	<b>Measuring the slope of the free surface</b>	<b>103</b>
6.1	Introduction . . . . .	103
6.2	Point measurements of the surface slope . . . . .	105
6.3	Measuring the slope in space and time . . . . .	107
6.3.1	Set-up for slope measurements along a line . . . . .	107
6.3.2	Synchronisation . . . . .	108
6.3.3	Data processing . . . . .	112
6.4	Assessment of the surface scanning method . . . . .	114
6.5	Conclusions . . . . .	119
<b>7</b>	<b>The nature of the surface ripples</b>	<b>121</b>
7.1	Spectra and correlations in time and space . . . . .	121
7.1.1	Correlation functions . . . . .	128
7.1.2	The surface spectrum . . . . .	129
7.2	Isotropy . . . . .	130
7.3	Synthetic surfaces . . . . .	133
7.4	Conclusions . . . . .	135
<b>8</b>	<b>Correlating the sub-surface turbulence and the surface shape</b>	<b>137</b>
8.1	Correlation between turbulence and the surface shape . . . . .	139
8.1.1	Taylor's hypothesis for free-surface turbulence . . . . .	140
8.1.2	Calculating the elevation . . . . .	144
8.2	Combining PIV and surface slope measurements . . . . .	146
8.3	A test case: vortex shedding . . . . .	149

8.4	Grid-generated turbulence . . . . .	155
8.5	Conclusions . . . . .	160
<b>9</b>	<b>General conclusions</b>	<b>163</b>
	<b>Summary</b>	<b>173</b>
	<b>Samenvatting</b>	<b>175</b>
	<b>Dankwoord / Acknowledgements</b>	<b>177</b>
	<b>Curriculum Vitae</b>	<b>179</b>



---

## INTRODUCTION

### 1.1 Turbulence

In general, the words *turbulent* and *turbulence* are used to describe situations that are wild, stormy, tumultuous, agitated, and above all unpredictable. To a certain degree, these descriptions are also true for turbulent flows. Most flows, both in nature and in technological applications, are turbulent. Atmospheric flow is turbulent, which is one of the causes of the unpredictable nature of our weather. Turbulence in the seas and oceans directly impacts our climate, and affects the distribution of, for instance, plankton, but also of algae and pollution. The chaotic motion inherent to turbulence is used for stirring and mixing chemicals in industrial applications, and, on a much smaller scale, in distributing milk and or sugar through a cup of tea. Combustion, for instance in power plants and car engines, is a turbulent process. In order to understand all these processes, and in case of technological applications in order to improve their efficiency, understanding turbulence is essential.

The equation of motion for a fluid is the well-known Navier-Stokes equation, which in essence is Newton's second law of motion applied to a fluid parcel \*:

$$\frac{D\mathbf{u}(\mathbf{x}, t)}{Dt} = -\frac{1}{\rho}\nabla p(\mathbf{x}, t) + \mathbf{g} + \nu\nabla^2\mathbf{u}(\mathbf{x}, t). \quad (1.1)$$

In this equation,  $\mathbf{u}(\mathbf{x}, t)$  is the fluid velocity at a location  $\mathbf{x}$  and a time  $t$ ,  $\rho$  is the density of the fluid,  $p(\mathbf{x}, t)$  is the pressure,  $\mathbf{g}$  is the gravitational acceleration, and  $\nu$  is the (kinematic) viscosity of the fluid. In principle, this equation, together with the continuity equation:  $\nabla \cdot \mathbf{u} = 0$ , fully describes the motion of a fluid, including that in turbulent flows. However, even though the basic equations that describe the fluid motion are known and have been known for

---

\*Already indicating some limitations, this equation as formulated here is only valid for a homogeneous, incompressible, and Newtonian fluid, without background rotation.



more than a century, turbulence essentially is an unsolved problem. The equations allow solutions of a bewildering complexity and exact solutions have only been found for rare and decidedly non-turbulent cases.

A feature of turbulent flows is the occurrence of structures, often called eddies, associated with rapidly fluctuating vorticity. The motion in a turbulent flow occurs over a wide range of length- and time scales. By vortex-stretching and vortex-breakup, two non-linear processes, the energy that is contained in large scale eddies is transferred to smaller structures, in what has become known as the energy cascade. Because of the unpredictable and seemingly random motions in turbulence, almost all descriptions and measurements of turbulence deal with statistical quantities such as averages, variances, correlation functions, and energy spectra. A major breakthrough in the development of a statistical description of turbulence was the work by A.N. Kolmogorov. Based on the notion of the energy cascade, he postulated that for strong turbulence the energy that is transferred from larger to smaller scales is dissipated by viscous effects only on the smallest scales in the turbulence. Accordingly, the turbulence statistics on the smallest scales depend on both the energy dissipation rate  $\epsilon$  and the viscosity of the fluid. By dimensional arguments Kolmogorov found that, thus, these smallest scales were of a size:  $\eta = (\nu^3/\epsilon)^{1/4}$ . He also hypothesised that, since viscosity does not play a role on larger scales, the statistics for these larger scales depend only on the energy dissipation rate. From this he derived his now-famous five-third law for the turbulent energy spectrum. The definition of the energy spectrum, which we will call  $E(k)$ , is based on Fourier-analysis:  $E(k)dk$  is the kinetic energy density in the velocity field contained in Fourier-modes with wavenumbers between  $k$  and  $k + dk$ . By dimensional analysis, Kolmogorov concluded that for scales in the flow larger than  $\eta$  (but smaller than the largest scales) the energy spectrum shows algebraic scaling with a scaling exponent of  $-5/3$ :

$$E(k) = C\epsilon^{2/3}k^{-5/3}, \quad (1.2)$$

with a constant  $C$  that is most probably universal, but for which no theory exists, unless the turbulence problem is solved. This scaling behaviour has since been observed in a wide variety of turbulent flows, including very large scale flows in the atmosphere and smaller scale flows in, for instance, wind tunnels. This theory will be the framework for interpreting our turbulence measurements. In particular, our question will be how this multitude of scales in turbulence is reflected in the size of structures that can be found at the free surface of the flow. A more detailed description of the theory and its consequences and limitations can be found in turbulence textbooks, such as the books by Frisch (1995) and Pope (2000).

## 1.2 Free-surface deformations

Turbulent flows in seas and oceans, as well as flows in rivers and channels, for instance, are special in the sense that they have a free surface. Turbulence close to the interface between water and air behaves very differently from turbulence near fixed walls, such as the walls of a flow channel or the ocean floor. One of the most obvious features of the air-water interface is that it is deformable. The small-scale roughness of the ocean's surface determines the exchange of heat and mass between the atmosphere and the ocean. These transport processes are crucial for the global distribution of momentum, heat and chemical species.

By far the most common type of surface deformation to occur in nature are waves, ranging from tiny thermally driven capillary waves, with wavelengths of a few micrometers and amplitudes of a few nanometers (Aarts *et al.*, 2004), to monstrous waves induced by earth-quakes, that can travel across the entire globe and that can reach heights of several meters (Titov *et al.*, 2005). A more common source of waves on the sea or ocean surface is turbulence in the wind above it, and pressure fluctuations and fluctuating shear stresses on the surface associated with this. The interaction of waves and wind is a complicated problem that has been studied for decades (see Phillips, 1957) and is in fact still being investigated.

The shape of the surface is determined by a delicate balance between vertical acceleration and pressure in the flow below the surface on one hand, and gravity and interfacial tension, i.e. stresses associated with surface curvature, on the other hand. Which force dominates this balance depends on the scale of the deformation. Generally, for large scale surface deformations, gravity balances vertical accelerations in the fluid, whereas for smaller scales surface tension plays a more important role. In a recent paper, Brocchini & Peregrine (2001) have classified the different types of structures and the behaviour that can occur at a free surface above turbulent flow, depending on which force dominates. Structures, other than waves, commonly seen on a free surface above turbulence are scars; sharp lines on the surface, most often associated with up- or down-welling of fluid at the surface. Additionally, low pressure in the core of sub-surface eddies can lead to dimples in the surface. These too are fairly common structures, visible in the wake behind bridge pillars in a river, behind oars on a boat, or in a cup of tea that is stirred with a spoon. Brocchini & Peregrine (2001) distinguish four different regimes of free surface distortions as a result of sub-surface turbulence, depending on a typical length-scale  $L$  and typical velocity scale  $U$  of the turbulence. Based on these scales, they define two dimensionless numbers: the Froude number, which is a measure of the potential energy due to gravity relative to the kinetic energy in the flow:

$$Fr = \frac{U}{\sqrt{2gL}}, \quad (1.3)$$

where  $g$  is the gravitational acceleration, and the Weber number, which gauges

the balance between inertial and surface tension forces:

$$We = \frac{U^2 L \rho}{2\sigma}, \quad (1.4)$$

where  $\sigma$  is the surface tension coefficient<sup>†</sup>. Depending on the values of the Froude and Weber numbers the following four regimes can be distinguished:

**Weak turbulence**  $Fr \ll 1, We \ll 1$ : The turbulence is not strong enough to cause significant surface disturbances.

**'Knobbly' flow**  $Fr \gg 1, We \ll 1$ : The turbulence is strong enough to deform the surface against gravity, but its length-scale is small. Surface tension causes the surface shape to be very smooth and rounded.

**Turbulence dominated by gravity**  $Fr \ll 1, We \gg 1$ : Surface distortions are primarily countered by gravity, resulting in a nearly flat free surface. The turbulent energy is sufficient to disturb the surface at relatively small scales, leading to small regions of waves, vortex dimples, and scars. This is the most common state in nature.

**Strong turbulence**  $Fr \gg 1, We \gg 1$ : The turbulence is strong enough to counter gravity and surface tension is no longer sufficient to prevent the surface from breaking up into droplets and bubbles.

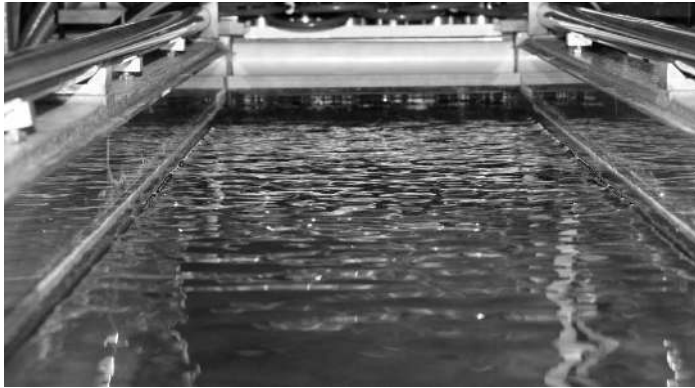
Since turbulence, by its very nature, does not have a single length-scale or time-scale, in the real world, one can expect to see many of these features occurring side-by-side, as was also pointed out by Brocchini & Peregrine (2001). For instance, even in relatively weak turbulence, localised events can lead to surface deformations.

### 1.3 Experiments

In this thesis we will study the wrinkling of the surface in still air, which is determined by the interaction between the free surface and the turbulent flow beneath it. The interaction between turbulence and a free surface is also known as free-surface turbulence (see, for instance, Rood & Katz, 1994; Shen *et al.*, 1999). The complexity of the boundary conditions on the free surface makes simulating the free-surface turbulence a daunting task. Experiments can reveal much information about this interaction that is not present in such simulations. This is in part due to the linearisations of the boundary conditions required in the numerical modeling and in part due to the high computational costs involved in simulating strong turbulence. Hence, we study free-surface turbulence in experiments in a water channel, in which we generate turbulence by means of a so-called active grid.

---

<sup>†</sup>For a clean air-water interface at room temperature  $\sigma = 0.73 \cdot 10^{-3} N/m$ .



(a)



(b)

FIGURE 1.1 — (a) Photograph of the free surface over the full width of the water channel (0.3 m) used in our experiments, from the active grid (located close to the top of the picture) to about 1.5 m downstream (b) Details of the surface at 2 m from the grid. The width of the photograph corresponds to approximately 0.1 m. See chapter 3 for details of the set-up and the turbulence generating grid.

Visual observations play an important role in fluid dynamics. This is certainly true for free-surface turbulence. Careful observations of features of the surface can provide a general idea of the nature of the surface deformations. Figure 1.1 shows photographs of light reflected in the surface above the turbulence we generate in our experiments. These photographs clearly show that the surface exhibits deformations on many different length-scales and in different directions. Obviously, photographs do not show either the turbulence or the dynamics of the surface. Even from video, that does show time-dependence, inferring whether, for instance, the surface deformations move at the same velocity as the mean stream velocity in the turbulence is almost impossible. Hence, instead of on observation, the focus in the experiments described in this thesis is on detailed measurements of the statistics of both the surface shape and of the turbulence beneath it. In order to be able to properly characterise the turbulence in terms of the Kolmogorov framework and to make the turbulence reproducible, we have chosen to use homogeneous and isotropic turbulence, which is generated by the active grid.

Measurement techniques in fluid dynamics have progressed rapidly in the

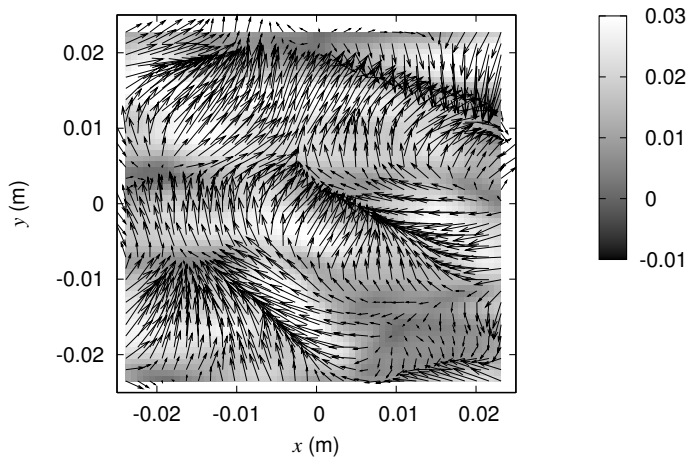


FIGURE 1.2 — Scan of the surface above grid-generated turbulence, at 2 m from the grid. The vectors indicate the local surface slope. The grey in the background is a measure for the slope magnitude. It was obtained from measuring the slope along a line in spanwise ( $x$ -) direction. The scans were extended in the streamwise ( $y$ -) direction by means of Taylor's frozen turbulence hypothesis. It should be noted that because of this, the image cannot be directly compared to a snapshot of the surface. See chapter 6 for more details on the measurement technique and chapter 8 for an explanation of Taylor's hypothesis as applied to a free surface above turbulence.

last decades, in part due to the increasing computational power of affordable computers, as well as, for instance, due to the development of digital cameras. These developments enable us to measure both the sub-surface velocity field and the surface gradient field with a sufficiently high resolution. The former is done with Particle-Image Velocimetry, an existing technique based on cross-correlating digital images of particle distributions in the flow, illuminated by means of a laser light sheet. For the surface shape measurements we have developed a new technique based on scanning the surface with a laser beam. Figure 1.2 shows the surface slope field above active-grid-generated turbulence, derived from these surface scans.

If we take  $U$  to be the root-mean-square velocity measured in our experiments and  $L$  the integral length-scale of the turbulence, which is a measure of the largest structures, we find  $We \approx 15$  and  $Fr \approx 0.01^\ddagger$ . Hence, the surface distortions are relatively small. This can also be seen from the values of the slope in figure 1.2. However, even this case is understood only poorly. For instance, how the shape of the free surface is connected to the sub-surface turbulence is essentially unknown. Our measurements will allow us to compare the statistics of both, and see what part of the turbulence, if any, is directly visible in the surface shape. This is of prime importance for interpreting geophysical observations of the surface shape, obtained by novel remote sensing techniques (Forbes *et al.*, 1993; Stammer, 1997).

## 1.4 Overview of this thesis

Much of this thesis is devoted to the description of and to tests of our measurement techniques, but we start in chapter 2 with formal definitions of the boundary conditions at a free surface and, based on these, mathematical descriptions of two distinctly different types of free-surface deformations: gravity capillary waves and dimples in the surface associated with low pressure in the cores of sub-surface vortices. These two examples illustrate some of the behaviour that can occur at a free surface and provide a framework for our results. Chapter 2 also gives an overview of previous studies of how the presence of the surface influences the turbulence and of the intricate interactions between structures in the turbulence and the surface.

As was already mentioned, the turbulence in most of our experiment is generated by actively stirring the flow by means of a so-called active grid. This type of grid can be used to generate the moderately strong turbulence we need and allows us to change the properties of the turbulence to some degree. A detailed description of the grid is given in chapter 3, as well as properties of the turbulence it generates. These properties were measured by means of point-measurements of the velocity with Laser-Doppler Velocimetry. A question that

---

<sup>‡</sup>Details of these measurements can be found in chapter 3.

receives particular attention in this chapter is how the forcing influences the isotropy of the turbulence.

Chapter 4 describes Particle Image Velocimetry (PIV). Unlike Laser-Doppler measurements, this technique provides a spatial measurement of the velocity: two components of the velocity in horizontal planes below the surface, in our case. This allows us to measure spatial correlations, derivatives of the velocity, and vorticity. However, the spatial information provided by PIV is in fact a spatially filtered representation of the actual velocity field. By evaluating synthesised particle images, generated with kinematic simulations of turbulence, the effects of this inherent averaging on the measured turbulence statistics are evaluated. A comparison is also given between results of PIV experiments in our water channel and measurements obtained with LDV.

The statistical analysis of turbulence in chapters 3 and 4, as well as in most turbulence text-books, involves spatial Fourier transforms and spatial correlations. Chapter 5 will show how, especially in the case of surface waves, a statistical description of the surface shape requires Fourier-analysis both in space and in time. Chapter 5 also provides a description of statistical properties for an isotropically deformed surface. This description and the space-time Fourier analysis that precedes it, provide a framework for interpreting our measurements of the surface shape.

Since it is essential to measure the surface shape in space and time, a novel measurement technique has been developed, based on scanning the surface along a line. This is done by means of a swiveling laser beam. The technique is described in chapter 6. Based on measurements of the free-surface above grid-generated turbulence, a number of features as well as limitations of this measurement technique are discussed.

Finally, with the sub-surface turbulence having been characterised and the measurement techniques detailed, in chapter 7 we proceed with the actual investigation of the relation between the sub-surface turbulence and the shape of the free surface. This is done by means of more space-time measurements of the free surface above active-grid-generated turbulence and includes a study of isotropy of the surface shape and its relation to the isotropy of the sub-surface turbulence.

The investigation into the relation between the surface shape and the turbulence is continued in chapter 8. In this chapter, we describe simultaneous measurements of the surface slope with our laser scanning technique and simultaneous PIV measurements of the sub-surface velocity field, in order to see what part of the surface shape is directly connected to the sub-surface turbulence.

---

## FREE-SURFACE TURBULENCE

As was already indicated in the Introduction, different types of surface deformations can co-exist above sub-surface turbulence. In this chapter, more detailed mathematical descriptions of two of these deformations will be given: gravity-capillary waves and dimples in the surface associated with sub-surface vortices. These descriptions are based on a formal definition of the equations of motion and the boundary conditions at the surface. Even though they cannot fully describe the shape of a free surface above turbulence, they will later form the reference frame for the interpretation of our experimental results. We will also take a closer look at how having a free surface as a boundary condition influences the sub-surface turbulence, a problem that has received a lot of attention in literature. This is followed by a description of how sub-surface turbulence can generate waves.

### 2.1 Boundary conditions at a free surface

Several different mathematical formulations of flows involving a free surface exist, involving different linearisations, different ways of expressing the pressure, numerous non-dimensionalised forms, and various different coordinate systems. Hence, we feel, it is important to mention the full nonlinear boundary conditions here. They define a free surface and serve as the basis for two distinctive free-surface deformations that can occur.

The full set of non-linear equations, albeit in a different coordinate system, can be found in Wehousen & Laitone (1960) and in a more concise manner in, for example, Tsai & Yue (1996) and Sarpkaya (1996). As mentioned in chapter 1, the governing equations for the fluid motion are the continuity equation (for an incompressible flow):

$$\nabla \cdot \mathbf{u} = 0 \tag{2.1}$$



and the Navier-Stokes equation:

$$\frac{\partial \mathbf{u}}{\partial t} + \mathbf{u} \cdot \nabla \mathbf{u} = -\frac{\nabla p}{\rho} + \nu \nabla^2 \mathbf{u} - g \mathbf{e}_z, \quad (2.2)$$

with the  $z$ -coordinate pointing upwards from the surface. The influence of gravity can be incorporated into the pressure by defining the dynamic pressure  $p_d$  as:

$$p_d = p + \rho g z. \quad (2.3)$$

This can be introduced into the Navier-Stokes equation:

$$\frac{\partial \mathbf{u}}{\partial t} + \mathbf{u} \cdot \nabla \mathbf{u} = -\frac{\nabla p_d}{\rho} + \nu \nabla^2 \mathbf{u}. \quad (2.4)$$

For two viscous, immiscible fluids separated by an interface  $S(\mathbf{x}, t) = 0$  a number of boundary conditions exist:

1. At the interface the tangential velocity is continuous.
2. The kinematic boundary condition: a fluid parcel cannot pass through the interface.
3. The dynamic boundary conditions: tangential stress at the interface is continuous, and, due to surface tension, a jump occurs in the normal stress, proportional to the curvature of the interface.

In order for the interface to be considered a free surface density, the velocity and the viscosity in the upper fluid are considered negligible. In our case, the free surface is the interface between air and water\*. Since the velocity of air is considered negligible, for the free surface the first boundary condition becomes irrelevant: the tangential velocity at the surface no longer needs to be continuous. Hence, the tangential velocity in the water at the surface is unbounded. The kinematic boundary condition can be formulated as follows: the material derivative of the function  $S(\mathbf{x}, t)$  that describes the interface is equal to zero. Hence:

$$\frac{DS}{Dt} = \frac{\partial S}{\partial t} + \mathbf{u} \cdot \nabla S = 0 \quad \text{on } z = h(x, y, t), \quad (2.5)$$

where  $\mathbf{u}$  is the velocity, now only in the water, and  $h(x, y)$  is the surface elevation. This is directly related to  $S$  through  $S(x, y, z, t) = z - h(x, y, t)$ . Since the viscosity of air is negligibly small compared to that of water, a consequence

---

\*At room temperature, for water the density is  $\rho = 0.998 \cdot 10^3 \text{ kg/m}^3$  and the dynamic viscosity  $\mu = \rho \nu = 1 \cdot 10^{-3} \text{ kgm}^{-1}\text{s}^{-1}$ , whereas for air  $\rho = 1.23 \text{ kg/m}^3$  and dynamic viscosity  $\mu = 1.27 \cdot 10^{-6} \text{ kgm}^{-1}\text{s}^{-1}$

of the dynamic boundary condition is that in the water the tangential stresses at the interface are zero. The normal stress in the water is balanced by the pressure in the air and the surface tension. These conditions can be combined in the following equation (Tsai & Yue, 1996):

$$\mathbf{T} \cdot \mathbf{n} = (\sigma\kappa)\mathbf{n} + Pa \quad \text{on } z = h(x, y), \quad (2.6)$$

where  $Pa$  is the atmospheric pressure, i.e. the pressure in the air above the surface,  $\mathbf{n}$  is the unit normal vector to the surface,  $\kappa$  is the local surface curvature,  $\sigma$  is the surface tension coefficient, and  $\mathbf{T}$  is the stress tensor. For a Newtonian fluid the elements of the stress tensor are given by:

$$T_{ij} = \delta_{ij}p - \mu \left( \frac{\partial u_i}{\partial x_j} + \frac{\partial u_j}{\partial x_i} \right), \quad (2.7)$$

in which  $\mu = \rho\nu$  is the dynamic viscosity of water. The local curvature of the surface can be written as:

$$\kappa = \frac{1}{R_1} + \frac{1}{R_2}, \quad (2.8)$$

where  $R_1$  and  $R_2$  are the local radii of curvature at the surface. A very common way to linearise this boundary condition is by substituting the second-order derivatives of the surface elevation for the curvature:

$$\kappa = \frac{\partial^2 h}{\partial x^2} + \frac{\partial^2 h}{\partial y^2}. \quad (2.9)$$

In principle, equations 2.1 to 2.7 fully describe the flow of a Newtonian fluid under a free surface.

In order to be able to understand the relative importance of the various forces acting on the surface, and to more formally establish the relevant non-dimensional numbers, these equations can be written in non-dimensional form, by scaling the velocities with a characteristic velocity scale  $U$ , length-scales with a characteristic length-scale  $L$  and the pressure as  $p' = p/(\rho U^2)$ , and similarly  $Pa' = Pa/(\rho U^2)$ . For a turbulent flow  $U$  could, for instance, be the root-mean-square velocity and  $L$  could be the integral length-scale. This scaling is similar to the scaling used by Tsai (1998). The continuity equation changes very little:

$$\nabla \cdot \mathbf{u}' = 0, \quad (2.10)$$

where the prime denotes a non-dimensional quantity. The non-dimensionalised Navier-Stokes equation becomes:

$$\frac{\partial \mathbf{u}'}{\partial t'} + \mathbf{u}' \cdot \nabla \mathbf{u}' = -\nabla p'_d + \frac{1}{Re} \nabla^2 \mathbf{u}', \quad (2.11)$$

with the Reynolds number:

$$Re = \frac{UL}{\nu}. \quad (2.12)$$

The non-dimensional dynamic pressure is:

$$p'_d = p' + \frac{z'}{Fr^2}, \quad (2.13)$$

where  $Fr$  is the Froude number, now defined as:

$$Fr = \frac{U}{\sqrt{gL}}. \quad (2.14)$$

The dynamic boundary condition becomes:

$$\left( \delta_{ij} \left( p'_d - \frac{h'}{Fr^2} \right) - \frac{1}{Re} \left( \frac{\partial u'_i}{\partial x'_j} + \frac{\partial u'_j}{\partial x'_i} \right) \right) \cdot \mathbf{n} = \left( \frac{1}{We} \kappa' + Pa' \right) \mathbf{n}. \quad (2.15)$$

with the Weber number:

$$We = \frac{\rho U^2 L}{\sigma}. \quad (2.16)$$

We have formally derived the Weber and Froude numbers that were used by Brocchini & Peregrine (2001) and were already mentioned in chapter 1. However, the definitions here are slightly different from those given in chapter 1:  $We = \rho U^2 L / 2\sigma$  and  $Fr = U / \sqrt{(2gL)}$ . The difference, a constant factor 2 and  $\sqrt{2}$ , respectively, is likely due to the latter definitions following from the non-dimensionalised energy equation, see for instance Tsai (1998). In any case, the Weber number indicates the relative importance of capillary forces at the surface, whereas the Froude number is an indication of the importance of gravity.

As can be seen from equations (2.11), (2.13), and (2.15), the choice of whether one uses dynamic pressure or not, only determines whether the influence of gravity (coupled to the Froude number) is visible in the Navier-Stokes equation itself or in the boundary condition at the surface. The latter is common in literature concerning free surfaces.

In order to find solutions to this set of non-linear equations, usually they are linearised. Two very different types of free-surface deformations, based on linearised boundary conditions, will now be introduced.

### 2.1.1 LINEAR GRAVITY-CAPILLARY WAVES

Waves are probably the most common surface deformation to occur in nature, as was indicated in chapter 1. We will briefly look at waves in a fluid of finite depth  $h_0$  that propagate in one direction. This derivation can also be found in common fluid dynamics textbooks (see Kundu, 1990; Lighthill, 1978). Gravity-capillary waves are considered to be inviscid and irrotational <sup>†</sup>. This means

---

<sup>†</sup>The effect of viscosity is twofold: waves are damped, the damping becoming larger as the wavelength of the waves decreases and even small waves can actually generate vorticity (Sajjadi, 2002).

that the flow can be treated as a potential flow with the potential  $\phi$  given by:

$$\nabla\phi = \mathbf{u}. \quad (2.17)$$

Since the velocity field  $\mathbf{u}(x, y, z)$  is incompressible, the potential  $\phi$  satisfies the Poisson equation:

$$\nabla^2\phi = 0. \quad (2.18)$$

This can now be solved with the appropriate boundary conditions. At the bottom the normal velocity  $w$  is zero. Hence:

$$\frac{\partial\phi}{\partial z} = 0 \text{ at } z = -h_0, \quad (2.19)$$

where the  $z$ -coordinate points upwards and its origin  $z = 0$  is located at the undisturbed surface. For waves with a small amplitude compared to their length, the kinematic and dynamic boundary conditions can be linearised: they are evaluated at  $z = 0$  instead of at  $z = h$ . The kinematic boundary condition reduces to:

$$\frac{\partial\phi}{\partial z} = \frac{\partial h}{\partial t} \text{ at } z = 0, \quad (2.20)$$

with  $h(x, y, t)$  the free surface elevation. Since the flow is considered to be inviscid, the dynamic boundary conditions for the tangential stresses are met: they are zero by definition. Since the flow is also irrotational, instead of the Navier-Stokes equation, a linearised form of Bernoulli's equation can be used:

$$\frac{\partial\phi}{\partial t} + \frac{p}{\rho} + gz = 0 \quad (2.21)$$

Combining this with the dynamic boundary condition given in (2.6), which gives the pressure at the surface, and with the surface curvature being approximated by equation (2.9), the dynamic boundary condition for the normal stress becomes:

$$\frac{\partial\phi}{\partial t} = \frac{\sigma}{\rho} \left( \frac{\partial^2 h}{\partial x^2} + \frac{\partial^2 h}{\partial y^2} \right) - gh \text{ at } z = 0, \quad (2.22)$$

where the atmospheric pressure  $Pa = 0$ . To summarise, instead of a complex set of non-linear equations, now we need to solve the Poisson equation (2.18), which is linear, with linearised boundary conditions (2.19), (2.20), and (2.22). The type of solution we are aiming for is, of course, in the form of a harmonic surface wave, with amplitude  $a$ , wavenumber vector  $\mathbf{k}$ , and frequency  $\omega_d$ :

$$h(x, y, t) = a \cos(\mathbf{k} \cdot \mathbf{x} - \omega_d t). \quad (2.23)$$

Substituting this in the Poisson equation, using separation of variables, and applying the boundary conditions gives:

$$\phi = \frac{a\omega}{k} \frac{\cosh k(z + h_0)}{\sinh kh_0} \sin(\mathbf{k} \cdot \mathbf{x} - \omega_d t), \quad (2.24)$$

in which  $k$  is the length of vector  $\mathbf{k}$ . In principle, the vertical and horizontal velocities associated with the wave motion can be calculated from this expression. Far more interesting, however, is the dispersion relation: the relation between the wavenumber and frequency for surface waves. This follows from the dynamic boundary condition, by substituting (2.23) and (2.24) in (2.22):

$$\omega_d(k) = \sqrt{\left(gk + \frac{k^3\sigma}{\rho}\right) \tanh(kh_0)}, \quad (2.25)$$

It is clear that this set of equations — of irrotational flow with linearised boundary conditions — allows a whole range of harmonic solutions, with different length-scales, time-scales, and velocities. In principle, a wavy surface can be described in terms of a sum of waves with different wavelengths, amplitudes and phases. For waves with small wavelengths/large wavenumbers  $k$  the dispersion relation is dominated by the term  $k^3/\sigma$ . The nature of such waves — capillary

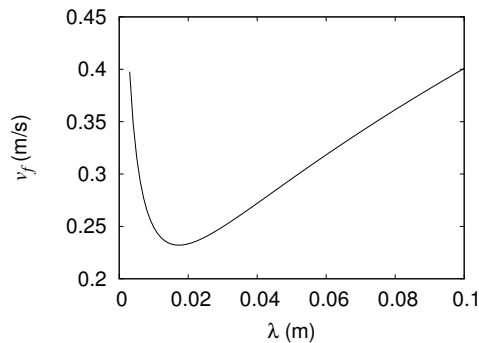


FIGURE 2.1 — The phase velocity of gravity-capillary waves as a function of their wavelength.

waves — is determined by a balance between vertical acceleration and surface tension. For waves with large wavelengths, gravity waves, the dispersion relation is dominated by the term  $gk$ . At the surface a balance exists between vertical acceleration and gravity. A consequence of the dispersion relation is that waves of different wavelengths have different phase-velocities  $v_f(k)$ :

$$v_f = \sqrt{\left(\frac{g}{k} + \frac{\sigma k}{\rho}\right) \tanh(kh_0)} = \sqrt{\left(\frac{g\lambda}{2\pi} + \frac{2\pi\sigma}{\rho\lambda}\right) \tanh \frac{2\pi h_0}{\lambda}} \quad (2.26)$$

with  $\lambda = 2\pi/k$  the wavelength. A graph of the phase velocity as a function of the wavelength is shown in figure 2.1. As can be seen in this graph, the phase velocity has a minimum value close to 23 cm/s for a wavelength of close to 17 mm.

Depending on their scale, the surface deformations are dominated by gravity or capillary forces. This is similar to the picture of surface distortions due to free-surface turbulence by Brocchini & Peregrine (2001), described in chapter 1. However, it is clear that describing the free surface above turbulence in terms of a superposition of linear waves is not realistic. The description of these waves is based on irrotational flow, which is incompatible with the importance of eddies and vortices in turbulence.

### 2.1.2 SUB-SURFACE STRUCTURES

The governing equations and boundary conditions at a free surface also allow a different type of surface deformation, closely associated with vorticity. In section 2.2 we will see that other researchers who study free-surface turbulence find correlation between the vertical component of vorticity and the surface elevation. The mechanism behind this is fairly straightforward. A core of a vortex is associated with a local maximum in vorticity and with a local pressure minimum. A consequence of this low pressure can be that the free surface above a sub-surface vortex shows a characteristic indentation. This can be illustrated from the following simple example, which was explored in more detail by Andersen (2003). As will become clear later, this model is much simplified, and cannot account for all the intricacies of free-surface turbulence. However, it allows us to illustrate the mechanism through which vorticity and the surface elevation are coupled and allows us to find a straightforward solution. For a weakly deformed surface — with a relatively small Froude number — the vertical velocity component is very small compared to the horizontal component. If we furthermore assume that the velocity does not depend on the depth, the flow can be assumed to be two-dimensional. If, in addition, we ignore the effect of viscosity (i.e. the Reynolds number is relatively large) and surface tension (the Weber number is relatively large) the flow becomes stationary and the Navier-Stokes equation reduces to the Euler equation, still in non-dimensionalised form:

$$(\mathbf{u}' \cdot \nabla) \mathbf{u}' = -\nabla p'_d. \quad (2.27)$$

In this two-dimensional case, tangential stresses are zero by definition and thus the dynamic boundary condition, given by equation (2.15), can be reduced to a scalar equation for normal stress alone:

$$p'_d - \frac{h'}{Fr^2} = Pa'. \quad (2.28)$$

This equation provides a clear link between the (dynamic) pressure and the surface deformation. Substituting this into the Euler equation leads to:

$$(\mathbf{u}' \cdot \nabla) \mathbf{u}' = -\frac{1}{Fr^2} \nabla h'. \quad (2.29)$$

The kinematic boundary equation tells us that:

$$\mathbf{u}' \cdot \nabla S = 0 \quad (2.30)$$

and, hence, that the gradient of the surface — the local surface slope — is perpendicular to the sub-surface velocity. In dimensional form we can write the total pressure as:

$$p(x, y) = \rho g[h(x, y) - z] + Pa \quad (2.31)$$

which is simply a hydrostatic pressure distribution. Consequently, the two components of the Euler equation, now in dimensional form, become:

$$\begin{aligned} u \frac{\partial u}{\partial x} + v \frac{\partial u}{\partial y} &= -g \frac{\partial h}{\partial x} \\ u \frac{\partial v}{\partial x} + v \frac{\partial v}{\partial y} &= -g \frac{\partial h}{\partial y}. \end{aligned} \quad (2.32)$$

These describe a balance between the advective acceleration on the left-hand side and the hydrostatic pressure distribution on the right-hand side. The kinematic boundary condition becomes:

$$u \frac{\partial h}{\partial y} + v \frac{\partial h}{\partial x} = 0 \quad (2.33)$$

Through equations (2.32) and (2.31), we can directly relate a property of the surface, namely the local surface slope, to properties of the velocity field, albeit under a number of very specific conditions.

One solution to this set of equations is a columnar vortex with an arbitrary tangential velocity profile  $v_\theta(r)$  and no radial velocity. By rewriting the Euler equations in polar coordinates we end up with a single scalar equation that relates the local surface slope to the velocity:

$$\frac{v_\theta^2}{r} = g \frac{dh}{dr}. \quad (2.34)$$

A cylindrically symmetric vortex has a core that is dominated by vorticity and an outer region that is dominated by strain. The vorticity, which in this case only has a component in the  $z$ -direction, can be expressed as:

$$\omega_z = \frac{1}{r} \frac{d(rv_\theta)}{dr} = \frac{d(v_\theta)}{dr} + \frac{v_\theta}{r}. \quad (2.35)$$

while the strain is given by:

$$\sigma_z = r \frac{d}{dr} \left( \frac{v_\theta}{r} \right) = \frac{d(v_\theta)}{dr} - \frac{v_\theta}{r}. \quad (2.36)$$

We can now rewrite equation (2.34) in terms of vorticity and strain:

$$\frac{dh}{dr} = \frac{1}{2g}v_\theta(\omega_z - \sigma_z). \quad (2.37)$$

Before proceeding to prescribing a velocity profile for the vortex, it is useful to rewrite these equations in non-dimensional form. With a typical velocity scale  $U$  and a length-scale  $L$ , we can rewrite equation (2.34) as

$$\frac{dh'}{dr'} = Fr^2 \frac{v_\theta'^2}{r'}, \quad (2.38)$$

where again non-dimensional variables are denoted by a prime. Similarly, we can rewrite equation (2.37) as:

$$\frac{dh'}{dr'} = Fr^2 v_\theta'(\omega_z' - \sigma_z'). \quad (2.39)$$

Now, take  $v_\theta$  in the form of a modified Rankine vortex<sup>‡</sup>:

$$v_\theta = \frac{\Omega r}{1 + (r/a)^2}, \quad (2.40)$$

with  $\Omega$  a measure of the strength of the vortex and  $a$  the vortex radius. In

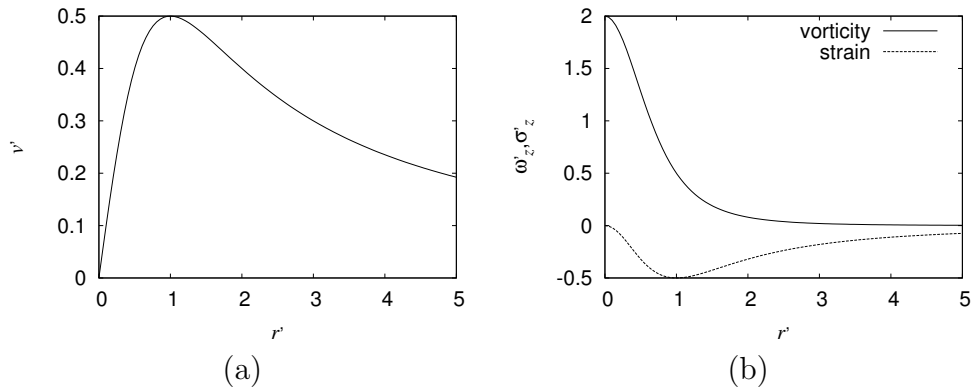


FIGURE 2.2 — Radial profiles of (a) non-dimensional tangential velocity  $v_\theta'$  and (b) the corresponding profiles for vorticity and strain.

<sup>‡</sup>A regular Rankine vortex is characterised by a core of radius  $a$ . Inside this core  $v_\theta = \Omega r$  (solid body rotation) and outside the core  $v_\theta = a^2\Omega/r$ . For this profile, the derivative of the velocity is discontinuous at  $r = a$ , which is why a smoothed version is used here instead.



order to non-dimensionalise this velocity profile, we take  $L = a$  as the length scale and we take  $U = a\Omega$  as the velocity scale. This leads to:

$$v'_\theta = \frac{r'}{1 + (r')^2}. \quad (2.41)$$

We can now calculate the strain and vorticity and, using equation (2.39), we can calculate their contributions to the slope. The velocity profile and the associated strain and vorticity are shown in figure 2.2. The vorticity is highest in the center of the vortex and decreases rapidly as  $r'$  increases towards  $r = 1$ . The absolute value of the strain has its maximum at  $r' = 1$  and then slowly decreases as  $r'$  increases. For this particular velocity profile, we can also explicitly calculate

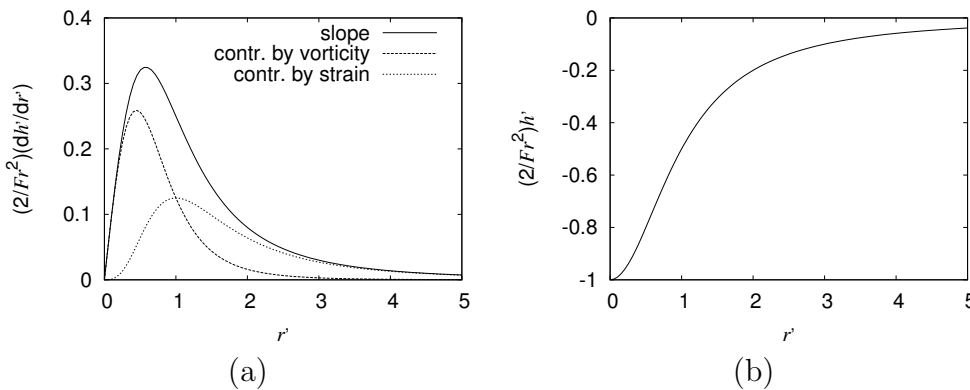


FIGURE 2.3 — Radial profiles of (a) the surface slope and contributions to it by strain and vorticity and (b) the surface height.

the surface elevation by integrating equation (2.38) over  $r'$  and taking  $h' = 0$  for  $r' \rightarrow \infty$ , with the following result:

$$h' = -\frac{Fr^2}{2} \frac{1}{1 + r'^2}, \quad (2.42)$$

which shows that as the Froude number increases, the depression becomes deeper. The contribution of strain and vorticity to the slope and the resulting surface elevation are shown in figure 2.3. For this very much simplified model, as indicated by equation (2.37), the exact shape of the surface depends on a mix of vorticity and strain. However, the deepest part of the depression in the surface coincides with the location where the vorticity has its maximum value.

Dimples in the surfaced above sub-surface vortices can quite commonly be seen in the wake of bridge pillars in a river. In chapter 8 we use a similar configuration — vortices shed behind a surface-piercing cylinder — in order to test our set-up for simultaneously measuring the sub-surface velocity field and

the surface shape. In that case, we can expect a relatively strong link between vorticity and elevation as well as between the Euler terms in equation (2.32) and the surface slopes.

The model described here is essentially two-dimensional. It describes a stationary columnar vortex that ends at the surface, without vertical velocities and with the velocity independent on the depth. It is clear that in reality, certainly for smaller vortices with a relatively low Reynolds number, viscosity will become more important, and the vortex will decay. This decay is coupled to a change in the shape of the surface, and consequently, at the surface, the velocity will no longer be purely tangential. Obviously, similar to the earlier description of linear waves, this model cannot completely describe the link between the surface slope and a turbulent sub-surface velocity field. Still, vortices in the sub-surface turbulence, with a concentration of vertical vorticity, will lead to depressions in the surface, essentially through the mechanism described here. Whether this holds in an experiment and whether it can explain the shape of the surface spectra will be key issues of this thesis. We can already say that at small scales surface tension must start to play a role, an effect that was excluded from the dynamic boundary condition in equation (2.28), and consequently in the balance between advective acceleration and hydrostatic pressure, equations (2.32), as well. A more complete model of the interaction between structures and the surface shape should also include vertical velocities.

## 2.2 Phenomenology of free-surface turbulence

### 2.2.1 TURBULENCE STATISTICS UNDER A FREE SURFACE.

In the preceding section we have looked at the consequences of the fact that, unlike a fixed wall, a free-surface is deformable. However, another important difference between a free surface and a fixed wall is that at a fixed wall the velocity equals zero. Accordingly, unlike at a free surface, at a fixed wall vorticity cannot be present. The turbulence does not only influence the shape of the free surface, but the presence of the free surface also influences the turbulence. Because of its obvious technological importance, for instance for ship or aircraft design, the behaviour of turbulence near fixed walls has been extensively studied for more than a century. Turbulent boundary layers near fixed-walls have become a standard ingredient for textbooks on turbulence. Not surprisingly, how the very different conditions at a free surface influence the sub-surface turbulence has also received considerable attention.

Many of the descriptions of the behaviour of turbulence near a free surface refer to the work of Hunt & Graham (1978), who described how turbulence statistics change, when an initially homogeneous turbulent flow, for instance in a wind tunnel, is convected past a wall moving at the same speed. They aimed to explain experimental results obtained in wind tunnels with a moving wall in the form of a conveyor belt mounted on one of the walls. In their study, Hunt

& Graham (1978) introduced the concept of two boundary layers at the wall. In a layer, which they called the “source layer”, with a depth approximately equal to the integral length of the turbulence, the vertical fluctuations are reduced from their values in the bulk to zero at the wall, by a source-like velocity distribution. In a much thinner viscous layer just below the surface, the horizontal fluctuations are reduced to zero at the wall. Using linear rapid-distortion theory, they showed that inside the source layer, while the vertical velocity fluctuations decrease, tangential fluctuations as well as integral scales actually increase. This linear model is only formally valid for short times, when non-linear terms in the equations of motion are negligible. Hunt and Graham’s results showed generally good agreement with the experiments with a moving wall.

Of course, turbulence moving past a wall moving with the same velocity is not the same as a free surface. Unlike a free surface, the wall is non-deformable and while the absence of a mean shear on the moving wall means that no turbulence is produced at the wall, the velocity fluctuation is zero, whereas for a free surface only the surface-normal gradient of the tangential velocity is zero. In a later paper Hunt (1984) gave a general description of the interaction between turbulence and a deformable free surface in terms of a source layer and a viscous sublayer. More recently, rapid-distortion theory, based on the work by Hunt & Graham (1978), has been applied to a flat stress-free surface by Teixeira (2000) and Teixeira & Belcher (2000), also showing an increase in horizontal velocity fluctuations close to a free surface. A flat stress-free boundary condition corresponds to a free surface with a small Froude and small Weber number, where the turbulence is not strong enough to deform the surface against gravity and surface tension.

The presence of the source layer, also called the “blockage layer” by other researchers, in which a decrease in vertical turbulence fluctuations coincides with an increase in horizontal fluctuations, has been confirmed both by numerical simulations and experiments. Most of the numerical studies use a flat non-deformable stress-free boundary as a model of a free surface. Handler *et al.* (1993), Pan & Banerjee (1995), Nagaosa (1999), and Nagaosa & Handler (2003), have used direct numerical simulations to study turbulent channel flow, in which the turbulence at the free surface originates in the turbulent bottom boundary layer. Perot & Moin (1995) as well as Walker *et al.* (1996) used direct numerical simulations in a slightly different configuration: by numerically inserting no-slip walls in initially homogeneous turbulence. Most experiments on free-surface turbulence have dealt with relatively weak turbulence, so with a nearly flat surface as well. By using a split film anemometer probe to measure horizontal and vertical velocities, Brumley & Jirka (1987) studied the behaviour of turbulence below a free surface, in a set-up in which turbulence was produced by means of a vertically oscillating grid. Loewen *et al.* (1986) studied decaying free-surface turbulence, generated by towing a vertical bar grid through a tank.

They studied structures by means of streak-line images, with aluminium tracer particles sprinkled on top of the free surface. Also using streak-line images, in their case with oxygen bubbles used as tracers, Rashidi & Banerjee (1988) studied the free-surface turbulence in a turbulent channel flow. The turbulence in these experiments originated in the turbulent bottom boundary layer in their water channel. In a later paper, Kumar, Gupta & Banerjee (1998) studied this problem by means of Particle Image Velocimetry to measure velocity fields and to study structures.

From their experiments (Rashidi & Banerjee, 1988; Kumar, Gupta & Banerjee, 1998), as well as from their numerical simulations (Pan & Banerjee, 1995), Banerjee and coworkers conclude that the turbulence near the surface is dominated by structures: upwellings, which are blobs of fluid impinging on the surface that originate from hairpin vortices in the bottom boundary layer, separated by downdraughts, where fluid from adjacent upwellings is forced downward, and spiral vortices. These originate from vortex tubes below that attach to the surface, in a process known as vortex (dis)connection. This will be explained in more detail shortly. Upwellings and downdraughts, also known as “splats” and “anti-splats”, were also noted by Perot & Moin (1995), Walker *et al.* (1996), and by Nagaosa (1999). These researchers agree that the inter-component energy transfer close to the free surface is the result of a net imbalance between upwellings and downdraughts. An upwelling leads to a stagnation point on the surface, with high pressure and a negative gradient of the normal velocity. This has consequences for the pressure-strain correlation. In a stagnation point, the pressure has a maximum. Consequently, the vertical component of the pressure-strain correlation is negative. This leads to a transfer of momentum to surface-parallel fluctuations. In downdraughts the situation is reversed. The vertical velocity gradient in that case is positive, and consequently, energy is transferred from horizontal to vertical fluctuations. Some controversy has arisen over the cause of this net imbalance. Nagaosa (1999) attributes it to the interaction of streamwise vortices with the surface, Perot & Moin (1995) attribute it to viscous effects, and Walker *et al.* (1996) attribute the growth in horizontal fluctuations to the anisotropy due to the vanishing vertical fluctuation. The latter argument is purely kinematic, similar to the rapid-distortion theory by Hunt & Graham (1978). This is supported by recent large-eddy-simulations by Calmet & Magnaudet (2003), who simulated open channel flow, with more intense turbulence than in previous simulations and experiments. Their results show quantitative agreement with the predictions by Hunt & Graham (1978) and Teixeira & Belcher (2000). More recently, by including vortical corrections to the rapid distortion theory, Magnaudet (2003) was able to extend the rapid distortion predictions to longer time-scales and showed that the inter-component energy transfer also depends on (an)isotropy of the turbulence below the free surface and on whether it is decaying or not. Consequently the behaviour close to the surface for isotropic decaying turbu-

lence, as generated with a grid, is expected to be slightly different from the anisotropic turbulence emerging from a turbulent bottom boundary layer.

Banerjee and coworkers note that one-dimensional velocity spectra obtained in their simulations (Pan & Banerjee, 1995), as well as the spectra measured in their experiments (Kumar, Gupta & Banerjee, 1998), show a scaling region  $\sim k^{-3}$ , which is consistent with the prediction for purely two-dimensional turbulence by Kraichnan (1967). According to Handler *et al.* (1993) typical eddies near the surface are flattened, as indicated from an increase in the spanwise scale of the streamwise velocity and, similarly, an increase in the streamwise scale of the spanwise velocity. Vortical structures in the source layer become more prominent as the turbulence decays. Pan & Banerjee (1995) note that if the turbulence decays, which in their numerical simulation can be achieved by 'switching off' the bottom no-slip wall that causes the turbulent bottom boundary layer, the turbulence near the surface becomes more and more dominated by long-lived attached vortices. These vortices interact and merge to form ever larger vortices. This was also noticed by Loewen *et al.* (1986) in their towed-grid experiments. The emergence of strong coherent vortices and their interactions, such as vortex merger, are crucial processes in two-dimensional turbulence (McWilliams, 1984; Maassen, 2000). However, Walker *et al.* (1996) showed that the contribution by vortex-stretching to the production of surface normal vorticity, which is associated with these spiral vortices or pancake-like eddies under the surface, has its maximum near the free surface. Vortex-stretching is a process that, by definition, is absent in two-dimensional flows, and accordingly, the turbulence can only be considered as fully three-dimensional.

### 2.2.2 FREE-SURFACE DEFORMATIONS

The theoretical, numerical, and experimental work on free-surface turbulence described so far does not deal specifically with surface deformations. The free surface was modeled as a non-deformable stress-free wall, corresponding to a situation in which surface deformations are effectively countered. In experiments, surface deformations were small, and received little attention, probably in part due to the difficulties involved in measuring them. We have also seen the importance attributed to various types of structures emerging in the turbulence and interacting with the surface. Understandably, in attempts to understand the more complicated interaction between turbulence and a free surface, interactions between individual structures and a free surface have been extensively studied.

In a review article, Sarpkaya (1996) identifies a whole range of vortical structures that can occur in turbulence, with the common property that they can connect to the free surface, resulting in a surface depression akin to the columnar vortex under a free surface, described in the previous section. The process of vortex tubes breaking up and attaching to the surface is known as vortex (dis)connection. It is illustrated in the cartoon in figure 2.4. Vortex

connection and vortex disconnection are in essence two different names for the same process. As a vortex-tube that is parallel to the surface, for instance the head of a hairpin vortex ejected from a turbulent bottom boundary layer or the front of a vortex-ring, approaches the surface, it tends to break into two sections (vortex disconnection). Subsequently, each of the ends attaches to the surface (vortex connection). A vortex ring is a structure that has been

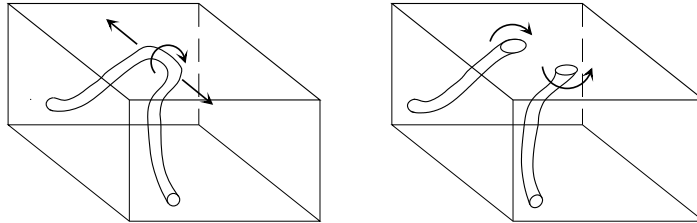


FIGURE 2.4 — Cartoon of vortex (dis)connection. A vortex tube that approaches the surface can break up into two separate parts (vortex-disconnection) that attach to the surface (vortex-connection).

commonly used in order to study vortex (dis)connection, both in experiments, for instance by Bernal & Kwon (1989), Song *et al.* (1992), Gharib & Weigand (1996) and Weigand (1996), and in numerical simulations by Zhang *et al.* (1999) among others. As a vortex ring approaches a free surface, it too tends to break up into smaller vortex tubes that end at the surface. In Weigand's experiments on vortex rings colliding with a free surface (Weigand, 1996), he combined shadowgraphy and Particle Image Velocimetry and found that the locations of large vertical vorticity magnitude corresponded to those of dimples in the surface. Song *et al.* (1992), who used shadowgraphy to visualise the free surface shape, report that the process of connection and disconnection is accompanied by the generation of short waves.

One of the few experiments in which velocity measurements were combined with a quantitative surface shape measurement technique was performed by Dabiri (2003). Particle Image Velocimetry was combined with a two-dimensional free-surface gradient detector developed by Zhang & Cox (1994). The flow being studied was a vertical shear layer, formed between two adjacent flows with different velocities into a channel. Dabiri notes a strong ( $\approx 0.8$ ) correlation between the magnitude of the vertical vorticity and the surface elevation. However, Zhang *et al.* (1999) note that the locations of the maxima of vorticity at the surface and the minimal surface elevation do not coincide, even for these very localised structures, unless the distribution of vertical vorticity at the surface associated with the structure, is cylindrically symmetric. They show this by calculating the free surface shape above a columnar vortex, the axis of which is not normal to the surface. For the example of a columnar vortex under a free surface in the previous section, the vorticity distribution was circular and

the maximum value of the vorticity coincided with the pressure minimum. The strong correlation found by Dabiri (2003), suggests that in a vertical shear layer, the vortices that have the largest influence on the surface in both cases, are large columnar structures. Using the direct link between pressure and the surface elevation, equation (2.28), Dabiri concludes that, since the pressure and the surface elevation are directly correlated, a measurement of the surface elevation over an area can be used to measure the spectrum of the sub-surface pressure. Due to difficulties inherent in measuring it, the pressure spectrum has proven to be elusive, although theoretical work (Batchelor, 1951; Monin & Yaglom, 1975) based on Kolmogorov's turbulence scaling theory has predicted an inertial range in the pressure spectrum with a  $-7/3$  scaling exponent, while theoretical work by George *et al.* (1984) has indicated that for an unbounded flow with a shear layer, the pressure spectrum has a scaling exponent of  $-11/3$ . Dabiri (2003) measured frequency spectra of the surface elevation above the vertical shear layer up to frequencies of 15 Hz. These spectra show a fairly steep scaling range with a scaling exponent of approximately  $-10/3$ . Sadly, the spatial resolution apparently was insufficient to measure spatial spectra as well.

Simulations of turbulence with a deformable interface, and not merely of isolated structures, have been performed by Shen *et al.* (1999) and Tsai (1998). Tsai uses weakly non-linear boundary conditions and direct numerical simulations. The initial condition in these simulations is a two-dimensional shear flow with an added three-dimensional fluctuation. Tsai shows that the correlation between the surface elevation and the absolute normal vorticity is rather low ( $\approx 0.5$ ), while the correlation between dynamic pressure and the surface elevation is much higher, as can be expected from equation (2.28). Obviously, the high pressure associated with the stagnation points that occur above upwellings and downdraughts is also expected to cause surface deformations, as was observed by Brocchini & Peregrine (2001), already referred to in chapter 1. Tsai shows a relatively strong correlation between tangential components of the vorticity below the surface and the surface elevation. Shen *et al.* (1999) investigate the same configuration, and compare a deformable surface with linearised boundary conditions to a flat-non-deformable surface. According to Shen *et al.* (1999), pressure variations due to splats and anti-splats are less pronounced for a deformable surface, since surface ripples tend to smooth local pressure fluctuations. They also remark on the effect of the turbulence generation: anisotropic turbulence generated in a mean shear flow or emerging from a turbulent bottom boundary layer on one hand and more isotropic turbulence, akin to grid-generated turbulence, on the other hand. In the latter case, upwellings and downdraughts are much more rare, and consequently, Shen *et al.* (1999) conclude that the inter-component energy transfer in case of homogeneous (decaying) turbulence is less prominent. As we have seen, Magnaudet (2003) reached this same conclusion based on rapid-distortion theory. With the exception of Song *et al.* (1992), few researchers have mentioned the formation

of waves.

### 2.2.3 THE GENERATION OF WAVES BY TURBULENCE

Work on the interaction between turbulence and free-surface waves has mainly been focused on the effect of wind-generated waves. The waves one sees at a water surface generally are the result of turbulence in the wind above the surface, instead of sub-surface turbulence. In a ground-breaking paper, Phillips (1957) expresses the growth of a Fourier component of the surface elevation in terms of Fourier components of the turbulent pressure fluctuations moving with the wind. The surface elevation and the pressure are coupled through the linearised dynamic boundary condition:

$$\frac{\partial \phi}{\partial t} = \frac{\sigma}{\rho} \left( \frac{\partial^2 h}{\partial x^2} + \frac{\partial^2 h}{\partial y^2} \right) - gh - \frac{p}{\rho} \text{ at } z = 0, \quad (2.43)$$

with  $p = p(\mathbf{x}, t)$  the pressure at the surface. The only difference with the boundary condition for regular linear gravity-capillary waves, equation (2.22), is that now the pressure is no longer constant. The desired relation is found by solving the Poisson equation with this dynamic boundary condition and the kinematic boundary condition given in equation (2.20). This is done in a frame of reference that moves with a convection velocity  $\mathbf{U}_c$ . A solution is found in terms of Fourier transforms of the pressure and the surface elevation in time and space.

Phillips finds that a turbulent pressure fluctuation in the wind, with a wavenumber  $k$ , can excite modes in the surface elevation spectrum, i.e. waves with wavenumber  $k$  traveling under an angle  $\alpha$  relative to the direction of the wind, if the pressure fluctuation moves with velocity  $U_c(k)$  such that:

$$U_c(k) \cos(\alpha) = v_f(k), \quad (2.44)$$

where  $v_f(k) = \omega/k$  is the phase velocity of the gravity-capillary wave in question. In other words, if the projection in a certain direction of the velocity with which the pressure fluctuations move, matches the phase-velocity of gravity-capillary waves of a similar length-scale, gravity-capillary waves can be excited in that direction. Phillips was hindered in comparing the results of his model to observed spectra by the very limited measurements of the pressure spectrum in the wind. Unfortunately, almost fifty years later this quantity remains elusive.

Although the problem of wind-driven water waves is different from the problem we study, the basic concept of how wind can lead to the growth of waves on a free surface can potentially provide a basis for understanding how sub-surface turbulence can lead to gravity-capillary waves. Such a mechanism is briefly mentioned by Brocchini & Peregrine (2001). Simply stated, if a turbulent pressure fluctuation of a certain length-scale  $L$  below the surface, for instance due to the presence of a sub-surface vortex, moves with a velocity



that matches the phase velocity corresponding to  $\lambda = L$ , then the turbulence can excite waves. However, since the phase-velocity of free-surface waves has a minimum of approximately 23 cm/s, as we have seen, this mechanism can only work if the turbulent velocity fluctuations are larger than 23 cm/s. Teixeira (2000), has attempted to use a Rapid-distortion model, based on the model by Hunt & Graham (1978) to study the generation of waves due to sub-surface turbulence. However, Teixeira also was hindered by the difficulties involved in finding a correct pressure evolution. This was further complicated by the nature of rapid-distortion theory, which in essence is kinematic.

In a notable experiment on wind-driven waves in a water tank, Zhang (1995) measured wavenumber spectra of wind-driven waves, by means of the free-surface gradient detector (see Zhang & Cox, 1994), which was also used by Dabiri (2003). Also in a study on wind-generated waves and their influence on sub-surface turbulence, Borue *et al.* (1995) performed direct numerical simulations of turbulence under a deformable interface with linearised boundary conditions and with wind-induced stress on the surface. This work is notable in the context of the problem we study because of one of the situations studied by Borue: surface waves in the absence of wind, i.e. waves generated by the sub-surface turbulence. Borue *et al.* (1995) show that the surface ripples agree reasonably well with the theoretical dispersion relation for linear gravity-capillary waves, equation (2.25), except for small wavenumbers. They also show wavenumber spectra of the surface elevation for these waves. These spectra exhibit a scaling range with a slope of approximately -4.5. The relatively low-intensity turbulence in this case was generated by means of a no-slip bottom wall, in combination with initial three-dimensional perturbations. Unfortunately, it is unclear whether the turbulent fluctuations exceed the minimum phase velocity for surface waves and Borue *et al.* (1995) remark that the coupling between sub-surface turbulence and these surface waves is not yet understood.

The interaction between sub-surface turbulence and the surface elevation is too complex to be captured in a simple model. Although the equations of motion and the boundary conditions at a free surface are known, they only have solutions for very specific linearised cases. Most of the previous work on the interaction between turbulence and the free surface has either focused on how the turbulence is affected by the presence of a free-surface, or — in studies that deal explicitly with free surface deformations — has focused on isolated structures, such as vortex rings that can emerge in turbulence. Although Tsai (1998), Teixeira (2000), and Borue *et al.* (1995), have studied the statistical properties of the surface deformations due to fully-developed three-dimensional turbulence below the surface, as far as we are aware, these statistical properties have never been measured in experiments. The potential formation of waves under influence of the sub-surface turbulence has also never been investigated in an experiment, and, as Borue *et al.* (1995) remark, indeed is not understood.

---

## BASIC PROPERTIES OF THE TURBULENCE

For our experiments it is desirable to use relatively strong and well-controlled turbulence, that preferably is both homogeneous and isotropic. Isotropic turbulence is rare in nature, but it is reproducible and relatively easily characterised. In experiments homogeneous and isotropic turbulence can be approximated by passing a mean flow through a grid. By using a so-called active grid, which uses moving rods with vanes attached to them to stir the flow, stronger turbulence can be produced than with a regular grid. The use of an active grid also allows us to control the properties of the turbulence to a certain degree. Laser-Doppler velocimetry is used to compare active-grid-generated turbulence to turbulence behind a similarly dimensioned static grid. The primary goal is to characterise the turbulence, in order to be able to later compare properties of the surface to those of the turbulence. This will be done in chapters 6, 7 and 8.

### 3.1 Active-grid-generated turbulence

Because of its relative simplicity, turbulence that is both homogeneous and isotropic has received considerable attention in both theory and experiments. In this context “homogeneous” means that the statistical properties of the turbulence are independent of the position in the flow and “isotropic” means that they do not depend on the orientation, or in other words are invariant under rotation. A standard method to generate turbulence in a laboratory setting, for instance in a wind tunnel or water channel, is by passing the flow through a grid consisting of vertical and horizontal bars. At a distance of approximately 40 times the mesh size behind the grid and outside of the boundary layers the generated turbulence is a fair approximation of homogeneous and isotropic turbulence, as was shown by for instance Comte-Bellot & Corrsin (1966). For a comparison of different grids a number of parameters can be used. One of these is the mesh Reynolds number, defined as:

$$Re_M = \frac{Mv_0}{\nu} \tag{3.1}$$

in which  $v_0$  is the mean stream velocity,  $M$  is the mesh size of the grid and  $\nu$  is the viscosity of the fluid. A further parameter is the grid solidity, which is the ratio of the area blocked by the grid divided by the total area of the cross-section of the tunnel or channel. The third parameter that characterises the turbulence itself is the well-known Taylor micro-scale Reynolds number, defined as:

$$Re_\lambda = \frac{v_{rms}\lambda}{\nu}, \quad (3.2)$$

in which  $\lambda$  is the Taylor micro-scale of the turbulence,  $v_{rms}$  is the root-mean-square velocity and  $\nu$  is the viscosity.

Within the Kolmogorov framework, the mesh Reynolds number and the Taylor micro-scale Reynolds number are related as:

$$Re_\lambda = C_f \sqrt{Re_m}, \quad (3.3)$$

with a constant  $C_f$  which depends on the details of the forcing. In case of grid turbulence  $C_f$  depends on the type and the solidity of the grid. Increasing the Taylor-based Reynolds number and thus the intensity of the turbulence in an existing set-up can be achieved through a number of means. One, often impractical option is increasing the mesh Reynolds-number, either by using larger grid-cells, or by increasing the mean-stream velocity, or perhaps even by using a fluid with different viscosity. As an alternative the grid geometry can be changed such that  $C_f$  becomes larger. A comparison by Comte-Bellot & Corrsin (1966) between different types of grids, with either round or square bars and of different solidity ratios, has shown that for a given mesh Reynolds number a large range of turbulence intensities and degrees of anisotropy is possible. Generally, increasing the solidity leads to an increase in turbulence intensity, but also to an increase in anisotropy. Using a so-called Norman grid -a static grid in which every other grid cell is blocked to form a checkerboard pattern- Pearson *et al.* (2002) have achieved a higher value of  $Re_\lambda$  than for similarly sized static grids, but also at the expense of higher anisotropy. More recent experiments by Hurst & Vassilicos (2004) with various types of fractal grids have shown an increase in  $Re_\lambda$  compared to regular static grids, with only a moderate increase in anisotropy.

A special type of grid is the so-called active grid, which was first used in a wind tunnel by Makita (1991) and later used by Mydlarski & Warhaft (1990). Poorte (1998) and Poorte & Biesheuvel (2002) used a similar grid in a water tunnel. An active grid consists of an array of axes with metal agitator wings attached to them. Each axis is driven in a random fashion by an electric motor according to a certain forcing protocol. Poorte (1998) has compared numerous experiments in which turbulence was generated with static grids, finding  $C_f$  to be approximately 0.5. Comparison of his own experiments, those by Makita, and those by Mydlarski and Warhaft showed that the value of  $C_f$  for active grids is close to 2.

## 3.1.1 GRID GEOMETRY

In our experiments we use both a static grid and an active grid. The grid is primarily intended as a tool to generate relatively strong turbulence and it is not our intention to study the effects of forcing with an active grid in detail. Thus, we do not want to stray too far from the territory already explored by Poorte (1998); Poorte & Biesheuvel (2002). Their active grid is the basis for the design of the grid used in the experiments described here. Poorte and Biesheuvel's grid was placed in a vertical water tunnel with a cross-section measuring  $0.45 \times 0.45 \text{ m}^2$  with a maximum mean stream velocity of  $0.4 \text{ m/s}$ . The grid had  $12 \times 12$  mesh cells, with a mesh size of  $3.75 \text{ cm}$ . Hence  $Re_M = 15,000$ . Poorte (1998) concludes that in order to generate a fair approximation of isotropic decaying turbulence by use of an active grid one should use a so-called staggered configuration, in which neighbouring agitator wings on each axis of the grid are perpendicular to each other, as shown in figure 3.2 (a). This configuration limits both the fluctuation and the maximum value of the solidity. However, since generally a higher solidity leads to a higher turbulence intensity, using a staggered configuration leads to a somewhat smaller turbulence intensity, as was shown by Poorte (1998). Our experiments are done in a water channel

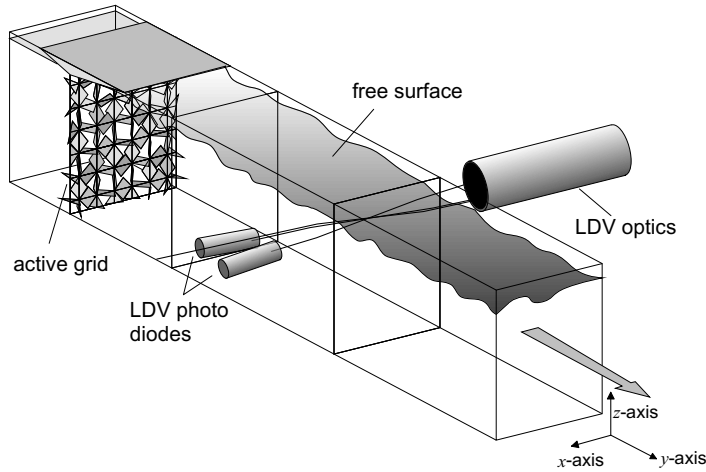


FIGURE 3.1 — Set-up for measuring properties of grid-generated turbulence.

with a width of  $0.3 \text{ m}$ , a water depth of approximately  $0.31 \text{ m}$  with a mean stream velocity from  $0 \text{ m/s}$  up to  $0.3 \text{ m/s}^*$  with a measurement section that is

---

\*The actual maximum velocity depends on the blockage due to the grid. For a static grid the blockage is less than for an active grid, resulting in a lower maximum mean velocity in the latter case

approximately 7.4 m long. It is illustrated in figure 3.1. The water channel itself was an already existing facility, previously used to study turbulent boundary layers over grooved surfaces (Pulles, 1988; van Manen, 1992). The regular

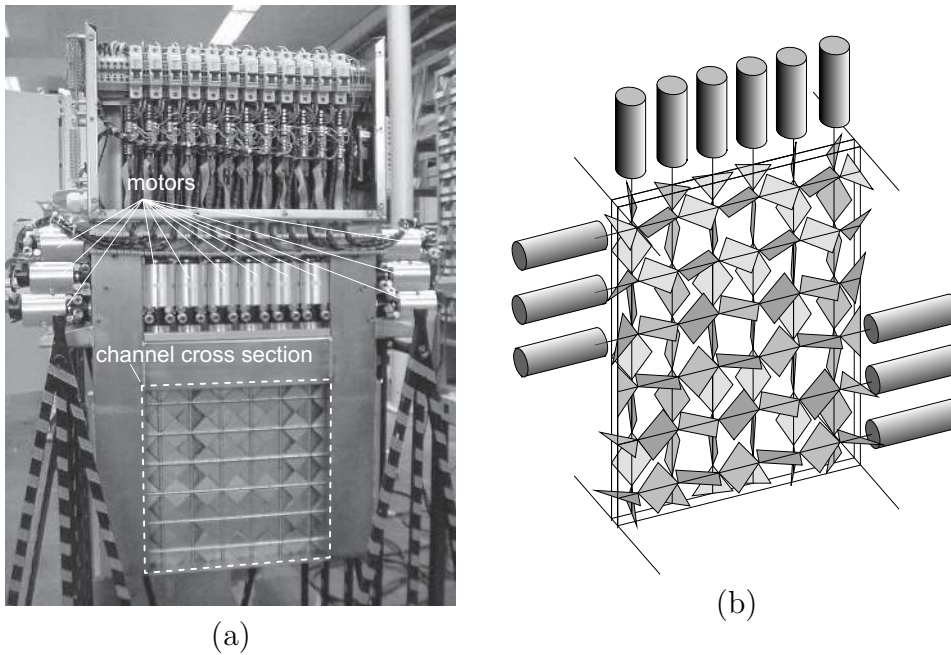


FIGURE 3.2 — (a) Picture of the active grid, with the vanes in non-staggered position. The part of the grid coinciding with the cross-section of the measurement section of the water channel is indicated by the white dashed line. (b) A schematic drawing of the grid, showing the vanes in staggered configuration and also showing the orientation of the motors. On the real grid, the horizontal axis are driven through belt-drives.

static grid used in our experiments consists of  $6 \times 6$  mesh openings. The mesh size  $M = 30/6 = 5$  cm. The open area of each cell measures an area of close to  $4 \times 4$  cm<sup>2</sup>, the cells are separated by square rods with an  $8 \times 8$  mm<sup>2</sup> cross-section and the overall solidity is 0.34. With a mean stream velocity of 0.3 m/s the mesh Reynolds number for this grid is  $Re_M = 15,000$ , which is the same as Poorte's active grid. Taking  $C_f = 0.5$  in equation (3.3), the Taylor-based Reynolds number  $Re_\lambda = 60$ . Obviously, the turbulence intensity that can be achieved with this static grid is rather low. In order to have the same  $Re_M$  for our active grid, it needs to have  $M = 5$  cm as well. The vanes are mounted in staggered configuration on rods of 5 mm in diameter and have a chord of 4.8 cm. A photograph of the grid is shown in figure 3.2 (a) and a schematic drawing of the grid is shown in 3.2 (b). The width of

the channel at its entrance is larger than in the measurement section. The difference in width is overcome by a contraction made out of PVC plating. This allowed building the grid as a self-contained unit that can be slotted into the channel from above by means of a small purpose-built crane. The horizontal axes are driven by belt-drives that run inside the grid's vertical supports and that are attached to motors mounted above the channel. This arrangement obviates the need for holes in the channel walls, thereby reducing the risk of leaks occurring and of the motors and associated electronics coming into contact with water. Because of the combination of high speeds and torque required, quite strong DC motors (Maxon Motors RE 40, 150 W, 48 V) in combination with a 1:4.3 reduction gear (Maxon Motors GP 42) were chosen to force each axis. Each motor is equipped with its own tacho encoder as well as an amplifier (Maxon ADS-E 12-50V, 5 A). A feedback-system, based on the velocity signal obtained from the tacho controllers, is used to ensure that each axis rotates at the prescribed velocity. The amplifiers are controlled through a PC (via a four-channel National Instruments PCI6711 and eight channel PCI6713 PCI-card in turn controlled through a LabView interface). The velocity of each axis, prescribed by the forcing protocol, is updated at a frequency of 20 Hz. A test of a single motor driving an axis back and forth at 7 Hz at  $\pm 7$  revolutions per second showed that in order to prevent overheating the motors needed to be cooled. Hence the motors and the electronics of the grid are water-cooled. The same test also showed that the motor was able to switch from -7 to +7 rev/s within only 10 ms.

### 3.1.2 FORCING PROTOCOLS

Our forcing protocols are based on those used by Poorte (1998); Poorte & Biesheuvel (2002). The type of protocol we use corresponds to what Poorte and Biesheuvel call double-random forcing protocols: each axis has a random angular velocity that is changed at random times. According to Poorte two dimensionless numbers are sufficient to describe forcing protocols for a given grid geometry. The first is the dimensionless angular velocity  $\Omega^*$  based on a comparison of the wing's tip velocity and the mean stream. It is defined by:

$$\Omega^* = \frac{\pi\Omega_0 c}{v_0} = \frac{V_{tip}}{v_0} \quad (3.4)$$

in which  $c$  is the agitator wing chord,  $v_0$  is the mean stream velocity,  $V_{tip}$  is the root-mean-square wing tip velocity and  $\Omega_0$  is the root-mean-square angular velocity. The second dimensionless number is dimensionless time  $T^*$  defined as:

$$T^* = \frac{v_0 T_0}{c} \quad (3.5)$$

where  $T_0$  is the integral time-scale of the forcing protocol. This can be found by integrating the auto-correlation function  $C(\tau)$  of the angular velocity of a given rod over time.

According to Poorte, in order to get homogeneous and isotropic turbulence both dimensionless numbers should be close to unity. However, for none of the protocols listed in Poorte (1998) and Poorte & Biesheuvel (2002) they indeed are both close to unity. In practical terms the actual protocol is defined by two settings: the maximum number of time-steps during which a given rod maintains its angular velocity and the maximum angular velocity. These determine  $T_0$  and  $\Omega_0$  and accordingly the dimensionless numbers  $T^*$  and  $\Omega^*$ . However, the dimensionless numbers are hard to determine à priori and hence they are determined after the protocol has been generated. The calculated auto-

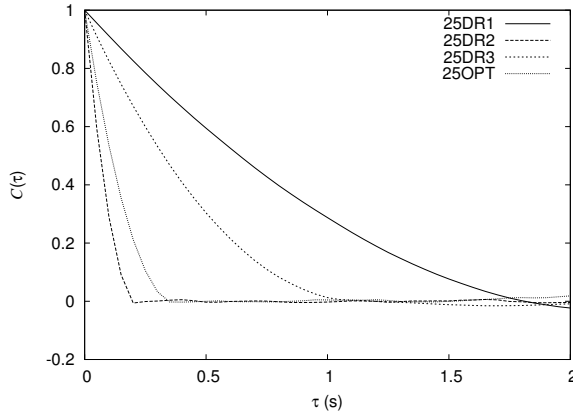


FIGURE 3.3 — Auto-correlation  $C(\tau)$  of the angular velocity for a single axis for protocols 25DR1, 25DR2, 25DR3, and 25OPT.

correlation function for several protocols for a mean-stream velocity close to 0.25 m/s are shown in figure 3.3. In these cases the velocity is already uncorrelated after less than two seconds. All protocols which we use are listed in table 3.1.

TABLE 3.1 — Forcing protocols for the active grid

name	$v_0$ (m/s) (approx.)	$\Omega_{max}$ (Hz)	$\Delta t_{max}$ (s)	$\Omega^*$	$T^*$
25DR1	0.25	0.85	2.25	0.28	5.5
25DR2	0.25	5.12	0.24	1.71	0.34
25DR3	0.25	5.12	1.09	1.71	2.48
25OPT	0.25	2.70	0.42	0.90	0.74
20OPT	0.20	2.10	0.52	0.87	0.83
15OPT	0.15	1.60	0.70	0.86	1.03

The protocols will be referred to by the names listed in the first column in the remainder of this thesis. Protocols (25DR1), (25DR2), and (25DR3) are intended to show some of the effects of changing  $\Omega^*$  and  $T^*$ . Since we vary the mean-stream velocity for some of our experiments, we need different protocols matched to the respective velocities. For these protocols, (15OPT), (20OPT), and (25OPT), both  $\Omega^*$  and  $T^*$  are close to unity. As an example, figure 3.4 (a) shows part of double random protocol (25OPT). In addition to these double-random protocols we also use a protocol (25RAN) in which each axis receives a different random angular velocity that is changed at a fixed frequency. The maximum velocity is 14 rev/s, much higher than for any of the others, and the velocity is changed at a fixed frequency of 7 Hz. Part of this protocol is shown in figure 3.4 (b).

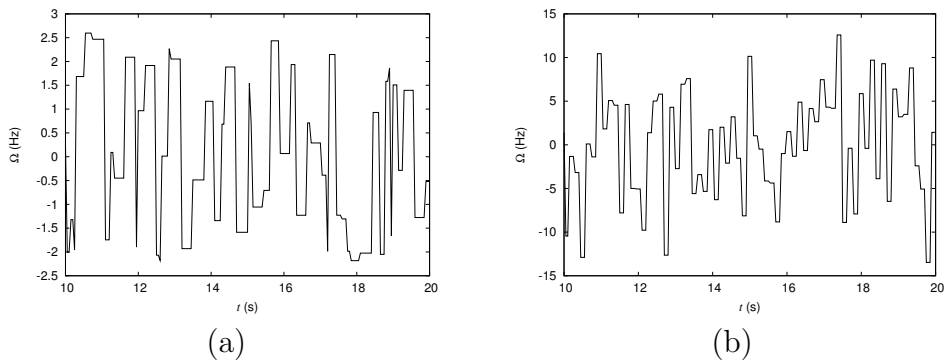


FIGURE 3.4 — Angular velocity for a single axis of the grid as a function of time for (a) double random forcing protocol (25OPT) and (b) the anisotropic protocol (25RAN).

## 3.2 Laser Doppler Velocimetry

In order to study the properties of the turbulence in our experiments we use Laser-Doppler Velocimetry (LDV). This has been the most important measurement technique for time-dependent measurements of the velocity in turbulent flows of water for decades. A detailed description of the fundamentals and applications of LDV can be found in Durst *et al.* (1981) and in a more recent article by Adrian (1996).

### 3.2.1 PRINCIPLE OF LDV

Laser-Doppler Velocimetry is based on measuring a frequency shift due to the Doppler effect occurring in (laser) light scattered off particles which are moving with the flow. Light from a laser beam pointing in a direction  $\mathbf{s}$  is scattered on



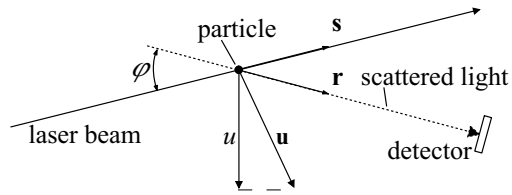


FIGURE 3.5 — Laser-Doppler velocimetry configuration.

a particle. The scattered light falls onto a detector located in direction  $\mathbf{r}$ . Both  $\mathbf{s}$  and  $\mathbf{r}$  are unit length, see figure 3.5. The Doppler-shift in the frequency of the light on the detector is given by:

$$f_d = (\mathbf{u} \cdot (\mathbf{r} - \mathbf{s}))/\lambda, \quad (3.6)$$

in which  $\lambda$  is the wavenumber of the incident light on the particle and  $\mathbf{u}$  is the velocity of the particle. The equation shows that the Doppler-shift has two velocity-dependent terms. One is proportional to  $\mathbf{u} \cdot \mathbf{r}$  and is due to the velocity component of the particle relative to the detector; the other is proportional to  $\mathbf{u} \cdot \mathbf{s}$  and is the result of the velocity of the particle relative to the light source. The combination of these two leads to the Doppler-shift being proportional to the length of the velocity component in the direction  $\mathbf{r} - \mathbf{s}$  (the scattering vector), so:

$$f_d = 2u \sin(\varphi/2)/\lambda \quad (3.7)$$

in which  $u$  now is the magnitude of the component of the velocity in the plane formed by  $\mathbf{r}$  and  $\mathbf{s}$ , and  $\varphi$  is the angle between the incident beam and the light that hits the detector; the angle between vectors  $\mathbf{s}$  and  $\mathbf{r}$ . A measurement of this frequency would reveal the magnitude of the velocity, but not its direction, since one can only measure positive frequencies  $f = |f_d|$ .

In most practical situations the frequency shift is very small compared to the frequency of the light itself. Because of this it is generally measured through interference. The method used for the measurements described here is the so-called reference beam method, which requires two beams to measure a velocity component: a so-called scattering beam and a reference beam. The principle is based on mixing of the scattered light, which includes the Doppler shift, with light of which the frequency is unchanged. The geometry is illustrated in figure 3.6. The detector receives light from a number of sources. Light from the reference beam is scattered by particles, but this does not lead to a Doppler-shift, since  $\mathbf{r} = \mathbf{s}$ . The two sources that matter are the reference beam itself, with frequency  $f_{ref}$  and light from the scattering beam, scattered by particles moving through it. The latter is Doppler shifted and has a frequency  $f_{sct} + f_d$ , in which  $f_d$  is the Doppler shift and  $f_{sct}$  is the frequency of the scattering beam. The detector, a photo diode in our case, operates as a quadratic detector with

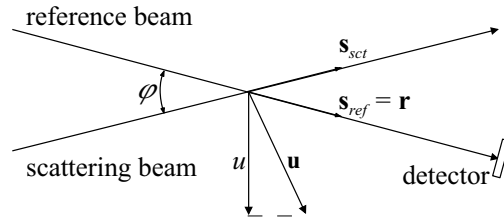


FIGURE 3.6 — Principle of the reference beam method for LDV measurements.

a limited frequency response, which only sees the difference of the incoming frequencies:

$$f = |f_{sct} + f_d - f_{ref}|. \quad (3.8)$$

This interference on the detector can only occur when the wave-fronts are parallel, that is when the scattered light originates from the intersection of the scattering- and reference beams (Adrian & Goldstein, 1971). Ideally this measurement volume lies in the waist of both beams since in that case the location is well-defined and the signal-to-noise ratio is improved due to the light intensity being higher inside the smaller volume. Furthermore, in this case the frequency measured does not depend on where the particle passes through the measurement volume (Durst & Stevenson, 1979).

It is customary to use a single laser in combination with a beam splitter to produce the scattering and the reference beams. This does mean that, without any further measures being taken, the measured velocity would be directionally ambiguous since  $f_{sct} = f_{ref}$  in equation (3.8). This can be overcome by shifting the frequency of one of the beams. In the set-up used for our experiments this is done by using a Bragg-cell placed in one of the beams. Light falling onto a crystal under the so-called Bragg-angle results in an interference pattern on the other side of the crystal. In the Bragg-cell a crystal is forced to resonate at a certain frequency under influence of an acoustic wave. As a result the interference maxima undergo a frequency shift equal to the acoustic frequency at which the Bragg cell is driven. The first maximum of the interference pattern is used as the scattering beam. The measured frequency now becomes:

$$f = |(f_{ref} + f_s + f_d) - f_{ref}|. \quad (3.9)$$

As long as  $f_s$  is chosen to exceed  $|2u \sin(\varphi/2)/\lambda|$ , this is directly related to the velocity through:

$$f = |f_s + f_d| = f_s + 2u \sin(\varphi/2)/\lambda. \quad (3.10)$$

without any directional ambiguity.

### 3.2.2 THE SET-UP FOR LASER-DOPPLER MEASUREMENTS

A schematic picture of the Laser-Doppler set-up is shown in figure 3.7. It uses a modular Dantec X55 optical system. The LDV optical system was built out

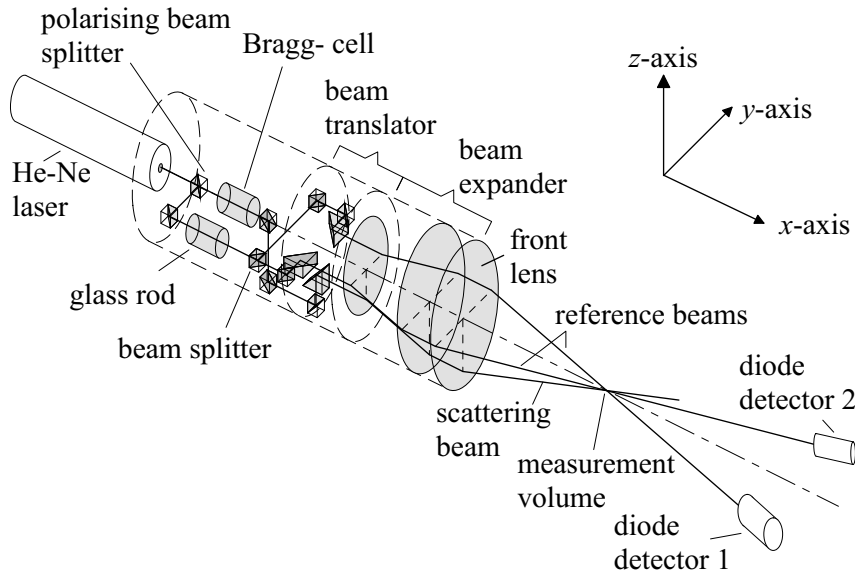


FIGURE 3.7 — The 55X LDV system for the water-channel.

of a number of Dantec X55 modules. These cylindrical modules contain the beam-splitters, a Bragg-cell and mirrors needed to create three beams, one of which has a pre-shift  $f_s$  of 40 MHz due to the inclusion of the Bragg-cell. This beam is used as the scattering beam. The other two unshifted beams are the reference beams. The use of two reference beams enables measurements of two velocity components. The change in optical path length in the scattering beam, resulting from its passage through the Bragg-cell is compensated for in the reference beams by passing them through a glass rod. This enables the use of lasers with a small coherence length. The entire cylinder can be rotated around its axis, facilitating the alignment. The entire optical system is mounted on a moveable yoke. This allows the measurement volume to be placed anywhere in the channel, from a depth of 23 cm up to the surface. As indicated in figure 3.7, we have chosen to use a coordinate system in which the  $x$ -axis corresponds to the spanwise direction, the  $y$  axis corresponds to the streamwise direction (with increasing  $y$  as the distance to the grid increases) and with the  $z$ -axis pointing upwards from the surface. The average height of the surface corresponds to  $z = 0$  and  $x = 0$  corresponds to the centre line of the channel. The orientation of the beams is such that it allows measurement of two velocity components: a

component in the plane formed by reference beam 1 and the scattering beam and a second component, perpendicular to the first, which lies in the plane formed by reference beam 2 and the scattering beam. These planes and the corresponding velocity components are illustrated in figure 3.8. The detectors are Dantec 55L21 photo-diodes. The Doppler shift  $f_{d1}$  in the signal measured

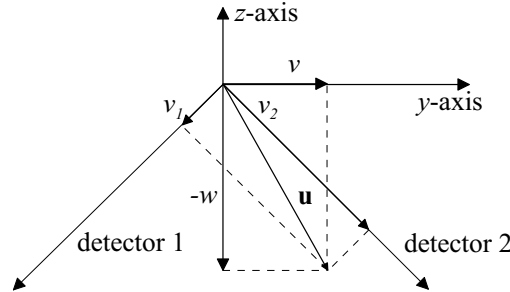


FIGURE 3.8 — Orientation of the velocity components in a plane  $x = \text{constant}$ , through the measurement volume. We directly measure components  $v_1$  and  $v_2$  of the velocity projected in the  $x = 0$  plane. In post-processing they are converted to vertical and streamwise components,  $w$  and  $v$ , respectively.

by detector 1 can be expressed as:

$$f_{d1} = v_1 \frac{2 \sin(\varphi/2)}{\lambda}, \quad (3.11)$$

and the Doppler-shift  $f_{d2}$  in the signal measured by detector 2 is:

$$f_{d2} = v_2 \frac{2 \sin(\varphi/2)}{\lambda}. \quad (3.12)$$

in which  $v_1$  and  $v_2$  are the velocity components in both planes and  $\varphi$  is the angle between either reference beams and the scattering beam. Through two straightforward geometrical relations the actual streamwise velocity component  $v$  and the vertical component  $w$  can be calculated:

$$v_1 = \frac{1}{\sqrt{2}}(-v - w) \quad (3.13)$$

and

$$v_2 = \frac{1}{\sqrt{2}}(v - w). \quad (3.14)$$

The signals from both detectors are each passed to a Dantec 55N12 shifter unit. These units electronically subtract the original pre-shift of 40 MHz and

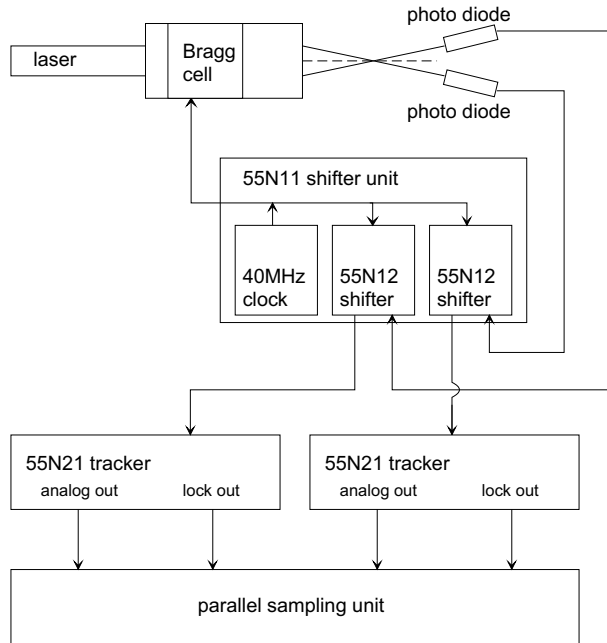


FIGURE 3.9 — Components of the signal processing.

add a selectable shift between 1 and 9000 kHz, because simply subtracting the optically introduced pre-shift of 40 MHz would reintroduce the directional ambiguity that was the reason for introducing a pre-shift in the first place. The signals with their new pre-shifts are sent to Dantec 55N20/55N21 tracker units. These use a phased-locked-loop to measure the frequency (Gardner, 1979). The tracker's output voltage is linearly dependent on the frequency in the incoming signal. A second output on the tracker indicates whether the phased-lock loop indeed is locked and can be used to assess the quality of the data. The trackers have a built-in low-pass filter with a cut-off at 100 Hz. The two signals for each tracker are sent to a 1 kHz PARSAM (parallel sampling) unit for A/D conversion, storage, and processing by a PC. In a measurement at any given location typically a million samples of each component were obtained, for a total duration of approximately 17 minutes. A set of Fortran programmes was used to convert the tracker's frequency signals to actual streamwise and vertical velocities through equations (3.10), (3.13) and (3.14). The angle  $\varphi$  was determined by the distance of the beams to the rotation axis of the X-55 system before placement of the final focusing lens combined with the focal length of that lens and, of course, the refractive index of the water.

### 3.3 Properties of the turbulence

#### 3.3.1 HOMOGENEITY

Since the location of the measurement volume of the laser-Doppler set-up can be changed in both vertical and spanwise direction it is possible to check the homogeneity of the turbulence in cross-sections of the channel. These measurements are done at 40 times the mesh size behind the grid, so at 2 m, where the turbulence can be expected to be fully developed. Figure 3.10 shows horizontal

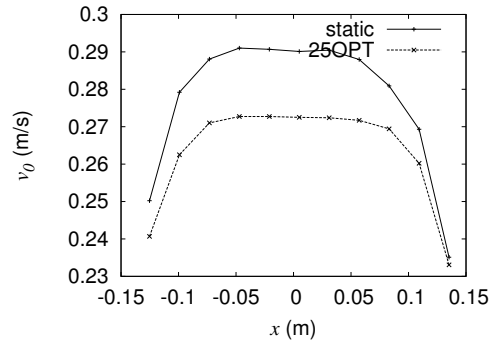


FIGURE 3.10 — Profiles of the mean-stream velocity for both the active grid with protocol 25OPT and the static grid.

profiles of the mean-stream velocity for both for the active and the static grid, for the same setting of the water-channel pump. As can be expected in turbulent channel flow, these profiles show a region near the channel centre where the mean-stream velocity is practically constant, flanked by regions, the boundary layers from the channel walls, where the mean-stream velocity is lower. Due to the higher blockage of the active grid, the mean-stream velocity is somewhat lower than in case of the static grid. In the wall boundary layers the streamwise fluctuation velocity is higher than in the centre. In the boundary layers the measured fluctuation velocities, which are tangential to the channel side-walls, are higher than near the channel centre. The increase is the strongest in the streamwise velocity component, which is obviously associated with anisotropy in the boundary layers. Spanwise measurements of both the streamwise and vertical components of the fluctuation velocity are shown in figure 3.11. Similar measurements in the vertical direction, shown in figure 3.12, show that the turbulence fluctuation is practically constant up to a certain depth below the surface, for both the streamwise and the spanwise fluctuations. Consequently, the ratio of  $v_{rms}/w_{rms}$ , shown in figure 3.13, is practically constant up to a certain depth. This observation is in full agreement with the existence of a source layer as described in the previous chapter: a layer below the surface, with a

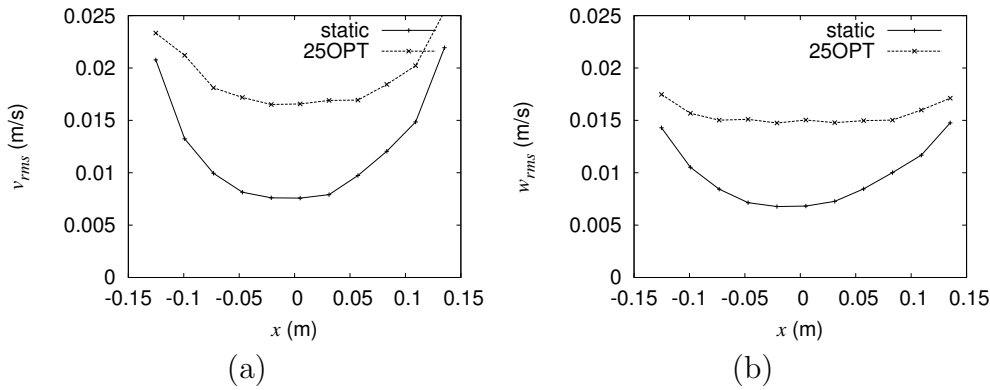


FIGURE 3.11 — Spanwise profiles of (a) streamwise turbulence fluctuation  $v_{rms}$  and (b)  $w_{rms}$  measured at 10 cm below the surface at 2 m from the grid.

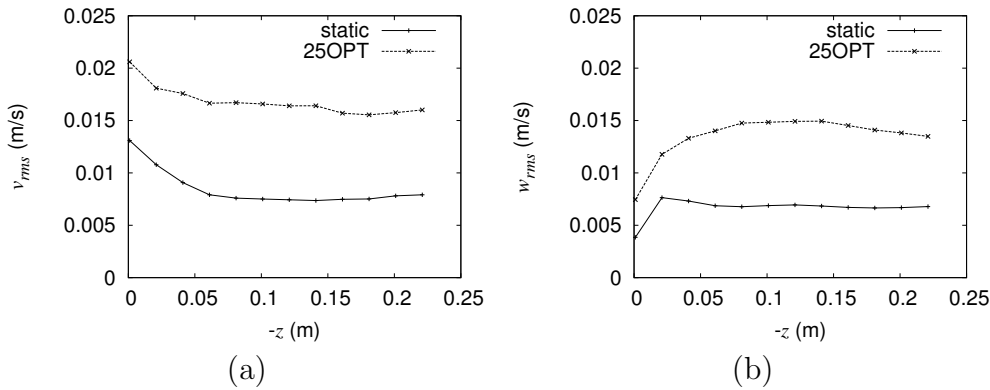


FIGURE 3.12 — Vertical profiles of (a) streamwise fluctuation velocity  $v_{rms}$  and (b) and the spanwise fluctuation velocity  $w_{rms}$  measured at the centre line of the channel ( $x = 0$ ) at 2 m from the grid.

thickness of roughly one integral length-scale, in which energy is redistributed from vertical to horizontal fluctuations. The bottom boundary layer can not be seen in these measurements, since it lies outside of the vertical range over which the measurement volume can be traversed. Figure 3.14 shows measurements of the velocity fluctuations with Laser-Doppler Velocimetry at approximately 7 cm below the surface. For isotropic decaying turbulence, the turbulence intensity scales algebraically with the distance to the grid. In our coordinate system, with  $y$  being the streamwise direction Mohamed & LaRue (1990):

$$\left(\frac{v_{rms}(y)}{v_0}\right)^2 \sim \left(\frac{y}{M}\right)^n, \quad (3.15)$$

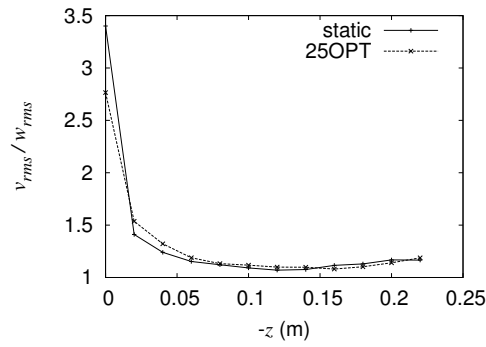


FIGURE 3.13 — Vertical profiles of the anisotropy ratio  $v_{rms}/w_{rms}$  measured at 2 m from the grid.

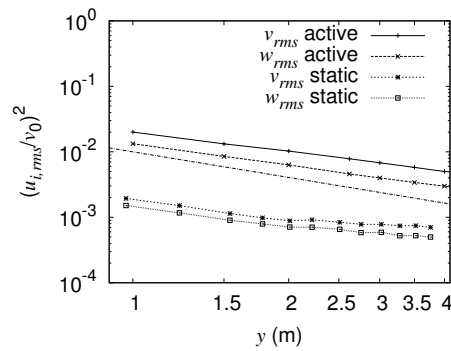


FIGURE 3.14 — Turbulence intensity (at 10 cm below the surface on the channel center line) as a function of the distance to the grid, for both the active grid, with protocol (25RAN) and the static grid (25STAT).

with a scaling exponent  $n \approx -1.3$ , and  $M$  the grid mesh size. A line with this slope is also shown in Figure 3.14. The turbulence generated with the active grid indeed seems to scale algebraically with the distance to the grid, albeit with a slightly different scaling exponent. The turbulence generated with the static grid decays more slowly for distances over 2 m and ( $y/M > 40$ ). A possible explanation for this is that, even though at 2 m it is nearly isotropic, beyond 2 m from the grid, the relatively weak turbulence generated by the static grid has decayed sufficiently for the turbulence from the bottom and side-walls of the channel to become important.

Overall, these measurements show that at 2 m behind the grid in a region of approximately 10 cm wide near the centre of the channel and up to about 6 cm



below the surface the turbulence generated by both the active and the static grid is approximately homogeneous in both the spanwise and vertical directions. Due to the presence of the surface and the associated source layer, the turbulence is no longer homogenous as we move closer to the surface, and it obviously is not homogeneous inside the boundary layers formed on the channel walls. Since the turbulence decays, the turbulence is obviously not homogeneous in the streamwise direction. However, since at 2 m we are relatively far removed from the grid the turbulence decays relatively slowly. Consequently, over a relatively small volume at 2 m from the grid, far below the surface and near the channel centre line, the turbulence can be considered approximately homogeneous.

### 3.3.2 TURBULENT SCALES

Our LDV measurements correspond to the most common way of measuring turbulence properties: through a point-measurement of one or multiple components of the velocity as a function of time. The turbulence properties measured

TABLE 3.2 — Overview of turbulence properties measured on the centre line of the channel at 2 m behind the grid and 10 cm below the surface.

name	$v_0$ (m/s)	$v_{rms}$ (m/s)	$\frac{v_{rms}}{v_0}$	$\frac{v_{rms}}{w_{rms}}$	$\epsilon$ ( $\text{m}^2\text{s}^{-3}$ )	$\lambda_{t,E}$ (cm)	$\lambda_{t,C}$ (cm)	$Re_\lambda$
25DR1	0.270	$1.52 \cdot 10^{-2}$	5.6%	1.08	$4.1 \cdot 10^{-5}$	0.92	1.0	140
25DR2	0.269	$1.80 \cdot 10^{-2}$	6.7%	1.10	$4.8 \cdot 10^{-5}$	1.0	1.2	180
25DR3	0.270	$2.37 \cdot 10^{-2}$	8.8%	1.14	$7.2 \cdot 10^{-5}$	1.1	1.3	256
25OPT	0.271	$1.62 \cdot 10^{-2}$	6.0%	1.10	$3.4 \cdot 10^{-5}$	1.1	1.2	173
20OPT	0.221	$1.27 \cdot 10^{-2}$	5.7%	1.05	$2.4 \cdot 10^{-5}$	1.0	1.1	128
15OPT	0.166	$9.70 \cdot 10^{-3}$	5.8%	1.05	$8.5 \cdot 10^{-6}$	1.3	1.3	126
25RAN	0.266	$2.29 \cdot 10^{-2}$	8.7%	1.15	$6.2 \cdot 10^{-5}$	1.1	1.2	252
25STAT	0.289	$7.50 \cdot 10^{-3}$	2.6%	1.10	$9.7 \cdot 10^{-6}$	0.73	0.83	70

for the different forcing protocols as well as the static grid are listed in table 3.2. It is immediately clear from this table that the streamwise fluctuation velocity  $v_{rms}$  varies widely with the forcing. The static grid leads to the lowest turbulence intensity, 2.6%, while depending on the protocol for the active grid it varies from 5.6% to 8.8%. The forcing by the active grid is such that the active grid at a low mean-stream velocity, protocol (15OPT), produces not only a higher turbulence intensity but actually a higher absolute value of  $v_{rms}$  than

the static grid at a mean-stream velocity that is almost twice as high, protocol (25STAT).

How the various other scales of the turbulence can be determined from point measurements can be found in standard textbooks on turbulence such as Frisch (1995) or Pope (2000). Hence, the description given here is somewhat concise. In the wave-number domain the inertial range behaviour of the one-dimensional longitudinal wavenumber spectrum of the velocity is given by:

$$E_{LL}(k) = \alpha k^{-5/3} \epsilon^{2/3} \quad (3.16)$$

in which  $\alpha \simeq 0.55$  is an empirical constant, see for instance Mohamed & LaRue (1990) and Pearson *et al.* (2002), and  $\epsilon$  is the dissipation. With LDV we can

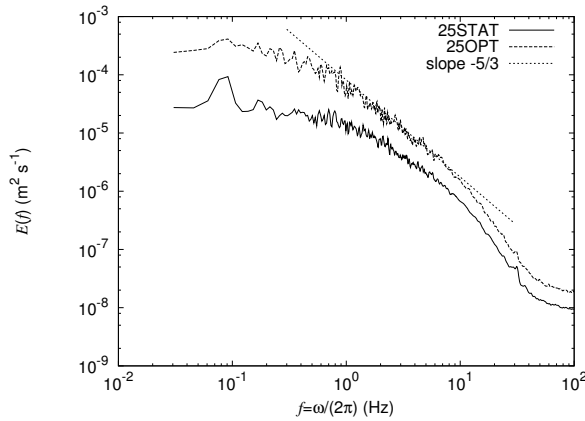


FIGURE 3.15 — Longitudinal energy spectra for the static grid and the active grid with protocol (25OPT), measured at 10 cm below the surface and 2 m behind the grid.

measure the frequency spectrum  $E_v(f)$  of the streamwise velocity component  $v$ . Assuming that Taylor's hypothesis can be used, we can relate this frequency spectrum to the longitudinal wavenumber spectrum, given in equation (3.16), through:

$$E_v(f) = E_{LL}(k(f)) \frac{dk(f)}{df}, \quad (3.17)$$

with Taylor's hypothesis entering into:

$$k(f) = \frac{2\pi}{v_0} f, \quad (3.18)$$

where  $v_0$  is the mean of the streamwise velocity. Similarly, from our measurement of the vertical component of the velocity, we could in principle calculate

the transverse wavenumber spectrum of the turbulence. The inertial range behaviour in the measured frequency spectrum of  $v$  can be expressed as:

$$E_v(f) = \left(\frac{2\pi}{v_0}\right)^{-2/3} \alpha f^{-5/3} \epsilon^{2/3} \quad (3.19)$$

Hence, the dissipation  $\epsilon$  can be determined by fitting a line with slope  $-5/3$  to measured frequency spectra. Two examples of such frequency spectra, one measured behind the active grid with protocol (25OPT) and the other measured behind the static grid, are shown in figure 3.15. The higher turbulence intensity obtained with the active grid is clearly visible in the larger area of the spectrum. Furthermore, the spectrum for the more intense turbulence generated with the active grid shows a clear range with Kolmogorov  $-5/3$  scaling, whereas this is not clearly present in the spectrum for weaker static-grid-generated turbulence.

The difference between the active and static grid becomes clearer when comparing their Taylor-microscale based Reynolds numbers, given previously in equation (3.2). The Taylor-microscale can be measured in a number of ways. The first of these is by means of the velocity auto-correlation function. The transverse Taylor-microscale  $\lambda_t$  can be measured from the transverse velocity auto-correlation function<sup>†</sup>, which for small separations  $r_y$  can be written as:

$$C_{TT}(r_y) = 1 - \left(\frac{r_y}{\lambda_t}\right)^2. \quad (3.20)$$

In our measurements the transverse correlation function  $C_{TT}(r_y)$  is represented by the correlation  $C(\tau)$  of the vertical velocity component  $w$  in time. This is transformed into  $C_{TT}(r)$  by again invoking Taylor's hypothesis:  $r_x = v_0\tau$ . As an example, the measured the transverse correlation function for two different protocols is shown in figure 3.16, together with two parabolic functions used to find  $\lambda_t$ . A second way of measuring the Taylor-microscale is through the dissipation found from the velocity energy spectrum. Provided that the turbulence is isotropic:

$$\epsilon = 15\nu \frac{v_{rms}^2}{\lambda_t^2}. \quad (3.21)$$

The transverse Taylor micro-scales for the various forcing protocols found from both the spectra and the correlation functions, denoted as  $\lambda_{t,E}$  and  $\lambda_{t,C}$ , respectively, are listed in table 3.2. In our measurements the difference between the two micro-scales generally is about 10 %, which gives an indication of the accuracy of the measurements.

With these Taylor-microscales we can see that, for the cases of which spectra were shown in figure 3.15,  $Re_\lambda=70$  for the static grid, whereas for the active grid

---

<sup>†</sup>In a similar fashion one can define a longitudinal Taylor microscale  $\lambda_l$  from the longitudinal correlation function. For isotropic turbulence  $\lambda_l = \sqrt{2}\lambda_t$  (Pope, 2000).

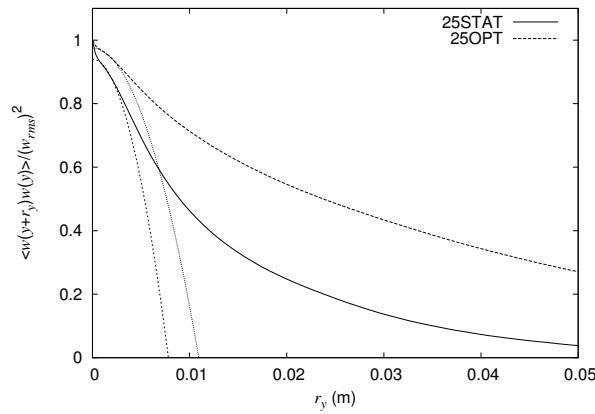


FIGURE 3.16 — Transverse velocity correlation function for the static grid and the active grid with protocol (25OPT), measured at 10 cm below the surface and 2 m behind the grid.

with protocol (25OPT)  $Re_\lambda=173$ , despite a slightly lower mean stream velocity in the latter case. The forcing constant  $C_f$  in equation (3.3) is 0.6 for the static grid and 1.5 for protocol (25OPT). The largest value  $Re_\lambda = 256$  was reached for protocol (25DR3), with  $C_f = 2.2$ . Interestingly, the very different protocol (25RAN) gives a very similar  $Re_\lambda$ .

Another length-scale that can be derived from the auto-correlation function is the integral length-scale. It follows from integrating the auto-covariance function over space. In longitudinal direction this becomes:

$$L_L = \int_0^\infty C_{LL}(r)dr, \quad (3.22)$$

where the spatial coordinate follows from time through Taylor's hypothesis<sup>‡</sup>. This equation shows that the integral length-scale is a measure for the longest distance over which motions in the turbulence are still correlated. It can be considered as the length-scale of the largest structures in the turbulence. These largest structures often reflect a typical length-scale of the forcing. For instance, in static-grid-generated turbulence this integral length-scale is generally close to the mesh-size of the actual grid. In practice one cannot measure over indefinitely long periods and measurements of the correlation over large separations are fraught with difficulty. Hence, in practice, it is fairly common to use a some sort of curve-fitting procedure to the measured correlation function. In our case we used the function  $1 - \exp(r/L)$ , with  $L$  the integral scale. Obviously

<sup>‡</sup>Of course a similar relation exists for the transverse integral length-scale  $L_t$ . For isotropic turbulence  $L_L = 2L_T$  (Pope, 2000).

TABLE 3.3 — Integral length-scales and the Kolmogorov scales for the static grid and two protocols for the active grid.

	STATIC	25OPT	25DR3	25RAN
$L_L$ (m)	$2.6 \cdot 10^{-2}$	$8.5 \cdot 10^{-2}$	$8.3 \cdot 10^{-2}$	$6.5 \cdot 10^{-2}$
$\eta_k$ (m)	$5.7 \cdot 10^{-4}$	$4.1 \cdot 10^{-4}$	$3.4 \cdot 10^{-4}$	$3.6 \cdot 10^{-4}$
$\tau_k$ (s)	0.32	0.17	0.12	0.13
$v_k$ (m/s)	$1.8 \cdot 10^{-3}$	$2.4 \cdot 10^{-3}$	$2.9 \cdot 10^{-3}$	$2.8 \cdot 10^{-3}$

this method only provides a fairly rough indication of the integral scale, but good enough to compare the different types of forcing. Some results are listed in table 3.3. It is obvious that turbulence produced with the active grid has a far larger integral scale than the static grid. In fact it would appear to be larger than the mesh-size of the grid, which can be understood as follows: the opening and closing of adjacent grid-cells due to the random movement of the agitator wings can produce a pattern with larger length-scales than the scale of each individual cell. Further scales often used to characterise the turbulence are the Kolmogorov scales, that follow from the following equations (Frisch, 1995): The Kolmogorov length-scale:

$$\eta_k = \left( \frac{\nu^3}{\epsilon} \right)^{\frac{1}{4}}, \quad (3.23)$$

the time-scale:

$$\tau_k = \left( \frac{\nu}{\epsilon} \right)^{\frac{1}{2}}, \quad (3.24)$$

and the corresponding velocity scale:

$$v_k = (\nu\epsilon)^{\frac{1}{4}}. \quad (3.25)$$

The Kolmogorov scales for a number of different protocols are also listed in table 3.3. We see that the Kolmogorov lengths, associated with the smallest vortices in the turbulent flow are smaller for the active grid than for the static grid, consistent with the turbulence being stronger in the former case.

### 3.3.3 ISOTROPY

For grid-generated turbulence, outside of the boundary layers, isotropy in planes perpendicular to the mean-stream direction is practically assured. However, measurements in other planes often show anisotropy. Isotropy can be defined in a number of different ways. The simplest measure of isotropy is the ratio

of fluctuation velocity components, in our case the ratio of  $v_{rms}$  over  $w_{rms}$ . Its value for the various protocols is listed in table 3.2. For static grids a difference between the streamwise and vertical root-mean-square velocities of up to 10 percent is fairly common Comte-Bellot & Corrsin (1966), and indeed for our static grid we find a 10% difference. The difference for the active grid ranges from 8% up to 15%. Interestingly, an increase of turbulence intensity is accompanied by an increase in the difference between  $v_{rms}$  and  $w_{rms}$ , something which was already noted for the comparison of various static grids by Comte-Bellot & Corrsin (1966).

A comparison of the turbulent velocities only reveals anisotropy existing at large scales. Scale-dependent anisotropy information can be obtained through analysing correlation functions. For incompressible three-dimensional isotropic turbulence the longitudinal and transverse correlation functions are related through (Pope, 2000):

$$C_{TT}(r) = C_{LL}(r) + \frac{1}{2}r \frac{d}{dr} C_{LL}(r) \quad (3.26)$$

Hence, the measured transverse correlation function can be compared to the transverse correlation function that follows from the measured longitudinal correlation function through equation (3.26). If they lie close together, this is an indication of isotropy. However, since the correlation functions are normalised with the respective root-mean-square velocities, such a comparison does not show the difference between  $v_{rms}$  and  $w_{rms}$ . This may be cured by considering the structure functions instead. These are related to the auto-correlations through:

$$S_{2,L} = \langle (v(y+r) - v(y))^2 \rangle = 2(v_{rms})^2(1 - C_{LL}(r)) \quad (3.27)$$

and

$$S_{2,T} = \langle (w(y+r) - w(y))^2 \rangle = 2(w_{rms})^2(1 - C_{LL}(r)). \quad (3.28)$$

In case of isotropy,  $v_{rms} = w_{rms}$  and hence we can find a relation between the longitudinal and transverse 2nd-order structure functions for isotropic turbulence. Analogous to equation (3.26), in isotropic turbulence they are related through:

$$S_{2,T}(r) = S_{2,L}(r) + \frac{1}{2}r \frac{d}{dr} S_{2,L}(r). \quad (3.29)$$

We can now compare the actually measured transverse 2nd-order structure function with that which follows from the measured longitudinal 2nd-order structure function through this equation.

Figure 3.17 shows results for all different types of forcing for the maximum mean stream velocity. Since one cannot expect there to be isotropy beyond the integral length-scale, the distance  $r$  for which the structure functions are shown ranges from 0 to  $r/L_L = 1$ . The structure functions shown in these graphs are actual measurements, while a fourth-order polynomial fit was used

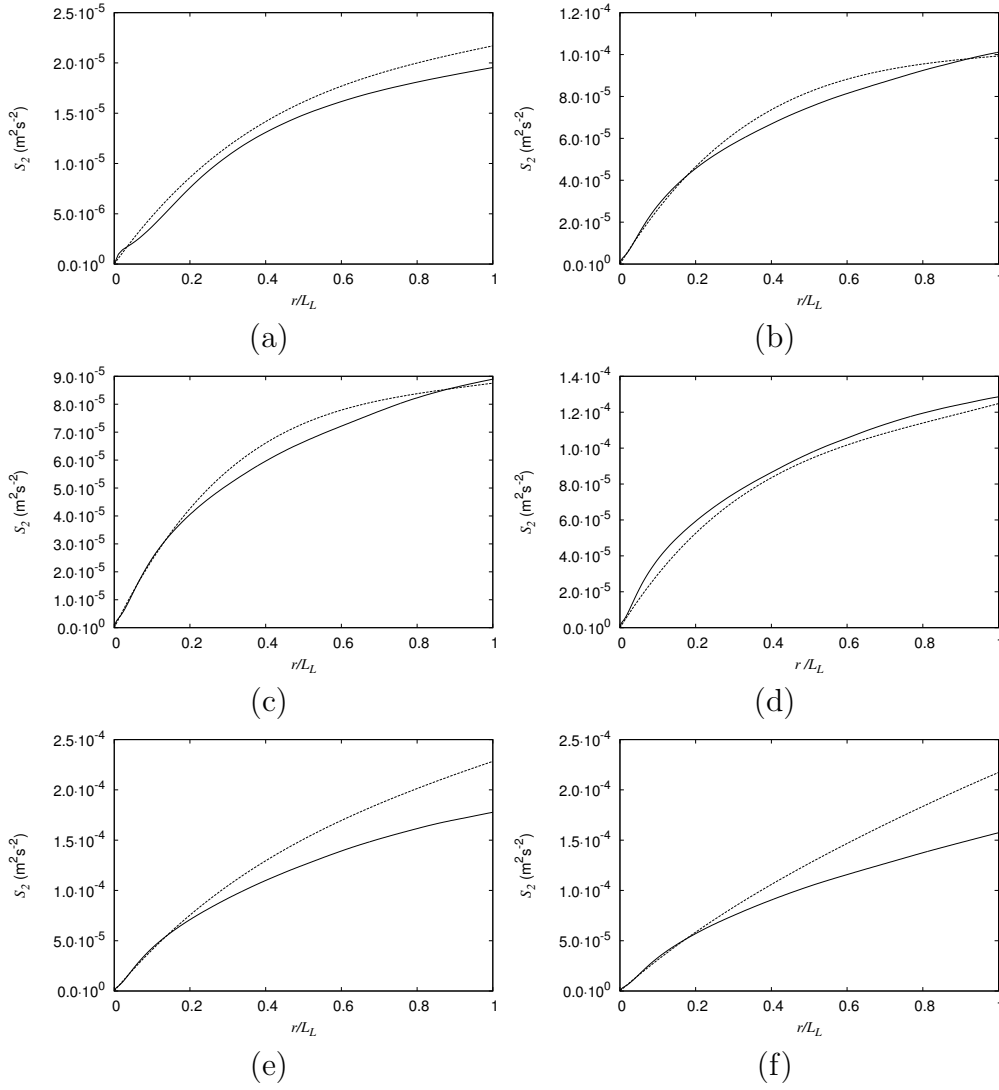


FIGURE 3.17 — Longitudinal and transverse 2nd-order structure functions for different forcing: (a) 25STAT, (b) 25OPT, (c) 25DR1, (d) 25DR2, (e) 25DR3, and (f) 25RAN. the solid line represents the measured transverse structure function and the dashed line represents the transverse structure function that follows from the measured longitudinal structure function through the relation for isotropic turbulence, equation (3.29).

to calculate the derivative of  $S_{LL}$ . For the static grid generated turbulence (25STAT) in figure 3.17 (a) the calculated and measured transverse structure

functions indeed lie fairly close together, although they start to deviate for larger separations. Thus the turbulence would seem to be practically isotropic. The structure functions for the three protocols intended to show the influence of the dimensionless parameters  $\Omega^*$  and  $T^*$ , (25DR1), (25DR2), and (25DR3) are shown in figures (c),(d) and (e). With the exception of the strongest turbulence, protocol (25DR3), they are broadly similar. For protocol (25DR3) as well as (25RAN) the calculated and measured  $C_{TT}$  already differ for small separations. This difference becomes even larger as the separation increases. Clearly the turbulence is anisotropic, as was already indicated by the ratio of  $u_{rms}/w_{rms}$ . Overall the forcing protocol with both dimensionless variables  $\Omega^*$  and  $T^*$  closest to one, (25OPT) shown in figure (b), offers a fair compromise between turbulence intensity and isotropy. The slightly stronger turbulence generated with protocol (25DR2), for which both dimensionless parameters are also fairly close to unity, see table 3.1, is very similar.

### 3.4 Conclusions

Using Laser-Doppler measurements we have compared the statistics of turbulence generated by an active grid to turbulence generated by a similarly dimensioned static grid. One of the reasons for using grid turbulence was that, typically, it is a fair approximation of homogeneous and isotropic turbulence. Our measurements show that for both the active grid and the static grid, outside of the boundary layers and relatively far below the surface, the turbulence can indeed be considered approximately homogenous. As was already clear from the literature, the active grid produces far stronger turbulence than the static grid, in our experiments with a Taylor-microscale based Reynolds number  $Re_\lambda = 70$  for the latter and up to  $Re_\lambda = 256$  with the former. Because of the larger intensity, the active-grid-generated turbulence exhibits clear Kolmogorov scaling. As an indication of the accuracy of our measurements, we have derived the Taylor length-scale in two different manners: via dissipation calculated from the spectrum and, more directly, through the velocity correlation function. The difference between both values is less than 10%. Coupled to the larger turbulence intensity, the integral length-scale of active-grid-generated turbulence is larger ( $\approx 8$  cm) than that of turbulence generated by the static grid ( $\approx 3$  cm). Another advantage of the active grid is that, by changing the forcing protocol, the isotropy of the turbulence can be changed. Our Laser-Doppler set-up is limited to measuring the vertical and the streamwise components of the velocity. Hence, we can only measure isotropy in those directions. We see that, in general, for protocols that generate the strongest turbulence the turbulence is also the most anisotropic. By scaling the protocol such that the dimensionless rotation velocity and dimensionless time given in equations (3.4) and (3.5) are close to unity, as suggested by Poorte (1998) and Poorte & Biesheuvel (2002), the active-grid-generated turbulence is very close to isotropic. The importance



of the isotropy will become more clear in chapter 7, where we describe measurements of the isotropy of the surface above the turbulence.

---

# MEASURING TURBULENCE PROPERTIES WITH PIV

## 4.1 Introduction

Particle Image Velocimetry (PIV) is a technique for measuring fluid velocities and velocity gradients in a plane. In our experiments on free-surface turbulence PIV is used to measure the turbulent sub-surface velocity field in our water-channel in order to compare it to the free-surface deformation connected with the turbulence.

PIV has seen widespread use in fluid dynamics, especially since the introduction of digital cameras with a sufficiently high frame rate and relatively high spatial resolution, (Willert & Gharib, 1991; Westerweel, 1993). The principle of PIV is very straightforward: small particles suspended in the flow are illuminated by a laser light sheet and the local fluid velocity is inferred from their displacement. In most applications for measuring turbulence, series of image pairs are recorded by a digital CCD camera. These digital images are sub-divided into smaller, usually square, areas called interrogation windows. If sufficient particles are present in the corresponding interrogation windows in two subsequent images, the cross-correlation of the intensity distributions in the windows has a distinct peak. The peak's position is a measure of the displacement of the particles in the interrogation window. The positions of the peaks from all of the interrogation window pairs in two subsequent images result in a vector field, which represents a snapshot of the velocity field in the plane illuminated by the laser\*.

The fact that PIV can be used to measure the velocity field in a plane offers a major advantage over the other velocimetry technique used in the water channel, Laser Doppler Velocimetry (LDV), which is a point measurement of the velocity

---

\*This assumes that the time between two images is short enough to consider the displacement as equivalent to the velocity.

as a function of time. In principle PIV can be used to obtain specific spatial information such as velocity gradients and vorticity. Spatial spectra of velocity, spatial velocity correlation functions and vorticity are also of interest. Unlike LDV, PIV does not require the use of Taylor's frozen turbulence hypothesis for obtaining spatial spectra and correlations. However, as is already clear from the description of the principle of PIV, the obtained velocity field is a spatially filtered representation of the actual velocity field. Obviously, structures that are larger than the region in the flow corresponding to the image cannot be seen, as well as structures in the flow that are smaller than the interrogation windows. Measuring turbulence by means of PIV requires a compromise: on one hand large interrogation windows improve the accuracy, as will be explained shortly. On the other hand using large interrogation windows compromises the spatial resolution that can be resolved.

We seek to answer the question what the relation is between the measured velocity field and the actual velocity field in a turbulent flow, focusing on the effect that PIV has on turbulence statistics such as velocity spectra and correlation functions as well as velocity gradients. Keane & Adrian (1991) showed that the measured velocity is a weighted spatial average of the actual velocity in the interrogation window. The low-pass filtering effect of this averaging on measured turbulence spectra was first described by Lourenco & Krothapalli (2000). There are further subtle issues that depend on the interrogation window size and that may have a dramatic effect on measured turbulence spectra. For example, choosing too small interrogation windows may result in noise, due to the emergence of spurious vectors.

It is fairly common to test the accuracy of PIV and new PIV algorithms by using a known velocity field to generate synthetic images and then comparing the actual field to the field obtained from evaluating those images with PIV. Some researchers have studied PIV by using single images based on a known velocity field of, for instance, a single Oseen vortex (Luff *et al.*, 1999), series of images derived from Monte-Carlo simulations (Keane & Adrian, 1990; Westerweel, 1993), or even images with uniform displacement (Forliti *et al.*, 2000). However, relatively few researchers have used spectra in their comparisons, despite the obvious benefits of using such a method. Understanding how PIV influences the spectrum also allows one to understand how the spatial averaging influences all other second-order statistics and allows an assessment of the influence of measurement noise. Foucaut & Stanislas (2002) and Foucaut, Carlier & Stanislas (2004) have compared spectra measured with PIV to spectra measured with hot-wire anemometry, confirming the description of PIV as a low-pass filter, and have also studied the influence of measurement noise on derivative calculations. Lecordier *et al.* (2001) have used direct numerical simulations to generate synthetic images and have compared spectrum obtained with PIV to those obtained from the numerical simulation, also using the spectrum as a tool for understanding how PIV measures root-mean square velocities.

We will take a look at the effect the filtering has on the spectrum based on results of kinematic simulations. These simulations are used to generate realistic PIV images of a turbulent velocity field with a prescribed velocity spectrum. The images are subsequently evaluated with PIV to allow us to compare the actual spectrum and the measured spectrum. Our method is unique as the input spectrum can be changed easily, in contrast to that of a direct numerical simulation, or that of an actual experiment. Rather than defining the quality of PIV through comparison of true and measured velocity fields, we define it through the statistical properties of the velocity field. Such an approach is most appropriate to our problem, as we will be interested in the statistical connection between the surface and the velocity field. From these spectra, other quantities — such as correlation functions — follow readily.

## 4.2 The principle of PIV

Before proceeding to describe the spectral issues, we will start by taking a closer look at a number of issues associated with PIV. The accuracy of the results that can be obtained by PIV is in part determined by the algorithm. Hence, it is important to describe its details. A schematic overview of the steps taken in the algorithm is shown in figure 4.1.

As a first step the images are sub-divided into interrogation windows and the cross-correlation functions between the intensity distributions in corresponding windows in subsequent images are calculated. This cross-correlation function contains a number of contributions: random correlations between particle images, correlation between the background intensities, noise, and a contribution due to the particle displacement<sup>†</sup>. The latter, the so-called displacement peak, is obviously the contribution that is important for PIV. The algorithm searches for the highest peak in the cross-correlation function. In order for this highest peak to actually be the displacement peak, a sufficiently large number of particles present in the interrogation window in the first image should also be present in the second image. Figure 4.2 shows the volume in the light sheet that corresponds to a single interrogation window. Particles that are present within this volume when the first image of a particle image pair is taken will have moved into a slightly deformed and slightly displaced volume by the time the second image is taken a time  $\Delta t$  later. Hence, some of the particles that were present within the interrogation volume in the first image will have moved out of the interrogation volume by the time the second image is taken. Similarly,

---

<sup>†</sup>Non-uniform background illumination typically leads to a contribution to the cross-correlation function with a maximum at zero displacement. Noise in the images is primarily the result of thermal noise in the camera. The effects of both non-uniform background radiation and thermal noise can be reduced by suitably pre-processing the images with a digital filter. However, these filters can have an adverse effect on the accuracy of the sub-pixel algorithms common in PIV codes.

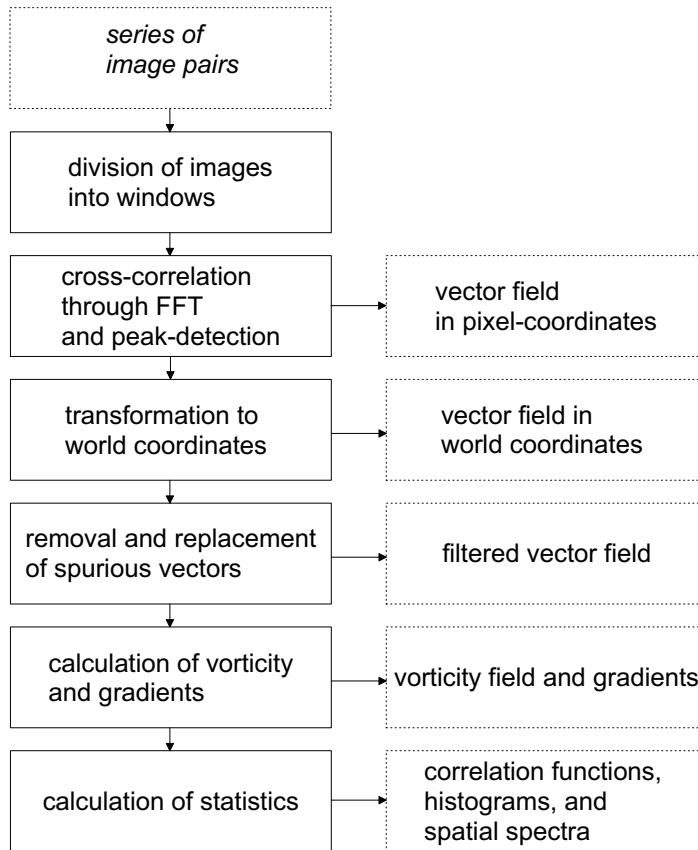


FIGURE 4.1 — Overview of the PIV-algorithm.

in the time between the two images, some particles will have moved into the interrogation volume. Only particles that are present in the overlap between both volumes will be present in both particle images and only those particles lead to a to the displacement peak. This effect is commonly called *particle loss*<sup>‡</sup>.

The result of too few particles being present in both images, which can be the result of particle loss, but also of too few particles being present in the flow overall, is a decrease in the relative size of the displacement peak in the cross-correlation function. The peak's height is also decreased by velocity gra-

<sup>‡</sup>Since it is associated both with particles being advected out of the interrogation volume as well as with particles being advected into it, i.e. particle gain, the term particle loss is somewhat misleading. Particle image pair loss would be a more appropriate term. However, since particle loss is the name used in most literature it will also be used here.

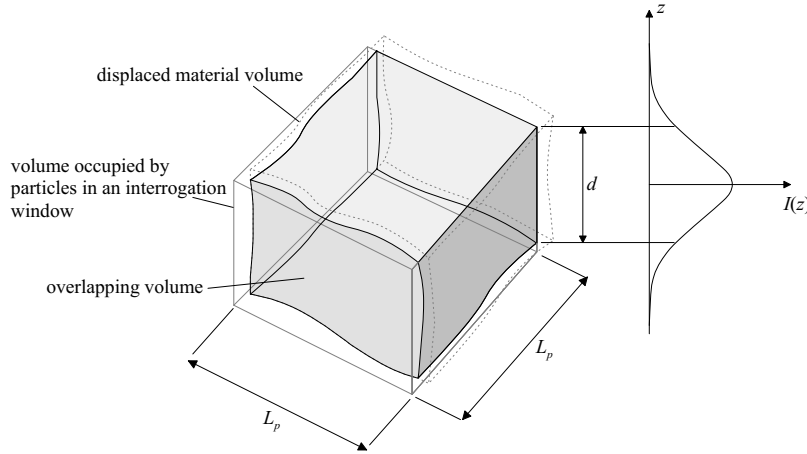


FIGURE 4.2 — An interrogation window corresponds to a volume within the light sheet. Due to turbulence, the material volume occupied by the particles when the first image is taken will be slightly deformed and displaced by the time that the second image is taken. As a consequence, particles move out of the interrogation volume and other particles enter the interrogation volume in the time between the two images. Only particles in the overlapping volume, indicated in grey in this figure, are present in both images.

dients inside of the interrogation window. In the worst case other contributions dominate the cross-correlation function and the algorithm will no longer identify the displacement. The result of this is commonly called a *spurious vector*. Usually, a spurious vector differs dramatically from its neighbours. Because of this, spurious vectors have a large detrimental effect on gradients and spectra calculated from the velocity field. However, this also makes spurious vectors relatively easy to identify. The likelihood of the occurrence of spurious vectors can be reduced by choosing the parameters of the PIV-experiment according to criteria derived by Keane & Adrian (1990, 1991):

- At least 15 particles should be present in an interrogation window.
- The time interval  $\Delta t$  between two images in a pair is a compromise between having a decent dynamic range and preventing in-plane particle loss. For the former the maximum displacement should be as large as possible, which will be explained in more detail later. For the latter, the in-plane displacement should be at most one quarter of the width  $L_p$  of the interrogation window or:

$$\frac{|U|\Delta t}{L_p} < 0.25, \quad (4.1)$$

where  $U$  is the in-plane component of the velocity field.

- Similarly, particles being advected perpendicular to the light sheet, so-called out-of-plane particle loss, can be limited by matching the depth  $d$  of the light sheet and the time between images  $\Delta t$  to the normal velocity such that:

$$\frac{|w|\Delta t}{d} < 0.25, \quad (4.2)$$

where  $w$  is the velocity normal to the light sheet.

In addition to increasing the likelihood of the occurrence of spurious vectors, in-plane particle loss can be expected to lead to a bias towards lower velocities, since particles in regions of fast-moving fluid are more likely to leave the interrogation window than slowly traveling particles.

Clearly, in a turbulent flow, the smallest length-scale that can be resolved, the smallest velocity difference that can be measured, and the time-delay  $\Delta t$  have to be compared to the Kolmogorov length-, velocity-, and time-scales, respectively. Typically, the turbulent energy  $E(k)$  is a rapidly decreasing function of the wavenumber  $k$ , and it is clear that spurious vectors especially influence the high wavenumbers and lead to larger errors in measured spectra.

Because of the use of a digital camera, the cross-correlation function can only be calculated in discrete points, meaning that the location of the peak in the correlation function can be resolved with a resolution of one pixel. As in most other algorithms, in our algorithm the cross-correlations is calculated using Fast-Fourier transforms. In many practical cases, to ensure a large enough number of particles in the interrogation window, an interrogation window size of  $32 \times 32$  pixels is a practical minimum. In that case the maximum allowed displacement is 8 pixels. Hence, the dynamic range of the measured velocities is very limited. Of course, increasing the size of the interrogation windows increases the dynamic range.

Most PIV algorithms, as well as ours, use Gaussian interpolation of the correlation peak in order to find the sub-pixel coordinates of the displacement peak, thereby increasing the dynamic range. This approach makes sense since the point-spread function, that describes how a small illuminated particle is imaged by a camera system, is approximately of Gaussian shape and the cross-correlation function of two Gaussian distributions is Gaussian as well. Sub-pixel resolution does require that the point spread function of the particles in the digital images covers multiple pixels, preferably an area of about  $2 \times 2$  pixels (Raffel *et al.*, 1998). If the particle diameters are small, the sub-pixel algorithm is biased towards integer pixel displacements. This effect is called pixel-locking. The root-mean-square error in the sub-pixel displacement is at best 0.05 (West-erweel *et al.*, 1997) to 0.1 pixel (H. Huang *et al.*, 1997). In order to improve the accuracy of the sub-pixel resolution the relative height of the displacement peak should be increased. Obviously, one way to do this is by having more particles

present in the interrogation window, which in an experiment can easily be done by increasing the size of the interrogation windows. This has the added benefit of decreasing in-plane particle loss. Not only does particle loss decrease the height of the displacement peak, it also increases the random correlations and particle loss is a major contributor to noise. Thus, having large interrogation windows increases sub-pixel accuracy, by decreasing in-plane particle loss and by increasing the number of particles present in each window. However, these trends are opposite to what is needed for a faithful measurement of turbulent flows: small velocity fluctuations — for which precise measurements help — occur at small scales, which are averaged over in large interrogation windows.

Another way to decrease the influence of particle loss and to increase the sub-pixel accuracy is by a technique called *window shifting* (Westerweel *et al.*, 1997). In this technique the second window in each pair is shifted over the integer number of pixels corresponding to the mean velocity in each window, after which the cross-correlation function is recalculated. This is used in many recent PIV-algorithms, some of which actually use a multi-scale iterative procedure in which as a first step large interrogation windows are used to obtain a rough estimate of the local velocity. Subsequently the cross-correlation is recalculated with shifted windows. In subsequent steps the interrogation window size is decreased (Scarano & Riethmuller, 1999). In our algorithm we use window shifting in order to compensate for the mean velocity present in the water channel in our experiments, but the interrogation window size is fixed.

In the algorithm, before proceeding with the removal of spurious vectors, the positions and lengths of the velocity vectors found from the images are converted into world coordinates, so from pixels to for instance m/s. In the experiments great care is taken to align the optical axis of the camera perpendicularly to the light sheet and a camera lens is used that does not lead to any dramatic distortions of the image. Transformation from displacements in pixels to world coordinates can then be done very easily, without any need for interpolation, by simply multiplying the coordinates in pixels with a constant. In order to calculate velocities, displacements can simply be divided by the time  $\Delta t$  between two images in a pair, provided that  $\Delta t$  is sufficiently small.

The next step in our algorithm is removing spurious vectors by means of a filter. This filter can use a number of different criteria to determine whether a vector is valid or not. If the difference between the length of an individual vector and the mean velocity exceeds a certain threshold, the vector is discarded. In a second, more stringent test the length of the vector can be compared to the median of the length of the surrounding vectors. If the difference between the individual vector and the median exceeds a second threshold the vector is discarded. These filters are an efficient way to identify spurious vectors (Westerweel, 1994), but may also remove turbulent structure. The removed vectors are replaced by using linear interpolation, this to facilitate the subsequent calculation of velocity gradients.



Velocity gradients and vorticity are calculated using a simple mid-point rule. We will take a closer look at measuring velocity gradients later. Finally, averages, spectra and correlation functions are calculated for the image series.

### 4.3 Inherent filtering by PIV

The smallest scale in the velocity field that can be resolved by PIV is determined by the interrogation window size. Then, according to the Nyquist sampling criterion the grid spacing should not be larger than half the window size.

It is fairly common to use a grid spacing of half the width of the interrogation windows, which means that neighbouring interrogation windows have a 50% overlap. Generally, in order to resolve small scales, one should use small interrogation windows, but in practice their minimum size is limited, as we have seen in the previous section. For a typical PIV camera of  $1024 \times 1024$  pixels, interrogation windows of  $32 \times 32$  pixels and 50 % overlap between neighbouring windows, the resulting velocity field only has  $63 \times 63$  data points. Because of this, typically, the range of scales in PIV is very limited compared to the range of scales for turbulence. In our case, with  $Re_\lambda \approx 200$ , the ratio of the largest to smallest scales is more than an order of magnitude larger than the number of interrogation windows per window size. Hence, the spatial resolution of PIV is insufficient for resolving the smallest scales in the flow. The measured velocity field is a spatially filtered version of the actual field. The question now is what the characteristics of this filter are and how the inherent filtering influences spectral quantities.

#### 4.3.1 A DESCRIPTION OF THE FILTER

A description of the filtering has been given by Keane & Adrian (1992). It is based on calculating the location of the peak in the cross-correlation function of the intensity distributions associated with the particle movement, for an arbitrary velocity field. This requires a number of assumptions: other contributions to the cross-correlation function should be negligibly small, the point spread function which describes how a particle is imaged, should be relatively small compared to the size of the interrogation window, all particle images are taken as identical, and the time between the images is short enough to allow displacements and velocities to be considered equivalent.

They conclude that the velocity measured for a given interrogation window in the image actually corresponds to the projection on a plane of the spatial average of the velocity. Because particles only contribute to the velocity if they are present in both images, the spatial average is the average over the overlap between the interrogation volume itself and the region to where the particles have been advected by the time that the second image of the pair is taken. This was already illustrated in figure 4.2. Mathematically it can be expressed as follows: the volumes can be represented by so-called window

functions, which equal 1 within a certain region and 0 outside that region. The volume corresponding to an interrogation window with size  $L_p \times L_p$  around coordinate  $(\mathbf{x}_0) = (x_0, y_0)$  and thickness  $d$  can be represented by a function:

$$W(\mathbf{x}, \mathbf{x}_0) = \begin{cases} 1, & |x - x_0| < L_p/2, \quad |y - y_0| < L_p/2, \quad \text{and} \quad |z| < d \\ 0, & \text{otherwise.} \end{cases} \quad (4.3)$$

The volume to where they are advected to can be represented by the window function  $W(\mathbf{x} + \mathbf{u}(\mathbf{x}, t)\Delta t, \mathbf{x}_0)$ . The overlapping volume can then be represented by the product  $P$  of both window functions:

$$P(\mathbf{x}, \mathbf{x}_0, \mathbf{u}) = W(\mathbf{x}, \mathbf{x}_0)W(\mathbf{x} + \mathbf{u}(\mathbf{x}, t)\Delta t, \mathbf{x}_0). \quad (4.4)$$

The velocity  $\bar{\mathbf{u}}_p(\mathbf{x}_0, t)$  measured for an interrogation window in the image centred around coordinate  $\mathbf{x}_0$ , can now be expressed as spatial average of the velocity over the volume represented by window function  $P$ :

$$\bar{\mathbf{u}}(\mathbf{x}_0, t) = \frac{\int_V P(\mathbf{x}, \mathbf{x}_0, \mathbf{u}) \mathbf{u}_p(\mathbf{x}, t) \, d\mathbf{x}}{\int_V P(\mathbf{x}, \mathbf{x}_0, \mathbf{u}) \, d\mathbf{x}}, \quad (4.5)$$

in which  $\mathbf{u}_p$  is the projection of the velocity in planes ( $z = \text{constant}$ ) and in which  $\int_V \dots d\mathbf{x}$  represents a volume integration.

#### 4.3.2 THE EFFECT OF SPATIAL AVERAGING ON TURBULENCE STATISTICS.

The velocity, averaged over the volume corresponding to an interrogation window, can be written as:

$$\bar{\mathbf{u}}(\mathbf{x}) = \int_{-\frac{d}{2}}^{\frac{d}{2}} \int_{-\frac{L_p}{2}}^{\frac{L_p}{2}} \int_{-\frac{L_p}{2}}^{\frac{L_p}{2}} \mathbf{u}(\mathbf{x}) \, dx \, dy \, dz, \quad (4.6)$$

where  $L_p \times L_p$  are the dimensions of the area of the light sheet represented by the interrogation window and  $d$  is the thickness of the light sheet. The projection of this in the plane  $z = 0$  corresponds to the velocity measured with PIV given in equation (4.5), provided that the effect of particle loss is neglected.

The longitudinal velocity spectrum  $E_{xx}(k_x)$  for turbulence follows from integration of the full three-dimensional spatial spectrum over  $k_y$  and  $k_z$ :

$$E_{xx}(k_x) = \iint E_{xx}(\mathbf{k}) \, dk_y \, dk_z, \quad (4.7)$$

where the three-dimensional spectrum in turn follows from:

$$E_{xx}(\mathbf{k}) = \langle |\tilde{u}(\mathbf{k})|^2 \rangle, \quad (4.8)$$

in which  $\tilde{u}(\mathbf{k})$  is the full three-dimensional Fourier transform of the velocity. Fourier transforming the measured spatially averaged velocity, given in equation (4.6), in three-dimensions would lead to the spatially averaged three-dimensional spectrum. Integrating that over  $k_y$  and  $k_z$  would lead to the one-dimensional longitudinal velocity spectrum as measured by PIV. Similarly, the measured longitudinal correlation function follows from:

$$\overline{C}_{xx}(r_x) = \iiint T(\mathbf{r}' - \mathbf{r}) C_{xx}(\mathbf{r}') d\mathbf{r}' \Big|_{r_y=0, r_z=0}, \quad (4.9)$$

where  $T(\mathbf{r})$  is a three-dimensional tent-map function with a width  $2L_p$  in the  $r_x$  and  $r_y$ -directions and a width  $2d$  in the  $r_z$ -direction.

In order to clarify the consequences of the spatial averaging, instead of using these rather complicated three-dimensional equations, we will use one-dimensional representations. In one dimension, still without particle loss, the averaging inherent to PIV expressed in equations (4.5) can be expressed in terms of a straightforward convolution product:

$$\overline{u}(x) = \int P(x - x') u(x') dx', \quad (4.10)$$

in which  $P(x)$  is a top-hat function representing the interrogation window and of the same width  $L_p$  as the interrogation window:

$$P(x) = \begin{cases} 0, & |x| > \frac{L_p}{2} \\ \frac{1}{L_p}, & |x| < \frac{L_p}{2}. \end{cases} \quad (4.11)$$

Equation (4.10) shows that measurement of a uniform mean-stream velocity in the flow will not be affected by the spatial averaging. Thus, it is unsurprising that PIV has few problems with measuring a mean-stream velocity. Since the measured velocity is a convolution of the actual velocity and the window function, the spatial Fourier transform of the measured velocity is simply the product of the Fourier transform of the actual velocity field, multiplied with the Fourier transform of the window function:

$$\tilde{\overline{u}}(k) = 2\pi \tilde{u}(k) \tilde{P}(k)^\S \quad (4.12)$$

in which  $\tilde{P}(k)$  is the Fourier transform of  $P(x)$ :

$$\tilde{P}(k) = \frac{1}{\pi k L_p} \sin \frac{k L_p}{2}. \quad (4.13)$$

Consequently, the measured (longitudinal) energy spectrum  $\overline{E}(k)$  is related to

---

<sup>§</sup>The factor  $(2\pi)$  in this expression is a result of the convolution theorem for our definition of the Fourier transform. We define a Fourier transform of an arbitrary function  $f(x)$  in space as  $\tilde{f}(k) = \frac{1}{2\pi} \int_{-\infty}^{\infty} f(x) e^{-ikx} dx$ . If  $h(x)$  is the convolution product of  $f(x)$  and  $g(x)$ , then the Fourier transform  $\tilde{h}(k) = 2\pi \tilde{f}(k) \tilde{g}(k)$ .

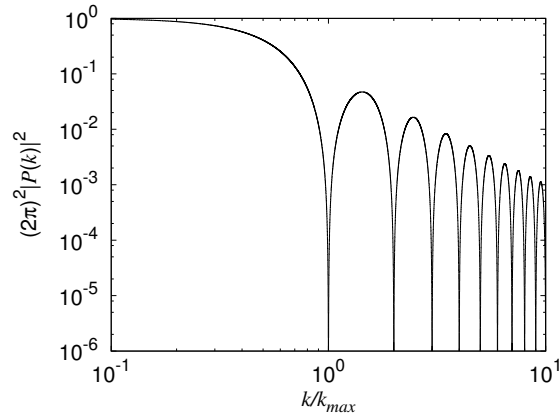


FIGURE 4.3 — Function  $|\tilde{P}(k)|^2$ , the spectral representation of the spatial averaging inherent to PIV. If the overlap between neighbouring windows is at most 50%, the maximum frequency in the measured PIV spectrum is equal to  $k_{max}$ . Hence, the higher orders shown in this figure will typically not be visible in a measured spectrum.

the actual (longitudinal) spectrum  $E(k)$  by:

$$\overline{E}(k) = (2\pi)^2 |\tilde{P}(k)|^2 E(k). \quad (4.14)$$

A graphical representation of  $(2\pi)^2 |\tilde{P}(k)|^2$  is shown in figure 4.3. It is clear that the spectrum is low-pass filtered. The first minimum in the filter lies at  $k_{max} = 2\pi/L_p$  and the filter has higher-order harmonics although at increasingly closely separated higher frequencies. As long as the cut-off frequency falls within the inertial range the area under the spectrum that is removed by the filter is relatively small compared to the overall area. This explains why PIV can provide a reasonably accurate measurement of the root-mean-square velocity.

This result, albeit without any explanation of its origin or a reference to the work by Keane & Adrian (1992), was first published by Lourenco & Krothapalli (2000). More recently Foucaut & Stanislas (2002) and Foucaut, Carlier & Stanislas (2004) showed that this low-pass filtering indeed describes the inherent filtering in PIV by comparing spectra obtained with PIV to spectra obtained with hot-wire anemometry (HWA). Kumar & Banerjee (1998), who measured turbulence spectra close to a free surface by means of PIV, conclude that their spectra have a scaling exponent of  $-3$  for high wavenumbers, similar to their spectra obtained from DNS for such a flow. However, it is likely that this scaling exponent in the PIV-spectra is actually the result of the inherent filtering by PIV. Finally, although they apparently did not realise it at the time, the spectra obtained by Lecordier *et al.* (2001) by evaluating synthetic images

of velocity fields generated from direct numerical simulations (DNS), also show behaviour associated with this low-pass filtering, albeit obscured slightly by relatively high noise in their spectra. There are many ways in which the PIV procedure can influence a measured spectrum, but the filtering action of the overlapping interrogation windows is the most important one and also the easiest to understand. It is, therefore, surprising that it was so ill-understood in the cited earlier work.

Of course, all second-order statistical quantities can equally well be expressed in wavenumber as in real space; the relation between them is a mere Fourier transform. However, in practical situations it is sometimes advantageous to directly work in real space. This is especially true in our case, where the dynamical range of spatial scales does not suffice to capture all of the spectral energy, which introduces errors in the Fourier transform needed to compute the correlation function  $C(r)$  from the spectrum  $E(k)$ . We will therefore, in parallel, discuss the influence of filtering on statistical quantities in real space. Still in one dimension, we can use equation (4.14) to find a relation between the measured correlation function  $\overline{C}(r)$  and the actual correlation function  $C(r)$ . The covariance function  $R(r)$  is the Fourier transform of the measured energy spectrum:

$$\begin{aligned}\overline{R}(r) &= \int_{-\infty}^{\infty} \overline{E}(k) e^{ikr} dk \\ &= \int_{-\infty}^{\infty} |P(k)|^2 E(k) e^{ikr} dk \\ &= \int_{-\infty}^{\infty} T(r-r') R(r') dr',\end{aligned}\quad (4.15)$$

where function  $T(r)$  is the Fourier transform of the product  $\tilde{P}(k)\tilde{P}^*(k)$ . As such, it is itself a convolution of the window function  $P(r)$ :

$$T(r) = \int_{-\infty}^{\infty} P(r-x)P(x)dx. \quad (4.16)$$

For the top-hat shaped  $P(r)$  given in equation (4.11),  $T(r)$  is a tent-function:

$$T(r) = \begin{cases} 0, & |r| > L_p \\ \frac{L_p - |r|}{L^2}, & |r| < L_p, \end{cases} \quad (4.17)$$

illustrated in figure 4.4. Since the correlation function  $C(r) = R(r)/(u_{rms})^2$  and the root-mean-square velocity are largely unaffected by PIV, in our one-dimensional description, the measured longitudinal correlation function is the convolution of the actual longitudinal correlation function with a tent-function, the width of which is determined by the interrogation window-size. For separations up to the window size, correlation is introduced artificially, due to the

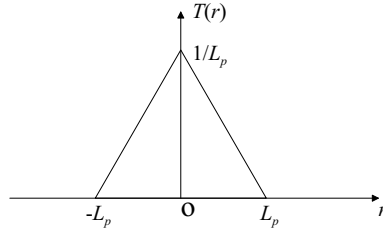


FIGURE 4.4 — Function  $T(r)$ , the convolution of the rectangular window function  $P(r)$  with itself.

velocity in adjacent grid points being at least partially determined by averaging over the same area. The consequence of this averaging is that the measured correlation function is broadened relative to the actual correlation function and will be broadened more as the interrogation window size increases.

The correlation function can be used to predict the influence of the filtering on velocity gradients as measured with PIV. Predicting the influence of averaging on velocity gradients can be also done by means of the spectrum, by realising that the spectrum of the velocity derivative  $k^2 E(k)$  and comparing this with the measured  $k^2 \overline{E(k)}$ , as was done by Foucaut & Stanislas (2002). However, since we will use correlation functions to study isotropy, correlation functions will be used here. The gradient of the  $x$ -component of the velocity in  $x$ -direction can be defined as:

$$\frac{\partial u}{\partial x} = \lim_{l \downarrow 0} \frac{u(x+l) - u(x-l)}{2l} \quad (4.18)$$

which means that:

$$\begin{aligned} \left\langle \left( \frac{\partial u}{\partial x} \right)^2 \right\rangle &= \lim_{l \downarrow 0} \left\langle \left( \frac{u(x+l) - u(x-l)}{2l} \right)^2 \right\rangle \\ &= \lim_{l \downarrow 0} \frac{1}{l^2} \{ \langle u^2(x+l) \rangle + \langle u^2(x-l) \rangle - 2 \langle u(x+l)u(x-l) \rangle \} \\ &= 2u_{rms}^2 \lim_{l \downarrow 0} \frac{1 - C(2l)}{4l^2}, \end{aligned} \quad (4.19)$$

in which  $C$  is the longitudinal velocity correlation function. Equation (4.19) expresses that the variation of the velocity derivative is related to the curvature of the correlation function near  $r = 0$ . As we have seen in chapter 3, for small separations  $r$  the correlation function can be written as:

$$C(r) = 1 - \left( \frac{r}{\lambda} \right)^2. \quad (4.20)$$

in which  $\lambda$  is the longitudinal Taylor length-scale. Substituting this in equation (4.19) leads to:

$$\left\langle \left( \frac{\partial u}{\partial x} \right)^2 \right\rangle = 2u_{rms}^2 \lim_{l \downarrow 0} \frac{1 - \left( 1 - \left( \frac{2l}{\lambda} \right)^2 \right)}{4l^2} = \frac{2u_{rms}^2}{\lambda^2} \quad (4.21)$$

and thus:

$$\left\langle \left( \frac{\partial u}{\partial x} \right)^2 \right\rangle^{\frac{1}{2}} = \sqrt{2} \frac{u_{rms}}{\lambda}, \quad (4.22)$$

which can also be found in, for instance, Pope (2000).

Using second-order centred differences, as suggested by Luff *et al.* (1999) and Foucaut & Stanislas (2002) and similar to equation (4.18), we define the filtered version  $\overline{\partial u / \partial x}$  of the gradient of the velocity as:

$$\frac{\overline{\partial u}}{\partial x} = \frac{\bar{u}(x + L_g) - \bar{u}(x - L_g)}{2L_g}, \quad (4.23)$$

with  $L_g$  being the separation between points in the grid. Similar to equation (4.19) we can write the variance of the gradient as:

$$\begin{aligned} \left\langle \left( \frac{\overline{\partial u}}{\partial x} \right)^2 \right\rangle &= \left\langle \left( \frac{\bar{u}(x + L_g) - \bar{u}(x - L_g)}{2L_g} \right)^2 \right\rangle \\ &= \frac{\langle \bar{u}^2 \rangle}{2L_g^2} (1 - \overline{C}(2L_g)). \end{aligned} \quad (4.24)$$

in which  $\overline{C}$  is the measured correlation function. Equation (4.24) shows that the measured root-mean-square velocity gradient is directly connected to the value of the measured correlation function at a separation that is twice the grid distance  $L_g$ , which, for the usual 50% overlap, equals the window size  $L_p$ . The dependence of  $\overline{C}$  on  $L_p$  introduces a correlation length  $\bar{\lambda}$  through:

$$\overline{C}(r) = 1 - \left( \frac{r}{\bar{\lambda}} \right)^2, \quad (4.25)$$

Due to the averaging,  $\bar{\lambda} > \lambda$  and, consequently, the fluctuation magnitude of the velocity is underestimated.

Knowing how PIV influences correlation functions allows us to take a closer look at isotropy, as we have seen in chapter 3. For isotropic turbulence, equation (3.26) gives a relation between the longitudinal and transverse correlation functions. For LDV measurements these were derived from point measurements of the transverse and longitudinal velocity as a function of time together with

the use of Taylor's frozen turbulence hypothesis<sup>¶</sup>. PIV provides this spatial information directly, albeit spatially averaged. Furthermore, because in its basic form, PIV can be used to measure two components of the velocity in two dimensions, it can be used to measure two longitudinal spectra,  $E_{xx}(k_x)$  and  $E_{yy}(k_y)$ , and two transverse spectra,  $E_{xx}(k_y)$  and  $E_{yy}(k_x)$ , as well as the four corresponding correlation functions. In isotropic turbulence all spectra and correlation functions are independent of the direction in which they are measured. Hence, in order to check isotropy with PIV, we can directly compare, for instance,  $E_{xx}(k_x)$  and  $E_{yy}(k_y)$  and/or their corresponding correlation functions.

Comparing longitudinal and transverse correlation functions by means of equation (3.26) is potentially problematic. If the filter action is taken longitudinally, and  $L_p$  becomes very small, it is possible to rephrase equation (3.26):

$$\begin{aligned}\overline{C}_{TT}(r) &= T(r) * \left( C_{LL}(r) + \frac{1}{2}r \frac{d}{dr} C_{LL}(r) \right) \\ &= \overline{C}_{LL}(r) + \frac{1}{2}T(r) * \left( r \frac{d}{dr} C_{LL}(r) \right) \\ &= \overline{C}_{LL}(r) + \frac{1}{2}r \frac{d}{dr} \overline{C}_{LL},\end{aligned}\tag{4.26}$$

with  $*$  denotes a convolution product. However, this is much simplified, and a complete three-dimensional treatment is necessary to fully understand the consequences of the averaging.

Of course, in our description of the filtering we have not included how the spectrum is influenced by the occurrence of spurious data and by noise. Sub-pixel resolution leads to an accuracy of at best 0.1 pixel. Hence, as the dynamic range decreases, the relative noise level in the spectrum becomes higher. These effects are primarily visible in the high frequencies in the spectrum, and at small separations in the correlation functions, and, accordingly, in the gradient fluctuation, as will be shown in the next sections. Besides leading to the occurrence of spurious data, (4.5) shows that particle loss also leads to a velocity dependent filtering. The effective width of the filter is decreased in regions of high velocity.

---

<sup>¶</sup>Since a comparison of correlation functions can potentially obscure large scale isotropy, with an associated dependence of the root-mean-square velocity on the direction, in our LDV measurements second-order structure functions were used instead of correlation functions. However, equation (3.29), which gives the relation between the transverse and longitudinal 2nd order structure function, follows directly from the relation between the transverse and longitudinal correlation functions.



## 4.4 Applying PIV to simulated velocity fields

In the previous section, a one-dimensional mathematical description was given of how the spatial averaging inherent to PIV influences measured turbulence statistics, based on the description of PIV by Keane & Adrian (1992). We now want to compare the spectrum found from applying PIV to simulated images to the spectrum of the actual velocity field. This comparison allows us to assess whether the spectra obtained from PIV indeed correspond to simple spatial averaging. Furthermore, the comparison serves to illustrate some of the effects of having a limited dynamic range and of the occurrence of spurious vectors, associated with particle loss, on the measured turbulence statistics.

The simulated velocity fields are generated by means of a kinematic simulation. We have chosen to use kinematic simulations because they allow us to prescribe the properties of the spectrum and because they are relatively cheap computationally, certainly compared to direct numerical simulation of turbulence.

### 4.4.1 KINEMATIC SIMULATIONS

A kinematic simulation is essentially based on generating random Fourier modes with a prescribed spectrum (Kraichnan, 1970; Fung *et al.*, 1992; Elenbaas, 2006). Each realisation of the simulated velocity field consists of a sum of Fourier components:

$$\mathbf{u}(\mathbf{x}, t) = \sum_{n=1}^N \mathbf{v}_n \cos(\mathbf{k}_n \cdot \mathbf{x} + \omega_n t) + \mathbf{w}_n \sin(\mathbf{k}_n \cdot \mathbf{x} + \omega_n t), \quad (4.27)$$

in which  $\mathbf{v}_n$  and  $\mathbf{w}_n$  are spatial Fourier amplitudes and  $\omega_n$  is a frequency. These amplitudes and this frequency depend on  $\mathbf{k}_n$ , the (discrete wavenumber vector). Exactly how they depend on  $\mathbf{k}_n$  determines the spectrum and all other properties of the resulting flow field. The velocity field can be made incompressible, i.e.  $\nabla \cdot \mathbf{u} = 0$ , by making sure that the vectors  $\mathbf{v}_n$  and  $\mathbf{w}_n$  are perpendicular to the wavenumber vector. The easiest way to do this is by defining two new vectors  $\mathbf{a}_n$  and  $\mathbf{b}_n$  and taking  $\mathbf{v}_n$  and  $\mathbf{w}_n$  as the cross-products of these vectors with the normalised vector  $\tilde{\mathbf{k}}_n = \mathbf{k}_n/k_n$ , so:  $\mathbf{v}_n = \mathbf{a}_n \times \tilde{\mathbf{k}}_n$  and  $\mathbf{w}_n = \mathbf{b}_n \times \tilde{\mathbf{k}}_n$ . The directions of vectors  $\mathbf{k}_n$  are chosen to be uniformly random. The velocity spectrum is determined by how the lengths of  $\mathbf{a}_n$  and  $\mathbf{b}_n$  depend on  $\mathbf{k}_n$ . For the purpose of these kinematic simulations we only model the inertial range behaviour of the turbulence energy spectrum function, already briefly mentioned in chapter 1:

$$E(k) = \begin{cases} C\epsilon^{2/3}k^{-5/3} & , k_c < k < k_\eta \\ 0 & , \text{otherwise} \end{cases} . \quad (4.28)$$

in which  $\epsilon$  is the dissipation rate of the turbulence and  $C$  is an empirical constant. In accordance with Kraichnan (1970), its value is taken as 1.5. The lower cut-off wavenumber  $k_c$  sets the largest scale of the turbulence spectrum. The large wavenumber cut-off,  $k_\eta$ , is associated with the Kolmogorov scale  $\eta_k$  of the turbulence.:

$$k_\eta = \frac{2\pi}{\eta_k}. \quad (4.29)$$

The lengths of the discrete wavenumber vectors  $\mathbf{k}_n$  are chosen according to a geometrical distribution:

$$k_n = k_c \left( \frac{k_\eta}{k_c} \right)^{\frac{n-1}{N_k-1}}. \quad (4.30)$$

and, subsequently, the lengths of the vectors  $\mathbf{a}_n$  and  $\mathbf{b}_n$  are taken from shells of the discrete spectrum such that:

$$\frac{3}{2}a_n^2 = \frac{3}{2}b_n^2 = E(k_n)\Delta k_n \quad (4.31)$$

where

$$\Delta k_n = \frac{k_{n-1} - k_{n+1}}{2}.$$

These choices set the spatial spectrum of the turbulence.

The model includes time evolution of the velocity field<sup>||</sup>. However, as is already indicated by their name, kinematic simulations do not model actual dynamics. This is, of course, the primary reason why kinematic simulations are computationally cheap compared to direct numerical simulations. Time evolution is included by means of the unsteadiness frequencies  $\omega_n$  in equation (4.27). A straightforward relation between  $\omega_n$  and  $k_n$  is preferred. In our simulations we use the model by Fung *et al.* (1992), in which the frequency of mode  $n$  is proportional to the eddy turnover time associated with wave-vector  $\mathbf{k}_n$ :

$$\omega_n = \xi \sqrt{k_n^3 E(k_n)} \quad (4.32)$$

where  $\xi$  is an adjustable (dimensionless) weighting factor.

The time-scale of the simulated velocity field is set both by the smallest eddy turnover time (the Kolmogorov time)  $\tau_k = (\nu/\epsilon)^{1/2}$  and the large-eddy turnover velocity  $u_{rms}$ . However, by selecting  $L$ ,  $\eta$ ,  $\epsilon$  and  $u_{rms}$ , the simulation is overdetermined. Consequently, several choices are possible. We use the value of  $\epsilon$  found from normalising the energy spectrum function. With

$$\int_0^\infty E(k)dk = \frac{3}{2}u_{rms}^2 \quad (4.33)$$

---

<sup>||</sup>In order to generate pairs of images of particles that are advected by the flow this is not strictly necessary. Calculating particle displacements through integration in a stationary velocity field would probably suffice for our purpose.

we find:

$$\epsilon = \left( \frac{3u^2}{2C} \right)^{3/2} \left( \int_{k_c}^{k_\eta} k^{-5/3} dk \right)^{-3/2}, \quad (4.34)$$

and consequently, the Kolmogorov time:

$$\tau_k = (2\pi)^{2/3} \epsilon^{-1/3} k_\eta^{-2/3}. \quad (4.35)$$

We could equally well have chosen  $\epsilon$  from the Kolmogorov relation

$$\epsilon = C_\epsilon \frac{u_{rms}^3}{L}, \quad (4.36)$$

where  $L$  is the integral scale of the turbulence and  $C_\epsilon$  is the effective dissipation constant.

Of course, this clear ambiguity is due to the absence of dynamics in the simulation. The ambiguity affects our choice of the time delay  $\Delta t$  between two snapshots of the velocity field. With our choice for  $\epsilon$ , once  $\eta_k$  has been selected, other properties of the turbulence follow: the integral length-scale, which can not only be found from the velocity auto-correlation function as in chapter 3, but also from the spectrum (see, for instance, Teixeira & Belcher, 2000).

$$L = \frac{3\pi}{4} \frac{\int_0^\infty k^{-1} E(k) dk}{\int_0^\infty E(k) dk}, \quad (4.37)$$

the effective dissipation constant

$$C_\epsilon = \frac{L\epsilon}{u_{rms}^3}, \quad (4.38)$$

and, finally, the Taylor-based Reynolds number:

$$Re_\lambda = \sqrt{15} C_\epsilon^{-3/2} \left( \frac{L}{\eta_k} \right)^{2/3}. \quad (4.39)$$

The filtering model given in the previous section deals specifically with the longitudinal spectrum. However, the spectrum as defined in equation (4.28) is the three-dimensional spectrum. The relation between the longitudinal spectrum and this spectrum is given by Pope (2000):

$$E_{LL}(k) = \int_k^\infty \frac{E(k')}{k'} \left( 1 - \left( \frac{k}{k'} \right)^2 \right) dk'. \quad (4.40)$$

In order to compare kinematic simulation results to those obtained from PIV, the computer programme we use for the kinematic simulation provides the longitudinal spectrum of the generated velocity fields.

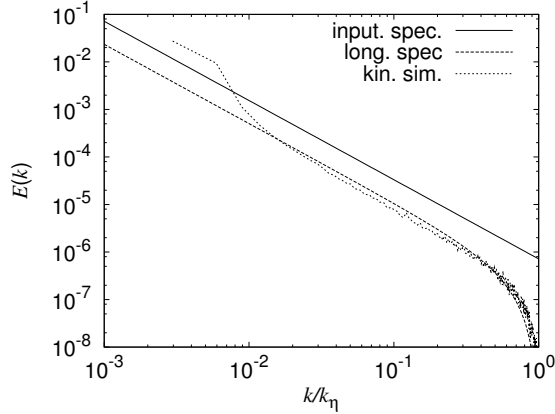


FIGURE 4.5 — Input energy spectrum function for the kinematic simulation (input. spec) as well as the theoretical longitudinal spectrum (long. spec) and the actual spectrum calculated from the kinematic simulation (kin. sim.). Note that the spectrum that follows from the kinematic simulation has a non-physical corner due to a low resolution in the spectrum at small wavenumbers.

The small wavenumber behaviour of the spectrum is due to the finite size of the window onto the velocity field. In fact, the spectra are so steep, that the Hanning filter used in calculating the spectrum is not effective, and the first two (discrete) wavenumbers should be disregarded. The scales of the turbulence used in our simulations were chosen such that the simulated turbulence is broadly comparable to the active-grid generated turbulence in our experiments. For the simulations  $Re_\lambda = 216$  and a ratio between the integral scale and the Kolmogorov scale  $L/\eta_k = 480$ , while depending on the forcing protocol in the experiments the maximum value of  $Re_\lambda = 256$  and the ratio  $L/\eta_k = 210$ . For these choices, the energy spectrum function, the corresponding longitudinal spectrum that follows from equation (4.40), and the longitudinal spectrum produced by the kinematic simulation are shown in figure 4.5.

#### 4.4.2 GENERATING REALISTIC PARTICLE IMAGES

From the simulated velocity fields we generate 12 bit digital images of  $1024 \times 1024$  pixels, corresponding to images that can be recorded with currently fairly common PIV cameras. The largest physical scale in the turbulence is the integral length scale  $L$ . Ideally, to simulate PIV images, we would sprinkle many particles in the volume  $L^3$  and obtain images from a thin two-dimensional slab with the same thickness as the laser light sheet. However, it is computationally economical to sprinkle particles in a three-dimensional volume of size  $L^2 \times h$ , with  $h \ll L$ , instead. Because these particles may be swept out of this volume

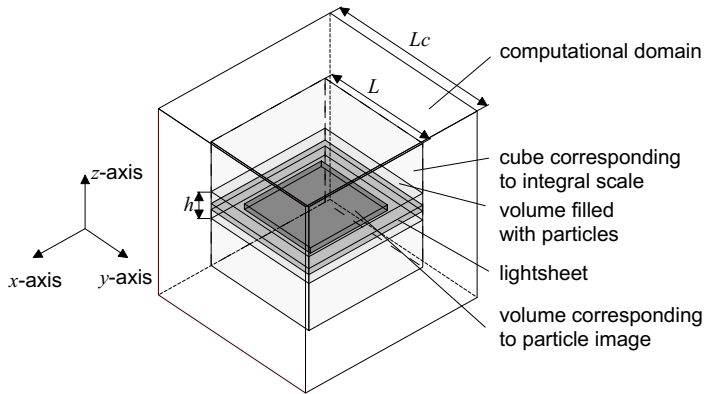


FIGURE 4.6 — The computational domain for the kinematic simulations.

by the velocity associated with large eddies ( $u_{rms}$ ),  $h$  must be chosen much larger than the thickness of the light sheet, while the area of the image must be chosen smaller than  $L^2$ . The geometry is illustrated in figure 4.6. As was explained in section 4.2, in actual PIV images the intensity distribution due to scattering from a particle is approximately Gaussian. Hence, the image of a particle is calculated by means of a two-dimensional Gaussian point spread function centred on the particle position, with the peak intensity dependent on the particle's position within the light sheet. The light sheet is homogeneous in the plane of the image and has a Gaussian intensity profile in the  $z$ -direction (normal to the plane), so  $I(z) = I_0 \exp(-(2z/d)^2)$ , where  $d$  is the  $1/e$ -width of the profile and  $I_0$  is the intensity in the centre. This is shown schematically in figure 4.2. The intensity in each pixel of the eventual image is obtained by taking the sum of the point-spread functions of all particles integrated over each pixel. The second image of the image pair is formed by integration of the velocity field in time and tracking the particles by means of a fourth-order Runge-Kutta scheme. According to Fung *et al.* (1992), in order to resolve the smallest flow features the integration time-step should be no more than  $1/10$  of the Kolmogorov time. In order to assess the effect of the various variables, the results of all simulations will be compared to the results from a baseline simulation. The values for the PIV parameters will be changed, while the turbulence will be kept the same. An overview of the various length scales and settings in this baseline simulation is given in table 4.1.

The settings for the thickness of the light sheet and time between images follow from the criteria derived by Keane & Adrian (1990, 1991), already given in equations (4.1) and (4.2). Since in our simulations we do not have a mean-stream velocity perpendicular to the light sheet we have chosen to use the root-mean-square velocity as a measure of the velocity component normal to

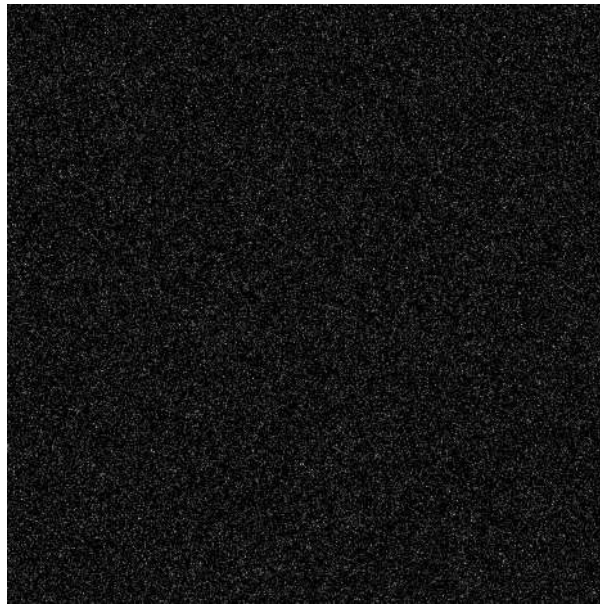


FIGURE 4.7 — Synthetic PIV particle image.

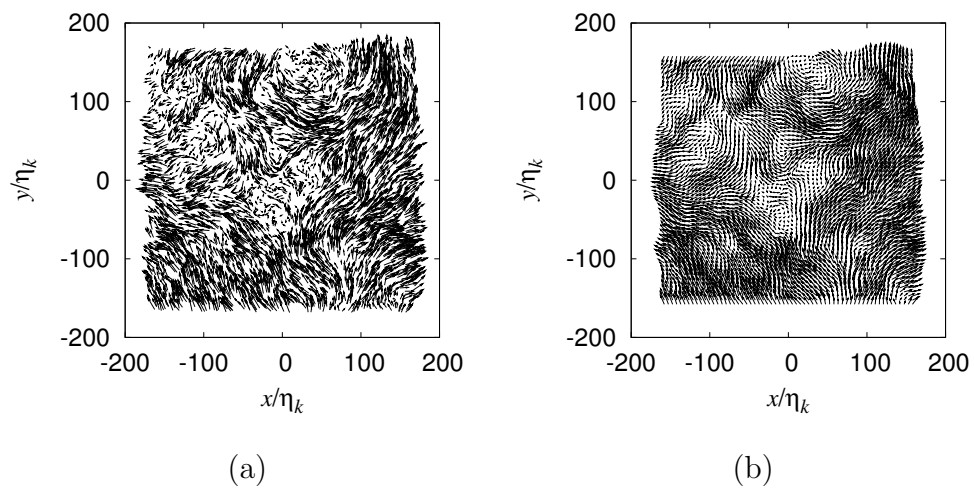


FIGURE 4.8 — (a) Snapshot of a number of particle displacements in a simulated velocity field. (b) Corresponding velocity field from PIV. The first image of the corresponding pair of particle images is shown in figure 4.7.

the light sheet, instead. For  $d$  we use the 1/e-width of the light sheet. Since the velocity perpendicular to the sheet can be expected to regularly exceed the root-mean square velocity, we have chosen our parameters such that for the baseline simulation  $u_{rms}\Delta t/d = 0.15$ . The interrogation window size was chosen to be 32 pixels, which corresponds to  $10 \eta$ . For most simulations we chose to use a 50% overlap between neighbouring windows. Our choice of  $\Delta t$  results in a maximum in-plane displacement of roughly 4 pixels, which limits in-plane particle loss. The total number of particles ( $10^6$ ) and the thickness of the computational box in which they were distributed ( $h = 0.1L = 48\eta_k$ ) were chosen such that on average more than 50 particles are present in each interrogation window, based on the 1/e width of the light sheet, which is far more than the minimum of 15 found by Keane & Adrian (1991, 1992).

An example of a particle image obtained is shown in figure 4.7. The corresponding velocity fields, both from the kinematic simulation and from PIV are shown in figure 4.8. All statistics are based on series of 500 velocity fields and the corresponding image pairs. The image pairs are evaluated with the algorithm described in section 4.2.

#### 4.4.3 COMPARISON OF TURBULENCE STATISTICS

Figure 4.9 (a) shows the velocity spectrum obtained directly from the kinematic simulation, that spectrum multiplied with the filter described in equation (4.13), and the corresponding spectrum found from PIV for the baseline simulation. The grid spacing determines the maximum frequency in the calculated PIV spectra. For a grid spacing  $L_g$ , the maximum observable wavenumber in the spectrum is  $k_{max} = \pi/L_g$  and with  $L_g = L_p/2$ ,  $k_{max} = 2\pi/L_p$ . For this simulation, as well as for all of the others, the measured root-mean-square velocity

TABLE 4.1 — Length-scales in the baseline kinematic simulation, scaled with the Kolmogorov length- scale  $\eta_k$  and the Kolmogorov time-scale  $\tau_k$ .

$L_c$	domain size	$3.2 \cdot 10^3 \eta_k$
$L$	integral scale	$480 \eta_k$
$\lambda_l$	longitudinal Taylor-scale	$22 \eta_k$
$L_s$	image size	$337 \eta_k$
$L_g$	grid spacing	$5 \eta_k$ (16 pixels)
$L_p$	interrogation window size	$10 \eta_k$ (32 pixels)
$d$	sheet thickness (1/e width)	$8 \eta_k$
$\Delta t$	time interval between images	$0.2 \tau_k$

was within 5 % of the actual value. It should be noted that the filtered version of the spectrum refers to the one-dimensional filter only, which is not strictly correct. However, the overall behaviour of the PIV spectrum in this figure corresponds to the filtered kinematic simulation spectrum. Figure 4.9 (b) shows results of evaluating the same particle images with three different interrogation window sizes: the baseline simulation evaluated with  $L_p = 32$  pixels as well as with  $L_p$  equal to 64 and 128 pixels, but with the same grid spacing  $L_g = 16$  pixels. Due to the higher overlap for both  $L_p=64$  and  $L_p=128$  pixels, which corresponds to  $20 \eta_k$  and  $40 \eta_k$  respectively, the PIV spectra also show energy at frequencies that are higher than the first cut-off frequency of the filter, corresponding to the higher-order harmonics of the filter. These PIV spectra are very similar to spectra measured by Foucaut & Stanislas (2002) and Foucaut, Carlier & Stanislas (2004) and those based on synthesised images of DNS by Lecordier *et al.* (2001). We conclude that the main effect of the finite size of the interrogation window is a filtering action on the spectrum, which is appropriately described by our one-dimensional version of the filter function. In any case, the simulations show that the inertial range in measured spectra is severely depressed by the choice of the interrogation windows in the experiments. Similar to the spectra, we can study the influence of the size of the interrogation window on measured correlation functions. The result is shown in figure 4.10. Keeping in mind our simple model, in which the influence of the finite size of the interrogation window is seen as a convolution with a tent

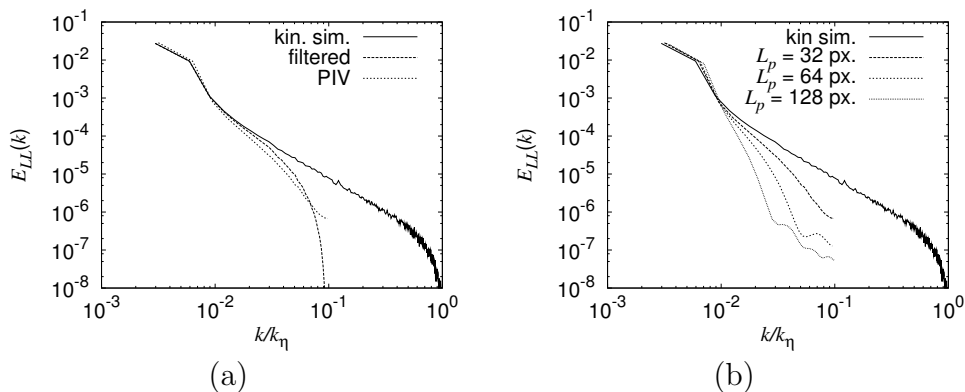


FIGURE 4.9 — Spectra obtained from kinematic simulations. (a) The velocity spectrum as obtained directly from a kinematic simulation, the filtered spectrum, and the spectrum found from evaluating the associated particle images with PIV. (b) Spectra that follow from evaluating this kinematic simulation with different PIV interrogation window sizes, but the same grid spacing (16 pixels). Onemore, due to low resolution for the small wavenumbers, there the spectra show an unphysical corner.



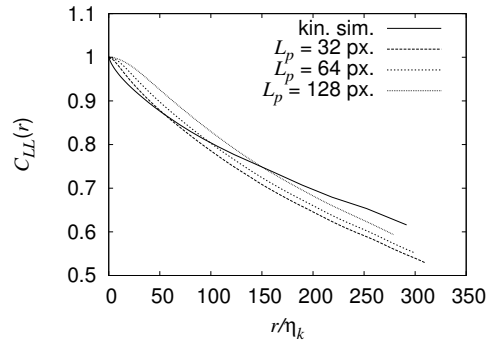


FIGURE 4.10 — Correlation functions obtained from kinematic simulations, corresponding to the spectra shown in figure 4.9 (b), so from evaluating the baseline simulation with different PIV interrogation window sizes.

map, we understand that by increasing the window size, we lift the correlation function near zero separation, and thus increase the apparent Taylor scale.

Since the Taylor-scale as well as the root-mean square velocity of the turbulence in the kinematic simulations are known, equation (4.22) can be used to calculate the root-mean-square velocity gradient. Since the turbulence properties are left unchanged, its value, 116, is the same for all simulations. This value can be compared to the values found from evaluating our synthetic images with PIV. For the baseline simulation we find  $\langle (\frac{\partial u}{\partial x})^2 \rangle^{\frac{1}{2}} = 38\tau_k^{-1**}$ . The dramatic difference is likely to be the result of the interrogation image size  $L_p$  not being small enough compared to the Taylor length  $\lambda_l$ . In the baseline simulation  $\lambda_l/L_p = 2.1$ , whereas in section 4.3 we explained that in order for PIV to provide an accurate root-mean-square velocity, the window size should be much smaller than the Taylor-length. By decreasing the size of the image relative to the integral length, i.e. by zooming in further on the turbulence, the ratio of  $\lambda_l$  over  $L_p$  can be increased. This has been done for three simulations (in which the number of particles within the interrogation windows was kept constant), the results of which are shown in table 4.2. As expected, as we zoom in further, the root-mean-square gradient approaches the expected value, even though for the maximum magnification in the simulations it still is significantly smaller. It should be noted that, for these simulations the time-interval  $\Delta t = 0.1\tau_k$  was kept constant. Hence, by zooming in further on the velocity field, we increase the dynamic range. Increasing the dynamic range actually leads to a decrease in noise (associated with the measurement uncertainty of at

\*\*The root-mean-square velocity gradient is expressed in terms of  $\tau_k$  because time in the simulation is scaled with  $\tau_k$ .

TABLE 4.2 — The measured root-mean-square velocity gradient as a function of the ratio of  $\lambda_l$ , as obtained directly from the kinematic simulation, over  $L_p$ .

$\frac{\lambda_l}{L_p}$	$\langle (\frac{\partial u}{\partial x})^2 \rangle^{\frac{1}{2}} T_k$
2.1	43
3.0	49
4.9	68

best  $\approx 0.1$  pixel) and, consequently to a (small) decrease in measured velocity gradient fluctuation. The velocity fields generated with kinematic simulations are incompressible and isotropic. Because of this, and as explained in section 4.3, the longitudinal spectrum of velocity component  $u$  should be the same as the longitudinal velocity spectrum of  $v$ , no matter how PIV influences the spectrum. Similarly, the longitudinal as well as the transverse correlation functions should be independent of the direction. Figure 4.11 (a) shows both longitudinal spectra,  $E_{xx}(k_x)$  and  $E_{yy}(k_y)$ , for the baseline simulation. As expected these spectra indeed are the same. The same rotation invariance was checked for the correlation functions in figure 4.11 (b), where we note that a small difference is seen for the longitudinal correlations at large separations. We ascribe this difference to the finite sample size of the simulation.

As it involves derivatives, we do not expect the relation between the longi-

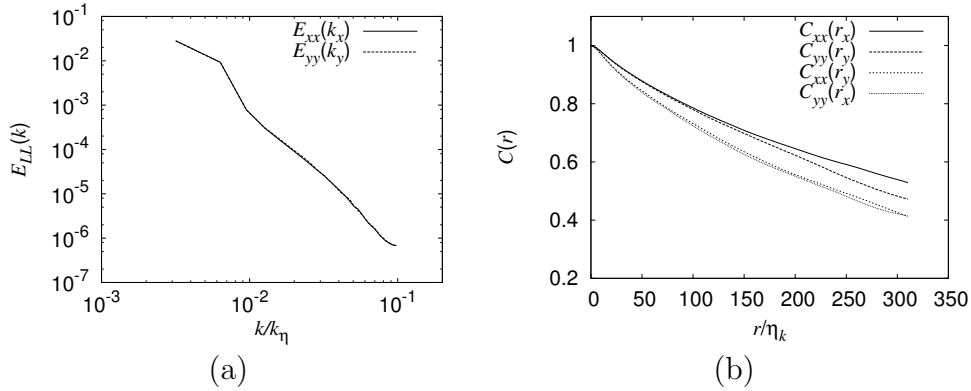


FIGURE 4.11 — (a) Longitudinal spectra in the  $x$  and  $y$ -direction obtained from PIV for the baseline simulation. (b) All four correlation-functions (two longitudinal and two transverse) for the same simulation.

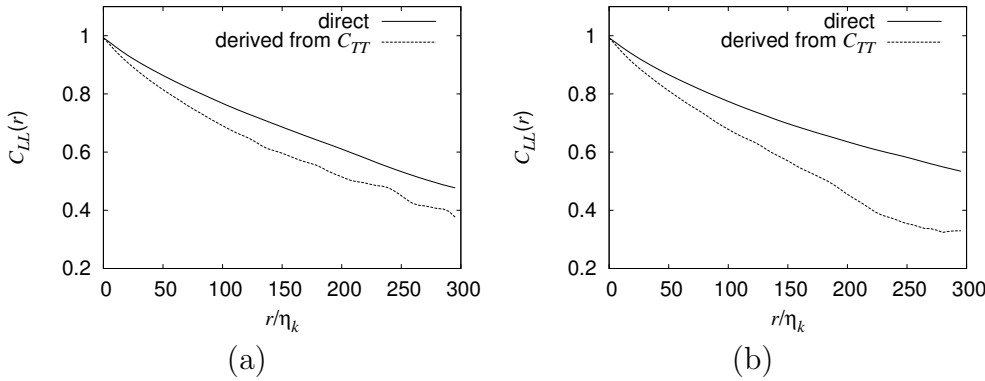


FIGURE 4.12 — Comparison between the longitudinal correlation function and the corresponding longitudinal correlation function that follows from applying the relation for isotropic turbulence, equation (3.26), to the measured transverse correlation function: (a) in  $x$ -direction,  $E_{LL} = E_{xx}(k_x)$  and  $E_{TT} = E_{yy}(k_x)$ , (b) in  $y$ -direction,  $E_{LL} = E_{yy}(k_y)$  and  $E_{TT} = E_{xx}(k_y)$ .

tudinal and transverse correlation functions, equation (3.26), to hold. This is illustrated in figure 4.12 for the baseline simulation. In this case, derivatives were simply done through the midpoint rule.

#### 4.4.4 THE INFLUENCE OF PARTICLE LOSS

In the kinematic simulations particle loss does occur. As was explained before, the most dramatic consequence of particle loss is the occurrence of spurious vectors. This is illustrated in figures 4.13 and 4.14. These show results of a simulation in which the time between the images and the thickness of the light sheet have been doubled relative to the baseline simulation. Hence in-plane particle loss is doubled, but out-of-plane particle loss should remain unchanged. The maximum in-plane displacement for this simulation is roughly 8 pixels, which is one fourth of the interrogation window size. Figure 4.13 (a) shows histograms of both velocity components found with PIV, as well as a Gaussian fit to the  $u$ -component. At a first glance the histograms for  $u$  and  $v$  are very similar, and as can be expected from a kinematic simulation, they are Gaussian. However, not shown in this histogram is a single data point with a  $v$ -component of 45, which obviously is associated with a spurious vector. A global mean filter, as suggested by Westerweel (1994), with a filter threshold of 2 can obviously easily identify this. Figure 4.13 (b) shows the percentage of vectors that is removed by this filter as a function of the realisation. In most realisations no vectors are identified as spurious. However, in a single realisation as much as 0.45 % of vectors are spurious, which corresponds to

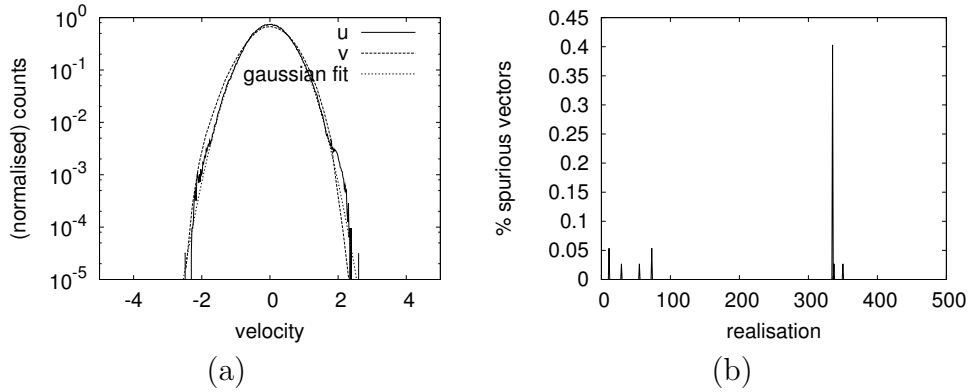


FIGURE 4.13 — (a) Histograms for both velocity components  $u$  and  $v$  as well as a Gaussian fit to the former. Note the logarithmic vertical scale. (b) Percentage of vectors identified as spurious based on a global filter that limits the normalised difference between any given vector and the global mean of 2.

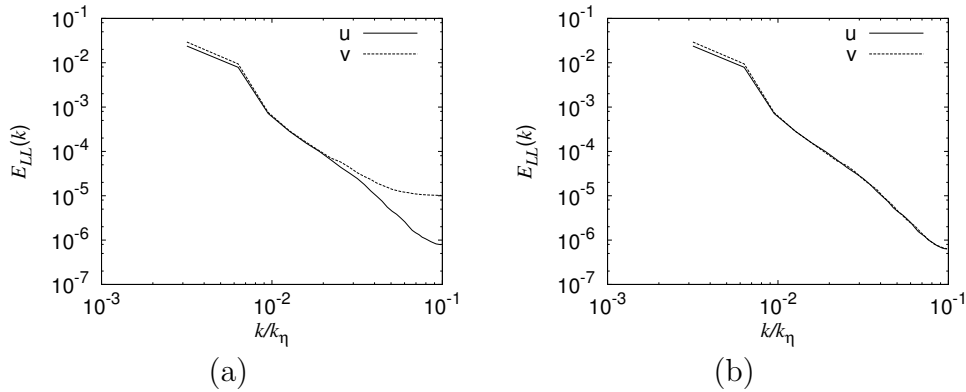


FIGURE 4.14 — (a) Longitudinal velocity spectra for both the  $u$  and  $v$  component of the velocity for velocity fields with a small number of spurious vectors. (b) Corresponding spectra for the same fields with the spurious vectors removed by a straightforward global mean filter.

12 vectors. In that particular realisation, within a small part of the image, the displacement exceeds 10 pixels. However, this small number of spurious vectors has a dramatic influence on the spectrum. The reason is, of course, that the used input spectrum,  $E(k) \sim k^{-\frac{5}{3}}$ , decreases rapidly with increasing  $k$ , which makes rare large wavenumber events, such as spurious vectors, stand out clearly. This again emphasises the benefits of the spectral approach in this chapter. Figure 4.14 (a) shows both longitudinal spectra,  $E_{xx}(k_x)$  and  $E_{yy}(k_y)$

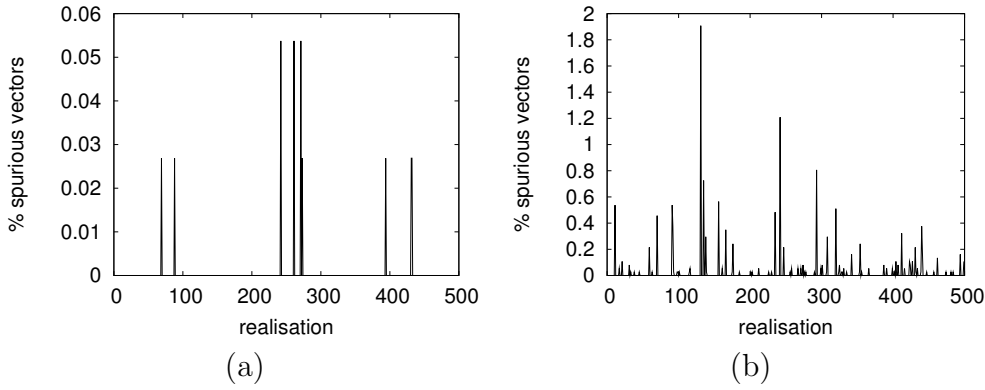


FIGURE 4.15 — Percentage of bad vectors as a function of the realisation for a sheet thickness (a)  $d = 6\eta_k$  and (b)  $d = 4\eta_k$ .

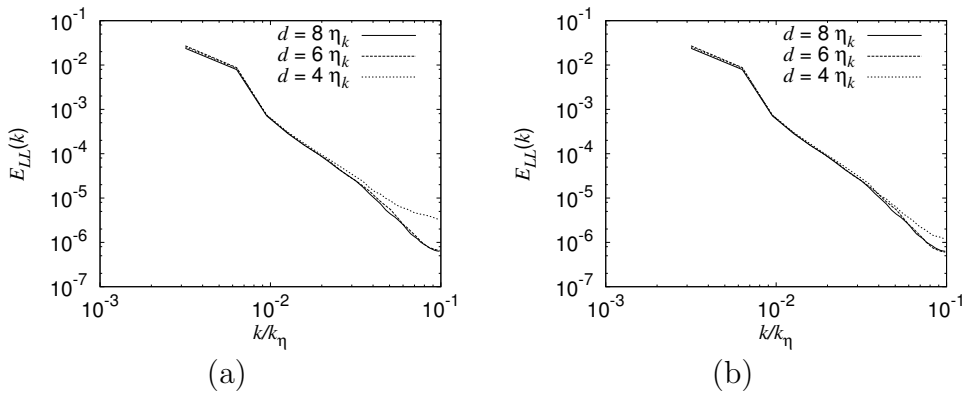


FIGURE 4.16 — Longitudinal velocity spectra for the  $u$  component of the velocity for simulations with different values for the thickness  $d$  of the light sheet. (a) For unfiltered velocity fields. (b) Corresponding spectra for the same fields with the spurious vectors removed by a global mean filter.

for unfiltered velocity fields. As we have seen before, the turbulence is isotropic. Hence the spectra should be the same. However, the spectra are very different for spatial frequencies  $k/k_\eta$  above  $2 \cdot 10^{-2}$ . This is due to the small percentage of spurious vectors. The corresponding spectra for the filtered velocity fields shown in figure 4.14 (b) are practically identical, showing the success of the filter. Out-of plane particle loss has the same effect. This is demonstrated in figures 4.15 and 4.16. These figures show the results of three different simulations: the baseline simulation, labeled  $d = 8\eta_k$  as well as two simulations with thinner light sheets with  $d = 6\eta_k$  and  $d = 4\eta_k$ . The particle density in these simulations

is set such that the number of particles within the sheet remains the same as in the baseline simulation. The time between the images is kept the same as well. The main difference between these simulations is out-of-plane particle loss, which is increased as the sheet is made thinner. Figure 4.15 shows the percentage of spurious vectors identified with a global mean filter with radius  $2u_{rms}$  for  $d = 6\eta_k$  and  $d = 4\eta_k$ . For the baseline simulation the percentage is 0. As expected, the percentage of bad vectors increases as the sheet gets thinner. Figure 4.16 (a) shows the longitudinal spectra for  $u$  for these three simulations. The spectrum for the baseline simulation as well as the spectrum for  $d = 6\eta_k$  are very similar, but the spectrum for the simulation with  $d = 4\eta_k$  starts to deviate for frequencies  $k/k_\eta$  above  $2 \cdot 10^{-2}$ . Figure 4.16 (b) shows the corresponding spectra for the velocity fields filtered with a global mean filter. Although as a result of this filter, the difference between the spectra becomes smaller, the spectrum with  $d = 4\eta_k$  still is clearly different.

A small number of spurious vectors can have a considerable effect on the measured spectra. In a properly performed actual PIV experiment on average 1 to 2 % of vectors per frame are spurious (Raffel *et al.*, 1998; Westerweel, 1994). One would hope that the effect of such bad vectors were small. However, we have seen that an even smaller number of bad vectors that occurs as a result of particle loss has a considerable effect on the measured spectra. For the spectra it is essential that they are effectively removed. Other statistics, such as mean and fluctuation velocities as well as correlation function fortunately are less affected. For the examples shown here a straightforward global mean filter seems to be fairly effective, as was already concluded by Westerweel (1994). However, our examples show that the criteria for particle loss by Keane & Adrian (1990, 1991) as well as the global mean filter have a clearly identifiable influence on the spectra.

## 4.5 Experiments

Our simultaneous PIV and surface slope measurements will be described in detail in chapter 8, following a description of the surface slope measurement technique and measurement results. Here we will compare PIV measurements of grid-generated turbulence in our water channel with LDV measurements in order to show how the averaging inherent to PIV is visible in the results of our experiments and to make sure that our PIV settings and set-up are reasonably suited for measuring the turbulence. We will also take a look at isotropy in horizontal planes. Three different forcing conditions have been studied: active grid turbulence with protocols (25OPT) and (25RAN), and the static grid (25STAT). The corresponding turbulence properties measured with LDV are listed in table 3.2.

For the PIV experiments we use a dual pulsed Nd:YAG laser (Spectron Lasers SL454, 200 mJ per pulse, 15 pulse pairs per second) to produce a light-

sheet in a horizontal plane below the surface. The flow is seeded with 100  $\mu\text{m}$  glass seeding particles (Dantec). A digital camera (Kodak ES 1.0, 8 Bit,  $1018 \times 1008$  pixels) is mounted below the water channel pointing upwards. It images an area of approximately  $5.5 \times 5.5 \text{ cm}^2$  of the light sheet. The position calibration of PIV was done by recording an image of a plate with a pattern of white dots against a black background, placed in the water channel instead of the light sheet. Since the camera was placed relatively far from the plate and was carefully aligned such that its optical axis was perpendicular to the plate, a simple multiplication with a factor, based on the distance between the points on the plate and in the camera image, is sufficient to perform the conversion from pixels to world coordinates. The integral scale of active-grid-generated turbulence found from our LDV measurements was approximately 8.5 cm. The ratio between the image size and integral scale is approximately the same in our experiments and in the kinematic simulations. We know from the LDV experiments that the root-mean-square velocity for active-grid-generated turbulence is less than 3 cm/s. The  $1/e$  width of the light sheet is approximately 1 mm. In order to limit the influence of out-of plane particle loss, we have chosen very conservative values for the time interval between the paired images of  $\Delta t = 1$  ms for the active-grid-generated turbulence and  $\Delta t = 3$  ms for the static grid, despite the criterion for out-of-plane particle loss by Keane & Adrian (1990, 1991), given in equation (4.2) allowing times between the images more than twice as high. Indeed, the number of spurious vectors is very small (less than 0.5%). For these experiments we have used window shifting, with the mean stream velocity corresponding to to 4 pixels in case of the active-grid-generated turbulence, whereas for the static grid generated turbulence it corresponds to 12 pixels. A drawback of our conservative choice for  $\Delta t$  is that the dynamic range is very limited, leading to a relatively high noise level in the spectra, as we will see. Since spurious data have a very large effect on the spectra as well as on locally measured gradients, we decided that preventing spurious vectors was more important than the dynamic range. Similar to the kinematic simulations, for these PIV experiments we take 500 image pairs and the images are evaluated with  $32 \times 32$  pixel interrogation windows and 50 % overlap between neighbouring windows.

#### 4.5.1 A COMPARISON OF PIV AND LDV MEASUREMENTS

Unlike for the kinematic simulations, in our experiments we cannot prescribe the spectrum of the turbulence. However, as described in chapter 3, we do have access to spectra and correlation functions measured by means of Laser-Doppler Velocimetry. Thus we can compare them to PIV measurements at the same locations in the water-channel. The PIV light sheet is placed horizontally in the water-channel. Thus, PIV provides the spanwise and streamwise components of the velocity, whereas the LDV system provides both the streamwise component and the vertical component. Hence, we can only compare measurements of

the streamwise component of the velocity,  $v$  in our coordinate system. As was explained in chapter 3, with LDV we cannot measure spatial spectra directly, and have to resort to using Taylor’s frozen turbulence hypothesis to convert frequency spectra into wavenumber spectra and, similarly, correlation functions in time to correlations in space.

It should be noted that the Laser-Doppler and PIV measurements cannot be performed simultaneously. Hence the LDV and PIV experiments were done on different days. Furthermore, the experiments for the static-grid-generated turbulence were done at a different time than those for the active grid, due to the work involved in removing the active grid from the channel. However, the set-up and the settings used for PIV were kept the same. Table 4.3 shows mean

TABLE 4.3 — Comparison between mean and root-mean-square velocities measured with Laser-Doppler Velocimetry and Particle Image Velocimetry for three forcing conditions.

	$v_0$ PIV (m/s)	$v_0$ LDV (m/s)	$v_{rms}$ PIV (m/s)	$v_{rms}$ LDV (m/s)
25OPT	0.285	0.271	$1.76 \cdot 10^{-2}$	$1.62 \cdot 10^{-2}$
25RAN	0.283	0.266	$2.54 \cdot 10^{-2}$	$2.29 \cdot 10^{-2}$
25STAT	0.284	0.289	$6.93 \cdot 10^{-3}$	$7.50 \cdot 10^{-3}$

and root-mean-square velocities for three different types of forcing: the active grid with protocols (25OPT) and (25RAN), and the static grid (25STAT), at 2 m behind the grid and at 10 cm below the surface. The table shows that the maximum difference in mean-stream velocities measured with PIV and LDV in this set of experiments is less than 6%. The difference between the root-mean-square velocities is slightly larger, but still is less than 11%. In the kinematic simulations we saw that PIV provides an accurate measurement of the root-mean-square velocities. Apparently the same applies to the experiments.

Figure 4.17 shows longitudinal spectra and correlation functions measured with LDV and the corresponding PIV measurements for the three conditions listed in table 4.3. The spectra in figures (a), (b), and (c) illustrate the dramatic difference in the range of scales that can be captured by PIV and LDV. By focusing on a relatively small area the large scales in the PIV spectra are under-sampled. However, as we have seen before, in order to accurately measure correlation functions at small separations we need a high spatial resolution. For a small range of wavenumbers, before the noise threshold is reached in both spectra, the spectra are very similar. The noise level is reached at approximately the same wavenumber, which can only be coincidental, since the causes for noise are completely different in both techniques. The wavenumber where



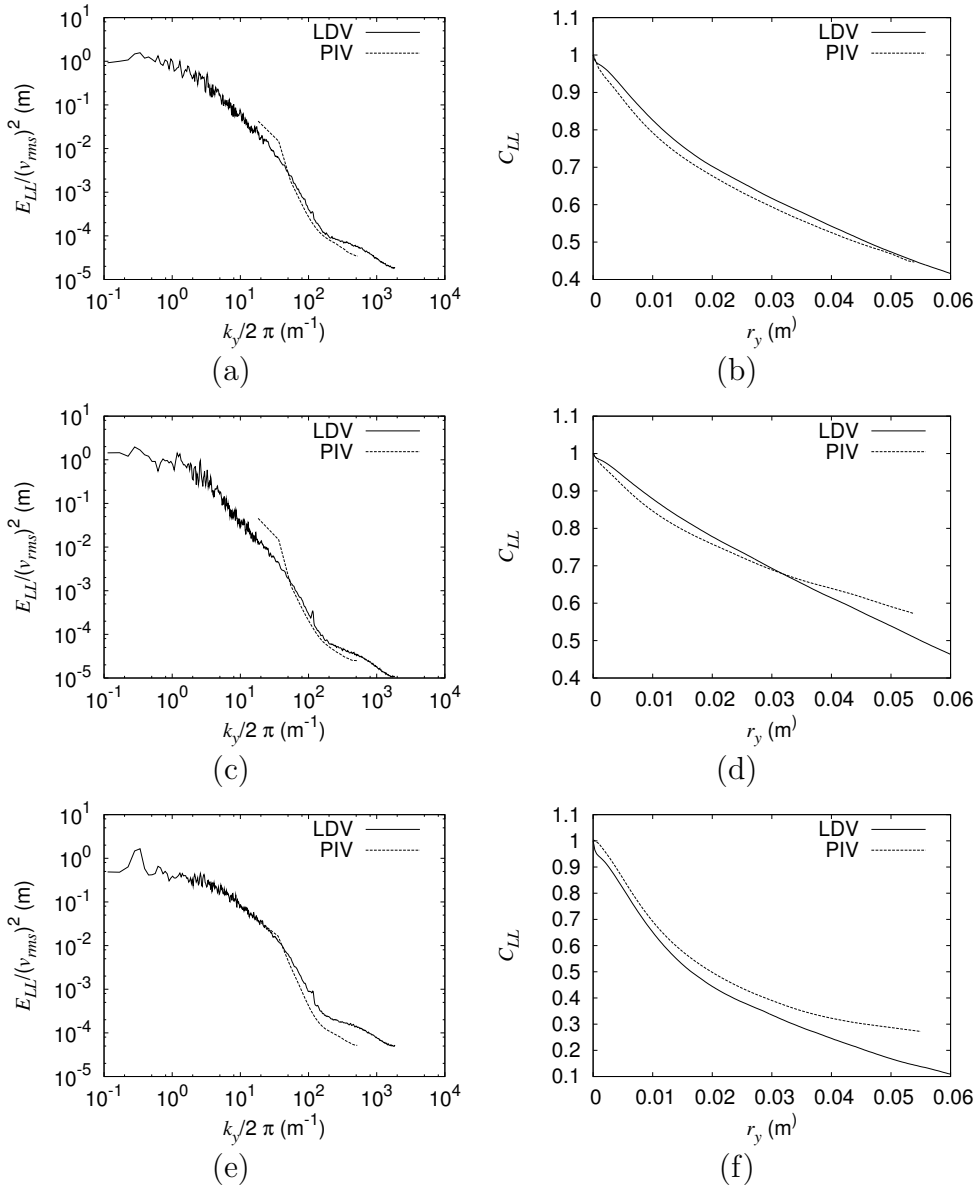


FIGURE 4.17 — Comparison of longitudinal spectra and correlation functions measured with LDV and PIV. (a) and (b): Active-grid-generated turbulence with protocol (25OPT), (c) and (d) with protocol (25RAN), and (e) and (f) static-grid-generated turbulence (25STAT).

the noise level is reached, in both spectra, is still quite far below the range where the inherent filtering in PIV starts to lead to a significant influence,

which obscures the influence of the spatial averaging. The similar comparison done by Foucaut & Stanislas (2002) and Foucaut *et al.* (2004) with spectra measured with hot-wire anemometry (HWA) showed a clear correspondence between the PIV measured spectrum and the HWA-spectrum multiplied with the appropriate filter.

The correlation functions in figure 4.17 (b), (d) and (e) show a small peak at zero displacement that was not present in the results of the kinematic simulations. This peak is the result of the high-frequency noise, which, of course, is perfectly correlated with itself. This peak was also observed in the correlation functions measured by Lecordier *et al.* (2001). This noise has only a small influence on the root-mean-square velocity, but it has a far larger influence on the measured fluctuation of the velocity gradients. In our experiments, velocity gradients are calculated using a simple mid-point rule. This derivative calculation is very susceptible to noise in the velocity data. If we consider that the spectrum of the velocity gradient  $\sim k^2 E(k)$ , it is clear that the noise tail in the velocity spectrum is amplified in the derivative spectrum. In terms of the correlation function it can be understood as follows: if we consider equation (4.24), we see that as a consequence of the peak at zero displacement, the correlation at  $r = 2L_g = L_p$  is underestimated. This can be seen in table 4.4, where the root-mean-square velocity gradient is listed for the three different forcing conditions listed in table 4.3 alongside the corresponding values derived from LDV measurements by means of equation (4.22). Because of this, the resulting velocity gradient is overestimated, despite  $L_p$  being smaller than the correlation length ( $\lambda_l/L_p = 8.4$  for both (25OPT) and (25RAN), while due to a smaller  $\lambda$  for (25STAT) the ratio is 5.3). According to Luff *et al.* (1999), who studied the vorticity field obtained from applying PIV to synthetic images of an Oseen-vortex, a dramatic improvement of the accuracy of the derivative calculation can be achieved by using a Gaussian weighted averaging of the velocity field, before calculating the derivatives. Hence, in addition to the inherent filtering, in that case the measured velocity is further convolved with a Gaussian window

TABLE 4.4 — Fluctuation strength of the velocity gradient,  $\langle (\frac{\partial u}{\partial x})^2 \rangle^{\frac{1}{2}}$ , measured with PIV and derived from LDV, for turbulence with different forcing.

	LDV	PIV	PIV $\frac{\sigma}{L_g} = 1.3$	PIV $\frac{\sigma}{L_g} = 3$
25OPT	1.4 s <sup>-1</sup>	3.2 s <sup>-1</sup>	2.4 s <sup>-1</sup>	1.3 s <sup>-1</sup>
25RAN	2.0 s <sup>-1</sup>	3.8 s <sup>-1</sup>	2.6 s <sup>-1</sup>	1.6 s <sup>-1</sup>
25STAT	1.1 s <sup>-1</sup>	1.4 s <sup>-1</sup>	1.0 s <sup>-1</sup>	0.67 s <sup>-1</sup>

function:

$$G(x) = \frac{1}{\sigma} \sqrt{\frac{2}{\pi}} e^{-2\left(\frac{x}{\sigma}\right)^2}, \quad (4.41)$$

where  $\sigma$  is the width of the filter. According to Luff *et al.* (1999) the optimal value for  $\sigma = 3L_g$ , but for turbulence, where spatial resolution is a bigger issue,  $\sigma = 1.3L_g$  would be more appropriate. Of course, this Gaussian averaging is another filter operation. It removes the noise tail from the velocity spectrum and the corresponding peak in the correlation function. This can be seen in the spectra and corresponding correlation functions shown in figure 4.18. Table 4.4 also lists the velocity fluctuations for the filtered PIV results. Clearly, the numerical values for the filtered fields are closer to the values derived from PIV, and the correlation function also is closer to that measured with PIV, but not without a price, as can be seen in the spectra in 4.18 (a).

#### 4.5.2 ISOTROPY IN HORIZONTAL PLANES

In chapter 3 we have seen that, depending on the type of forcing, the isotropy of the turbulence in vertical planes ( $x = \text{constant}$ ) changes. Since in our set-up PIV provides velocity fields in planes parallel to the surface, in similar fashion as for the kinematic simulations in the previous section, PIV allows us to study isotropy in those planes. Figure 4.19 shows both longitudinal spectra as well as the two longitudinal and transverse correlation functions for all three forcing conditions.

The two longitudinal spectra for active-grid-generated turbulence with protocol (25OPT) in figure 4.19 (a), as well as the two spectra for the static grid in figure 4.19 (e), are practically identical. Similarly, shown in figures (b) and (f), the longitudinal correlation functions for these two conditions overlap, as

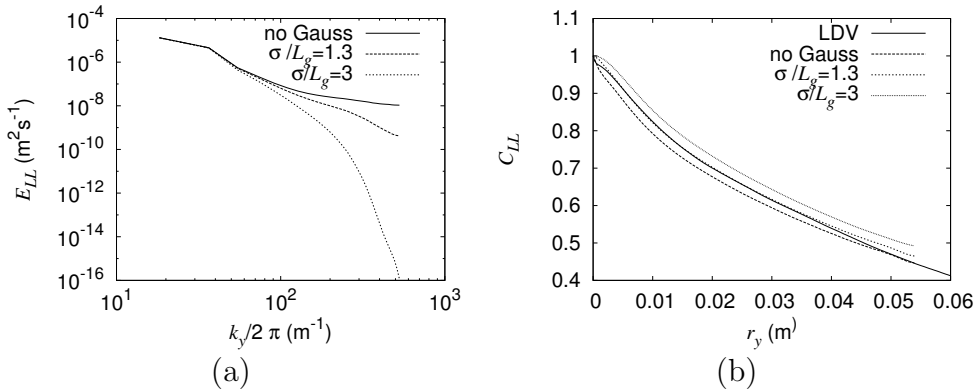


FIGURE 4.18 — Comparison of spectra and correlation functions for grid-generated turbulence with protocol (25OPT) without Gaussian filtering and with Gaussian filtering with two different widths.

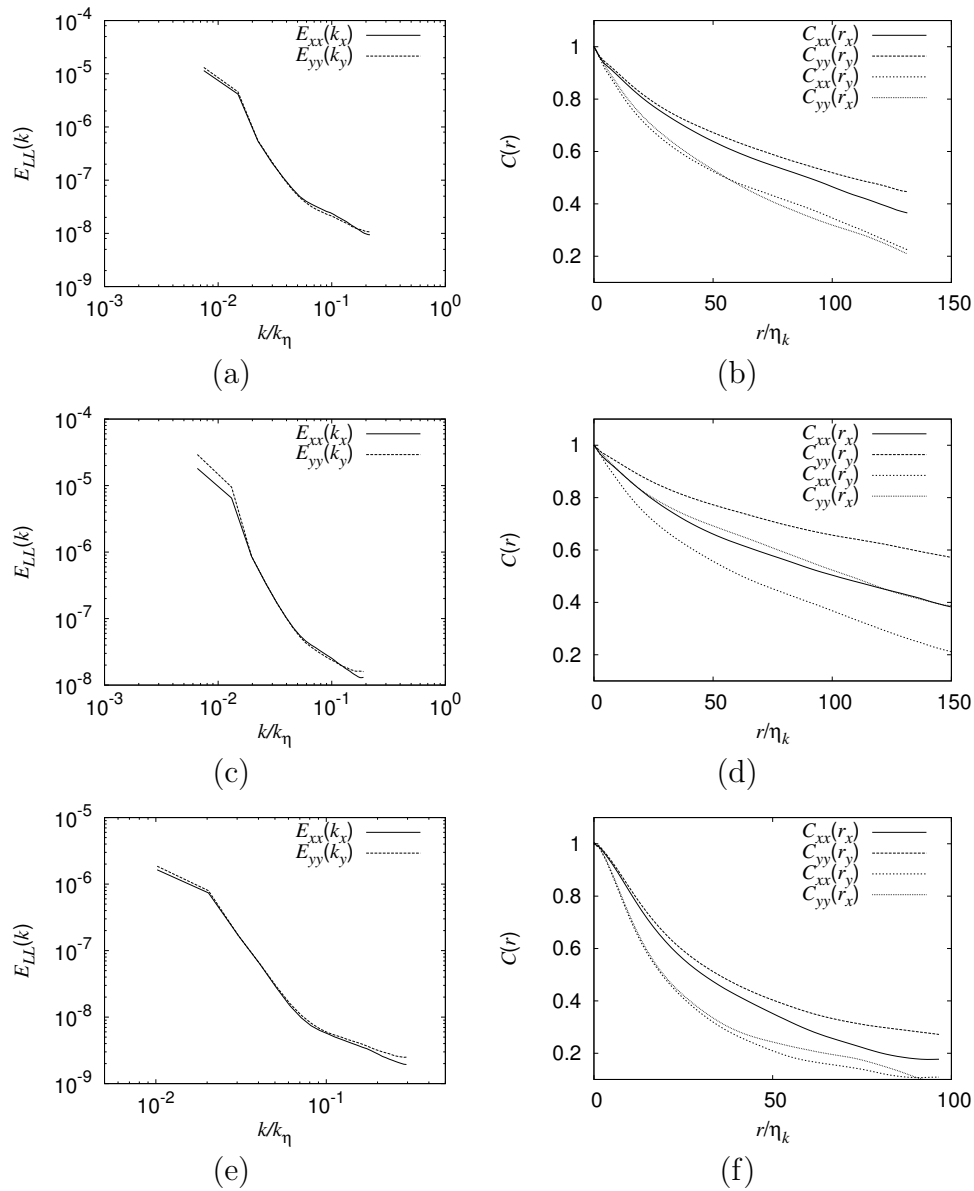


FIGURE 4.19 — Longitudinal spectra in the  $x$  and  $y$ -direction, as well as all four correlation-functions (two longitudinal and two transverse) obtained from PIV. (a) and (b): Active-grid-generated turbulence with protocol (25OPT), (c) and (d) active-grid-generated turbulence with protocol (25RAN), and (e) and (f) static-grid-generated turbulence (25STAT).

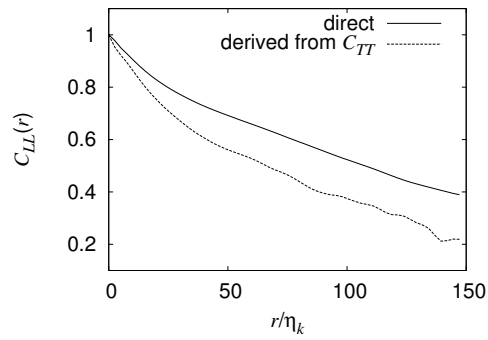


FIGURE 4.20 — Comparison of the transverse velocity correlation function measured with PIV with the transverse correlation function derived from the relation for isotropic turbulence, equation (3.26), for active-grid-generated turbulence with protocol (25RAN).

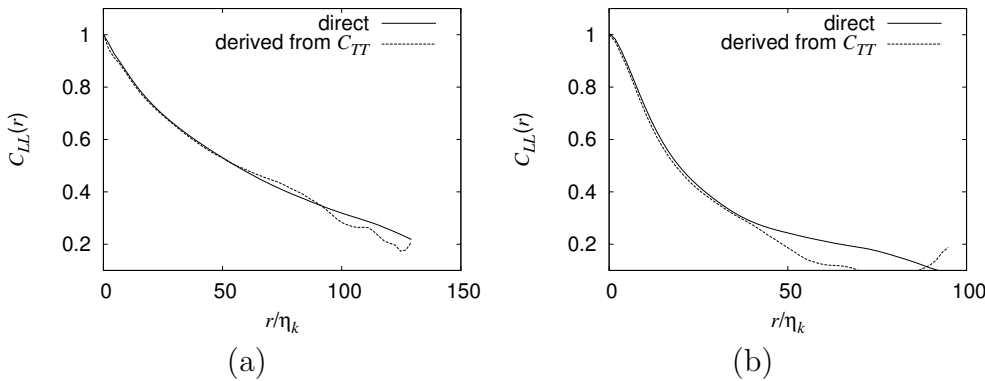


FIGURE 4.21 — The isotropic relation, equation (3.26), applied to (a) active-grid-generated turbulence with protocol (25OPT) and (b) static-grid-generated turbulence.

well as the transverse correlation functions. In chapter 3 we have already seen that the turbulence for these conditions was nearly isotropic in vertical planes. Figure 4.19 now clearly shows that the same applies to isotropy in horizontal planes. In chapter 3 it was also shown that the turbulence generated with protocol (25RAN) was less isotropic in vertical planes. The velocity spectra for this protocol in figure 4.19 (c) and the correlation functions in 4.19 (d) show that it is more anisotropic in horizontal planes as well. [b] Finally, we can take a look at the validity of the relation between the longitudinal and transverse correlation functions for isotropic turbulence as obtained from PIV. In the previous section we have seen that for our kinematic simulations, where  $\lambda_l/L_p = 2.1$  it

was not applicable.

Figure 4.20 shows both the measured longitudinal correlation function as well as the longitudinal correlation function derived from the isotropic relation for active-grid-generated turbulence with protocol (25RAN). However, somewhat surprising in light of the failure of this approach for the kinematic simulations, corresponding images for the isotropic turbulence generated with protocol (25OPT) and with the static grid in figure 4.21 show that the relation does hold. The most likely explanation for this is that in our measurements, the ratio of  $\lambda_l/L_p$  was larger than in our kinematic simulations. In case of the active-grid-generated turbulence it was  $\approx 9$ , and for the static grid it was somewhat smaller, but still  $\approx 6$  due to  $\lambda_l$  being smaller in that case.

## 4.6 Conclusions

In order to understand how PIV affects measured turbulence statistics, we have introduced a simple model, which can be characterised as ‘spectrum in, spectrum out’. The great advantage of this approach is that experimental circumstances can be easily tuned, including the spectral energy. A disadvantage is that higher order statistics cannot be modelled: a kinematic simulation produces a Gaussian velocity field and only the second-order statistics are correct. The results of our model agree with the description of PIV in terms of a spatial average over the interrogation window by Keane & Adrian (1992). We have shown that this spatial averaging is the principal influence of PIV on the spectrum. It completely dominates over other artifacts of PIV such as particle loss, leading to spurious vectors. As predicted by Westerweel (1994), these can be easily cured by simply removing them. This effect is clearly visible in our spectra.

Finally, we have compared experimental PIV results for grid-generated turbulence with those obtained from LDV. Despite the occurrence of considerable noise, mostly due to a limited dynamic range, within the equally limited range of spatial scales, the PIV spectra were roughly comparable to those measured with LDV. By measuring correlation functions with PIV we were able to take a closer look at isotropy of the grid-generated turbulence in our set-up. Turbulence that was shown to be isotropic in vertical planes, by means of LDV, was shown to be isotropic in horizontal planes as well. We have demonstrated that for these measurements it is vital that the interrogation window size is much smaller than the correlation length, i.e. the Taylor length-scale  $\lambda$  of the turbulence.

Due to the dramatic effect of the spatial averaging, PIV is not particularly suited for measuring velocity spectra, unless digital cameras with far higher resolution become available. Even with a high resolution camera, the filtering inherent to PIV starts to influence the measurements even at larger scales than the size of the interrogation windows. Nonetheless, we have shown that un-

derstanding what PIV does to the spectrum is key to understanding how PIV affects other measured properties. For instance, our description of the spatial averaging explains why PIV can provide reasonable measurements of mean and root-mean-square velocities.

One way to overcome the inherent limitations of PIV is by means of so-called high-resolution particle velocimetry (see Scarano & Riethmuller, 1999). This is a combination of PIV and Particle Tracking Velocimetry, in which the location of the cross-correlation in a given interrogation window — corresponding to a spatial average of the displacement — is used as a first estimate for the displacement of individual particles. If this displacement is known, individual particle images in the first frame in a pair can be matched to the corresponding particle images in the next frame. In principle this allows a higher spatial resolution. However, the resolution in this case is no longer uniform across the image, since it depends on the number of particle pairs that can be matched.

---

## A STATISTICAL DESCRIPTION OF THE SURFACE SHAPE

Similar to turbulence, a description of the surface shape above sub-surface turbulence lends itself well to Fourier analysis. Unlike most descriptions of turbulence, however, analysis of the free surface should involve both information in space and in time. This is essential, since waves can only be properly identified by looking at their behaviour in space and time, i.e. their dispersion relation. In this chapter an overview of the various spectra and correlation functions of the surface shape is given. The spatial measurements also allow us to study isotropy. In this chapter we will derive relations between the spectra and correlation functions for isotropic surface deformations.

### 5.1 Basic definitions

In general, the height of the surface is a function of spatial coordinates  $x$  and  $y$  and of time  $t$ , so  $h(x, y, t)$ . Similarly, the slopes  $h_x = \partial h / \partial x$  and  $h_y = \partial h / \partial y$  are functions of  $x$ ,  $y$ , and  $t$ . For a scalar function  $\eta(x, y, t)$  we can define the auto-covariance function as:

$$R_\eta(r_x, r_y, \tau) = \langle \eta(x + r_x, y + r_y, t + \tau) \eta(x, y, t) \rangle, \quad (5.1)$$

where  $\langle \dots \rangle$  denotes an ensemble average\*. The auto-covariance function is the ensemble average over all possible values of  $t$  and  $x$  of the product of  $\eta$  in a point  $(x, y)$  at a time  $t$  with  $\eta$  in a different point  $(x + r_x, y + r_y)$  at a different time  $t + \tau$ . Following Phillips (1980) the Fourier transform of an arbitrary function  $g(t)$  in time is defined as:

$$\tilde{g}(\omega) = \frac{1}{2\pi} \int_{-\infty}^{\infty} g(t) e^{i\omega t} dt \quad (5.2)$$

---

\*In many practical cases, instead of the covariance function  $R$ , we shall use its normalised equivalent: the correlation function  $C_\eta(r_x, r_y, \tau) = R_\eta(r_x, r_y, \tau) / (\eta_{rms})^2$ .



with inverse:

$$g(t) = \int_{-\infty}^{\infty} \tilde{g}(\omega) e^{-i\omega t} d\omega. \quad (5.3)$$

More appropriately, since physically only  $\omega \geq 0$  makes sense:

$$\tilde{g}(\omega) = \begin{cases} 0, & \omega < 0 \\ \frac{1}{\pi} \int_{-\infty}^{\infty} g(t) e^{i\omega t} dt, & \omega \geq 0. \end{cases} \quad (5.4)$$

Using similar definitions for Fourier transforms in space as in time<sup>†</sup> the Fourier transform of an arbitrary function  $f(x)$  in one-dimensional space can be defined as:

$$\tilde{f}(k) = \frac{1}{2\pi} \int_{-\infty}^{\infty} f(x) e^{-ikx} dx \quad (5.5)$$

with inverse:

$$f(x) = \int_{-\infty}^{\infty} \tilde{f}(k) e^{ikx} dk \quad (5.6)$$

in which  $k$  is the wavenumber. Using these definitions, the Fourier transform of  $\eta(x, y, z)$  in both space and time is:

$$\tilde{\eta}(\mathbf{k}, \omega) = \frac{1}{(2\pi)^3} \iiint \eta(\mathbf{x}, t) e^{-i(\mathbf{k} \cdot \mathbf{x}) + i\omega t} d\mathbf{x} dt \quad (5.7)$$

in which  $(\mathbf{k} \cdot \mathbf{x})$  is the inner product of vector  $\mathbf{x} = (x, y)$  and the wavenumber vector  $\mathbf{k} = (k_x, k_y)$ . The inverse of this is:

$$\eta(\mathbf{x}, t) = \iiint \tilde{\eta}(\mathbf{k}, \omega) e^{i(\mathbf{k} \cdot \mathbf{x}) - i\omega t} d\mathbf{k} d\omega. \quad (5.8)$$

Based on this, we can define the so-called wave spectrum of  $\eta(x, y, t)$ : the Fourier transform in space and time of the auto-covariance function  $R_\eta(r_x, r_y, \tau)$ :

$$E_\eta(k, \omega) = \frac{1}{(2\pi)^3} \iiint R_\eta(r_x, r_y, \tau) e^{-i(\mathbf{k} \cdot \mathbf{r}) + i\omega \tau} d\mathbf{r} d\tau, \quad (5.9)$$

in which  $\mathbf{r} = (r_x, r_y)$ . This is directly related to the Fourier transform in space and time of  $\eta(x, y, t)$  itself through:

$$E(\mathbf{k}, \omega) = \langle |\tilde{\eta}(\mathbf{k}, \omega)|^2 \rangle. \quad (5.10)$$

The auto-covariance in time is the cross-section of  $R_\eta(r_x, r_y, \tau)$  for  $r_x, r_y = 0$ , so

$$R_\eta(0, 0, \tau) = \langle \eta(t) \eta(t + \tau) \rangle, \quad (5.11)$$

---

<sup>†</sup>The difference in the sign of the exponent between the Fourier transform in space and that in time is to ensure that for a Fourier transform in both time and space, which follows, a wave with a positive value of  $k_x$  travels in the positive  $x$ -direction

which is symmetric relative to  $\tau = 0$ . Its Fourier transform is the frequency spectrum:

$$E_\eta(\omega) = \frac{1}{2\pi} \int R_\eta(0, 0, \tau) e^{i\omega\tau} d\tau. \quad (5.12)$$

It can also be obtained more directly from a point measurement of  $\eta$  in time:

$$E_\eta(\omega) = \langle |\tilde{\eta}(\omega)|^2 \rangle \quad (5.13)$$

where  $\tilde{\eta}(\omega)$  is the Fourier transform of  $\eta(t)$  measured in a point. The frequency spectrum follows from the wave-spectrum through integration over wavenumber space:

$$\begin{aligned} E_\eta(\omega) &= \int_{-\infty}^{\infty} \int_{-\infty}^{\infty} E(\mathbf{k}, \omega) d\mathbf{k} \\ &= \int_{-\infty}^{\infty} R_\eta(0, 0, \tau) e^{i\omega\tau} d\tau \\ &= 2 \int_0^{\infty} R_\eta(0, 0, \tau) \cos(\omega\tau) d\tau. \end{aligned} \quad (5.14)$$

To summarise: the frequency spectrum follows from the wave spectrum through integration over time and it is the Fourier transform in time of the auto-covariance function in time.

Similar to the frequency spectrum a spatial spectrum can be defined. This follows from integration of the wave-spectrum over all possible  $\omega$ :

$$\begin{aligned} E_\eta(\mathbf{k}) &= \int_{-\infty}^{\infty} E(\mathbf{k}, \omega) d\omega \\ &= \int_{-\infty}^{\infty} R_\eta(\mathbf{r}, 0) \exp(-i(\mathbf{k} \cdot \mathbf{r})) d\mathbf{r} \\ &= 2 \int_0^{\infty} R_\eta(\mathbf{r}, 0) \cos(\mathbf{k} \cdot \mathbf{r}) d\mathbf{r} \end{aligned} \quad (5.15)$$

in which  $R_\eta(\mathbf{r}, 0)$  is the cross-section of the auto-covariance function in space:

$$R_\eta(r_x, r_y, 0) = \langle \eta(x + r_x, y + r_y, t) \eta(x, y, t) \rangle, \quad (5.16)$$

which is symmetric relative to  $\mathbf{r} = 0$ . So, the spatial spectrum is the integral over all frequencies of the wave-spectrum, and the Fourier transform in space of the auto-covariance function in space.

## 5.2 Statistics of the slope at a point

As was explained in chapter 3, measurements of turbulent flow are often point measurements, in wind-tunnels usually with hot-wire anemometry and in this

thesis with Laser Doppler Velocimetry. In a point measurement of the slope we measure  $h_x(t)$  and  $h_y(t)$  as a function of time. This enables calculation of the correlation functions for  $h_x$  in time:

$$R_{xx}(t) = \langle h_x(t_0 + t)h_x(t_0) \rangle \quad (5.17)$$

and  $h_y$ :

$$R_{yy}(t) = \langle h_y(t_0 + t)h_y(t_0) \rangle \quad (5.18)$$

as well as the frequency spectrum in time for  $h_x$ :

$$E_{xx}(\omega) = \frac{1}{2\pi} \int R_{xx}(t)e^{i\omega t} dt = \langle |\tilde{h}_x(\omega)|^2 \rangle \quad (5.19)$$

and similarly for  $h_y$ :

$$E_{yy}(\omega) = \frac{1}{2\pi} \int R_{yy}(t)e^{i\omega t} dt = \langle |\tilde{h}_y(\omega)|^2 \rangle. \quad (5.20)$$

Unlike measurements of the turbulent velocity at a point as a function of time, however, these frequency spectra of the surface slope cannot easily be transformed into spatial spectra, since in the presence of free surface waves Taylor's hypothesis is not applicable. As a result of the Doppler effect, for waves that are moving on top of a mean flow with a certain velocity  $v_0$ , frequencies measured in the non-moving frame are shifted relative to the frequencies in the frame that moves with the flow. This is illustrated in the following comparison between a hypothetical measurement of the surface elevation in a coordinate frame that moves with the mean-stream velocity and a similar measurement in a fixed laboratory frame. The coordinate system used is shown in figure 5.1. If the actual shape of the surface in the coordinate system that moves with the mean stream velocity is  $h(x, y, t)$ , in the fixed laboratory frame we would measure  $h_m(x, y, t)$ , related to  $h(x, y, t)$  through a straightforward coordinate transform:

$$h_m(x, y, t) = h(x, y - v_0 t, t). \quad (5.21)$$

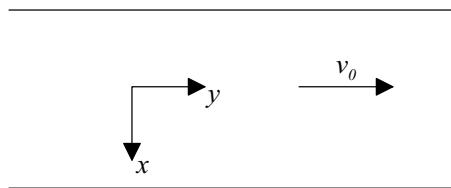


FIGURE 5.1 — Top view of the coordinate system in the water-channel.

Its Fourier transform in time and space is given by:

$$\begin{aligned}
\tilde{h}_m(k_x, k_y, \omega) &= \frac{1}{(2\pi)^3} \int e^{i\omega t - ik_x x - ik_y y} h(x, y - v_0 t, t) dx dy dt \\
&= \frac{1}{(2\pi)^3} \int e^{i\omega t - ik_x x - ik_y y' - ik_y v_0 t} h(x, y', t) dx dy' dt \\
&= \frac{1}{(2\pi)^3} \int e^{i(\omega - v_0 k_y)t - ik_x x - ik_y y'} h(x, y', t) dx dy' dt \\
&= \tilde{h}(k_x, k_y, \omega + v_0 k_y).
\end{aligned} \tag{5.22}$$

This means that for the wave spectrum the relation between the actual wave spectrum  $E$  and the measured spectrum  $E_m$  is given by:

$$E(k_x, k_y, \omega) = E_m(k_x, k_y, \omega - v_0 k_y), \tag{5.23}$$

which shows that wavenumber and frequency information are intertwined. The measured frequency is Doppler-shifted due to the convection. This situation is complicated further for waves, where the frequency itself is dependent on the wavelength. A further complication can arise due to fluctuations in the advection velocity due to sub-surface turbulence. As was shown before, the frequency spectrum is the integral of the wave spectrum over  $k$ . As such, in the measured frequency spectrum it is impossible to unravel the behaviour of the surface either in space or time. The frequency spectrum at any given frequency can contain contributions from waves with different wavenumbers. For instance, slowly traveling short waves can contribute to the same frequency as fast traveling longer waves. Furthermore, the direction in which the waves travel plays a role. Contributions to a single frequency can consist of a wave of a certain wavelength traveling upstream with a certain phase-velocity, as well as waves with a different wavelength traveling downstream with a different velocity. The solution to this problem is through a measurement of frequency and wavenumber in the direction  $y$  of the convection velocity. The actual frequency spectrum of the surface scanned in the streamwise direction then follows from:

$$E_{yy}(\omega) = \int E_m(0, k_y, \omega - k_y v_0) dk_y. \tag{5.24}$$

### 5.3 Slope statistics in time and space

In the previous section we have seen that, especially in the case of surface waves, measurements of the slope both in time and space are essential for understanding the nature of the surface deformations. Our approach is to measure the slope along lines on the surface. From these measurements we can calculate spectra of the surface slope in time and space. These can show whether part of the surface in fact consists of gravity-capillary waves. Furthermore, by

measuring spatial correlation functions of the surface slope we can determine whether or not the shape of the surface is isotropic.

### 5.3.1 DISPERSIVE SURFACE WAVES

For gravity-capillary waves the frequency of a wave is directly related to the wavenumber through the following well-known dispersion relation, the derivation of which was shown in chapter 2:

$$\omega_d(k) = \sqrt{\left(gk + \frac{k^3\sigma}{\rho}\right) \tanh(kh_0)}, \quad (5.25)$$

in which  $h_0$  is the depth of the fluid (water),  $\rho$  is its density,  $\sigma$  is the surface tension,  $g$  is the gravitational acceleration, and  $k$  is the length of wavenumber vector  $\mathbf{k}$ . In most text-book examples, see for instance Kundu (1990), this relation is derived for one-dimensional waves, and even though in Kundu (1990) examples are given of two-dimensional wave-fields it is easy to overlook that in real-world cases for a two-dimensional wavefield  $\mathbf{k}$  has two components. In wavenumber-frequency space, the dispersion relation represents a so-called dispersion surface, also known as a dispersion shell (Senet *et al.*, 2001), shown in figure 5.2 (a). For each wave-number vector  $\mathbf{k} = (k_x, k_y)$  there is one matching

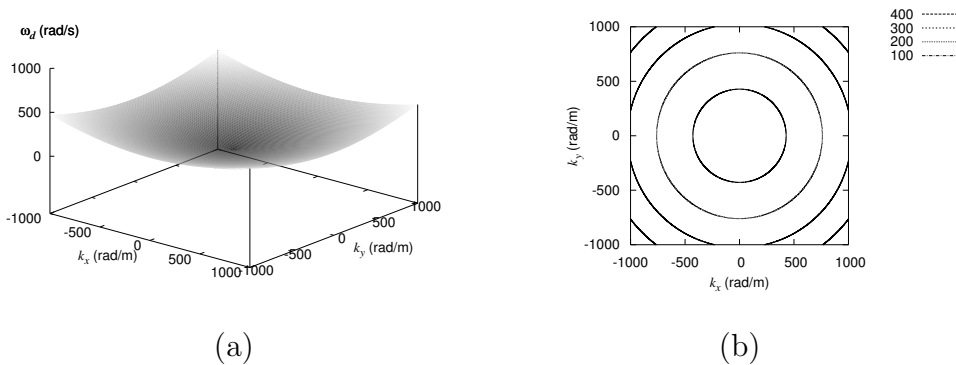


FIGURE 5.2 — (a) The dispersion relation in wavenumber-frequency space. (b) Contours of  $\omega_d(k)$ .

frequency  $\omega_d$ . Obviously the dispersion surface is cylindrically symmetric relative to  $(k_x, k_y) = (0, 0)$  which is also evident from the contours of  $\omega_d(k)$  shown in figure 5.2 (b).

In our set-up, we have a mean stream velocity in the  $y$ -direction. For waves moving on top of a mean-stream velocity the dispersion-surface is deformed

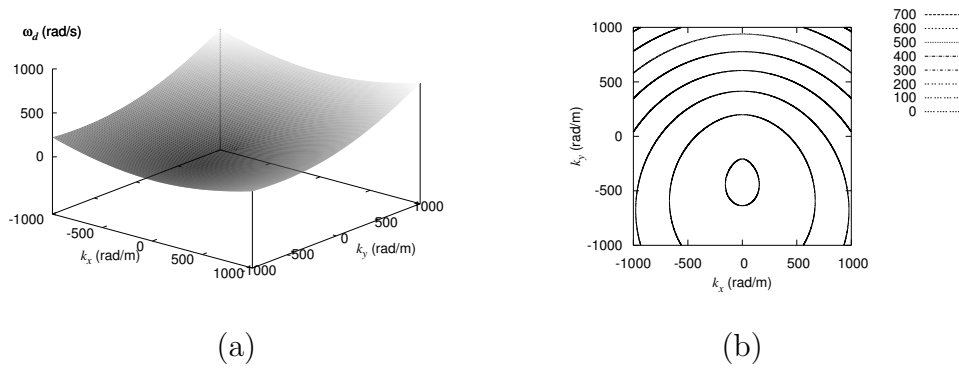


FIGURE 5.3 — The effect of a Doppler-shift due to a mean-stream velocity of 0.25 m/s in  $y$ -direction. (a) The dispersion relation in wavenumber-frequency space. (b) Contours of  $\omega_d(k)$ .

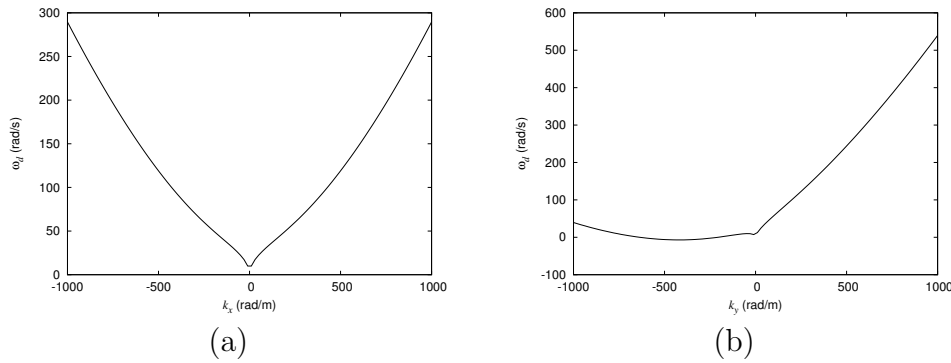


FIGURE 5.4 — Cross-sections of the dispersion-surface with a mean-stream velocity of 0.25 m/s in the  $y$  direction: (a) cross-section for  $k_y = 0$ , (b) cross-section for  $k_x = 0$ . The former remains symmetric because it is unaffected by the Doppler-shift. The latter is influenced by the Doppler-shift. Waves for which  $k_y < 0$  (upstream) appear to have lower frequencies whereas waves for which  $k_y > 0$  (downstream) appear to have higher frequencies.

through the Doppler effect. For a mean-stream velocity  $v_0$  in the  $y$ -direction the measured in non-moving frame of reference becomes:

$$\omega_d(k) = \sqrt{\left(gk + \frac{k^3\sigma}{\rho}\right) \tanh(kh_0) + v_0 k_y} \quad (5.26)$$

where  $v_0 k_y$  is the contribution due to the Doppler-shift. Figure 5.3 (a) shows a graphical representation of the resulting dispersion surface with contours of

$\omega_d(k)$  shown in figure 5.3 (b). Obviously it is no longer cylindrically symmetric. The influence of the Doppler-shift is also clear from the cross-sections shown in figure 5.4. The cross-section in the  $k_x$ -direction is unaffected by the Doppler-shift and remains symmetric relative to  $k_x = 0$ , whereas the cross-section in  $k_y$  direction is Doppler-shifted, leading to waves with  $k_y < 0$  appearing to have lower frequencies than expected from the dispersion relation and waves with  $k_y > 0$  appearing to have higher frequencies.

### 5.3.2 SPECTRA IN TIME AND SPACE

For a field consisting only of linear gravity capillary waves the wave-spectrum is directly related to the wave-number spectrum through the dispersion relation:

$$E(\omega, \mathbf{k}) = E(\mathbf{k})\delta(\omega - \omega_d(k)), \quad (5.27)$$

where the  $\delta$  indicates the Dirac  $\delta$ -function. In practice much of the energy in the wave spectrum of plane gravity-capillary waves is contained in wavenumbers and frequencies around  $\omega = \omega_d(k)$ . This is actually applied in a maritime setting in order to measure the near-surface current in the ocean. The current is derived from a fit of the Doppler-shifted dispersion shell to the wave-spectrum of the surface elevation in time and space, which is measured with a ship-mounted radar (Senet *et al.*, 2001).

In our measurements we cannot access all of this information directly, since we do not have access to both spatial coordinates simultaneously. From a measurement in the spanwise direction we can determine covariance functions in time and space along the spanwise line:

$$R_{xx}(r_x, 0, \tau) = \langle h_x(x + r_x, y, t + \tau)h_x(x, y, t) \rangle \quad (5.28)$$

and

$$R_{yy}(r_x, 0, \tau) = \langle h_y(x + r_x, y, t + \tau)h_y(x, y, t) \rangle \quad (5.29)$$

and their two corresponding spectra:

$$E_{xx}(k_x, \omega) = \int_{-\infty}^{\infty} E_{xx}(k_x, k_y, \omega)dk_y = \frac{1}{(2\pi)^2} \iint R_{xx}(r_x, 0, \omega)e^{-ik_x r_x + i\omega\tau} dr_x d\tau \quad (5.30)$$

and

$$E_{yy}(k_x, \omega) = \int_{-\infty}^{\infty} E_{yy}(k_x, k_y, \omega)dk_y = \frac{1}{(2\pi)^2} \iint R_{yy}(r_x, 0, \omega)e^{-ik_x r_x + i\omega\tau} dr_x d\tau. \quad (5.31)$$

Similarly from streamwise measurements we can determine:

$$R_{xx}(0, r_y, \tau) = \langle h_x(x, y + r_y, t + \tau)h_x(x, y, t) \rangle \quad (5.32)$$

and:

$$R_{yy}(0, r_y, \tau) = \langle h_y(x, y + r_y, t + \tau)h_y(x, y, t) \rangle. \quad (5.33)$$

The corresponding spectra follow from the Fourier transforms or from integration of the respective wave-spectra over  $k_x$  and  $k_y$  in similar fashion as in equations (5.30) and (5.31). Some of the properties of these spectra can already be understood, without any prior knowledge of the exact nature of the surface deformations. The water channel is symmetric relative to  $x = 0$ , as well as the statistical properties of the grid and the turbulent flow it generates. Hence, the covariance functions of the slope measured in  $x$ -direction are symmetric relative to  $x = 0$  and consequently the spanwise spectra are symmetric relative to  $k_x = 0$ . In streamwise direction the symmetry is broken by the mean-stream velocity. Hence the time-space spectra in streamwise direction are not symmetric relative to  $k_y = 0$  and the time-space correlation functions are not symmetric relative to  $y = 0$ . For gravity-capillary waves travelling on top of a mean-stream velocity this is reflected in the dispersion shell and its cross-sections, previously shown in figure 5.3.

In addition to the one-dimensional time-space spectra we still have access to the frequency spectra of the slopes, that can also be determined from point measurements already given in equation (5.19) and equation (5.20). They are related to the four line spectra in time and space through integration over the respective component of  $\mathbf{k}$ , so:

$$E_{xx}(\omega) = \int_{-\infty}^{\infty} E_{xx}(k_x, \omega) dk_x = \int_{-\infty}^{\infty} E_{xx}(k_y, \omega) dk_y \quad (5.34)$$

and

$$E_{yy}(\omega) = \int_{-\infty}^{\infty} E_{yy}(k_x, \omega) dk_x = \int_{-\infty}^{\infty} E_{yy}(k_y, \omega) dk_y. \quad (5.35)$$

Finally, we can also calculate four one-dimensional spatial spectra. These are related to the spectra in time and space through integration over  $\omega$ , so:

$$E_{xx}(k_x) = \int_{-\infty}^{\infty} E_{xx}(k_x, \omega) d\omega \quad (5.36)$$

and similarly  $E_{xx}(k_y)$ ,  $E_{yy}(k_x)$ , and  $E_{yy}(k_y)$ . They can also be calculated more directly from the measurements by Fourier transforming the slopes in space:

$$E_{xx}(k_x) = \langle |\tilde{h}_x(k_x)|^2 \rangle \quad (5.37)$$

and likewise  $E_{xx}(k_y)$ ,  $E_{yy}(k_x)$ , and  $E_{yy}(k_y)$ .

As a consequence of measuring the slope as a function of space and time along a line, the length of the wavenumber vector is unknown. This means that some of the drawbacks of point-measurements still remain. In the measured spectra in time and space a range of wavenumbers  $k > k_x$  can contribute to



the spectrum in  $k_x$  as and similarly wavenumbers  $k > k_y$  can contribute to the spectrum at  $k_y$ . Hence it is not immediately clear if and how the dispersion relation will even be visible. Later we will see that the experimental results are also complicated by the presence of other structures than waves on the surface and the fact that the sources of the waves are actually passing through the measurement location.

### 5.3.3 ISOTROPY IN THE SURFACE SLOPES

As we have seen in chapters 3 and 4, one of the standard ways to study isotropy in a turbulent flow is by comparing longitudinal and transverse correlation functions of the velocity. For incompressible three-dimensional isotropic turbulence a relation between the two can be derived (Pope, 2000):

$$C_{TT}(r) = C_{LL}(r) + \frac{1}{2}r \frac{d}{dr}C_{LL}(r), \quad (5.38)$$

which was previously used to study isotropy in our LDV turbulence measurements in section 3.3.3. Its equivalent expression for isotropic two-dimensional incompressible turbulence is:

$$C_{TT}(r) = C_{LL}(r) + r \frac{d}{dr}C_{LL}(r). \quad (5.39)$$

Unlike the velocity measurements in chapter 3, isotropy of the surface shape can only be measured by means of spatial measurements. This is because of the influence of the Doppler-effect explained in section 5.2. We can find a relation between the transverse and longitudinal correlation functions for the surface slopes, similar to equation (5.39). The surface elevation can be described by a function  $h(x, y)$ <sup>‡</sup>. The surface slope is obviously the gradient of the surface elevation:

$$h_x \mathbf{e}_x + h_y \mathbf{e}_y = \nabla h. \quad (5.40)$$

In our measurements the longitudinal covariance function  $R_{LL}(r)$  corresponds to both  $\langle h_y(x, y+r, t)h_y(x, y, t) \rangle$ , which can be obtained from a measurement along a streamwise line, and to  $\langle h_x(x+r, y, t)h_x(x, y, t) \rangle$  from a spanwise measurement. The transverse covariance function  $R_{TT}(r)$  corresponds to  $\langle h_x(x, y+r, t)h_x(x, y, t) \rangle$  from a streamwise measurement and to  $\langle h_y(x, y+r, t)h_y(x, y, t) \rangle$  from a spanwise measurement. The correlation functions  $C_{LL}$  and  $C_{TT}(r)$  are the covariance functions  $R_{LL}(r)$  and  $R_{TT}(r)$  divided by the root-mean-square of the slope in any given direction, since for an isotropic surface this is independent of the direction in which it is measured. A way to check for isotropy

---

<sup>‡</sup>Of course  $h(x, y, t)$  is also a function of time. However, the dependence on time for now is assumed implicitly since ensemble averages and temporal averages will be taken equivalent.

is to see whether the measured longitudinal correlation function is indeed independent of the direction of the line along which we measure (spanwise or streamwise).

A consequence of the fact that  $h_x$  and  $h_y$  are the gradient of scalar field  $h(x, y)$  is that they form a potential field:

$$\nabla \times (\nabla h) = \frac{\partial}{\partial x} h_y - \frac{\partial}{\partial y} h_x = 0. \quad (5.41)$$

We can use this to derive the relation between the transverse and longitudinal correlation functions for the surface slopes, via the surface slope covariance tensor, defined by:

$$\mathbf{R}(\mathbf{r}) = \begin{pmatrix} R_{xx}(\mathbf{r}) & R_{xy}(\mathbf{r}) \\ R_{yx}(\mathbf{r}) & R_{yy}(\mathbf{r}) \end{pmatrix} = \begin{pmatrix} \langle h_x(\mathbf{x})h_x(\mathbf{x} + \mathbf{r}) \rangle & \langle h_x(\mathbf{x})h_y(\mathbf{x} + \mathbf{r}) \rangle \\ \langle h_y(\mathbf{x})h_x(\mathbf{x} + \mathbf{r}) \rangle & \langle h_y(\mathbf{x})h_y(\mathbf{x} + \mathbf{r}) \rangle \end{pmatrix} \quad (5.42)$$

Using equation (5.41) we find that:

$$\begin{aligned} \frac{\partial}{\partial r_x} R_{xy}(\mathbf{r}) - \frac{\partial}{\partial r_y} R_{xx}(\mathbf{r}) &= \\ \frac{\partial}{\partial r_x} \langle h_x(\mathbf{x})h_y(\mathbf{x} + \mathbf{r}) \rangle - \frac{\partial}{\partial r_y} \langle h_x(\mathbf{x})h_x(\mathbf{x} + \mathbf{r}) \rangle &= \\ \langle h_x(\mathbf{x}) \frac{\partial}{\partial r_x} h_y(\mathbf{x} + \mathbf{r}) \rangle - \langle h_x(\mathbf{x}) \frac{\partial}{\partial r_y} h_x(\mathbf{x} + \mathbf{r}) \rangle &= 0 \end{aligned} \quad (5.43)$$

and similarly:

$$\frac{\partial}{\partial r_y} R_{yx}(\mathbf{r}) - \frac{\partial}{\partial r_x} R_{yy}(\mathbf{r}) = 0. \quad (5.44)$$

In any isotropic field, we can write the covariance tensor as a combination of  $r_i r_j$  and  $\delta_{ij}$ , which defines the (scalar) longitudinal covariance function  $R_{LL}(r)$  and the transverse covariance function  $R_{TT}(r)$  (Pope, 2000):

$$R_{ij}(\mathbf{r}) = (R_{LL}(r) - R_{TT}(r)) \frac{r_i r_j}{r^2} + R_{TT}(r) \delta_{ij}. \quad (5.45)$$

The individual components of the tensor can now be written in terms of these functions:

$$\begin{aligned} R_{xx}(\mathbf{r}) &= (R_{LL}(r) - R_{TT}(r)) \frac{r_x^2}{r^2} + R_{TT}(r) \\ R_{xy}(\mathbf{r}) &= (R_{LL}(r) - R_{TT}(r)) \frac{r_x r_y}{r^2} \\ R_{yx}(\mathbf{r}) &= (R_{LL}(r) - R_{TT}(r)) \frac{r_x r_y}{r^2} \\ R_{yy}(\mathbf{r}) &= (R_{LL}(r) - R_{TT}(r)) \frac{r_y^2}{r^2} + R_{TT}(r), \end{aligned} \quad (5.46)$$

which serves to show that  $R_{LL}$  indeed is the longitudinal covariance function. Substituting, for instance,  $\mathbf{r} = (r_x, 0)$  in  $R_{xx}$  leads to  $R_{xx}(r_x, 0) = R_{LL}(r_x)$ . Similarly, substituting  $\mathbf{r} = (r_x, 0)$  in  $R_{yy}$  leads to  $R_{yy}(r_x, 0) = R_{TT}(r_x)$ , the transverse covariance function. Either equation (5.43) or (5.44) can now be used to find the relation between  $R_{LL}(r)$  and  $R_{TT}(r)$ . We start by calculating explicitly the derivatives:

$$\begin{aligned} \frac{\partial R_{xy}}{\partial r_x} &= \frac{r_x r_y}{r^2} \left( \frac{dR_{LL}}{dr} - \frac{dR_{TT}}{dr} \right) \frac{\partial r}{\partial r_x} + (R_{LL} - R_{TT}) \left( \frac{\partial}{\partial r_x} \frac{r_x r_y}{r^2} \right) = \\ &= \left( \frac{dR_{LL}}{dr} - \frac{dR_{TT}}{dr} \right) \frac{r_x^2 r_y}{r^3} + (R_{LL} - R_{TT}) \frac{r_y}{r^2} \left( 1 - \frac{2r_x^2}{r^2} \right) \end{aligned} \quad (5.47)$$

and

$$\begin{aligned} \frac{\partial R_{xx}}{\partial r_y} &= \frac{r_x^2}{r^2} \left( \frac{dR_{LL}}{dr} - \frac{dR_{TT}}{dr} \right) \frac{\partial r}{\partial r_y} + (R_{LL} - R_{TT}) \left( \frac{\partial}{\partial r_x} \frac{r_x^2}{r^2} \right) + \frac{dR_{TT}}{dr} \frac{\partial r}{\partial r_y} = \\ &= \left( \frac{dR_{LL}}{dr} - \frac{dR_{TT}}{dr} \right) \frac{r_x^2 r_y}{r^3} - (R_{LL} - R_{TT}) \frac{2r_y r_x^2}{r^4} + \frac{dR_{TT}}{dr} \frac{r_y}{r}. \end{aligned} \quad (5.48)$$

Substituting these expressions in equation (5.43) leads to:

$$\begin{aligned} &\left( \frac{dR_{LL}}{dr} - \frac{dR_{TT}}{dr} \right) \frac{r_x^2 r_y}{r^3} + (R_{LL} - R_{TT}) \frac{r_y}{r^2} \left( 1 - \frac{2r_x^2}{r^2} \right) \\ &- \left( \frac{dR_{LL}}{dr} - \frac{dR_{TT}}{dr} \right) \frac{r_x^2 r_y}{r^3} + (R_{LL} - R_{TT}) \frac{2r_y r_x^2}{r^4} - \frac{dR_{TT}}{dr} \frac{r_y}{r} = 0 \end{aligned} \quad (5.49)$$

which leads to the following relation between the transversal and longitudinal covariance functions:

$$R_{LL} = R_{TT} + r \frac{d}{dr} R_{TT}. \quad (5.50)$$

and since the root-mean-square of the slope is independent of the direction the desired relation between the longitudinal and transverse correlation function becomes:

$$C_{LL} = C_{TT} + r \frac{d}{dr} C_{TT}. \quad (5.51)$$

Performing similar substitutions in equation (5.44) obviously leads to the same result.

It is very interesting to compare this equation to the equivalent equation for two-dimensional isotropic turbulence given in equation (5.39). For the velocity field, for which  $\nabla \cdot \mathbf{u} = \mathbf{0}$ , the occurrence of a difference in velocity components along a line, so in longitudinal direction, is hindered by incompressibility, whereas the transverse velocity component is unaffected. Hence, in an isotropic velocity field the longitudinal correlation length is larger than that in transverse direction.

The effect of the free surface gradient field being irrotational is that the roles of the longitudinal and transverse correlation functions are reversed. Here the occurrence of a difference in the transverse slope in two points on a line is hindered by it being associated with twisting of the surface. A difference in longitudinal slope is associated with bending, as is illustrated in figure 5.5. Because of the different nature of these surface deformations, for an isotropic irrotational field the transverse correlation length is larger than the longitudinal correlation length.

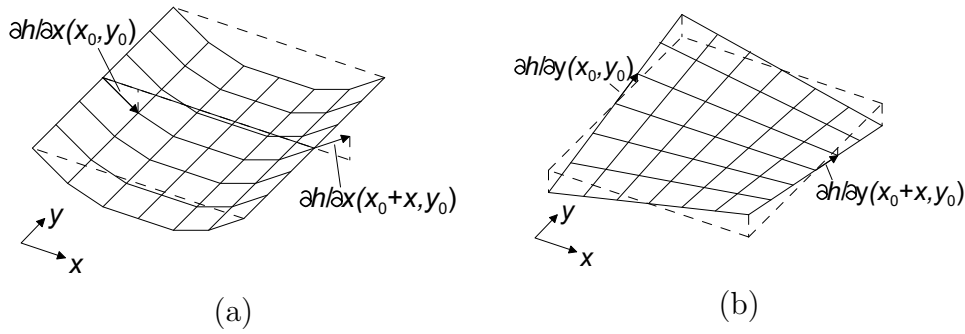


FIGURE 5.5 — Illustration of the different type of deformation associated with a difference in (a) the slope along a line (longitudinal) and (b) the slope perpendicular to a line (transverse).

Similar to the correlation functions, which were reduced from four functions to only two, for isotropic surface waves the four one-dimensional wave spectra obtained from the measurements are reduced to two: the longitudinal and transverse spectra. The longitudinal spectrum is the Fourier cosine transform of the longitudinal covariance function:

$$E_{LL}(k) = \frac{2}{\pi} \int_0^{\infty} R_{LL} \cos(kr) dr. \quad (5.52)$$

For isotropic surface waves it corresponds to  $E_{xx}(k_x)$  and  $E_{yy}(k_y)$  as defined in equations (5.36) and (5.37). Similarly the transverse spectrum corresponds to  $E_{xx}(k_y)$  and  $E_{yy}(k_x)$  and is the transform of the transverse covariance function:

$$E_{TT}(k) = \frac{2}{\pi} \int_0^{\infty} R_{TT} \cos(kr) dr \quad (5.53)$$

By taking the Fourier cosine-transform of equation (5.51) we find the following relation between the longitudinal and transverse spectra:

$$E_{LL}(k) = -k \frac{d}{dk} E_{TT}(k). \quad (5.54)$$

Similar to the relation between the correlation functions given in equation (5.51), this equation can, in principle, be used to check whether the surface shape is isotropic.

---

## MEASURING THE SLOPE OF THE FREE SURFACE

From an experimental point of view, measuring the surface slope at a point as a function of time is relatively straightforward. Similar to, for instance, one-point hot-wire velocity measurements in a wind-tunnel, point measurements of the slope enable calculation of the frequency spectrum and the auto-correlation function of the slope in time. However, as shown in the previous chapter, these spectra offer only a limited view of the nature of the surface deformations. Measurements of the surface in space and time are an absolute necessity. In this chapter, an existing technique for measuring the surface slope at a point is explained. It forms the basis for a novel technique that allows measurement of the surface slope in space and time along a line. A comparison of experimental results obtained with both techniques allows us to test this new set-up.

### 6.1 Introduction

One of the first quantitative measurements of the surface gradient field involved pictures of the sun glittering on the ocean surface (Cox & Munk, 1954). In our work we use the refraction of a focused laser beam by the surface to measure the two components of the surface gradient at a point. By rapidly scanning the incident laser beam along a line, while at the same time sampling the location of the refracted laser beam, we measure the time-dependent gradient field along a line. For strongly curved surfaces, scanning techniques are unavoidable because whole-field measurements are thwarted by caustics and ambiguities. A similar scanning slope gauge has been described by Bock & Hara (1995) and Hara, Bock & Donelan (1997). Their device, which was successfully used for the measurement of wind-driven waves, is suited for relatively low frequencies and large wavelengths (largest frequency  $\approx 35$  Hz, smallest wavelength  $\approx 4$  mm) and scans a circle on the surface. For our experiment a linear scan and a much better space-time resolution was needed.

Jähne *et al.* (1994) review quantitative imaging techniques of ocean wind waves and conclude that scanning techniques for measuring the gradient field are most promising. It is good however, to put these techniques in the perspective of whole field measurements. In this context, an often-used technique to look at spatial surface deformations is shadowgraphy (Settles, 2001). In shadowgraphy images are formed as a result of the refraction of light passing through a transparent material of varying density. In the case of a free surface, this refraction occurs at the interface and the resulting image provides a view of the shape of the surface. For free-surface flows, shadowgraphy has mainly been used to study the interaction of structures with the surface. For instance, Walker *et al.* (1995) has used shadowgraphy to study the interaction between a turbulent jet and a free surface. Sarpkaya & Suthon (1991), and Gharib and Weigand (Weigand, 1996; Gharib, 1994; Gharib & Weigand, 1996) have used shadowgraphy to study vortex (dis)connection and the interaction between vortex rings and a free surface. However, obtaining quantitative information from shadowgraphy is often impossible and shadowgraphy is primarily a tool to qualitatively visualise the surface shape.

Zhang & Cox (1994) and Kurata *et al.* (1990) show that quantitative information about the surface gradient field can be obtained from images of a (coloured) pattern that is either refracted in or reflected by the surface. By reducing the scale of these patterns, Dalziel *et al.* (2000) developed a synthetic schlieren technique in which a randomly dotted pattern is refracted by the free surface. Quantitative information about the surface shape is obtained by applying a cross-correlation algorithm, similar to that used for Particle Image Velocimetry, to a picture of the undisturbed pattern and a picture of the refracted pattern. All of these techniques are image-based. The actual image itself provides the (two-dimensional) spatial information. The spatial resolution of these techniques is limited by the density of the pattern used, or in case of the synthetic schlieren technique by the minimum size of the interrogation windows used for cross-correlating the images. The resolution in time in these techniques is limited by the frame-rate of the camera. Increasing the frame-rate, through the use of a high-speed camera, has consequences for the measurement of low frequencies, since the duration of the measurement is limited by the maximum number of frames that can be stored.

In a geophysical setting, on an entirely different scale both in space (from several meters up to kilometers) and in time (frequencies lower than 1 Hz), several different techniques are used to measure wave-fields, including radar (altimeter) measurements from ships (Senet *et al.*, 2001) or even from satellites (Forbes *et al.*, 1993; Stammer, 1997) and photographs of sea surface glint taken from aircraft (Dugan & Piotrowski, 2003), as well as measurements from *in situ* arrays of buoys and pressure transducers (Holland, 2001).

## 6.2 Point measurements of the surface slope

The principle of the technique used to do point measurements of the slope is based on refraction of a laser beam. Previously, this method was successfully used to measure waves on the surface of a vertically oscillated fluid (Faraday waves) (see Westra, Binks & van de Water, 2003).

The technique is illustrated in figure 6.1. A laser beam, originating from a small 1 mW diode laser is sent perpendicularly through the transparent bottom of the water-channel and onwards to the surface, where it is refracted. The refracted beam then proceeds onto a so-called Position Sensitive Device (PSD). This sensor is a dual lateral photo-diode, the layout of which is shown in fig-

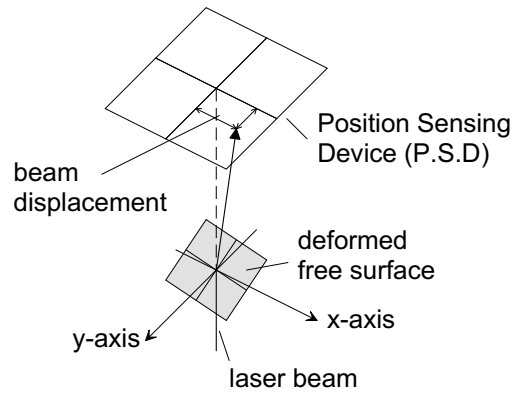


FIGURE 6.1 — The principle of slope measurements in a point. A beam is refracted by the surface. The beam's displacement is measured with a Position Sensitive Device.

ure 6.2. The sensor used in the point measurements measures  $1 \times 1 \text{ cm}^2$  and was manufactured by UDT sensors. It consists of a three-layer semi-conducting silicon structure, biased with a bias voltage  $V_{bias}$ . Incident light on the photo-diode's surface generates free electrons that change the local resistivity of the semi-conducting material. As a result of this, the ratios of the cathode and anode currents  $I_{c1}, I_{c2}, I_{a1}$ , and  $I_{a2}$ , as indicated in figure 6.2, change and as such their ratios can be used as a measure of the position of the illuminated spot on the surface of the detector. For a square PSD of size  $L \times L$  the positions follow from:

$$x_{PSD} = \frac{I_{a1} - I_{a2}}{2I_{ph}} L \quad (6.1)$$

and

$$y_{PSD} = \frac{I_{c1} - I_{c2}}{2I_{ph}} L, \quad (6.2)$$



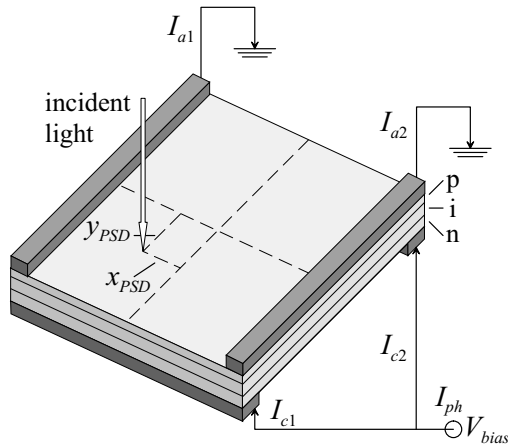


FIGURE 6.2 — Layout of a Position Sensitive Detector.

in which  $I_{ph}$  is the total photo-current. Because of these ratios, the sensor is insensitive to the intensity of the laser spot, with the position signal reflecting the centre of mass of the laser spot. We emphasize that this only works if the four photocurrents can be measured exactly simultaneously and the transport of the photo charges across the sensor is instantaneous. The currents are measured and the various subtractions and divisions are performed in an analogue Phillips PSD processor board (type CTR 531.91.0017). This provides two output voltages  $V_x$  and  $V_y$ , which correspond to the positions  $x_{PSD}$  and  $y_{PSD}$ . The response speed of the measurement technique in this configuration is limited by the electronic circuitry in the processor board, but generally a PSD offers a far better resolution in time than a pixel-based detector such as a CCD or CMOS. The spatial resolution of the PSD is limited by both shot noise and thermal noise of the resistive layer. The linearity of the response is primarily dependent on the quality of the substrate layers of the PSD. In practice we use a linear transformation from voltages to positions, based on a separate calibration of the PSD. The PSD-Voltages are digitised for processing and storage on a computer by means of a PhyDAS PARSAM (PARallel SAMpling) unit, with a sample frequency of 30kHz.

The free surface gradient in  $x$  and  $y$ -directions can be calculated from the displacements  $\delta x$ ,  $\delta y$  of the spot on the PSD surface from:

$$\frac{\partial h}{\partial x} = \frac{-\delta x}{H - n_w \sqrt{H^2 + (\delta x)^2 + (\delta y)^2}} \quad \text{and} \quad \frac{\partial h}{\partial y} = \frac{-\delta y}{H - n_w \sqrt{H^2 + (\delta x)^2 + (\delta y)^2}}. \quad (6.3)$$

The displacements  $\delta x$ ,  $\delta y$  are calculated by subtracting the average position of the spot taken over the entire measurement time from the instantaneous

position,

$$\delta x = x_{PSD} - \langle x_{PSD} \rangle, \quad \delta y = y_{PSD} - \langle y_{PSD} \rangle, \quad (6.4)$$

where  $x_{PSD}$  and  $y_{PSD}$  are the instantaneous positions and  $\langle x_{PSD} \rangle$  and  $\langle y_{PSD} \rangle$  are the corresponding averages.

This method is based on the notion that on average a turbulent surface is horizontal. Since the right-hand-side of equations (6.3) depends non-linearly on  $\delta x$  and  $\delta y$ , a zero average of  $\partial h/\partial x$  and  $\partial h/\partial y$  is not the same as a zero average of  $\delta x$  and  $\delta y$ , but we found the error to be negligible. Calibration requires a measurement of the height  $H$  of the PSD above the (undisturbed) surface and the conversion of measured PSD voltages to position, which was calibrated in a separate experiment. All other information needed to convert measured voltages to surface slopes follow from the measured time series. This method is straightforward, sensitive, and linear. However, it only provides the time-dependence of the surface slope in a point. For a surface that is advected by the mean flow, this information is ambiguous as temporal fluctuations may also be caused by spatial fluctuation which are swept past the measurement location. We next describe the extension of this technique to measurement of the time-dependent gradient field along a line.

### 6.3 Measuring the slope in space and time

#### 6.3.1 SET-UP FOR SLOPE MEASUREMENTS ALONG A LINE

As already mentioned, in order to measure the surface slope in space and time we have chosen to measure the slope along a line. The technique used for this is an extension of the existing technique used for point measurements. The new set-up is illustrated in figure 6.3. Instead of being aimed at a single point of the surface, now the laser beam is swiveled back and forth by a rapidly oscillating mirror (an Electro Optical Products Corp. SC-30 resonant scanning mirror). Changes in the signal that occur more rapidly than those due to the oscillating motion are interpreted as spatial variations of the surface slope along the line. A drawback of this technique compared to image-based surface slope measurements is that it only provides one spatial coordinate. However, it does offer a much higher resolution in time as well as a higher spatial resolution along the line. Obviously, it is impossible to measure structures on the surface that are actually smaller than the size of the light spot on the surface, which is why the laser beam is passed through a lens that focuses it on the surface. As will be explained in more detail shortly, the length of the line on the surface is too large to allow the refracted beam to be projected directly onto the PSD. Hence, after passing through the free surface the refracted beam falls onto a plate of high quality frosted glass. This leads to an illuminated dot being visible on the top side of the frosted glass, at the location where the beam hits it. This spot is projected onto the PSD. By sampling the PSD signals at a higher rate  $f_s$

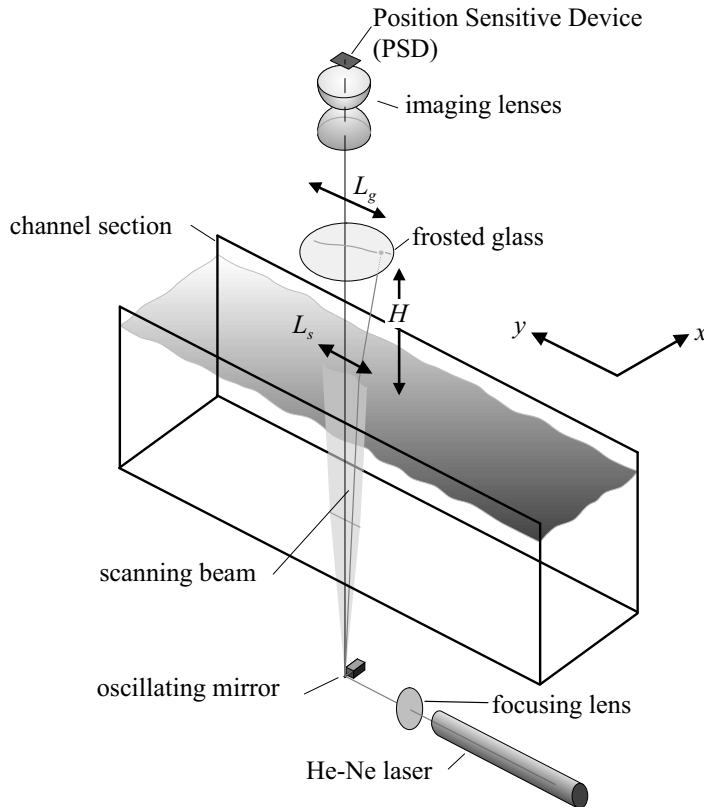


FIGURE 6.3 — Set-up for measuring the surface slope along a line.

than the oscillation frequency  $f_m$  of the mirror, the position of the spot on the PSD is measured multiple times during each mirror period, thereby providing the slope in multiple points on the line. In our case we can measure the slope in 152 points along a 5 cm line.

### 6.3.2 SYNCHRONISATION

The electronics that control the oscillating mirror also provide a periodic square wave voltage, at the frequency at which the mirror oscillates. This signal serves as a triggering signal for a purpose-built electronic timing unit, which in turn delivers a predetermined number  $n$  of trigger signals at a fixed frequency to the ADC. This means that the positions on the line at which the PSD voltages are sampled are fixed in time relative to the phase of the mirror. This is illustrated in figure 6.4. Let us call  $p$ , with  $p = 1, \dots, n$ , the index of a sample in each block of  $n$  samples and  $q, q = 1, 2, \dots$  the index of a block. Then the index  $p$

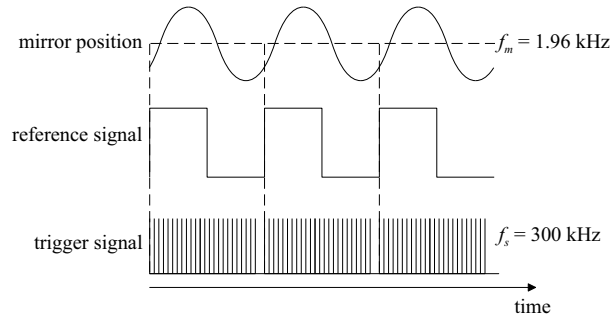


FIGURE 6.4 — Synchronisation of the surface gradient scanner. The mirror control unit provides a block signal with the same frequency as the mirror movement ( $f_m = 1.96$  kHz). This triggers a timing unit which sends blocks of 152 trigger signals at sample frequency  $f_s = 300$  kHz to the ADC. Each line sample is one cycle of the mirror, in which each point on the line is visited twice. The unit has further provisions to synchronize the line scan to a particle image velocimetry system.

corresponds to a point on the scanned line, while  $q$  is an index,  $f_q = q/f_m$ , corresponding to the time at which the line was measured. We will now show how the samples define the surface gradient  $h_x(x, y, t)$  and  $h_y(x, y, t)$ .

Let us assume that the laser beam is scanned in the  $x$ -direction. After refraction through the surface the signal of the PSD contains two components:  $V^x$  and  $V^y$  corresponding to the deflections of the laser beam in the  $x$ - and  $y$ - directions, respectively. The samples  $V_{p,q}^x$  include two contributions: a large contribution due to the beam being swiveled back and forth by the oscillating mirror and a smaller contribution resulting from the actual changes in slope in the points of the line. The other sampled voltage,  $V_{p,q}^y$ , only contains a contribution from the changes in slope\*. Provided that the imaging by this system is linear, the position  $x_{p,q}^g$  of the spot on the glass and the voltage  $V_{p,q}^x$  from the PSD are related through:

$$V_{p,q}^x = Ax_{q,p}^g + B^x, \quad (6.5)$$

in which  $A$  is a proportionality constant that is the same for deflections in  $x$ - and  $y$  directions and  $B^x$  is an offset that depends on the component of the measured deflection. These constants can be easily found from the measurement. Since on average the surface is flat, the time ( $q$ ) average of the measured voltage  $V^x$

---

\*In practice one can expect there to be some misalignment, leading to a small contribution due to the scanning also being present in  $V^y$ . However, this has no effect on the measurement of the slope itself, since the average trace of the spot in the surface is subtracted, as will be explained later.

is

$$V_p^x = \langle V_{p,q}^x \rangle_q = Ax_p^g + B^x, \quad (6.6)$$

where  $x_p^g$  are the positions corresponding to the trace of the line on the glass if the surface were flat. Thus the peak-to-peak amplitude  $V_a^x$  of  $V_p^x$  corresponds to the length of the line on the glass. The proportionality constant  $A$  now follows from dividing the peak-to-peak amplitude  $V_a^x$  by the actual physical length of the line on the glass,  $L_g$ :

$$A = \frac{V_a^x}{L_g}. \quad (6.7)$$

Of course, since the relation between the surface slope and the laser beam deflection is non-linear, this procedure is not strictly correct. However, we have ascertained that, similar to the point measurements, the error is negligible. The constants that determine the coordinates  $(x_p^w, y_p^w)$  on the actual water surface are determined analogously to those on the glass; for example the corresponding proportionality constant would be  $V_a^x/L_s$ , in which  $L_s$  is the length of the line on the water surface.

Finally, the equations for the measured surface gradient field are similar to those of the point measurement, equation (6.3):

$$\left. \frac{\partial h(x, y, t)}{\partial x} \right|_{x=x_p^w, y=y_p^w, t=q/f_m} = \frac{-\delta x_{p,q}}{H - n_w \sqrt{H^2 + (\delta x_{p,q})^2 + (\delta y_{p,q})^2}} \quad (6.8)$$

and

$$\left. \frac{\partial h(x, y, t)}{\partial y} \right|_{x=x_p^w, y=y_p^w, t=q/f_m} = \frac{-\delta y_{p,q}}{H - n_w \sqrt{H^2 + (\delta x_{p,q})^2 + (\delta y_{p,q})^2}} \quad (6.9)$$

in which  $H$  is the height of the glass above the undisturbed surface and  $\delta x_{p,q}$  and  $\delta y_{p,q}$  are displacements of the spot on the glass with respect to the traced averaged curve:

$$\delta x_{p,q} = x_{p,q} - x_p = \frac{V_{p,q}^x - V_p^x}{A} \quad (6.10)$$

and:

$$\delta y_{p,q} = y_{p,q} - y_p = \frac{V_{p,q}^y - V_p^y}{A}. \quad (6.11)$$

Obviously, for a correct assignment of the gradient field it is crucial to carefully keep track of the various signs of displacements and digitised voltages.

Calibration of this slope measurement technique requires only straightforward measurements of three lengths, also indicated in figure 6.3 :

1. The height of the glass above the surface  $H$  is needed in order to calculate the slopes from the displacement on the frosted glass from equations (6.8) and (6.9).

2. The length of the scan-line  $L_g$  on the glass is needed to find the proportionality constant  $A$  in equation (6.7). If it is known, the actual positions on the glass can be calculated.
3. The length of the line on the surface  $L_s$  is required in order to calculate the actual position of each point on the line on the water surface.

It should be noted that due to the use of a swiveling beam the beam crosses both the bottom of the channel as well the surface at a small angle. The effect of this is almost completely removed by subtracting the averages. Its residual effect may be a small bias, which may become somewhat more pronounced for the extreme points on the line. In theory it is possible to correct for this. The exact position where the light beam falls onto the frosted glass depends on the slope at the surface as well as on the elevation of the surface. However, in our set-up changes of the position on the glass relative to the average position are interpreted as resulting from a change of the slope at the surface. As with the point measurements, the influence of changes in the elevation of the surface is neglected, since their effect is very small compared to the effect of a change in the slope, especially since the anticipated changes in the elevation (at most a few mm) are tiny compared to  $H$  (30 cm).

The use of a plate of frosted glass is an unfortunate necessity. Directly projecting the line onto the PSD is not possible, despite the use of a larger  $2 \times 2 \text{ cm}^2$  PSD for these measurements. The reason is that the optics needed to directly project the refracted laser beam onto the PSD is subject to incompatible requirements. In order to accommodate the largest possible surface gradient ( $S_m = \mathcal{O}(0.3)$ ) in our experiments, the lens must be placed as near to the surface as possible, with its focal length  $F$  as the minimal distance. Then, if the length of the scanned line is  $L_s$ , the diameter of the lens should at least be  $2 F S_m + L$ . Although lenses with  $S_m = 0.3$  do exist, they are difficult to manufacture and their imaging is far from ideal. The problem is that in direct imaging of the refracted laser beam, angle and position are coupled. Further, with the surface in the focal plane of the lens, the position on the PSD would depend on both the angle and the position at which the laser beam enters the lens. However, the surface gradient itself is only reflected in the angle of the laser beam. Unravelling these contributions by calibrating would be exceedingly difficult. The major benefit of using the frosted glass is that now angle and the position become decoupled. A drawback of this method is, however, a large loss of light intensity and the introduction of speckles in the light spot. To optimise the light intensity the laser spot on the frosted glass is imaged onto the PSD detector surface by using two very strong large-diameter lenses. To further increase the intensity of the light on the PSD a relatively powerful (approx. 30 mW) He-Ne laser was used.

In order to increase the response speed of the measurement technique, the processor board we used for the point measurements, has been replaced by a

purpose-built new electronic circuit, which amplifies the four PSD currents and separately converts them to voltages. These four voltages are then individually sampled by means of a four-channel parallel Analogue to Digital converter (National Instruments Ni-DAQ 6115) at the sample frequency of 300 kHz. Instead of measuring voltages  $V^x$  and  $V^y$ , the (relative) positions on the PSD are now actually calculated in post-processing by means of equations (6.1) and (6.2). The time response of the PSD itself now determines the smallest changes the surface slope along the line that we can find with our scan technique. Since the position signal of the light spot depends on intensity ratios, the position signal is insensitive to intensity fluctuations of the refracted laser beam. In our experiment intensity fluctuations are caused by scattering off particles in the flow (used in PIV experiments) and by speckles of the frosted glass screen. However, the intensity normalisation can only work if all currents are measured simultaneously. The problem is that photo-charges in the PSD have a finite velocity, set by the capacity of the light-sensitive layer. The propagation delay is a few  $\mu\text{s}$ , which in our case corresponds to the used sampling frequency ( $f_s = 300$  kHz). At those frequencies intensity variations are seen as position variations. Without a faster PSD, no further improvement of the signal-to-noise ratio is possible.

The positions  $x^p$  on the scan line are sampled sinusoidally: the points crowd near the extremes of the sweep, and they are sampled fastest near the zero-crossings of the sweep. We expect that a further effect of the propagation delays of the photo-charges is that samples of the surface slope near the zero-crossings will have different properties from those at the extremes of  $x^p$ . We will assess this possible source of inhomogeneity below.

The overall set-up is more complicated than the set-up used for point measurements. Moving the optical system along the water channel is far more difficult. Because of this we have chosen to place the set-up at a fixed position two meters downstream from the turbulence generating grid, not coincidentally the same position as where we performed the Laser-Doppler measurements of the turbulence properties described in chapter 3.

### 6.3.3 DATA PROCESSING

The data processing is done with a series of computer programmes. In order to obtain surface gradient information from the stored data, the file (typically several GBytes in size) is first unravelled in samples  $V_{p,q}^x$  and  $V_{p,q}^y$ . If, for example, the laser beam is scanned in the  $x$ -direction sample  $V_{p,q}^x$  contains the relevant information about the scan. Since perfect synchronisation is crucial for this method, the relative phase of the samples  $V_{p,q}^x$  is monitored constantly through computing the auto-correlation function of  $V_{p,q}^x$ . Phase drifts may occur due to temperature changes of the resonant mirror. A measurement of the phase reveals that the relative phase-shift of the mirror is  $\mathcal{O}(10^{-3})$  over the duration of the longest measurement, which is negligible. Next, the coordinates

$(x_p, y_p), p = 1, \dots, n$  are computed from phase-sensitive averages of  $V^x$  and  $V^y$ . Finally the surface gradients  $h_x(x_p, y_p, t_q)$  and  $h_y(x_p, y_p, t_q)$  are computed.

The key questions are about the homogeneity of the measurement technique along the scan line and its spectral response. Several useful statistical quantities can be computed from the measured gradient field and may be used to answer these questions. In the case of homogeneous turbulence, the normalized space-time correlation function

$$R_{xx}(x_i, x_j, \tau) = \frac{\langle h_x(x_i, t + \tau) h_x(x_j, t) \rangle}{\langle h_x^2(x_i, t) \rangle^{1/2} \langle h_x^2(x_j, t) \rangle^{1/2}} \quad (6.12)$$

and similarly  $R^{yy}, R^{xy}$ , depends only on the separation  $r = x_i - x_j$ , and not on the individual coordinates  $x_i, x_j$ . As different points  $x_i$  on the scan line are traversed with different velocities of the swiveling laser beam, the question is whether this property holds for the measured correlation function. We approach the correlation function through the cross-spectral density

$$\tilde{C}_{xx}(x_i, x_j, \omega) = \langle \tilde{h}_x(x_i, \omega) \tilde{h}_x^*(x_j, \omega) \rangle. \quad (6.13)$$

where  $\tilde{h}_x$  is the temporal Fourier transform of  $h_x$ . The advantage of the cross-spectral density is that it involves Fourier transforms in the homogeneous time direction, but it retains the dependence on the spatial coordinates. In order to improve the statistical accuracy of  $\tilde{C}_{xx}$  we perform a frequency average

$$\int K(\omega, \omega') \tilde{C}_{xx}(x_i, x_j, \omega') d\omega', \quad (6.14)$$

where the kernel  $K(\omega, \omega')$  is a tent-function centred on  $\omega$ , and whose width in  $\omega'$  increases exponentially with increasing  $\omega$ . Such an average is most appropriate for energy spectra that have an algebraic dependence on the frequency. From the cross-spectral density we can compute the frequency spectrum at each spatial point,  $E_{xx}(x_i, \omega) = \tilde{C}_{xx}(x_i, x_i, \omega)$ . Finally, the covariance function Eq. 6.12 is only a Fourier transform away

$$R_{xx}(x_i, x_j, \tau) = \frac{\Re \int_0^\infty e^{i\omega\tau} \tilde{C}_{xx}(x_i, x_i, \omega) d\omega}{\left( \int_0^\infty \cos(\omega\tau) \tilde{C}_{xx}(x_i, x_i, \omega) d\omega \int_0^\infty \cos(\omega\tau) \tilde{C}_{xx}(x_j, x_j, \omega) d\omega \right)^{1/2}}, \quad (6.15)$$

where  $\Re$  denotes the real part. We will demonstrate that to good approximation the covariance function  $R$  only depends on the separation of the points, and not on their individual coordinates:

$$r_k = x_i - x_j, \quad k = 1, \dots, n(n-1)/2. \quad (6.16)$$

However, significant errors exist. Clearly, computing the space-time correlation function of the surface gradient by means of the cross-spectral density is the



only practical option, as direct computation in the time domain would take prohibitively long.

Direct computation of the spectrum of the surface gradient,  $\tilde{h}(k_x, \omega)$ , is possible by resampling the coordinates along the line,  $x_p$  in our example, and then performing a fast-Fourier transform both in space and time. The surface fields  $h_x(x, y, t)$  and  $h_y(x, y, t)$  themselves are stored for further processing, for example in order to assess the validity of Taylor's frozen turbulence hypothesis for the surface. Although we only have information about a single spatial dimension (and time), the gradient field signals allow us to measure statistical quantities of a turbulent surface which, to our knowledge, have not been measured before.

#### 6.4 Assessment of the surface scanning method

Before proceeding with the experimental results for the surface above grid-generated turbulence as well as a first physical interpretation, we will first take a look at a number of tests of the surface scan technique. We need to test whether the imaging of the scan line through the frosted glass, the lenses and the PSD is linear, since this is one of the assumptions made in the previous section. Further tests revolve around the frequency response of the PSD. The PSD needs to be able to follow changes in the position of the spot on its surface faster than the mirror frequency (approximately 2 kHz), since these are to be interpreted as spatial variations. Our first interest will be the average positions  $x_p^w$  and  $y_p^w$ .

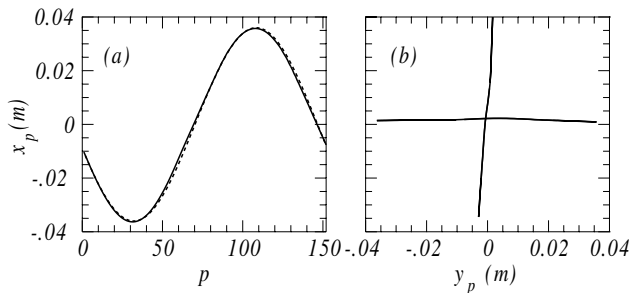


FIGURE 6.5 — Linearity of the imaging by the surface scan set-up. (a) A harmonic scan in streamwise direction. Full line the average coordinate  $y_p^w$  computed for a turbulent surface. Because of the harmonic scan,  $y_p^w$  should ideally be  $\propto \sin(2\pi p f_m / f_s + \varphi)$ . Dashed line:  $A \sin(2\pi p f_m / f_s + \varphi)$ , with amplitude  $A$  set to the amplitude of  $y_p^w$  and measured phase  $\varphi = 1.088 \pi$ .

The oscillating mirror swivels the laser beam approximately harmonically in time. Hence for a scan line in  $x$ -direction the average position of the spot on the PSD surface should depend on  $p$  as  $\sin(2\pi p / f_s + \varphi)$ . This is very nearly

so, as is illustrated in Figure 6.5 (a). We conclude that non-linearity effects in the imaging are small<sup>†</sup>. Figure 6.5 (b) shows  $x_p$  versus  $y_p$ , i.e. the trace of the surface scan for both a spanwise and streamwise scan. This figure shows that the adjacent points in a scan form an approximately straight line, as intended. Furthermore, Figure 6.5 (b) shows that the PSD and its associated electronics can follow the illuminated spot on the surface, even though it moves back and forth at almost 2 kHz. Any phase difference between the measured  $x$ - and  $y$ -deflections would have resulted in a Lissajous-loop.

The alignment of the set-up is relatively straightforward. The hardest part is aligning the direction of the scan line. Changing the direction of the scan line, which is very useful when studying the isotropy of the surface gradient field, involves moving the oscillating mirror, the focusing lens, and several mirrors. Yet, it is possible to properly align the scan-line in spanwise direction as well as aligning it in a practically perpendicular, i.e. in streamwise direction, at essentially the same location in the channel, as can also be seen from Figure 6.5 (b). A first impression of the detector homogeneity can be obtained from the probability distribution function (PDF) of surface gradients on a turbulent channel flow. The variation of the PDF along the scanned line is shown in Fig. 6.6. In this experiment, the scanned line points in the  $x$ -direction. As the length  $L_s$  of the scanned line is 5 cm, which is much smaller than the width of the channel (30 cm), we can assume that the turbulence is homogeneous. The measured PDF is very nearly independent of the position on the scanning line, but a small systematic effect for the rare large  $|dh/dx|$  events can be seen. Figure 6.6 also demonstrates that the gradient fluctuations are very nearly Gaussian. A quite similar result was obtained for scans in the streamwise ( $y$ ) direction. In this direction the grid-generated turbulence decays, but the variation of its statistical properties over the length of the scan line is negligible as  $L_s = 5$  cm is small compared to the distance (2 m) of the scanner behind the turbulence generating grid.

In order to see how scanning affects the signal-to-noise ratio, we now compare frequency spectra of the surface slope at a point measured with the surface scanning technique to spectra measured under the same experimental conditions with an actual point-measurement. In the last case, the surface slope follows directly from the registered signal, while in the former case is wrapped in the spatial scan in the first case. The frequency spectrum obtained from the line scan in this case is actually the frequency spectrum in one of the 152 points on the 5 cm long line. Results obtained with both techniques for static grid generated turbulence, are shown in Figure 6.7 (a). Up to a frequency of 50 Hz the spectra are very similar, despite the different PSD signal processing electronics, different PSDs, the very different optical systems as well as the difference in

---

<sup>†</sup>The quality of the harmonic fit is not only due to the linearity of the imaging. Deviations of the harmonic dependence and curved scan lines can also occur due to the axis of rotation of the mirror not being parallel to the mirror surface.

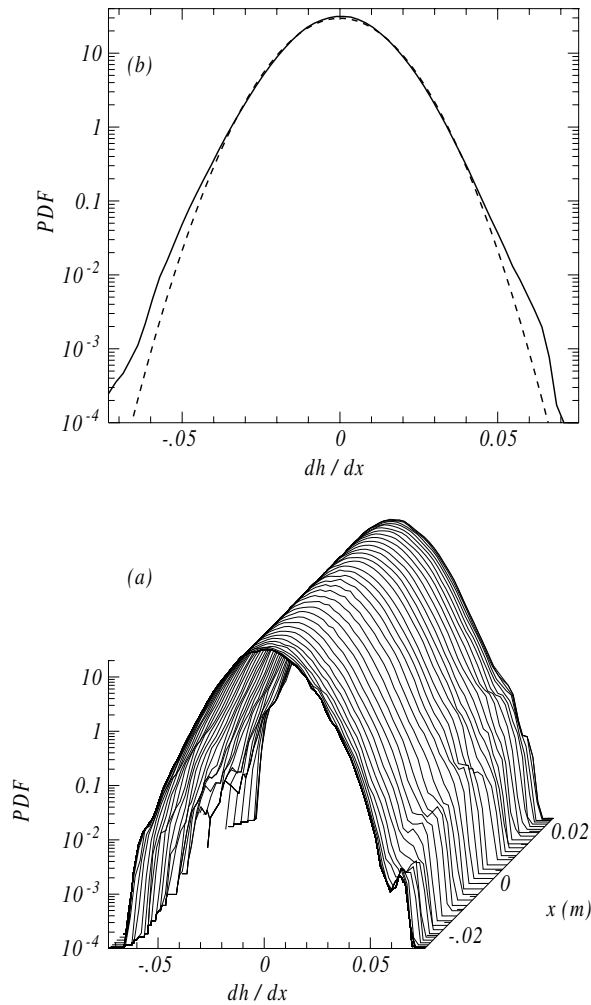


FIGURE 6.6 — (a) Probability density function (PDF) of surface gradients  $dh/dx$  as a function of the position  $x$  on the scan line. The scan line is oriented perpendicularly to the mean flow velocity in the channel. (b) Full line: PDF averaged over  $x$ , dashed line: Gaussian fit. The turbulence with mean velocity  $U = 0.25$  m/s is generated with the active grid.

calibration methods. Above 50 Hz the spectra from the scan are drowned in noise, while the point spectra continue up to roughly 1 kHz. This is not due to a limitation in frequency response, however, since we have already seen that the PSD and its electronics can follow the spot moving back and forth at almost 2 kHz. The difference between the spectra is due to the lower signal-to-noise

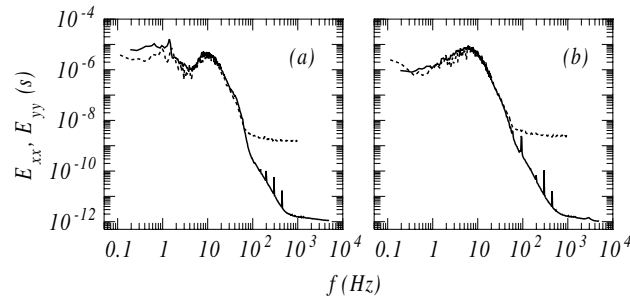


FIGURE 6.7 — Comparison of frequency spectra of the slope measured with point-measurements and derived from line measurements. The turbulence with mean-stream velocity of  $U = 0.28$  m/s was generated with a static grid. (a)  $E_{yy}$ , point spectra of the streamwise slope. (b)  $E_{xx}$ , point spectra of the spanwise slope. Full lines: using a point measurement, dashed lines: spectra at one of the points of a line measurement.

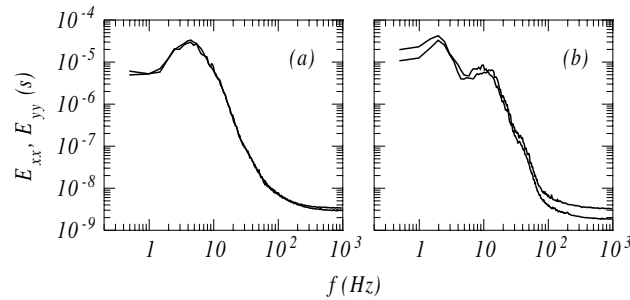


FIGURE 6.8 — (a) Point spectrum of the spanwise slope,  $E_{xx}$ , from both a spanwise and streamwise scan. (b) Point spectrum of the streamwise slope,  $E_{yy}$ , from both a spanwise and streamwise scan. The turbulence with mean velocity  $U = 0.25$  m/s was generated using the active grid.

ratio as a result of the spot's relatively low light intensity, and the presence of the ground glass screen. Still, the spectrum from the scan covers several orders of magnitude.

A comparison of spectra measured in a spanwise scan with those measured with the scan line in the streamwise direction can potentially reveal limitations in the detector's frequency response. The position signal in the scan direction changes much more rapidly than that in the perpendicular direction. Hence, limitations in the frequency response of the PSD are most likely to affect the measurement of the slope in the scan direction. However, the frequency spec-

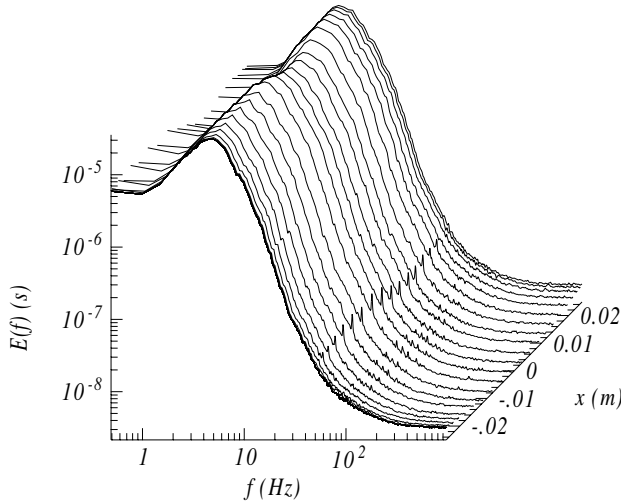


FIGURE 6.9 — Point frequency spectra as a function of the position of the point  $x$  on the scan line. The depression in the centre of the scan line signifies a reduction of the gradient-detector sensitivity.

trum of the slope at a point on a surface scan line should be completely independent from the direction of that line. However, if the frequency response is a problem, they will differ. In Fig. 6.8 we show frequency spectra  $E_{xx}$  and  $E_{yy}$  of the slopes obtained from measurements along both a streamwise and spanwise line, averaged over the line, for active grid generated-turbulence. Indeed the frequency spectrum of either slope is practically independent of the direction of the scan line, demonstrating that the registered signals can be unravelled adequately in position and slope information.

The next concern is the frequency-dependent homogeneity of our surface scan detector. Figure 6.9 shows the dependence of measured frequency spectra on the position on the scan line. The fluctuations appear slightly depressed in the centre of the scan line, in a way that does not depend on frequency. Most probably, this reduction of the sensitivity is related to the variation of the scan speed, which is largest in the centre, in combination with the speckle patterns of the ground glass screen. This effect can be eliminated adequately by normalizing measured wave slopes by their root mean square values  $\langle h_x^2 \rangle^{1/2}$  and  $\langle h_y^2 \rangle^{1/2}$ . Let us finally turn to the spatial correlation function  $C(x_i, x_j, \tau)$  at  $\tau = 0$ . In Fig. 6.10 we plot  $C_{xx}(r_k, \tau)$  and  $R^{yy}(r_k, \tau)$ , where  $r_k$  is the separation  $r_k = x_i - x_j, k = 1, 2, \dots, 11476$  and  $\tau = 0$ . Clearly, the correlation function is not just a function of the separation, but also of the individual coordinates  $x_i, x_j$ . The resulting deterministic noise is determined by the different scan speeds with which the laser beam passes different points on the scan line. The noise affects measured spatial spectra at high wavenumbers. In the correlation

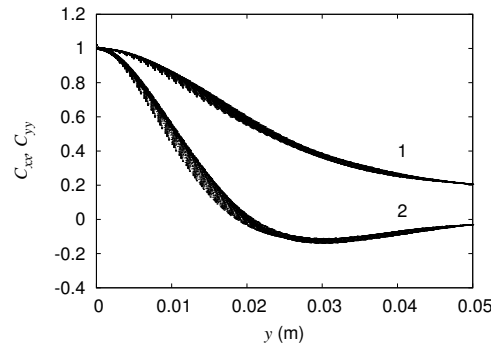


FIGURE 6.10 — Transverse (1) and longitudinal (2) spatial correlation functions measured along a streamwise line as a function of the separation  $r_k = x_i - x_j$ . We draw as many points  $r_k$  as there are separations between  $x_i, i = 1, \dots, 152$  on the scan line. The residual dependence on the individual coordinates  $x_i$  shows as deterministic noise.

functions shown later, this effect was cured by fitting a 6th order polynomial to their  $r$ -dependence.

Scanning techniques are unavoidable for measuring the surface gradient field. The challenge is to unravel gradient- from position information. Its success is determined by the optics and by the response time of the position detector, both of which compromise the signal-to-noise ratio. Clearly, the scan frequency should be adapted to the problem at hand. Currently,  $f_m = 1.96$  kHz, but judging from Figure. 6.7, a reduction to 1 kHz would be possible, resulting in an improvement of the signal-to-noise ratio.

## 6.5 Conclusions

Characterising a turbulent surface through refraction of a focused laser beam is precise, linear and, since the signal depends on the surface gradient, can resolve large surface wavenumbers. However, using this technique to obtain space-time information presents a challenge. In this chapter, we have described a scanning method in which a laser beam is rapidly scanned over a surface and its position after refraction is measured synchronously. The synchronisation problem can be solved readily, but this method challenges the speed of current position sensing detectors. Further, imaging requirements necessitated the use of a translucent screen, resulting in a deterioration of the signal-to-noise ratio. The result is a device that can measure the space-time gradient field of a turbulent free surface with good precision.

The resolution in space is set by the size of the focus of the laser beam ( $\approx 0.3$  mm), whereas in principle the resolution in time is half the swiveling

frequency  $f_m$  of the mirror ( $f_m/2 \approx 1$  kHz). However, for our very steep spectra of the surface slope above turbulence the noise threshold is reached at 100 Hz. The alignment of the scanning set-up is straightforward and it requires no calibration other than a measurement of a few lengths. In principle the technique can easily be adapted for measuring reflection instead of refraction. By using lasers with different wavelengths and separating the images using laser line filters, this technique can be easily combined with other optical diagnostics, such as particle image velocimetry. This will be explained in more detail in chapter 8.

We have discussed a number of statistical quantities that can be measured from space-time signals. Although a complete discussion of the meaning of these quantities falls outside the scope of chapter, we demonstrate that spectra and correlation functions can be measured precisely.

---

## THE NATURE OF THE SURFACE RIPPLES

In this chapter measurements of the statistical properties of the free surface above the turbulent flow in our water channel will be discussed. We will argue how a physical model about the origin of surface ripples can be found from our experimental results. First we will show how the surface activity in a point evolves when we move away from the grid, where the sub-surface turbulence decays. Clearly, as explained in chapter 5, a measurement in a point is ambiguous, as fluctuations may be either due to a true time dependence of the surface shape, or due to a spatial dependence that is swept by the measurement point by the mean-stream velocity. Hence we will turn to space-time measurements with the surface scanning method described in chapter 6. A key problem in the interpretation of the wavenumber-frequency spectra that can be measured with this technique is the Doppler-effect due to the mean-stream velocity in the water channel. Nevertheless, strong evidence is found that a major role is played by gravity-capillary waves. Further evidence is found in measured space-time correlation functions.

A unique property of the active grid is that the properties of the turbulence it generates can be tuned by changing the stirring protocol of the grid. Thus, it is possible to change both the strength and the anisotropy of the turbulence. First we will study how the surface statistics depend on the strength of the turbulence. Then the anisotropy of the sub-surface turbulence will be altered, in order to see how this affects the anisotropy of the surface ripples.

The emerging view will be that isotropic surface waves originate from sources that are uniformly distributed over the surface. Therefore, the Doppler-effect influences the measurements in a complicated manner. Finally, we will try to understand this by considering a simple model.

### 7.1 Spectra and correlations in time and space

Figure 7.1 shows frequency spectra of the spanwise surface slope, measured with the point measurement technique described in section 6.2, and frequency



spectra of the streamwise component of the velocity measured with LDV, just below the surface, both for static-grid-generated turbulence. It is immediately

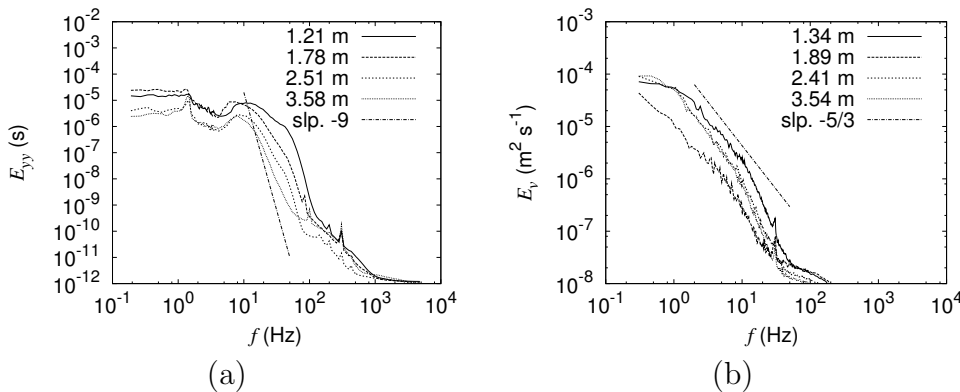


FIGURE 7.1 — (a) Frequency spectra of the streamwise slope ( $\partial h/\partial y$  in our coordinate system) of the surface at the channel centre line, for a number distances from the grid. (b) Frequency spectra of the streamwise component of the velocity ( $v$ ) measured at a few mm below the surface at the channel centre line for and at roughly the same distances from the grid. In both cases the turbulence was generated by means of the static grid.

clear from these figures that the surface slope spectrum is dramatically different from the velocity spectrum of the sub-surface turbulence. Of course, some of the differences are due to the limitations of the respective measurement techniques. For instance, at roughly 50 Hz the LDV spectrum reaches the noise threshold, whereas for the point measurements of the surface slope the noise threshold is reached at a far higher frequency of 1 kHz. Apart from this difference, however, it is also clear that while the turbulence spectrum shows a negative slope over the entire range of measured frequencies, with a characteristic  $-5/3$  scaling exponent in part of this range, the slope spectrum starts to decrease only at higher frequencies, and with a far steeper slope. There is no simple explanation for this difference. In part this is because, certainly in the presence of waves, there is no straightforward way to transform the frequency spectra of the slope into spatial spectra, as we have explained in chapter 5. Without this spatial information, it is virtually impossible to interpret these frequency spectra. This is different for the the frequency spectra of the velocity, where we can use Taylor's frozen turbulence hypothesis. Similar to the point measurements of the velocity with LDV, the point measurements of the surface slopes are, however, very useful for studying the decay of the surface deformations. Since the experiments were done in a water channel, in which turbulence was generated by means of a grid, the turbulence intensity decays when the flow moves away from the grid. In chapter 3 we found the

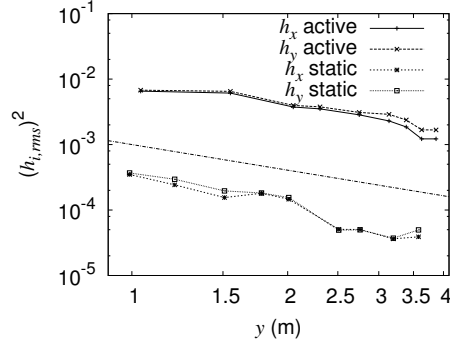


FIGURE 7.2 — Root-mean-square surface slopes as a function of the distance to the grid, measured by means of point measurements, for both the active grid, with protocol (25RAN) and the static grid (25STAT). The corresponding decay of the sub-surface velocity fluctuations can be found in figure 3.14.

characteristic decay for the turbulent velocity fluctuations given by equation (3.15):

$$\left(\frac{v_{rms}(y)}{v_0}\right)^2 \sim \left(\frac{y}{M}\right)^n,$$

with  $n = 1.3$ . Point measurements allow us to see how the surface fluctuations decay with  $y$ . The results are shown in figure 7.2. The surface fluctuations are near-isotropic,  $\langle h_x^2 \rangle^{1/2} \approx \langle h_y^2 \rangle^{1/2}$ , and decay at roughly the same rate as the sub-surface velocity fluctuations. For the static grid the generated turbulence is relatively weak ( $Re_\lambda \approx 70$ , compared to  $Re_\lambda \approx 250$  for the active grid with the current protocol, both measured at 2 m from the grid). The fluctuations of the surface slope are an order of magnitude smaller than those for the active grid. Only measurements in time and space, as measured with the surface scanning set-up also described in chapter 6 can provide a clear view of the surface. Wavenumber-frequency spectra are shown next, now for the active grid. For the case with the strongest turbulence (25 OPT, see table 3.2), the spectra are shown in figure 7.3. We show all four spectra  $E_{\alpha\alpha}(k_\beta)$ , with  $\alpha = x, y$  and  $\beta = x, y$ . Clearly, for these spectra, the isotropy is broken by the Doppler-effect, so that  $E_{xx}(k_x) \neq E_{yy}(k_y)$ . However, it will later be shown that the surface ripples are nevertheless isotropic. Also shown in 7.3 are lines corresponding to the Doppler-shifted dispersion-relation for gravity-capillary waves, together with the line  $\omega = v_0 k$ , which corresponds to advection with the mean-stream velocity  $v_0$ . It should be realised that this dispersion relation corresponds to plane waves.

A surprisingly large part of the spectrum matches the dispersion relation. This can be seen most clearly in the streamwise spectra shown in figures 5.4 (c)

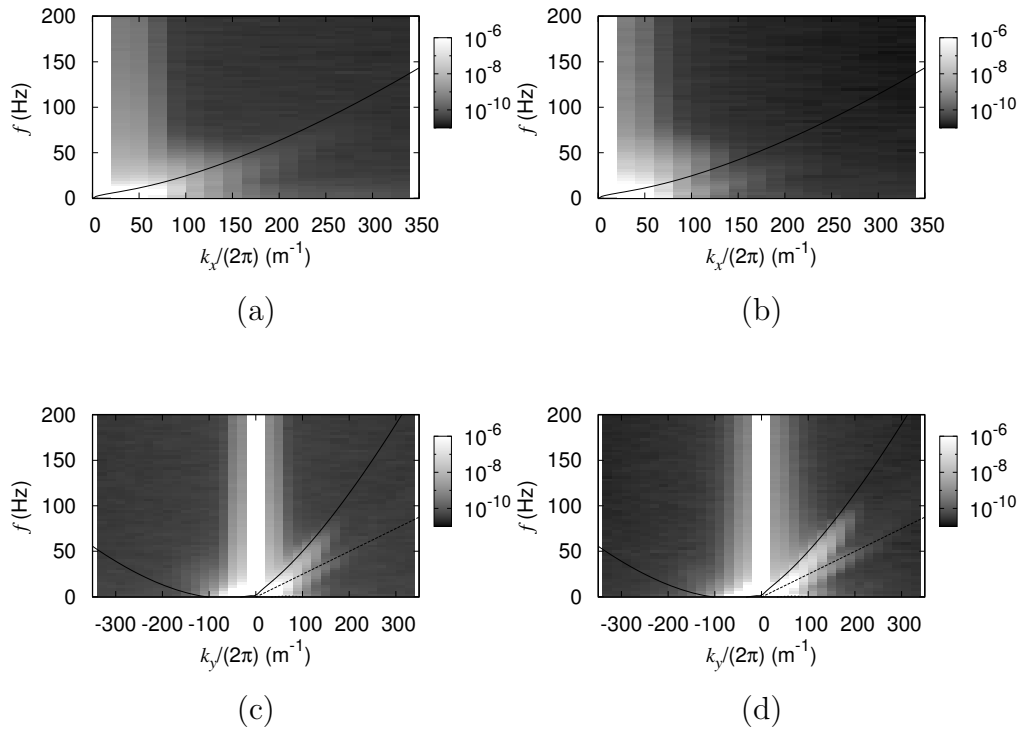


FIGURE 7.3 — Space-time spectra for the active grid with protocol (25OPT). Span-wise measurements: (a)  $E_{xx}(k_x, \omega)$ , (b)  $E_{yy}(k_x, \omega)$ . The solid lines shown in both spanwise spectra represent the dispersion relation for gravity capillary waves, previously shown in figure 5.4 (a). Span-wise measurements: (c)  $E_{xx}(k_y, \omega)$ , (d)  $E_{yy}(k_y, \omega)$ . In both (c) and (d) the solid lines represent the Doppler-shifted dispersion relation as shown previously in figure 5.4 (b). The dotted line corresponds to the mean-stream velocity, which in this case is approximately 26 cm/s. The white band in the centre of the streamwise spectra and at the right of the spanwise spectra corresponds to spatial frequencies that lie outside of the range of our measurement.

and (d), and confirms that part of the surface shape indeed consists of gravity-capillary waves that travel on top of the mean-stream velocity. Waves that travel downstream, with  $k_y > 0$ , are clearly visible. The presence of waves in the spanwise spectrum, coupled to its symmetry, implies that the spanwise waves travel both towards the left and the right of the channel. Upstream-traveling waves are not clearly visible in the streamwise spectra. The waves in spanwise direction are not very clearly visible either, because they too predominantly are

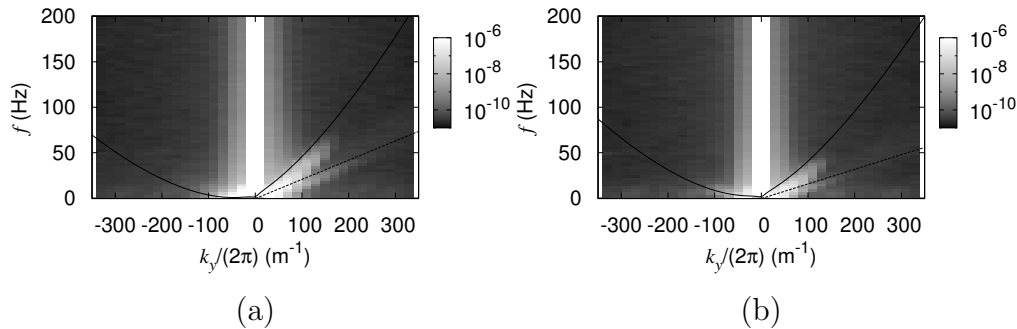


FIGURE 7.4 — Frequency-wavenumber spectra  $E_{yy}(k_y, \omega)$  for active-grid-generated turbulence with (a) protocol (20OPT) and (b) protocol (15OPT). Once more the dotted lines represent the mean-stream velocities of 22 and 17 cm/s, respectively, and the solid lines correspond to the Doppler-shifted dispersion relation.

associated with low frequencies.

Figure 7.4 shows the spectrum  $E_{yy}(k_y, \omega)$  from streamwise measurements for turbulence generated with the active grid, with lower mean-stream velocities of 0.22 m/s and 0.17 m/s, respectively, and the accordingly modified forcing protocols (20OPT) and (15OPT), listed in table 3.2. Now, a branch of upstream-traveling waves has become visible. It is clear that gravity-capillary waves are traveling on top of the free surface, and that they travel in all directions across the surface. It is not unreasonable to suspect that waves measured at a downstream location are generated at the grid and then advected to the measurement location. However, the fact that we also see waves that travel upstream and in the spanwise direction is an indication that this is not the case. The waves we see are not generated directly by the grid, but are generated locally. This will become more clear in section 7.2, where a closer look is taken at isotropy. The reason why upstream-traveling waves are practically invisible for higher mean-stream velocities is quite obvious. The minimum phase-velocity of gravity-capillary waves is approximately 23 cm/s. Except for very short waves (shorter than  $\lambda \approx 1$  cm) both the phase- and group velocity vary only slowly with the wavelength. For the turbulence with a mean stream velocity of 27 cm/s, as well as for turbulence with a mean-stream velocity of 22 cm/s, shown in 7.4 (a), most of the upstream-traveling waves are practically stationary in the frame of reference of our measurement technique. Hence, they primarily lead to contributions in the streamwise spectra at very low values of  $\omega$ , close to the lower limit of the frequency range in the measurements.

The branches in the streamwise spectra that correspond to the mean-stream velocity show that, in addition to waves, some of the surface deformations are

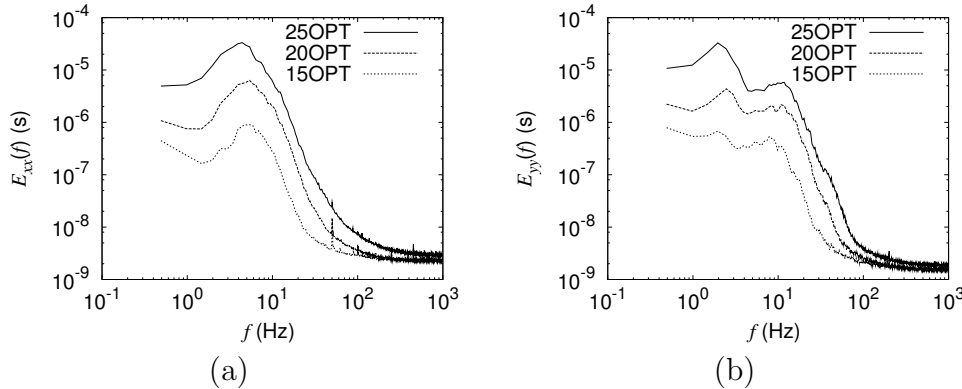


FIGURE 7.5 — Frequency spectra for turbulence generated with the active grid, for three different mean-stream velocities and accordingly modified forcing protocols. (a)  $E_{xx}(f)$  and (b)  $E_{yy}(f)$ .

advected with the mean-stream velocity. These deformations are a direct surface signature of the sub-surface turbulence. These are the most likely sources of the waves.

Having seen that part of the surface consists of waves, it is quite tempting to interpret the frequency spectra shown in figure 7.5 in terms of waves. The frequency spectra  $E_{xx}$  all have a relatively broad peak around roughly the same frequency, 4.5 Hz for 0.27 m/s and 5.5 Hz for 0.17 m/s, for the cases (25OPT) and (15opt), listed in table 3.2 on page 43.

Let us further assume that the  $E_{xx}$  spectra are mainly sensitive to waves traveling in the  $x$ -direction, which are unaffected by Doppler-shifts. Then these frequencies may be associated with gravity-capillary waves with wavelengths between 6 (15OPT) and 8 cm (25OPT) and phase-velocities between 32 (15OPT) and 36 (25OPT) cm/s. These waves should also be visible in the  $E_{yy}$  spectra. If we also assume that the  $E_{yy}$  spectra are dominated by waves in the  $y$ -direction, the waves identified in  $E_{xx}$  should come with a Doppler-shift. Consequently, in the stream-wise frequency spectrum downstream-traveling waves with a wavelength  $\lambda$  of 6 cm and a matching phase-velocity  $v_f = 31$  cm/s will appear around  $(v_0 + v_f)/\lambda \sim 8$  Hz, while upstream-traveling waves will appear around  $(v_f - v_0)/\lambda \sim 2$  Hz. Similarly, waves of 8 cm in length traveling on top of turbulence generated with protocol (25OPT) will show up at around 8 Hz and 1 Hz, respectively. The corresponding spectra of the streamwise slope, in figure 7.5 (b) indeed show maxima approximately around these frequencies.

Of course, this argument can only be semi-quantitative. If indeed the sources are distributed uniformly over the surface, the Doppler effect will be more complicated. This issue will be addressed in section 7.3.

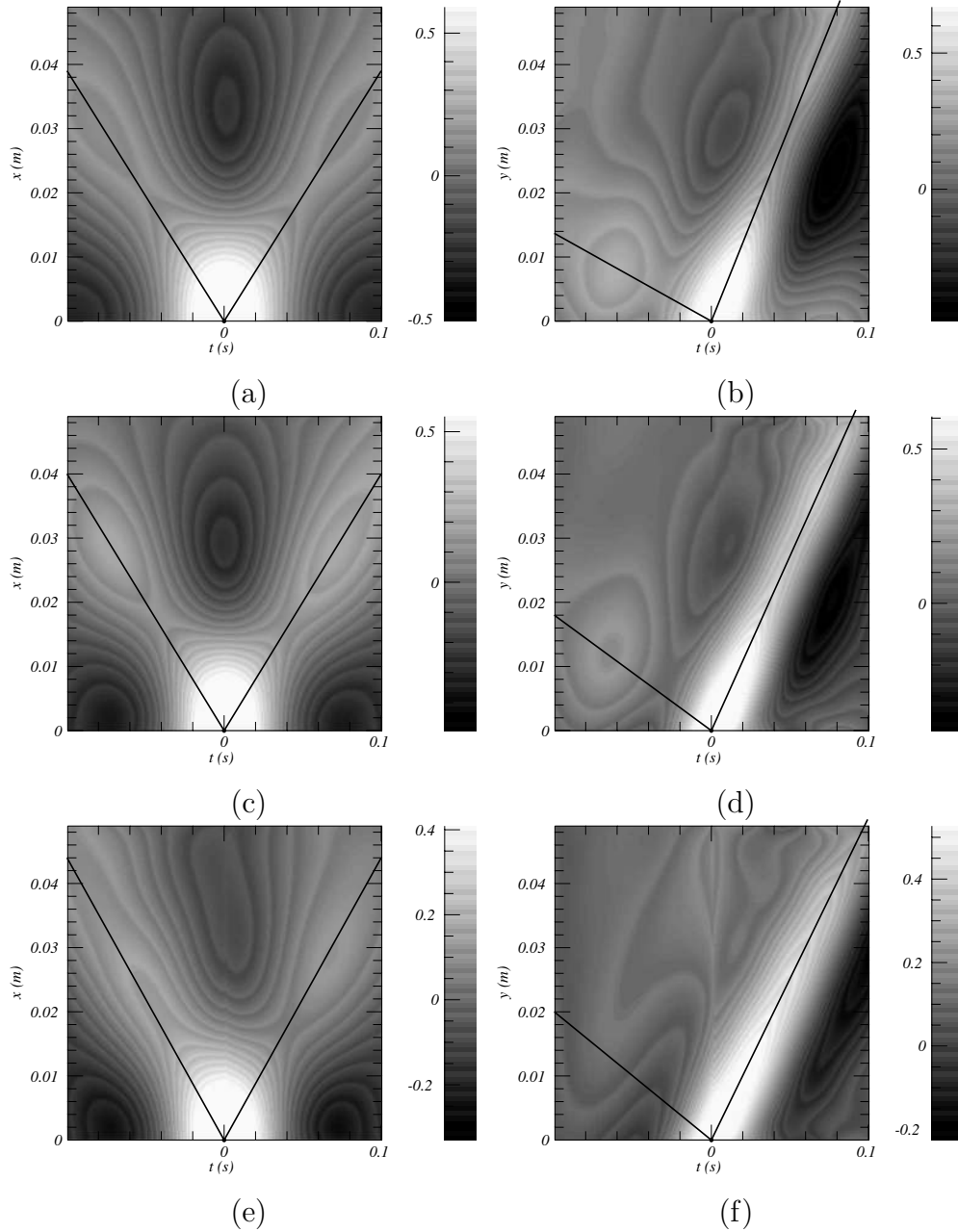


FIGURE 7.6 — Space-time correlation functions of the surface slope for turbulence generated with the active grid, for three different mean-stream velocities,  $v_0 = 0.27$  m/s,  $0.22$  m/s and  $0.17$  m/s, respectively, and accordingly modified forcing protocols (25OPT), (20OPT), and (15OPT). (a)  $C_{xx}(r_x, 0, \tau)$  and (b)  $C_{yy}(0, r_y, \tau)$  for protocol  $v_0 = 0.27$  m/s, similarly (c) and (d) for  $0.22$  m/s, and (e) and (f) for  $0.17$  m/s. The (hand drawn) lines in the streamwise correlation functions correspond to structures traveling across the surface with velocities  $v_0 \pm v_f$ , where  $v_f$  is approximately  $0.37$  m/s. In the spanwise correlations, which are symmetric, similar lines are shown with velocities  $\pm v_f$ , where  $v_f$  is close to  $0.4$  m/s.

## 7.1.1 CORRELATION FUNCTIONS

The space-time correlation functions show a complementary view. In general, correlation functions emphasize the large energetic structures. In figure 7.6 we show  $C_{yy}(0, r_y, t)$  and  $C_{xx}(r_x, 0, \tau)$  for the surface slopes above active-grid-generated turbulence at three different mean flow velocities (and turbulence intensities). In the measured graphs, clear structures can be seen which appear to move with a constant velocity. These velocities were traced (by hand) in all three cases. The streamwise correlation functions  $C_{yy}(0, r_y, t)$  show a ridge corresponding to velocities  $v_0 \pm v_f$ , where  $v_f \approx 0.37$  m/s in all three cases. The correlation functions  $C_{xx}(r_x, 0, \tau)$  (the spanwise slope measured in the spanwise direction), shown in figure 7.6 (a), (c), and (e), are symmetric relative to  $r_x = 0$ . It is tempting to associate the structures in these correlation functions with waves traveling in the spanwise direction with a velocity close to 0.4 m/s.

If it is true that the surface shape is marred by waves with a wavelength  $\lambda \approx 8$  cm, this wavelength is perhaps associated with the integral scale of the turbulence. We can test this by comparing turbulence, with approximately the same flow velocity, but different types of forcing. We are going to compare static-grid-generated turbulence (25STAT) with the active grid with two different protocols, (25RAN) and (25OPT). The turbulence properties are listed in table 3.2. The corresponding frequency spectra are shown in figure 7.7. For the active-grid generated turbulence with protocols (25OPT) and (25RAN),

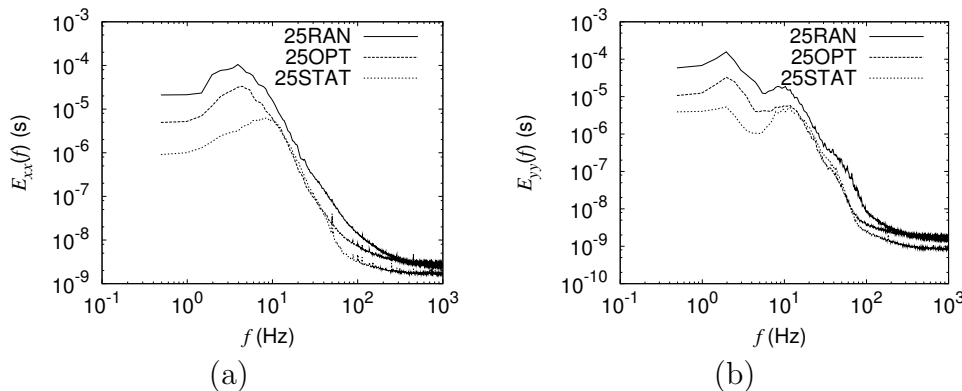


FIGURE 7.7 — Frequency spectra for turbulence generated with three different types of forcing: the active grid with protocols (25OPT) and (25RAN) and the static grid. (a)  $E_{xx}(f)$  and (b)  $E_{yy}(f)$ .

the maxima in the spectrum of the spanwise slope, corresponding to the most energetic waves on the surface, lie at approximately 4.5 Hz, corresponding to waves with a wavelength of 8 cm. The integral scales of the turbulence for these cases are, respectively, 8.5 cm and 6.5 cm (see table 3.3). For the static grid, the maximum in  $E_{xx}(f)$  lies at a frequency of 8.4 Hz. This corresponds to a

smaller wavelength of approximately 3 cm, which agrees well with decreased integral length-scale of the turbulence in this case:  $L = 2.6$  cm.

### 7.1.2 THE SURFACE SPECTRUM

Using the scanning device the surface wavenumber spectrum can now also be measured directly. The longitudinal spectra  $E_{xx}(k_x)$  and  $E_{yy}(k_y)$  for different mean velocities –  $v_0=0.27$  m/s, 0.22 m/s, and 0.17 m/s with accordingly modified protocols (25OPT), (25RAN), and (25STAT) – are shown in figure 7.8. Regrettably, however, the length of the scan line is smaller than the integral

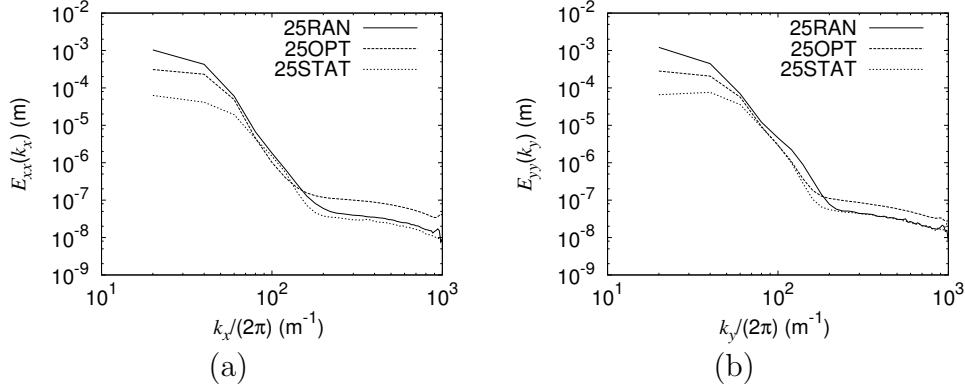


FIGURE 7.8 — wavenumber spectra for turbulence generated with the active grid, for three different mean-stream velocities and accordingly modified forcing protocols. (a)  $E_{xx}(k_x)$  and (b)  $E_{yy}(k_y)$ .

length-scales (it is approximately the same as the integral scale of the turbulence generated with the static grid), so that the dominance of waves with wavelengths equal to the integral scales cannot be tested directly.

Remarkably, for relatively large wavenumbers the spectra are very similar, despite the different forcing. They show a scaling region with a scaling exponent of approximately -6.5, albeit over a relatively limited wavenumber range. This scaling region is only present for wavelengths that are smaller than 17 mm. This corresponds to the scale below which capillary forces start to dominate the balance of forces at the surface.

In both frequency and wavenumber spectra, the noise levels are different for different experiments. This is most likely caused by PIV tracer particles in the water. As was explained in chapter 6, tracer particles that move through the scanning beam are a major contributor to noise. The experiments with the active grid with protocols (25OPT), (20OPT), and (15OPT) were performed on the same day. Figure 7.5 shows that as the mean-stream velocity increases and, consequently, more particles move through the scanning beam, the noise level increases. The noise levels in the spectra in figure 7.7 are difficult to compare,



since several months passed between these measurements. During this time, the water in the channel was replaced several times.

## 7.2 Isotropy

As already stated before, stirring a flow with an active grid provides control over the isotropy of the produced turbulence. We are therefore in the unique position to see how (an)isotropy of the sub-surface turbulence is expressed in the (an)isotropy of the surface wrinkles above it.

Three flows have been generated with a varying degree of anisotropy. Case (i) is static-grid-generated turbulence with a mean-stream velocity of 29 cm/s. In chapter 3 and chapter 4 it was shown that this was isotropic in horizontal and vertical ( $x=0$ ) planes (see, for instance, figure 4.21 (b)). Case (ii) is turbulence generated with protocol (25OPT). This turbulence was shown to have slight anisotropy (figure 4.21 (a)). Finally, case (iii) is turbulence generated with the active grid and protocol (25RAN). This is very anisotropic (figure 4.20).

In chapter 5 it was explained how anisotropy of the surface slope field can be quantified by using the spatial correlation functions. Briefly, all correlation functions  $C_{xx}(r_\alpha)$ ,  $C_{yy}(r_\alpha)$ , and  $C_{xy}(r_\alpha)$  should be independent of the direction of  $r_\alpha$ . Furthermore, isotropy relations were derived that link the longitudinal to the transverse correlations. The surface scans allow measurements of four correlation functions:  $C_{xx}(r_x)$  and  $C_{yy}(r_x)$  from a spanwise scan, and  $C_{xx}(r_y)$ ,  $C_{yy}(r_y)$  from a streamwise scan. These four functions, for both cases (i) and (ii) are shown in figure 7.9. The corresponding correlation functions for (iii), are shown in figure 7.10. For both case (i) and (ii), the transverse correlation function indeed is practically independent of the direction. For case (i), the

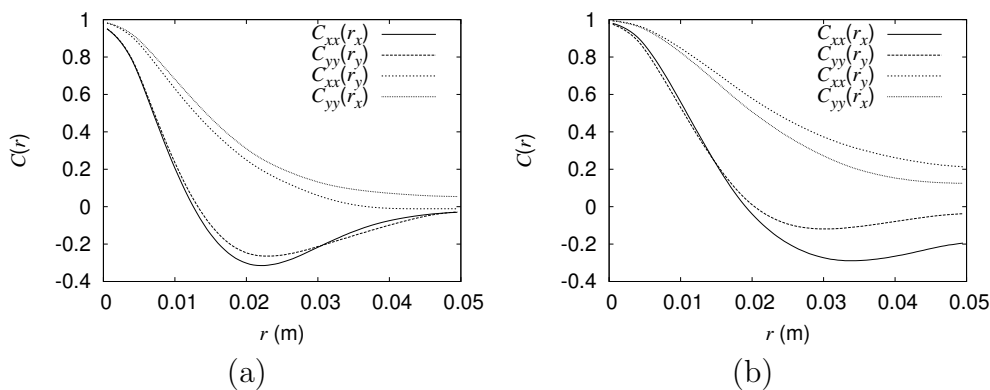


FIGURE 7.9 — Spatial correlation functions (a) for case (i), isotropic turbulence generated with the static grid, and (b) for case (ii), the active grid with protocol (25OPT).

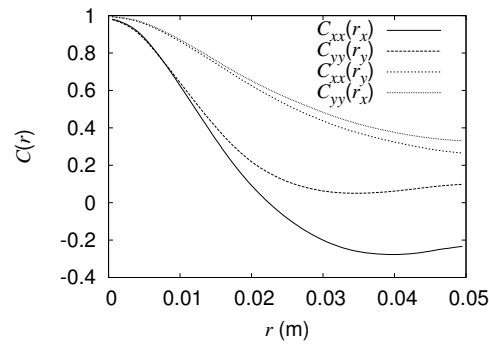


FIGURE 7.10 — Spatial correlation functions for case (iii), anisotropic turbulence generated with the active grid with protocol (25RAN).

isotropic turbulence, the longitudinal correlation functions are very similar as well, but for the slightly more anisotropic turbulence in case (ii) they begin to differ for separations larger than 2 cm. Figure 7.10 shows corresponding correlation functions for the anisotropic turbulence in case (iii). In this case the longitudinal correlation functions measured in spanwise and streamwise directions start to deviate for even smaller separations and the transverse correlation functions differ as well.

In chapter 5 the relation between the transverse and longitudinal surface slope correlation functions was derived for an isotropic surface slope field. Figure 7.11 shows the result of applying this relation, equation (5.51), to the surface, for all three forcing conditions considered here. We compare the longitudinal correlation function, found from applying the isotropic relation to the measured transverse correlation function, to the actually measured longitudinal correlation function. This is done for both the spanwise and streamwise measurements. For case (i), shown in figures 7.11 (a) and 7.11 (b), respectively, the correlation functions overlap. This confirms that the surface in this case indeed is isotropic. For the nearly isotropic turbulence in case (ii), the surface is also reasonably isotropic, although the correlation functions for the spanwise measurement, shown in figure 7.11 (c), deviate for separations larger than roughly 3 cm. For case (iii), the anisotropic turbulence, the surface too is anisotropic, as evidenced from figure 7.11 (e). For the spanwise measurement, the measured longitudinal correlation function and the correlation function calculated from the isotropic relation are very different.

We come to the remarkable conclusion that the waves do not only travel in all directions, but that — provided that the turbulence far below the surface is isotropic — the surface is in fact isotropic as well. Furthermore, the isotropy of the surface wrinkles follows that of the turbulent velocity fluctuations beneath the surface, since the surface shape become anisotropic if we change the forcing protocol such that the sub-surface turbulence becomes anisotropic. This is

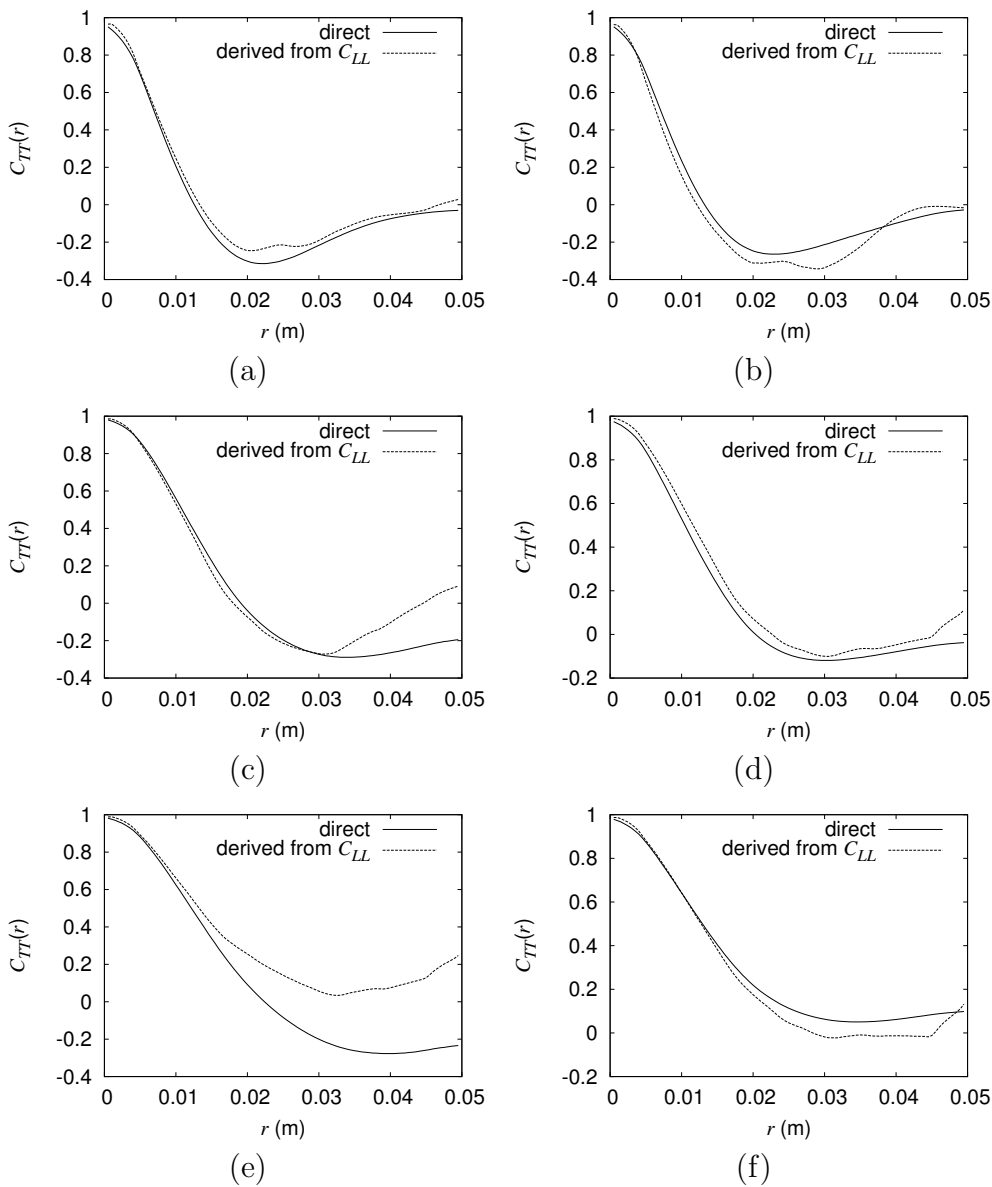


FIGURE 7.11 — Comparison of the measured longitudinal correlation function with the longitudinal correlation function derived from equation (5.51), for spanwise (left column) and stream-wise (right column) measurements. (a) and (b): case (i), isotropic turbulence. (c) and (d): case (ii), slightly anisotropic turbulence, and (e) and (f): case (iii) anisotropic turbulence)

remarkable, because we have also shown that the link between the surface and the sub-surface turbulence is not very strong. Finally, the isotropy of the surface in our experiment proves conclusively that the observed surface wrinkles are not just caused by the active grid and merely advected downstream, but are a true consequence of the turbulence.

### 7.3 Synthetic surfaces

The overall image that emerges from our experiments is that waves are emitted by sources that emanate from events in the sub-surface turbulence, and that are distributed randomly over the surface. All sources move with the mean velocity. For each of these sources, the Doppler-effect will be different, which complicates the interpretation of our results. We will therefore analyse a simple model in which random sources are sprinkled on a moving surface. The geometric arrangement of this simulation is shown in figure 7.12. The synthetic surfaces

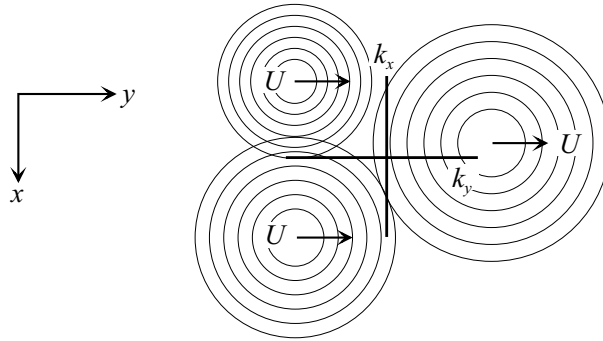


FIGURE 7.12 — The geometric arrangement of the simulation. Scans perpendicular to the convection velocity provide access to  $E_{x,y}(k_x, \omega)$ , scans in the direction of  $\mathbf{U}$  provide  $E_{x,y}(k_y, \omega)$ .

consist of  $N$  sources at random locations  $\mathbf{x}_i(t), i = 1, \dots, N$  which are advected past the line-scan detector by the mean velocity field,  $y_i(t) = U t$ . At the measurement location  $\mathbf{x}$ , the time-dependent surface height is:

$$h(\mathbf{x}, t) = \sum_{i=1}^N A(k_i) e^{i k_i r_i(t) + i \omega_i t}, \quad (7.1)$$

with  $r_i(t) = |\mathbf{x} - \mathbf{x}_i(t)|$  and wave amplitudes  $A(k_i)$ , that follow from an assumed energy spectrum  $A(k_i) = E(k_i)^{1/2} \exp(i\phi_i)$  with phase angles  $\phi_i$  that are distributed uniformly randomly on the interval  $[0, 2\pi]$ . The frequencies  $\omega_i$

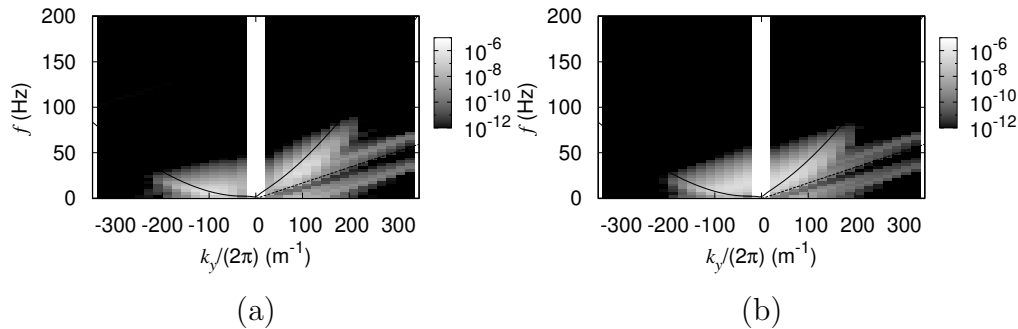


FIGURE 7.13 — Simulated spectrum  $E_{yy}(k_y, \omega)$  of gravity-capillary waves traveling on a surface which is moving in the  $y$ -direction with  $U = 0.17$  m/s. (a)  $E_{yy}(k_y, \omega)$ , (b)  $E_{xx}(k_y, \omega)$ . The sources emit waves which satisfy the capillary-gravity dispersion relation. Dashed lines: blue and red-shifted capillary-gravity dispersion relations  $k_x = \omega_d(k_x) + U k_x$ , and  $k_x = \omega_d(k_x) - U k_x$ , respectively.

and wavenumbers  $k_i$  are linked through the dispersion relation  $\omega_i = \omega_d(k_i)$ , with  $\omega_d(k)$  given by:

$$\omega_d^2 = g k + \frac{\sigma}{\rho} k^3, \quad (7.2)$$

with  $\sigma$  the surface tension and  $\rho$  the density of water. Therefore, each source  $i$  emits a wave with a single wavenumber  $k$  and a frequency  $\omega_i$ . Each wave also has a phenomenological damping factor  $\exp(-r_i(t)/\xi_i)$ , with  $\xi_i = v_f/\nu k_i^2$  with the phase velocity  $v_f = \omega/k_i$ , and  $\nu$  the kinematic viscosity. From the surface height we determine the surface slope field with components  $h_x, h_y$

$$h_x(\mathbf{x}, t) = \sum_{i=1}^N A(k_i) \zeta_{i,x} e^{i k_i r_i(t) + i \omega(k_i) t}, \quad (7.3)$$

with  $\zeta_{i,x} = k_i (x - x_i(t))/r_i(t)$ , and analogously for  $h_y$ . Figure 7.13 shows the typical spectra of a moving surface with embedded sources. These sources have wave amplitudes  $A(k)$  drawn from the distribution  $\exp(-((k - k_0)^2/\sigma_k^2))$ , with  $\sigma_k = 260$  and  $k_0 = 78$ , corresponding to length-scales of 2.4 cm and 8 cm, respectively. Waves arrive at the point of observation from all directions and the resulting spectra  $E_{xx}(k_y, \omega)$  and  $E_{yy}(k_y, \omega)$  are very similar. Although the transformation of the amplitude distribution of the measured waves to the measured spectra is highly nontrivial, similar to the measured slope spectra, the dispersion relation can easily be recognised in figure 7.13. It comes in two branches, one with the blue-shifted frequency  $\omega + U k_y$ , and one with the red-

shifted frequency  $\omega - Uk_y$ . Figure 7.13 (b) shows the spectrum  $E_{yy}(k_x, \omega)$  with the wavenumber perpendicular to the advection velocity.

The simulated spectra involve the dispersion relation in a complicated fashion. Remarkably, all features of these spectra are a trivial consequence of the geometrical arrangement of the measurement, the spectral distribution of the sources and the Doppler shift. However, we have no simple way to unfold the true spectrum of the sources from the measured spectra.

## 7.4 Conclusions

We have found that the free surface above turbulence consists largely of gravity capillary-waves. The waves are clearly identifiable from spectra of the surface slope in time and space, most notably in streamwise spectra. The majority of the energy present in these  $\omega - k$  spectra lies in a ridge close to the Doppler-shifted dispersion relation for linear gravity-capillary waves. A consequence of this is that much of the surface shape consists of structures that travel across the surface at velocities different from the the mean stream velocity. Waves that travel in all directions are also visible in corresponding space-time correlation functions of the surface slope. Although isotropic turbulence is rare in nature, the emphasis on isotropic turbulence has a clear benefit in our experiments. Isotropy allows us to conclusively state that the waves are generated locally by to the sub-surface turbulence, since spatial correlation functions of the surface slopes clearly show that, provided that the sub-surface turbulence is isotropic in horizontal planes below the surface, the surface shape itself is isotropic as well. This is not only clear from a comparison of longitudinal and transverse correlation functions measured along lines in different directions. In addition, the theoretical relation between the longitudinal and transverse correlations derived in chapter 5 for an isotropic surface holds. Furthermore, if we change the forcing protocol of the active grid such that the sub-surface turbulence becomes anisotropic, the surface shape becomes anisotropic as well.

The emergence of these waves is remarkable. In chapter 2 we saw that resonant wave-growth, akin to resonant growth of surface waves due to turbulent wind, can really only be expected for fluctuation velocities in the turbulence that are larger than the minimum phase-velocity of for gravity-capillary waves ( $\approx 23$  cm/s). However, even for the most intense turbulence generated in our water channel, the root-mean-square velocity fluctuations are ten times as small as this (2.3 cm/s), and yet we clearly see waves. Obviously, resonant wave-growth is not the mechanism by which these waves are formed. We have also seen that, out of the wide range of length-scales present in our sub-surface turbulence, only the largest scales have a direct influence on the surface shape. This is shown most clearly in the wavenumber spectra shown in figure 7.8. The most energetic waves have wavelengths that correspond to the integral length-scales of the sub-surface turbulence. A clear indication for this follows

from comparing the surface above turbulence generated with the active grid to the surface above turbulence generated with the static grid. The integral scale of the turbulence in the former case is significantly larger than in the latter case, as is the dominant wavelength of the waves above the turbulence. The streamwise space-time spectra show that, in addition to the waves, part of the surface energy is contained in a ridge at  $\omega/k = v_0$ , with  $v_0$  the mean stream velocity. These deformations are clearly directly connected to the sub-surface turbulence, and as such are the most likely sources of the waves, instead of resonant wave-growth. The exact mechanism through which the sub-surface structures generates waves remains unclear, however. It is possible, as suggested by Brocchini & Peregrine (2001) that waves are generated around upwellings in the sub-surface turbulence. Deformations that are directly connected to the turbulence will be studied in more detail in the next chapter.

On scales that are smaller than 17 mm, below which capillary forces start to dominate the reaction of the surface to vertical accelerations, the wavenumber spectra of the surface slope are very similar, irrespective of the intensity of the sub-surface turbulence. For these wavenumbers, the spectra show a very steep scaling range, with a scaling exponent of -6.5. This exponent corresponds to a -8.5 scaling exponent for the associated surface elevation spectra. Dabiri (2003), for the surface elevation above a turbulent shear layer, measured a scaling exponent in a frequency spectrum of -10/3. Borue *et al.* (1995) found a -4.5 scaling exponent from their numerical simulations above turbulent channel flow with a no-slip bottom boundary. Clearly, the wave-number spectra above our more intense homogenous turbulence are far steeper.

---

## CORRELATING THE SUB-SURFACE TURBULENCE AND THE SURFACE SHAPE

Although, perhaps naively, one might expect the surface shape above fully developed three-dimensional turbulence to primarily be determined by attached vortices, we have already seen a part of the surface shape above turbulence consists of gravity-capillary waves. These waves travel in all directions across the surface, radiated by sources moving with the turbulence. We have also seen that part of the free surface structures move at the same velocity as the mean-stream velocity. We have postulated that these are structures originating in the turbulence, and they act as sources for the waves. Such structures could be attached vortices, but also upwellings and downdraughts, as explained in chapters 1 and 2.

In order to study what part of the sub-surface turbulence is directly visible in the free surface shape, we are going to look at cross-correlations between properties of the sub-surface velocity field and properties of the surface slope field, by measuring both fields simultaneously and at the same location. Experiments in which methods to measure the surface slope are combined with simultaneous measurements of the velocity field are rare. The introduction to chapter 6 gave a number of methods used to measure the surface slope over a certain area of the surface. Not surprisingly, these methods have also been combined with PIV. Weigand (1996) combines information on the surface shape obtained from shadow-graphy with information from PIV and uses this to study the interaction between a vortex ring and a free surface in order to better understand vortex (dis)connection. As explained in chapter 2, vortex (dis)connection is the process in which a surface parallel vortex tube, such as part of a vortex ring under the surface, breaks apart (disconnection), after which the open ends attach to the free surface (connection). Weigand notes that the locations of the maxima of the vertical component of vorticity, associated with vortex tubes that are attached to the free surface, coincide with the positions where the surface elevation is lowest. However, in Weigand's experiments, the shadowgraphy



only provides a qualitative image of the surface. Dabiri & Gharib (2001) and Dabiri (2003) combine the free-surface gradient detector developed by Zhang & Cox (1994) with simultaneous Digital PIV in horizontal planes just below the surface. In the situation they study the turbulence is associated with a vertical shear layer that forms between two adjacent inflows into a channel, with different velocities. In this shear layer, the majority of the vorticity that is generated is in the surface-normal direction. Unlike shadowgraphy the free surface gradient detector does allow a quantitative measurement of the surface slope and by integration the surface elevation. Because of this Dabiri (2003) can quantify the correlation between the vertical component of vorticity and the surface elevation. Inside the shear layer, the width of which is determined from velocity profiles, they find that the cross-correlation coefficient between the surface elevation and the surface-normal component of vorticity has a value  $\approx 0.2$ . Dabiri (2003) notes that, due to the nature of the shear layer, in the frame of reference in these experiments, most of the surface-normal vorticity is negative. By conditionally correlating only values of negative vorticity below a threshold ( $\omega_z < -1 \text{ s}^{-1}$ ) and negative values of the elevation, i.e. depressions in the surface, the correlation coefficient is increased to 0.8. Naturally, the large value of the correlation coefficient is severely biased by the conditional average. By setting a threshold for the vorticity, Dabiri excludes smaller and less intense sub-surface vortices. As was already mentioned in chapter 2, Zhang *et al.* (1999) have studied the interaction between a vortex-ring and a free surface by means of numerical simulations. They conclude that the correlation between the surface-normal component of vorticity and the surface elevation is relatively poor, unless the vortex associated with the depression in the surface has a cylindrically symmetric distribution of surface-normal vorticity.

To our knowledge, we are the first to perform simultaneous measurements of the surface shape and the sub-surface velocity field for fully developed three-dimensional turbulence. The only other quantitative values for the correlation between properties of the surface shape and sub-surface follow from numerical simulations by Tsai (1998). He simulated the free surface above turbulence generated by a horizontal shear, and found that the correlation coefficient between the absolute value of the wall-normal vorticity and the surface elevation is ( $\approx 0.5$ ), which he calls relatively poor. The reason why Tsai takes the absolute value of the wall-normal vorticity is fairly obvious: the average wall-normal vorticity in the situation he studies is 0, or, in other words, on average, there is as much positive vorticity as negative vorticity on the surface. However, both positive and negative vorticity lead to depressions in the surface. Tsai also shows that the correlation between surface-parallel vorticity, below the surface, and the surface roughness is larger ( $\approx 0.7$ ). He concludes that upwellings and downdraughts, which primarily are associated with surface-parallel vorticity increase surface roughness.

Measurements of the sub-surface velocity field, by means of PIV, combined

with our surface scanning technique allow us, for the first time, to measure the correlation between the vertical component of the vorticity and the surface elevation for homogeneous and isotropic turbulence. In addition we look at the correlation between the surface slopes and the velocity field. Before this combined technique was applied to fully developed three-dimensional turbulence, it was tested by applying it to vortex shedding behind a surface-piercing vertical cylinder. Since in that case, certainly relatively close to the cylinder, most of the generated vorticity is in the surface-normal direction, we should measure similar values for the correlation between the surface-normal vorticity and the elevation as Dabiri (2003) measured for their vertical shear layer. These measurements can then be compared to measurements above fully-developed turbulence. By using both the static grid and the active grid — with different protocols — to generate the turbulence, we can assess the influence of changing the properties of the sub-surface turbulence.

### 8.1 Correlation between turbulence and the surface shape

A way to look for a direct link between the sub-surface turbulence and the surface shape is by calculating two-dimensional cross-correlations in space between properties of the surface and properties of the sub-surface velocity field.

The spatial cross-correlation between the absolute value of the vertical component of the vorticity is given by

$$C_e(x, y) = \frac{\langle |\omega_z(x_0 + x, y_0 + y)| h(x_0, y_0) \rangle}{\langle \omega_z^2 \rangle^{\frac{1}{2}} \langle h^2 \rangle^{\frac{1}{2}}}, \quad (8.1)$$

where  $\langle \dots \rangle$  denotes an average over the surface  $(x_0, y_0)$  and over all registered surfaces in the experiment. The value of the  $C_e$  in the origin, so  $C_e(0, 0)$ , would be -1 if the surface elevation and the vertical component of vorticity were perfectly correlated, since  $|\omega_z|$  is positive and vorticity leads to a negative surface elevation, i.e. an area that is lower than its surroundings. The value of  $-C_e(0, 0)$  corresponds to the cross-correlation coefficient measured by Dabiri & Gharib (2001); Dabiri (2003) for vortices in a vertical shear layer and calculated by Tsai (1998) for numerical simulations of turbulence generated by a horizontal shear. The values of the cross-correlation coefficient found by these researchers,  $\approx 0.2$  and  $\approx 0.5$ , respectively, were less than 1, showing probably not a simple one-to-one link between the surface elevation and vorticity.

The Euler equations, as given by equation (2.32), in a frame co-moving with the mean stream velocity  $v_0$ , provide another link between the surface slope and the sub-surface velocity-field. Starting with the velocity field measured with PIV, by using the Euler equations we can derive what the corresponding slope field would be, if the Euler equations were an accurate description of the link between the surface shape and the velocity field. The surface slope field

corresponding to the measured velocity field is given by:

$$\begin{aligned}\frac{\partial h}{\partial x} &= -\frac{1}{g} \left( u \frac{\partial u}{\partial x} + v \frac{\partial u}{\partial y} \right) \\ \frac{\partial h}{\partial y} &= -\frac{1}{g} \left( u \frac{\partial v}{\partial x} + v \frac{\partial v}{\partial y} \right),\end{aligned}\quad (8.2)$$

where the right-hand-sides are measured with PIV. Hence, as an alternative to cross-correlating the surface elevation and  $|\omega_z|$  through equation (8.1), we can also cross-correlate the actually measured surface slope field with the slope field derived from the velocity field through equation (8.2). Since the Euler equations have both an  $x$  and  $y$ - component, we correlate the inner product of the measured surface slope gradient vector  $\nabla h = h_x \mathbf{e}_x + h_y \mathbf{e}_y$  and the advective acceleration  $\mathbf{A} = A_x \mathbf{e}_x + A_y \mathbf{e}_y = (u \frac{\partial u}{\partial x} + v \frac{\partial u}{\partial y}) \mathbf{e}_x + (u \frac{\partial v}{\partial x} + v \frac{\partial v}{\partial y}) \mathbf{e}_y$ :

$$C_s(x, y) = \frac{\langle A_x(x_0 + x, y_0 + y) h_x(x_0, y_0) + A_y(x_0 + x, y_0 + y) h_y(x_0, y_0) \rangle_*}{\langle A_x^2 + A_y^2 \rangle^{\frac{1}{2}} \langle h_x^2 + h_y^2 \rangle^{\frac{1}{2}}}, \quad (8.3)$$

Of course, we already know that, since it is derived for a quasi-stationary flow with very small vertical velocities and gradients, the Euler equations cannot account for all of the intricacies of the relation between surface shape and velocity field either. For instance, upwellings and downdraughts have an influence on the surface shape as well. They are associated with relatively large vertical velocities, and relatively large vertical and tangential vorticity below the surface.

### 8.1.1 TAYLOR'S HYPOTHESIS FOR FREE-SURFACE TURBULENCE

In equations (8.1) and (8.3) we relate the spatial snapshots of the velocity field to a spatial snapshot of the surface. However, the surface shape is measured by means of a scan along a line. The only way to create two-dimensional images of the surface from these scans, is by means of Taylor's hypothesis.

In turbulent flows with a relatively large mean flow, Taylor's hypothesis can be invoked to turn time-dependent measurements in a stationary point to space-dependent measurements. The idea is that turbulent fluctuations remain frozen while they are advected by the mean flow. In measurements of the turbulent velocity field with moderate turbulence intensity,  $v_{rms}/v_0 \lesssim 0.1$ , Taylor's hypothesis works well (see Gledzer, 1997), and we have successfully used it in chapter 3. PIV measurements allow us to verify the applicability of Taylor's hypothesis to the grid-generated turbulence in our experiments. If it is

---

\*We have chosen the name  $C_s$  for this correlation since it involves the surface Slopes. The correlation between  $|\omega_z|$  and  $h$  is called  $C_e$ , because this correlation involves the surface Elevation.

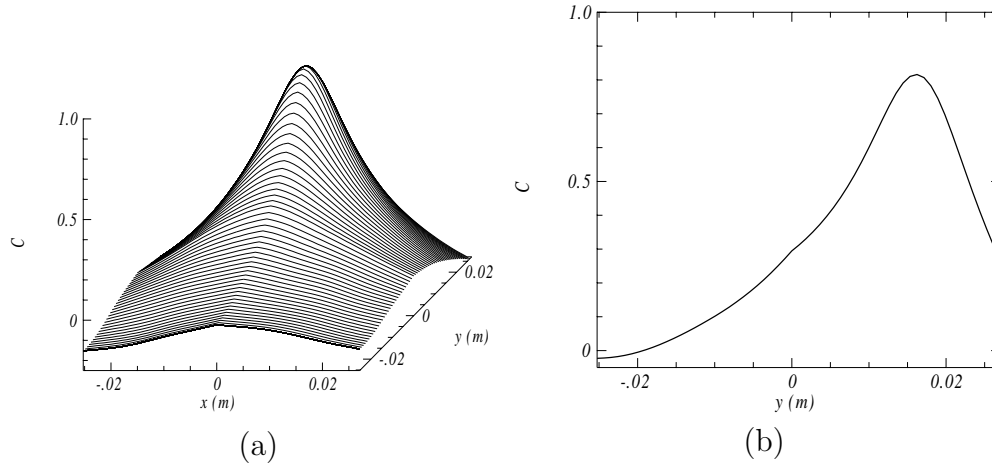


FIGURE 8.1 — (a) The cross-correlation of the velocity fields in two subsequent PIV snapshots that are taken 67 ms apart (b) Cross-section of this function in streamwise direction. The turbulence was generated with the active grid and had a mean flow velocity of 0.25 m/s. The presence of perceptible ridges along the lines  $x = 0$  and  $y = 0$  is due to peak-locking, associated with the PIV sub-pixel interpolation algorithm.

applicable, a spatial measurement along a line in the streamwise direction, that can be obtained from snapshots of the velocity field, can be interpreted as a time-dependent measurement in point. This can be checked by cross-correlating subsequent snapshots of the velocity field, of course provided that the displacement of two subsequent images is less than the size of the image. Such a cross-correlation function (obtained for active-grid-generated turbulence) is shown in figure 8.1 (a). In our PIV set-up, which is explained in more detail in section 4.5, we capture image pairs at a frequency of 15 Hz. For the experiment shown in figure 8.1, the mean flow velocity in the water channel was 25 cm/s. Hence, the displacement of the velocity fields for subsequent frames is 1.67 cm, with our PIV camera imaging a  $5.5 \times 5.5 \text{ cm}^2$  area of the flow field. The streamwise cross-section through the cross-correlation function in figure 8.1 (b) indeed shows a clear peak for a displacement of 1.67 cm. Evidently, Taylor's hypothesis indeed is applicable to the PIV measurements.

The question now is whether we can safely apply Taylor's hypothesis to the scans of the free surface above the turbulence. Clearly, Taylor's hypothesis does not hold if the turbulent surface changes rapidly while it is advected through the scanning line by the mean velocity.

In order to arrive at an estimate of the error made, we realize that the true surface is potential, so that the circulation of the gradient field taken around a

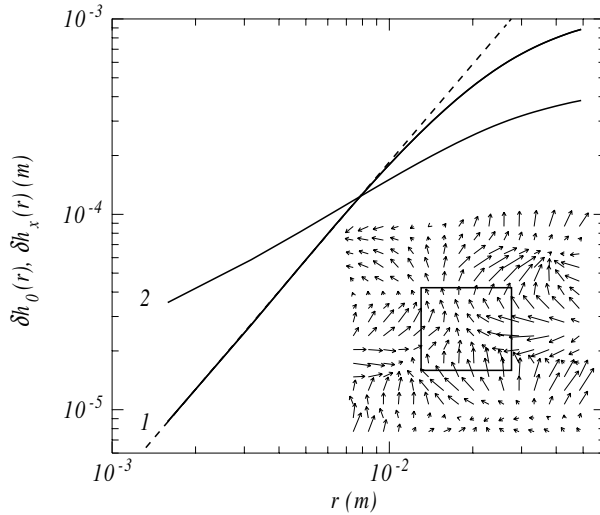


FIGURE 8.2 — Error made when assuming Taylor's frozen turbulence hypothesis for surfaces above turbulence. (1) Full line: root mean square circulation  $\delta h_0(r)$ , dashed line:  $\delta h_0(r) \sim r^{1.7}$ . (2): Root mean square elevation  $\delta h_x(r)$  measured along the scan line. The inset shows the vector field  $\nabla h(x, y)$  which was constructed using the frozen turbulence hypothesis. The error is quantified by the value of the circulation of  $\nabla h(x, y)$  taken around squares with sides  $r$ . The turbulence with mean velocity  $U = 0.25$  m/s was generated using the active grid.

loop of size  $r$ ,

$$\Gamma_r = \oint_S \nabla h(x, y) \cdot \mathbf{s} \, ds$$

vanishes for any loop  $S$ . If the surface is not frozen,  $\Gamma_r$  will be non-zero with its absolute value increasing for increasing  $r$ . We have computed  $\Gamma_r$  for our measured turbulent surfaces; for the loops we chose squares with size  $r$ . Because  $\Gamma_r$  is a fluctuating quantity with mean zero, we take

$$\delta h_0(r) = \langle \Gamma_r^2 \rangle^{1/2}$$

as a measure for the error, which can be viewed as an error in the elevation of the surface measured over a distance  $r$ . Registered time series of line measurements were tiled in non-overlapping two-dimensional surfaces, and the average was done both over all surfaces and over the area of each surface. We can compare  $\delta h_0(r)$  to the root-mean-square surface elevation

$$\delta h_x(r) = \left\langle \left( \int_r h_x(x) \, dx \right)^2 \right\rangle^{1/2},$$

which is measured in the scan direction and is not affected by the frozen turbulence hypothesis. In figure 8.2 we show both  $\delta h_0(r)$  and  $\delta h_x(r)$  as a function of  $r$ . Both quantities increase algebraically; as expected  $\delta h_0(r)$  increases more quickly than  $\delta h_x(r)$  as it embodies the temporal fluctuations of the surface.

Figure 8.2 clearly demonstrates that Taylor's frozen turbulence hypothesis works poorly for a free surface above a turbulent flow. On one hand, this is quite remarkable as it works well for the turbulent velocity field beneath it. On the other hand, the turbulent velocity field excites capillary-gravity waves on the surface. As is well known, for water the minimum phase velocity of capillary-gravity waves is approximately 0.23 m/s, which is comparable to the mean flow velocity in our experiments.

In hindsight, the breakdown of the frozen turbulence hypothesis is already illustrated in figure 7.6, where we showed the space-time correlation functions  $C_{yy}(y, \tau)$  measured in streamwise scans of the surface. If indeed Taylor's hypothesis would hold, the correlation function would reduce to the ridge  $C_{yy} = \delta(y - \tau v_0)$ , with  $v_0$  the mean velocity. This is clearly not the case. Instead, two ridges can be discriminated, *not* at the mean velocity, but at velocities  $v_0 \pm v_f$ , with  $v_f = 0.37$  m/s.

Nonetheless, we will reconstruct two-dimensional surface gradient fields by invoking Taylor's hypothesis in the manner illustrated in figure 8.3. Subsequent spanwise lines in the surface scans are interpreted as neighbouring lines in space. Obviously, unlike the velocity field PIV obtained from PIV, the two-dimensional surface gradient field is not an actual snapshot. The presence of waves, that leads to Taylor's hypothesis working poorly for the surface, leads to errors in the constructed field.

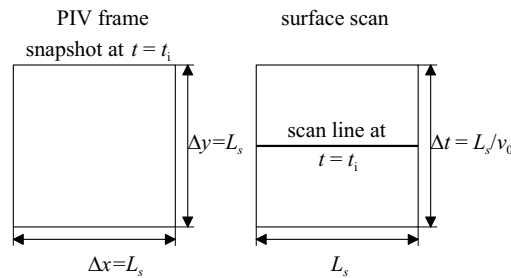


FIGURE 8.3 — The location and length  $L_s$  of the surface scan-line determines the (square) region of the velocity field obtained with PIV used for the cross-correlation. The surface scan is extended in streamwise ( $y$ -) direction by use of Taylor's hypothesis.

However, that part of the surface shape that is directly connected to the sub-surface velocity field, actually does move with the mean-stream velocity, while the changes in the surface slope associated with the waves do not travel with the

mean-stream velocity and, consequently, are not correlated with the sub-surface turbulence. Hence, by using Taylor's hypothesis in this manner, we can find the link between structures on the surface that do move with the mean-stream velocity and the turbulence. As such, Taylor's hypothesis in essence functions as a filter for correlating structures that travel with the mean velocity.

### 8.1.2 CALCULATING THE ELEVATION

Calculating the correlation between the vertical component of vorticity and the surface elevation in equation (8.1) is complicated by the fact that we measure the surface gradient and not the actual elevation, since it requires the computation of the elevation  $h(x, y)$ , now not just along a single line, but over the entire area over which the cross-correlation is to be calculated<sup>†</sup>. The gradient field, as obtained from Taylor's hypothesis, has components  $(h_x(\mathbf{x}), h_y(\mathbf{x}))$ . We calculate the matching elevation  $h(x, y)$  by starting with  $h = 0$  for  $\mathbf{x} = (0, 0)$ , the centre of the field, and then integrating along the paths indicated by the arrows in figure 8.4 (a). This approach is based on the work by Imaichi Imaichi & Ohmi (1983). For grid points on the line  $y = 0$  we integrate the slopes in

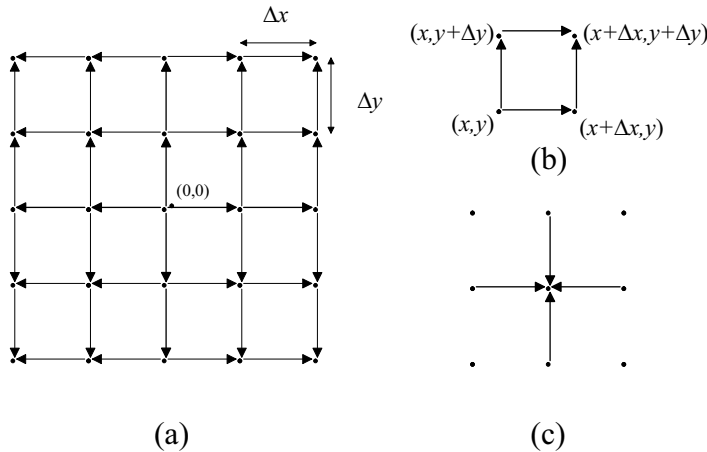


FIGURE 8.4 — Calculating the surface elevation from the surface slope field. (a) integration paths. (b) the surface elevation in point outside the lines  $x = 0$  and  $y = 0$  follow from integration over two paths. (c) In the iterative steps, the surface elevation follows from an average over the slope-integrals from four neighbouring points.

<sup>†</sup>Calculation of the vorticity is fairly straightforward:  $\omega_z = \frac{\partial v}{\partial x} - \frac{\partial u}{\partial y}$ , where the velocity gradients are calculated with the mid-point rule, see for instance equation (4.23).

x-direction over  $x$ , so:

$$h(x + \Delta x, 0) = h(x, 0) + \Delta x \frac{h_x(x + \Delta x, 0) + h_x(x, 0)}{2}, \quad (8.4)$$

where  $\Delta x$  is the grid spacing in the  $x$ -direction, and similarly,

$$h(0, y + \Delta y) = h(0, y) + \Delta y \frac{h_y(0, y + \Delta y) + h_y(0, y)}{2}. \quad (8.5)$$

where  $\Delta y$  is the grid spacing in the  $y$ -direction. For points not on these lines, the elevation is based on the average of the integration over two different paths, as illustrated in figure 8.4 (b):

$$\begin{aligned} h(x + \Delta x, y + \Delta y) &= \frac{1}{2} \{h(x + \Delta x, y) + h(x, y + \Delta y)\} \\ &+ \Delta x \frac{h_x(x + \Delta x, y + \Delta y) + h_x(x, y + \Delta y)}{4} \\ &+ \Delta y \frac{h_y(x + \Delta x, y + \Delta y) + h_y(x + \Delta x, y)}{4}. \end{aligned} \quad (8.6)$$

This reduces the effect of measurement errors in both  $h_x$  and  $h_y$ . This integration is also affected by Taylor's hypothesis, since it determines the length  $\Delta y$  of steps taken in the streamwise direction. If Taylor's hypothesis were to apply, and without measurement noise, the integral over different paths would be the same. Averaging over multiple paths is an attempt to cope with the reconstruction problem. The elevation field that results from this procedure strongly depends on the position of the starting point. A way to overcome this is by starting not in  $(0, 0)$ , but by starting in a point  $(x_0, y_0)$  instead, and then averaging the result for all possible values of  $(x_0, y_0)$  in the field. This is computationally expensive, however. Alternatively, to refine this field, we use a variation of Gauss-Seidel iteration. The elevation field calculated by integrating along the paths indicated in figure 8.4 (a) and (b) serve as a starting point for this. We subsequently recalculate the elevations in all grid points in an iterative procedure. If  $h_0(x, y)$  is the elevation in a point  $(x, y)$  of the field at the start of each iteration, the elevation at the end is  $h(x, y) = (1 - a)h_0(x, y) + ah'(x, y)$ , where  $a$  is a constant and  $h'(x, y)$  follows from integrating the slopes along paths starting in neighbouring points, as shown in figure 8.4 (c), by means of equations (8.4) and (8.5). The procedure stops once the relative change in elevation per iteration is below  $1/1000$  for each point. The constant  $a$  determines the convergence of this procedure. In our case, with  $a = 0.7$ , the procedure ends within 5 iterations. Finally, the average elevation in the field is calculated. This average is then subtracted from the elevation in each point, thereby setting the average elevation for each frame to 0.



## 8.2 Combining PIV and surface slope measurements

The set-up used for these experiments is an extension of the set-up used for our surface scans, previously shown in figure 6.3, now combined with the PIV set-up that was briefly described in section 4.5. The combined set-up is shown in figure 8.5. The oscillating mirror of the surface scanner is positioned such

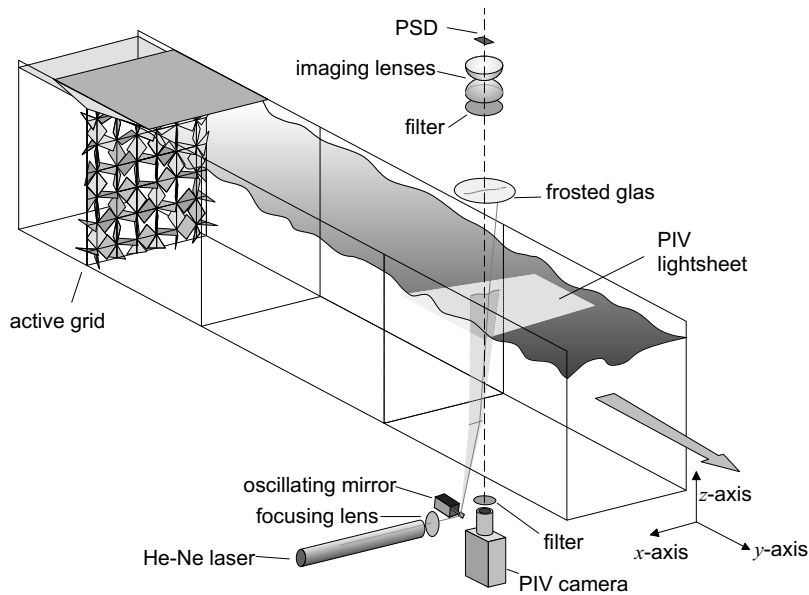


FIGURE 8.5 — Set-up for combined PIV and surface measurements.

that the line along which the slope is measured lies in spanwise direction. In most of the experiments, the PIV light sheet is positioned as close as possible (approx. 1 mm) below the surface.

To ensure that the surface scan measurements are not affected by the light emitted by the PIV laser, an optical laser-line filter is placed in front of the PSD. Similarly, a line-filter is placed in front of the camera to ensure that light from the surface scan laser does not influence the PIV data.

The entire optical system is aligned such that the surface scan line lies close to the centre of the PIV image. The part of the flow-field imaged by the PIV camera is slightly larger than the area covered by the image of the surface slope that was derived from Taylor's hypothesis. Obviously, in order to calculate the spatial cross-correlation between PIV and the surface scan, the data from both measurements should be located on the same spatial coordinate grid. PIV provides the velocity in approximately  $60 \times 60$  points on a  $5 \times 5$  cm<sup>2</sup> area, while the surface slope is measured in 152 points on a 5 cm line,

albeit non-equidistantly due to the harmonic nature of the scan. The grid on which the PIV data is located is coarser than that of the surface data and, consequently, it forms the basis for a new joint grid for both measurements. In order to calculate the desired cross-correlation functions, the surface slope data is interpolated onto this new grid by means of bi-linear interpolation. The joint

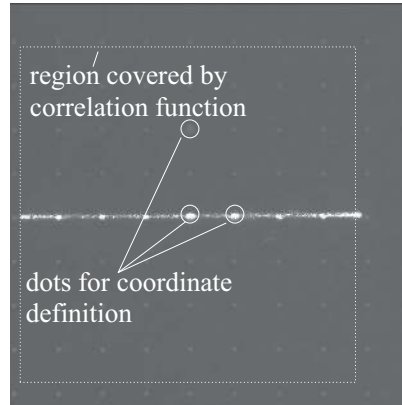


FIGURE 8.6 — In order to perform the position calibration for PIV a plate with a dotted pattern is imaged with the PIV camera. To enable the PIV camera to also see the 5 cm long surface-scan line the line-filter in front of the camera has been removed. The length of the scanning line determines the extent of the region where the cross-correlation function can be calculated. The dots that lie outside of this line are very faint in the images. This is the result of the camera diaphragm being set to its smallest setting, which was done to protect the camera from the scanning laser. For the actual PIV calibration, the scanning laser was shut down, and the diaphragm was opened.

grid is defined by means of a picture taken with the PIV camera without its line-filter, such as the picture shown in figure 8.6. In order to take this picture, a plate with a pattern of white dots against a black background is placed in the water channel at the height of the PIV light sheet. Since the actual distance between the dots on the calibration plate is known, the corresponding distance in the image provides the calibration factor needed to convert pixels in the PIV images to meters in the actual flow. This same calibration technique was used in the PIV experiments described in chapter 4.

In order to match the spatial coordinates of the surface scan to those of the new grid, it is vitally important to define the location of the origin and to align the orientation of the coordinate axes. The orientation of the axes in the PIV data is defined by an L-shaped pattern of three larger dots on the calibration plate. As was explained in section 6.3, the orientation of the coordinate system in the surface scan data is dependent on the orientation of the axes of the

PSD. In practice, matching both to our coordinate systems involves rotating and mirroring the axes. One of the three larger dots on the calibration plate, indicated in figure 8.6, is used as the origin for the new grid. The plate with the pattern is placed in the water-channel such that this particular dot lies on the channel centre-line and at 2 m from the grid. The PIV camera is aligned such that this dot lies close to the centre of the camera image. After this, the surface scanning set-up is aligned such that, with the oscillating mirror stationary in its centre position, the scanning beam is also aimed at this dot. This ensures that the position of the centre of the scan line corresponds to the origin in the joint grid. Figure 8.6 was taken with the oscillating mirror switched on. The projection of the scan line on the calibration plate is clearly visible in the image. Finally, its length defines the size of the square region in the PIV data that corresponds to the surface scan.

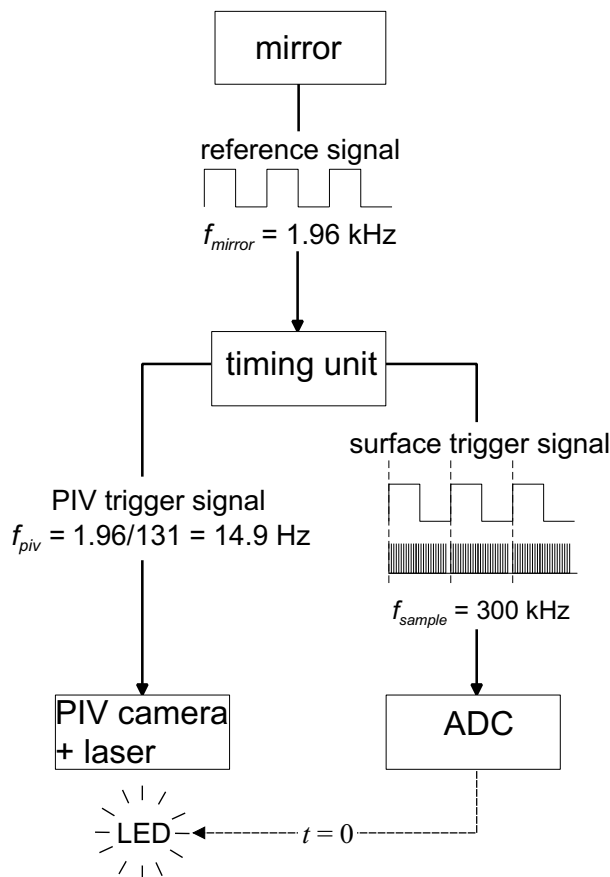


FIGURE 8.7 — Synchronising the surface scan and PIV measurements.

Not only should the data be located on the same spatial coordinates, but it should also be obtained at the same time. A given PIV snapshot needs to be matched to the correct part of the surface scan data and viceversa. Synchronisation is achieved by means of a purpose-built electronic timing unit, already briefly mentioned before in section 6.3 as part of the surface scanning set-up. Now, in addition to providing trigger pulses at 300 kHz for the ADC used for the surface slope scanner, once per 131 scan lines this timing unit triggers the PIV system. With approximately 2000 scan lines per second this means that the PIV system is triggered at close to its optimum frequency of 15 frame pairs per second. When the sampling of the surface scan data is started, a green Light Emitting Diode (LED)<sup>‡</sup> located within the field of view of the PIV camera is briefly illuminated, thereby setting time  $t = 0$  for both measurements.

The cross-correlation between both measurements will show whether all of this is done correctly, since its maximum or minimum, depending on whether we are looking at the correlation  $C_s$  (between the slopes and the Euler terms) or  $C_e$  (between  $|\omega_z|$  and  $h$ ), respectively, should lie in the origin.

### 8.3 A test case: vortex shedding

Because of the complicated timing and the difficulties in aligning both measurements, we have taken a look at a situation for which we know that sub-surface vortices are closely linked to surface deformations, namely vortex shedding in the wake of a surface-piercing vertical cylinder, as shown in the cartoon in figure 8.8. In chapter 2 we explained that a clear correlation between the sur-

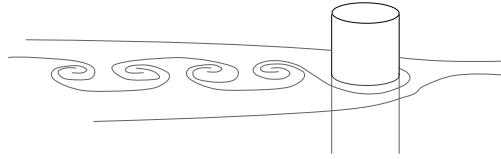


FIGURE 8.8 — Cartoon of vortices being shed in the wake of a surface-piercing vertical cylinder.

face elevation and the vertical component of vorticity can be only expected if the vertical vorticity distributions in the sub-surface structures are cylindrical. In addition, the two-dimensional relation between the surface slopes and the Euler-terms of the sub-surface velocity field, equation (2.32), that is at the basis of  $C_s$  is only appropriate for quasi-stationary and columnar vortices.

The wake behind a cylinder has been investigated for more than a century. In a wide range of Reynolds numbers the wake is characterised by a

---

<sup>‡</sup>The diode is green in order for it to be visible to the PIV camera through its green line-filter.

periodic shedding of columnar vortices, with their axes aligned with the cylinder axis, and alternating positive and negative vorticity. For this type of flow, the Reynolds number is usually defined in terms of the cylinder diameter  $D$  and the mean-stream velocity  $v_0$ , so  $Re_D = v_0 D / \nu$ . The frequency  $f$  at which the vortices are shed is often non-dimensionalised in terms of the Strouhal number:  $St = fD/v_0$ . The shedding frequency and, consequently, the Strouhal number change as the Reynolds number of the flow changes. An early detailed study of the effect of the Reynolds number on the wake and the Strouhal number, for a large range of Reynolds numbers, was done by Roshko (1952), by means of experiments with hot-wire anemometry in a wind tunnel. For  $40 < Re_D < 150$  the shed vortices form a stable so-called Von Kármán vortex-street. In this range of Reynolds numbers the Strouhal number increases rapidly with increasing Reynolds numbers. For  $150 < Re_D < 300$  a number of different instabilities can occur in the wake, leading to the wake becoming more three-dimensional and leading to large fluctuations in the Strouhal number. In Roshko's experiments for  $Re_D$  up to  $10^4$  periodic coherent vortices are still clearly visible in the wake, but beyond a distance of approximately 50 times the cylinder diameter the wake becomes fully three-dimensional. In this range of Reynolds numbers, the Strouhal number is 0.21, practically independent of the Reynolds number.

For our experiments on vortex shedding the grid was removed from the water channel and a cylinder with a diameter of 1.2 cm was placed in the measurement section of channel instead. Measurements were done with four different mean stream velocities, corresponding to  $Re_D = 225, 446, 902, \text{ and } 1860$ . The distance between our measurement location and the cylinder was 40 cm, which is 33 times the cylinder diameter, and thus periodic vortices are clearly visible. Figure 8.9 shows four coinciding images of different properties of the flow, measured in the wake, for  $Re_D = 1860$ . The surface slope field in figure 8.9 (a), derived from the surface scan by means of Taylor's hypothesis, shows the presence of a circular area of low slope surrounded by a ring of high slope: a depression in the surface. The corresponding surface slope field derived from PIV by means of the Euler equations, equation (8.2), in (b) shows a similar structure and the vorticity distribution shown in (d) has a clear peak at the same location. The integrated surface slope field in (c) shows that the maximum depth of the surface depression is only a few tenths of a millimeter. Evidently, the structure in question is a vortex, with an associated depression in the surface above it. For this structure, the surface slope field derived from the sub-surface velocity field with equation (8.2), is very similar to the actually measured surface slope field, both qualitatively and quantitatively. This can be seen in more detail in figures 8.10 (a) through (d), which show a number of cross-sections through the vortex core, for the vortex shown in figure 8.9. For these figures, the centre of the core has been defined as the point where the surface elevation has its minimum. The velocity profiles in spanwise and streamwise direction, in figure (a), show that the location where the angular

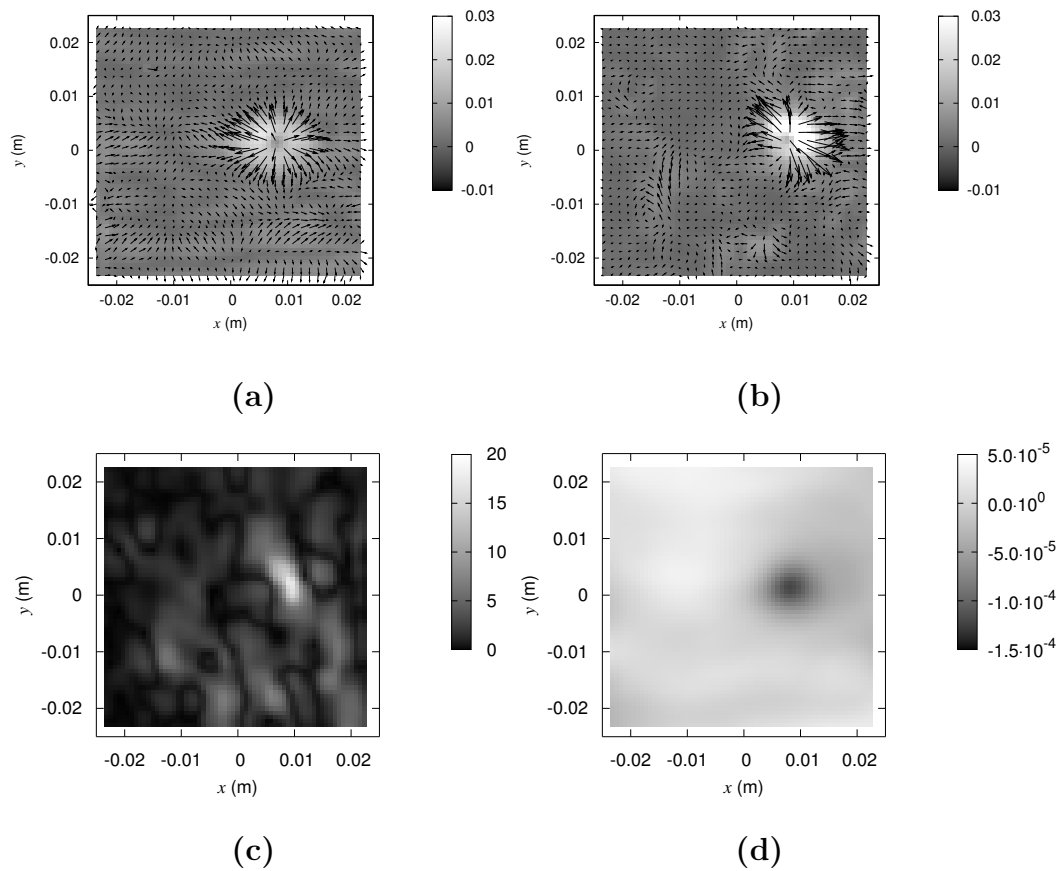


FIGURE 8.9 — Images of a vortex in the cylinder wake. (a) Surface slope field obtained from a measured PIV velocity field through the Euler equations, equation (8.2), with only one in four measured vectors shown. The grey value represents the slope magnitude. (b) Corresponding image of the surface slope field obtained from a surface scan, extended in streamwise direction by means of Taylor's hypothesis and interpolated on the grid formed by the PIV data. (c) The absolute value of the vertical component of vorticity, obtained from PIV. (d) The surface elevation (in meters) obtained from a surface scan.

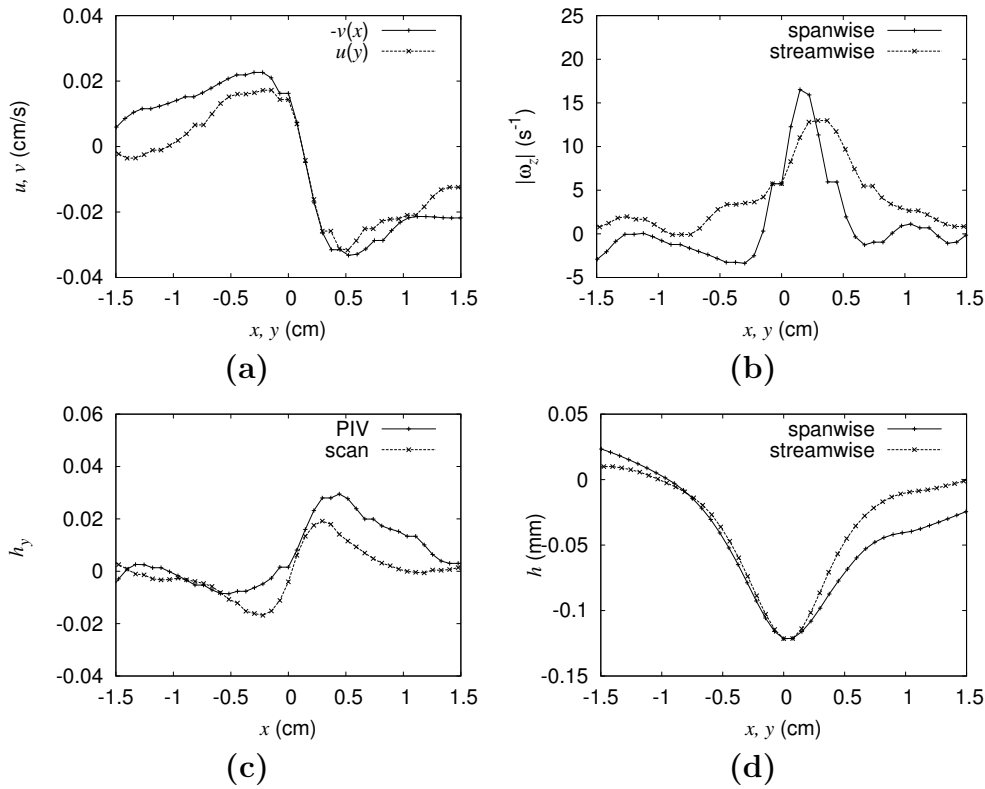


FIGURE 8.10 — Cross-sections through the snapshots of the vortex shown in figure 8.9. The point  $(x, y) = (0, 0)$  is the point where the surface elevation has its minimum. (a): Velocity profiles through the core of the vortex. (b): Profiles of the vorticity. (c): The slope  $h_y(x)$  as derived from PIV by means of the Euler equations, equation (8.2), and as actually measured. (d): Profiles of the elevation through the core of the vortex

velocity equals zero coincides with the point of lowest elevation, but that the vortex is slightly asymmetric. Profiles of the vorticity in (b) show that the vorticity distribution in the vortex is not completely cylindrically symmetric, and that, consequently, the point of maximum vorticity does not coincide with the minimum in elevation, as predicted by Zhang *et al.* (1999). Figure (c) shows profiles (in spanwise direction) of the slope  $h_y = \partial h / \partial y$  derived from PIV by means of the Euler equations, equation (2.32), as well as the directly measured slope, showing that both are broadly the same. Finally, figure (d) shows that the profiles of the surface elevation in the spanwise and the streamwise direction are practically identical. Not surprisingly, the vortex is roughly of the same size as the cylinder.

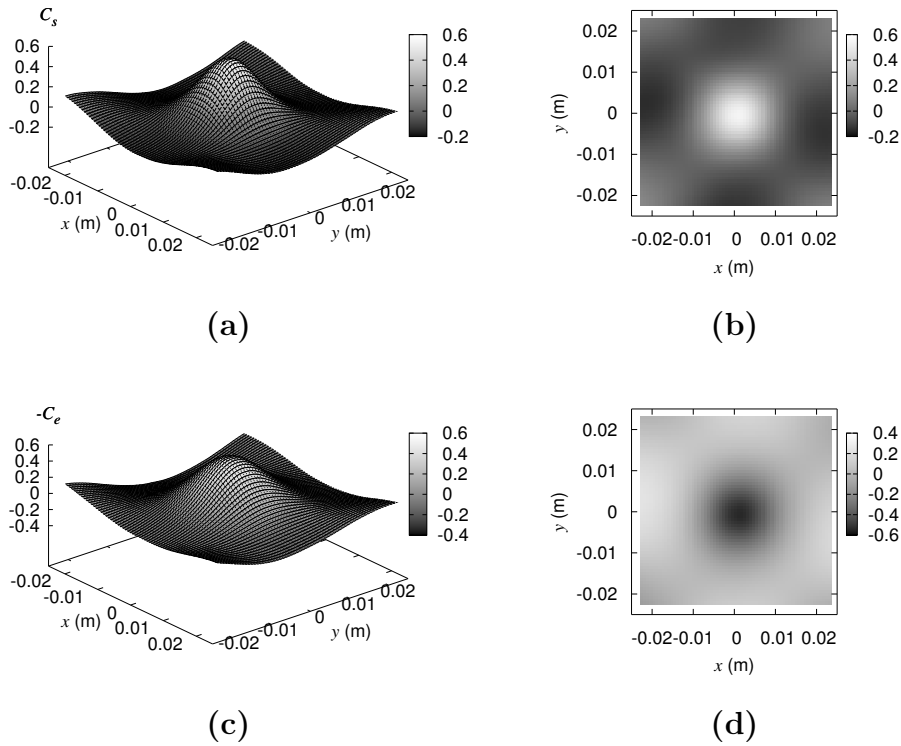


FIGURE 8.11 — Cross-correlation functions in the cylinder wake for  $Re_D = 1860$ . (a) and (b): Cross-correlation  $C_s$  between the measured slopes and the slope field derived from simultaneous PIV measurements of the sub-surface velocity field by means of the Euler equations, equation (8.2). (c) and (d): Cross-correlation  $C_e$  between the surface elevation and  $|\omega_z|$ . Note that in (c) the vertical scale has been inverted in order to better show the minimum.

The cross-correlations  $C_s$  and  $C_e$ , averaged over 800 subsequent frames, for this same experiment are shown in figure 8.11. The correlation  $C_s$  between the slopes and the Euler terms, shown in figure 8.11 (a), has a distinctive peak with a height of close to 0.5, at  $(x, y) = (0, 0)$ . This can also clearly be seen in the corresponding contour plot in figure (b). Similarly, the correlation between the elevation and vorticity, correlation function  $C_e$  in figure (c) has a distinctive negative peak with a depth of close to 0.5, with the corresponding contour image shown in (d). That the peaks are located around  $(0, 0)$  demonstrates that alignment of the grids of both measurements was successful and that the synchronisation works as well. Let us emphasise that the correlations involve two-dimensional surfaces that were constructed from line measurements. In



figure 8.11 the correlation peaks have a circular cross-section only if we choose the convection velocity needed for this construction equal to the mean flow velocity.

The size of both peaks clearly suggests a fairly strong correlation between the measured properties. However, the peak value also depends on the parameters used for PIV. In chapter 4 we have seen that velocity gradients and vorticity that can be derived from PIV measurements depend on the PIV interrogation window size, the density of the grid, and the radius of optional Gaussian filtering.

Briefly, the effect of both the finite size of the interrogation window and the extent of the Gaussian velocity filter is a spatial filtering of the velocity field. Decreasing the size of the interrogation windows increases the spatial resolution. Decreasing the size also leads to an increase in the percentage of bad vectors, and in practice this determines the minimum window size. In our experiments, as well as those in chapter 4, we use interrogation windows of  $32 \times 32$  pixels, which corresponds to an area of  $2 \times 2 \text{ mm}^2$  in the actual flow, and we use 50 % overlap between neighbouring windows. With these settings, we found that the number of spurious vectors still lies below 1%. A final parameter that can be chosen is the radius of the Gaussian filter, as defined in equation (4.41). It is clear that the cross-correlations we are concerned with here are also be influenced by the filtering. We expect that if the correlation between the velocity field and the surface were to be perfect, the actually measured correlation would increase with increasing spatial filter size, would reach a maximum, and would then start to decrease again, as the filter size becomes larger than the size of the vortices. Figure 8.12 shows how the peak values  $C_s(0,0)$  and  $C_e(0,0)$  of the cross-correlation functions, depend on the chosen value of  $\sigma$  for the Gaussian weighted averaging, for two different Reynolds numbers. For

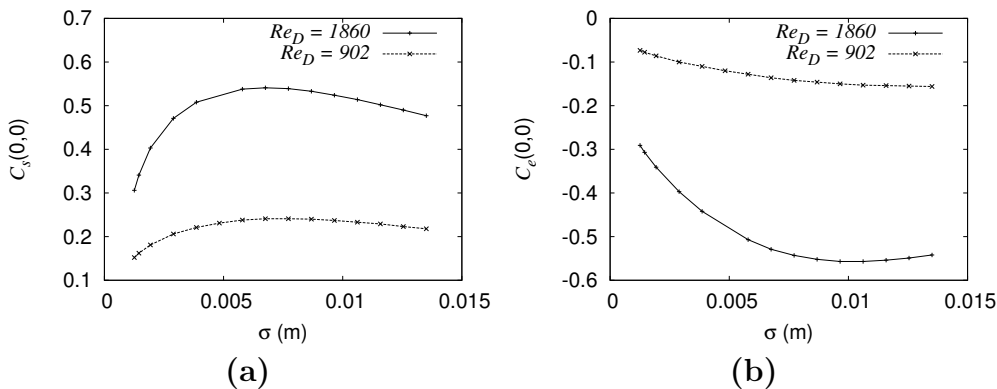


FIGURE 8.12 — Peak value of the cross-correlation functions for the slopes ( $C_s$ ) and the elevation ( $C_e$ ) as a function of the radius of the Gaussian filter used to filter the PIV results.

both Reynolds numbers,  $C_s(0,0)$  has its maximum value for  $\sigma=7$  mm, which is close to the radius of the cylinder. Hence, the results shown in figure (8.11) have been obtained from Gaussian averaging the velocity field with  $\sigma=7$  mm. Table 8.1 lists the peak values found for  $\sigma=7$ mm for three highest Reynolds numbers in our experiments. The table shows that, as the Reynolds number increases, the correlation we measure becomes stronger. For the fourth and lowest Reynold number in our experiments,  $Re_D = 225$ , the correlation functions no longer showed any clear peaks, primarily as a result of noise. The surface deformations in that case are too small to still be picked up in our surface scan. Clearly, despite the difficulties in quantitatively interpreting the

TABLE 8.1 — Peak values of  $C_s$  and  $C_e$  as a function of the Reynolds number for vortex shedding. The values of  $Re_D$  follow from the mean-stream velocity measured in the experiment by means of PIV.

$Re_D$	$C_s(0,0)$	$C_e(0,0)$
446	0.14	$-9.3 \cdot 10^{-2}$
902	0.24	-0.13
1860	0.54	-0.51

cross-correlation functions, as the Reynolds number increases and the vortices in the wake become stronger, their surface signature becomes more and more visible and the correlation between the surface shape and sub-surface velocity field becomes stronger.

However, the most important conclusion that can be drawn from these results is that the difficult alignment of both measurement techniques as well as the synchronisation is successful. We are capable of simultaneously measuring both the surface shape and the sub-surface velocity field at the same location, and can calculate cross-correlations between properties of the surface and the sub-surface velocity field.

## 8.4 Grid-generated turbulence

Having seen that the synchronisation and alignment can be done successfully, we can now do similar experiments for grid-generated turbulence. In order to be able to compare the turbulence results to those of the vortex-shedding, here too we chose  $\sigma=0.7$ mm.

Figure 8.13 shows measured cross-correlation functions  $C_s$  and  $C_e$  for active grid-generated turbulence with a mean-stream velocity of 25.7 cm/s and protocol (25OPT). Even though the correlation functions are not as well-behaved

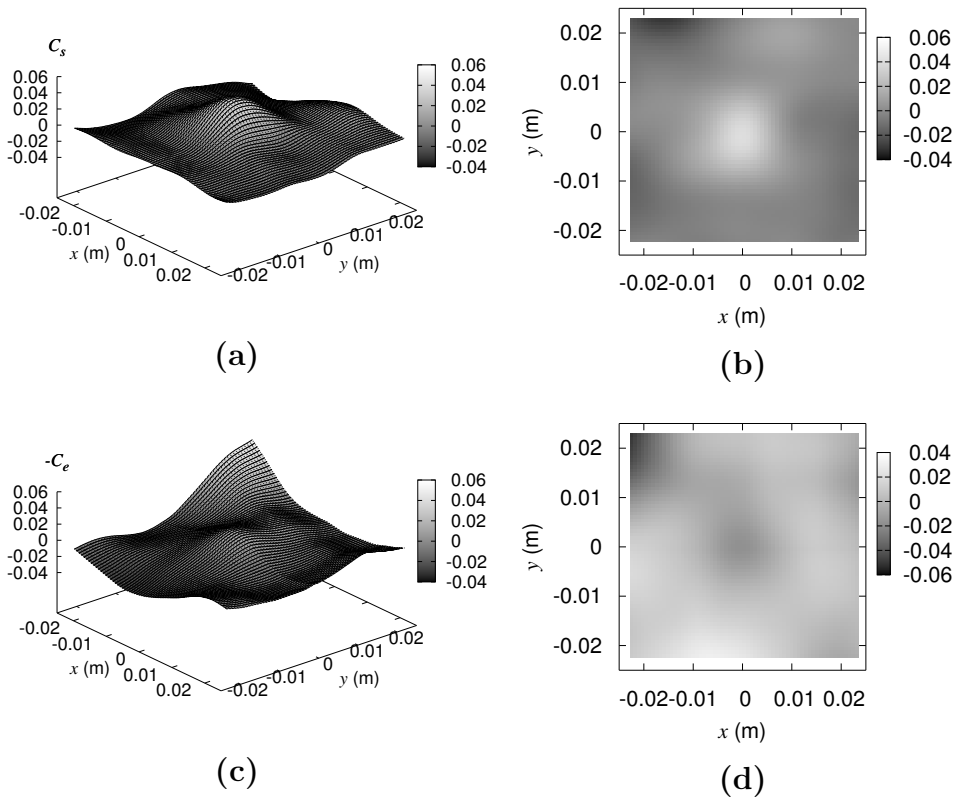


FIGURE 8.13 — Cross-correlation functions for active-grid-generated turbulence with protocol (25OPT). (a) and (b): Cross-correlation  $C_s$  between the measured slopes and the slope field derived from simultaneous PIV measurements of the sub-surface velocity field by means of the hydrostatic balance, equation (8.2). (c) and (d): Cross-correlation  $C_e$  between the surface elevation and  $|\omega_z|$ . Note that in (c) the vertical scale has been inverted in order to better show the minimum.

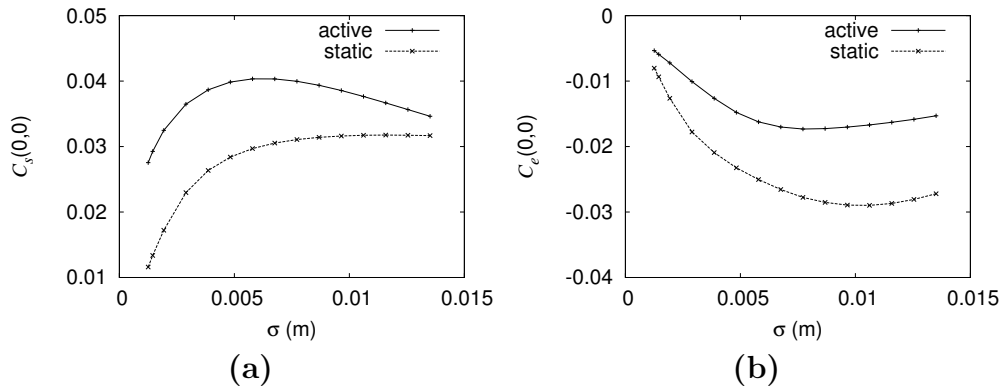


FIGURE 8.14 — Peak value of the cross-correlations function, **(a)**  $C_s$  and **(b)**  $C_e$ , as a function of the width of the Gaussian filter. The active-grid-generated turbulence, with a mean-stream velocity of 0.257 m/s, was generated with protocol (25OPT). The turbulence generated with the static grid had a mean-stream velocity of 0.174 m/s.

as the corresponding correlation functions for vortex shedding, shown in figure 8.11, especially towards the edges, they still show a clear peak at the origin.

In the previous section, we have seen that the peak-value of the cross-correlation function can be influenced by changing the value of  $\sigma$  in the Gaussian averaging of the velocity field. Figure 8.14 shows the influence of  $\sigma$  on the peak values for active-grid-generated turbulence, as well as for turbulence generated with the static grid. Apart from the fact that the peak values are much smaller, the general trend is the same as that for vortex shedding shown in figure 8.12.

Figure 8.15 shows cross-correlation functions for active grid-generated turbulence with two lower mean stream velocities, and with accordingly modified forcing protocols. These correlation functions are broadly the same as those shown in figure 8.13, showing that, as the turbulence becomes weaker and, accordingly, the surface deformations become smaller peaks are still clearly visible near the origin. As emphasised before, the use of reconstructed surfaces (through Taylor's hypothesis) filters structures that move with the mean flow velocity. From the rotation symmetry of our measured correlation peaks we learn that the measured correlations indeed gauge these structures. Surface structures which do not move with the mean flow, such as gravity-capillary waves, would spoil this correlation.

The values found for the active grid, corresponding to the correlation functions shown in figures 8.13 and 8.15, as well as for static-grid-generated turbulence, are listed in table 8.2. Generally, with the exception of the static grid generated turbulence, similar to vortex shedding, an increase in mean-stream velocity, and correspondingly an increase in the grid's mesh Reynolds number

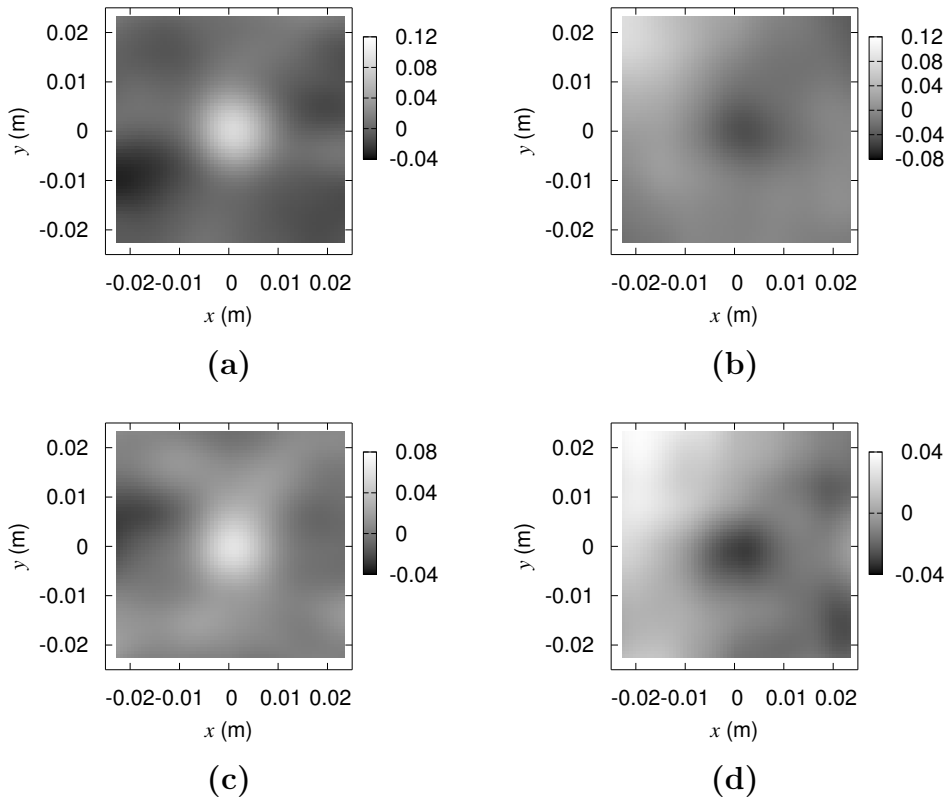


FIGURE 8.15 — Cross-correlation functions between the surface and the sub-surface velocity field for active-grid-generated turbulence: (a)  $C_s$  and (b)  $C_e$  for a mean-stream velocity of 16.6 cm/s and forcing protocol (15OPT), (c)  $C_s$  and (d)  $C_e$  for a higher mean stream velocity of 22.1 cm/s and forcing protocol (20OPT).

TABLE 8.2 — Peak values of  $C_s$  and  $C_e$  for different forcing conditions. The turbulence statistics for the active-grid generated turbulence, measured at 10 cm below the surface by means of LDV are listed in table 3.2. The velocities listed here were measured by means of PIV, just below the surface.

	$v_0$ (m/s)	$v_{rms}$ (m/s)	$C_s(0,0)$	$C_e(0,0)$
static	0.174	$5.4 \cdot 10^{-3}$	$3.0 \cdot 10^{-2}$	$-2.5 \cdot 10^{-2}$
15OPT	0.257	$1.6 \cdot 10^{-2}$	$8.4 \cdot 10^{-2}$	$-4.3 \cdot 10^{-2}$
20OPT	0.212	$1.4 \cdot 10^{-2}$	$6.0 \cdot 10^{-2}$	$-3.0 \cdot 10^{-2}$
25OPT	0.163	$1.1 \cdot 10^{-2}$	$4.0 \cdot 10^{-2}$	$-1.6 \cdot 10^{-2}$

leads to a decreasingly strong link between the surface shape and the sub-surface velocity field. The peak values are much smaller than the corresponding values for vortex-shedding, listed in table 8.1.

It is likely that only structures up to a certain depth below the surface influence the surface shape. In order to study this in more detail, a series of experiments was done, in which the distance between the light sheet and the surface was increased from its minimum value of approximately 1 mm up to more than 2 cm. The peak values of the cross-correlation functions  $C_s$  and  $C_e$ , evaluated with similar PIV settings, are shown in figures 8.16 (a) and (b), respectively. The figure shows that the peak value  $C_s(0,0)$  of the correlation between the Euler terms and the surface slopes steadily decreases for increasing

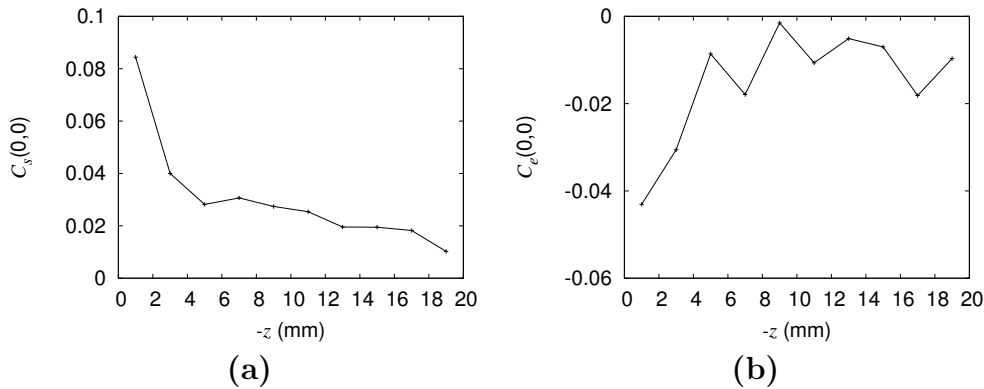


FIGURE 8.16 — Peak value of the cross-correlation functions  $C_s$  (slopes) and  $C_e$  (elevation), for active grid-generated turbulence with protocol (25OPT), as a function of the depth below the surface.

depth. Although the statistical fluctuations of  $C_e(0, 0)$  are large, the overall trend in figure 8.16 (b) is similar. The correlation between the elevation and the vertical component of vorticity also decreases for increasing depth. For depths below 19 mm, the cross-correlation functions no longer show a clear maximum or minimum. This indicates that the depth of the layer in the turbulence responsible for deforming the surface, at least for turbulence generated with this protocol, is approximately 2 cm. In chapter 3 we have measured velocity profiles as a function of depth by means of Laser-Doppler-Velocimetry at the same location. These profiles show that within a layer with a depth of a few cm below the surface, the horizontal velocity fluctuations increase, whereas the vertical fluctuations decrease. This is most notable in figure 3.13, which shows that in a layer with a depth of 2 cm the ratio of  $v_{rms}$  over  $w_{rms}$ , i.e. of the horizontal fluctuation velocity over the vertical fluctuation velocity is dramatically increased. This is in agreement with the presence of a source-layer, first suggested by Hunt and Graham Hunt & Graham (1978) and discussed before in chapter 2. Apparently, that part of the surface deformation that is directly associated with the sub-surface turbulence, is primarily connected to large, pancake-like structures present within this source layer.

## 8.5 Conclusions

We have combined our existing surface scanning method with PIV, in order to measure the spatial correlation between the surface shape and the sub-surface velocity field. The main difficulties in combining these techniques lie in making sure that the data in both measurement techniques is located on the same grid and is measured simultaneously. A further difficulty in our measurements is caused by the fact that the surface scanning technique only provides the slope along a line. In order to cross-correlate the surface slope measurements with the two-dimensional images of the velocity field, measured with PIV, the lines have been extended to two-dimensional images by means of Taylor's frozen turbulence hypothesis.

We have tested our procedures in a vortex-shedding experiment and obtained a fairly strong correlation ( $C \approx 0.5$ ) between surface elevation and the absolute value of the vorticity. For similar vortices in a vertical shear layer, Dabiri & Gharib (2001) and Dabiri (2003) measured a cross-correlation coefficient between the vertical component of vorticity, which in their case was primarily negative, and the surface elevation of  $\approx 0.8$ . For the Reynolds numbers we considered in our cylinder wake experiments, the wake is turbulent, but still shows clear periodic shedding of large vortices. As can be expected from columnar vortices, we find a clear correlation between the surface slope and the Euler terms of the sub-surface velocity field. The cross-correlation coefficients found from this comparison are similar to those between vorticity and the elevation. Directly comparing our results to those of Dabiri *et al.* is complicated,

since, unlike Dabiri *et al.*, we did not use any conditions for the minimum magnitude of the vorticity or the elevation. We have also seen that the numerical value of the cross-correlation coefficient is influenced by the spatial filtering in PIV, which is not reported by Dabiri *et al.*

Similar measurements have been performed on grid-generated-turbulence. The only quantitative information on the cross-correlation coefficients for fully developed three-dimensional turbulence were found by Tsai (1998), who simulated turbulence generated by a horizontal shear layer. He found a cross-correlation coefficient between the magnitude of the vertical vorticity and the surface elevation  $\approx 0.5$ . The maximum value we found for grid-generated-turbulence was  $\approx 0.04$ . The cross-correlation coefficient based on the hydrostatic balance was higher,  $\approx 0.08$ .

There is a clear discrepancy between Tsai's correlation coefficients and the measured values. Obviously, something is missing in the simulation, and we conclude that the surface shape is more than a reflection of some property of the velocity field beneath it. In chapter 7 we have shown that the surface is wrinkled by gravity-capillary waves that may originate from structures in the sub-surface velocity field, but that travel with a relatively large velocity over the surface. These waves would spoil the correlations, and they may be absent in Tsai's numerical simulations. A subtle issue in our experimental procedure is the invocation of Taylor's frozen turbulence hypothesis to reconstruct a two-dimensional image from line scans. This procedure favours structures that travel with the mean flow velocity. However, we believe that our measured correlations are not affected strongly by this procedure. This was learned from correlating individual line scans of the surface with lines in the measured two-dimensional velocity field. Although the statistical fluctuations in the measured correlations are larger, the maximum correlation coefficient did not change much.

Tsai (1998) measured an even higher cross-correlation between surface-parallel vorticity (below the surface) and the surface elevation. He associated this with up-wellings and downdraughts. Sadly, with our current set-up, we cannot identify these structures, since we do not have access to the vertical component of the velocity, nor the surface parallel components of the vorticity. These could in principle be accessed by placing the laser sheet vertically in the channel, instead of parallel to the surface. Such experiments are highly recommended if this subject is to be further investigated. Another more complicated option is simultaneously measuring all three components of the velocity in a plane. This is possible by means of stereoscopic PIV, with a practically unchanged experimental set-up. Measuring all components of the vorticity requires even more complicated measurements, for instance with simultaneous PIV measurements in two closely-spaced parallel light-sheets, or with holographic PIV.

Finally, by changing the distance between the surface and the plane in which we measure the velocity field, we have seen that the correlation disappears below



a certain depth. This depth corresponds to that of the source-layer, a layer in which kinetic energy is redistributed from vertical velocity fluctuations into horizontal fluctuations. The space-time spectra of the surface slope in chapter 7 showed that part of the surface moved with the mean-stream velocity. The presence of peaks in the cross-correlations clearly shows that these deformations indeed are directly connected to structures in the turbulence below the free surface, specifically in the source layer.

---

## GENERAL CONCLUSIONS

The main goal of this thesis was to find out what the shape of the free surface above turbulence reveals about the properties of the sub-surface turbulence. This was studied by means of detailed experiments in a water channel in which we measured properties of both the surface shape and the sub-surface turbulence.

In most of the experiments the turbulence was generated by means of an active grid. Far below the surface and depending on the forcing protocol used to control the grid, the generated turbulence was a reasonably close approximation of homogeneous and isotropic turbulence. Straightforward point measurements of the surface offer insufficient information to understand the nature of the surface, since due to the Doppler-effect it is impossible to untangle spatial and temporal information. Hence, we have developed a novel technique to measure the surface slope with a high resolution in space and time along a line on the surface. These space-time measurements of the surface shape show the presence of gravity-capillary waves above the turbulence, that can be identified through their dispersion relation. Spatial measurements of the surface have allowed us to measure the isotropy of the surface. While isotropic turbulence is rare in nature, the choice for isotropic turbulence in our experiments provides crucial information. We have seen that for turbulence that is isotropic far below the surface, the surface shape is isotropic as well. Furthermore, if we change the forcing protocol such that the turbulence becomes anisotropic, the surface shape becomes anisotropic as well. This shows conclusively that the waves on the surface are generated not directly by the grid, but locally by the turbulence, instead.

In previous studies on sub-surface turbulence, other researchers have shown that deformations of the surface are coupled to low pressure in the cores of sub-surface vortices, and in experiments on a vertical shear layer (Dabiri & Gharib, 2001; Dabiri, 2003) as well as in numerical simulations of turbulence generated by a horizontal shear (Tsai, 1998) have found correlation coefficients

between the vertical component of vorticity and the elevation of  $\approx 0.8$  and  $\approx 0.5$ , respectively. In similar experiments, in which we combined our surface scanning technique with Particle Image Velocimetry, we also find a correlation coefficient of  $\approx 0.5$  for the turbulent wake behind a surface-piercing cylinder. However, although for our grid-generated turbulence a distinct correlation peak still is visible, the correlation coefficient in that case is significantly smaller:  $< 0.1$ . The most obvious explanation for this discrepancy is the presence of gravity-capillary waves.

That the turbulence excites waves is somewhat unexpected. Existing theory on the generation of surface waves by turbulence predicts that they can only be generated if the fluctuation velocities in the turbulence exceed the minimum phase-velocity for gravity-capillary waves. In our experiments the fluctuation velocities are an order of magnitude smaller. The mechanism for the generation of these waves remains unknown. However, our measurements do show that the majority of the waves on the surface have wavelengths that are approximately the same as the integral scale of the sub-surface turbulence and out of the wide range of scales present in the turbulence, only the largest scales are visible in the surface shape.

## BIBLIOGRAPHY

- AARTS, D.G.A.L., SCHMIDT, M. & LEKKERKERKER, H.N.W. 2004 Direct visual observation of thermal capillary waves. *Science* **304**, 847–850.
- ADRIAN, R.J. 1996 Analysis of a laser doppler anemometer. In *Fluid Mechanics Measurements, 2nd edition* (ed. R. J. Goldstein), pp. 175–299. Washington: Taylor & Francis.
- ADRIAN, R.J. & GOLDSTEIN, R.J. 1971 Analysis of a laser doppler anemometer. *J. Phys. E: Sci. Instr.* **4**, 505–511.
- ANDERSEN, A. 2003 Vortex flows with a free surface and random matrix theory and acoustic resonances. PhD thesis, The Technical University of Denmark.
- BATCHELOR, G.K. 1951 Pressure fluctuations in isotropic turbulence. *Proc. Cambridge Philos. Soc.* **47**, 359–374.
- BERNAL, L.P. & KWON, J.T. 1989 Vortex ring dynamics at a free surface. *Phys. Fluids A*. **1**, 449–451.
- BOCK, E.J. & HARA, T. 1995 Optical measurements of capillary gravity waves using a scanning laser slope gauge. *J. Atmos. Oceanic Technol.* **12**, 395–403.
- BORUE, V., ORSZAG, S.A. & STAROSLESKY, I. 1995 Interaction of surface waves with turbulence: direct numerical simulations of turbulent open channel flow. *J. Fluid Mech.* **286**, 1–23.
- BROCCHINI, M. & PEREGRINE, D.H. 2001 The dynamics of strong turbulence at free surfaces. part 1. description,. *J. Fluid Mech.* **449**, 225–254.
- BRUMLEY, B.H. & JIRKA, G.H. 1987 Near-surface turbulence in a grid-stirred tank. *J. Fluid Mech.* **183**, 235–263.
- CALMET, I. & MAGNAUDET, J. 2003 Statistical structure of high-reynolds-number turbulence close to the free surface of an open-channel flow. *J. Fluid Mech.* **474**, 355–378.

- COMTE-BELLOT, G. & CORRISIN, S. 1966 The use of a contraction to improve the isotropy of grid-generated turbulence. *J. Fluid Mech.* **25**, 657–682.
- COX, C. & MUNK, W. 1954 Statistics of the sea surface derived from sun glitter. *J. Marine Res.* **16**, 199–225.
- DABIRI, D. 2003 On the interaction of a vertical shear layer with a free surface. *J. Fluid Mech.* **480**, 217–232.
- DABIRI, D. & GHARIB, M. 2001 Simultaneous free surface deformation and near surface velocity measurements. *Exp. in Fluids* **30**, 381–390.
- DALZIEL, S.B., HUGHES, G.O. & SUTHERLAND, B.R. 2000 Whole-field density measurements by ‘synthetic schlieren’. *Exp. in Fluids* **28**, 322–335.
- DUGAN, J.P. & PIOTROWSKI, C.C. 2003 Surface current measurements using airborne visible image time series. *Remote Sens. Environ.* **84**, 309–319.
- DURST, F., MELLING, A. & WHITELAW, J.H. 1981 *Principles and Practice of Laser-Doppler Anemometry, 2nd. edition*. Academic Press.
- DURST, F. & STEVENSON, W.H. 1979 Influence of gaussian beam properties on laser doppler signals. *Applied Optics* **18**, 516–524.
- ELENBAAS, T. 2006 Writing lines in turbulent air using air photolysis and recombination tracking. PhD thesis, Eindhoven University of Technology.
- FERNANDO, H.J.S. & HUNT, J.C.R. 1997 Turbulence, waves and mixing at shear-free density interface. part1. a theoretical model. *J. Fluid Mech.* **347**, 197–234.
- FORBES, C., LEMAN, K., OLSON, D. & BROWN, O. 1993 Eddy and wave dynamics in the south atlantic as diagnosed from geosat altimeter data. *J. Geophys. Res.* **12**, 297–314.
- FORLITI, D.J., STRYKOWSKI, P.J. & DEBATIN, K. 2000 Bias and precision errors of digital particle image velocimetry. *Exp. in Fluids* **28**, 436–447.
- FOUCAUT, J.M., CARLIER, C. & STANISLAS, M. 2004 Piv optimization for the study of turbulent flow using spectral analysis. *Meas. Sci. Tech.* **15**, 1046–1058.
- FOUCAUT, J.M. & STANISLAS, M. 2002 Some considerations on the accuracy and frequency response of some derivative filters applied to particle image velocimetry vector fields. *Meas. Sci. Tech.* **13**, 1058–1071.

- FRISCH, U. 1995 *Turbulence, The Legacy of A.N. Kolmogorov*. Cambridge Univ. Press.
- FUNG, J.C.H., HUNT, J.C.R., MALIK, N.A. & PERKINS, R.K. 1992 Kinematic simulation of homogeneous turbulence by unstead random fourier modes. *J. Fluid Mech.* **236**, 281–318.
- GARDNER, F.M. 1979 *Phaselock Techniques, 2nd. edition*. Wiley Interscience.
- GEORGE, W.K., BEUTHER, P.D. & ARNDT, R.E.A. 1984 Pressure spectra in turbulent free shear flow. *J. Fluid Mech.* **148**, 155–191.
- GHARIB, M. 1994 Some aspects of near surface vortices. *Appl. Mech. Rev* **47**, S157–S162.
- GHARIB, M. & WEIGAND, A. 1996 Experimental studies of vortex disconnection and surface connection at a free surface. *J. Fluid Mech.* **321**, 59–86.
- GLEDZER, E. 1997 On the Taylor hypothesis corrections for measured energy spectra of turbulence. *Physica D* **104** (2), 163–183.
- H. HUANG, H., DABIRI, D. & GHARIB, M. 1997 On errors of digital particle image velocimetry. *Meas. Sci. Tech* **8**, 1427–1440.
- HANDLER, R.A., SWEAN, T.F., LEIGHTON, R.I. & SWEARINGEN, J.D. 1993 Length scales and the energy balance for turbulence near a free surface. *AIAA Journal* **31**, 1998–2007.
- HARA, T., BOCK, E.J. & DONELAN, M. 1997 Frequency-wavenumber spectrum of wind-generated gravity-capillary waves. *J. Geophys. Res.* **102**, 1061–1072.
- HODGES, B.R. & STREET, R.L 1999 On simulation of turbulent nonlinear free-surface flows. *J. Comput. Phys.* **151**, 425–457.
- HOLLAND, T.K. 2001 Application of the linear dispersion relation with respect to depth inversion and remotely sensed imagery. *IEEE Trans. Geosci. Remote Sensing* **39**, 2060–2072.
- HUNT, J.C.R. 1984 Turbulence structure and turbulent diffusion near gas-liquid interfaces. In *Gas Transfer at Water Surfaces* (ed. W. Brutsaert & G.H. Jirka), pp. 67–82. Reidel.
- HUNT, J.C.R. & GRAHAM, J.M.R. 1978 Free-stream turbulence near plane boundaries. *J. Fluid Mech.* **84**, 209–235.

- HURST, D. & VASSILICOS, J.C. 2004 Experiments in fractal-induced turbulence. In *Advances in Turbulence X* (ed. H.I. Andersson & P.-Å. Krogstad), pp. 355–358. Barcelona: CIMNE.
- IMAICHI, K. & OHMI, K. 1983 Numerical processing of flow-visualisation pictures - measurement of two-dimensional vortex flow. *J. Fluid Mech.* **129**, 283–311.
- JÄHNE, B., KLINKS, J. & WAAS, S. 1994 Imaging of short ocean wind waves: a critical theoretical review. *J. Opt. Soc. Am. A* **11** (8), 2197–2209.
- KEANE, R.D. & ADRIAN, R.J. 1990 Optimization of particle image velocimeters. part i: double pulsed systems. *Meas. Sci. Tech.* **1**, 1202–1215.
- KEANE, R.D. & ADRIAN, R.J. 1991 Optimization of particle image velocimeters. part ii: multiple pulsed systems. *Meas. Sci. Tech.* **2**, 963–974.
- KEANE, R.D. & ADRIAN, R.J. 1992 Theory of cross-correlation analysis of piv images. *Appl. Sci. Res.* **49**, 191–215.
- KRAICHNAN, R.H. 1967 Inertial ranges in two-dimensional turbulence. *Phys. Fluids* **10**, 1417–1423.
- KRAICHNAN, R.H. 1970 Diffusion by a random velocity field. *Phys. Fluids* **13**, 22–31.
- KUMAR, S. & BANERJEE, S. 1998 Development and application of a hierarchical system for digital particle image velocimetry to free-surface turbulence. *Phys. Fluids* **10**, 160–177.
- KUMAR, S., GUPTA, R. & BANERJEE, S. 1998 An experimental investigation of the characteristics of free-surface turbulence in channel flow. *Phys. Fluids* **10**, 437–456.
- KUNDU, P.K. 1990 *Fluid Mechanics*. Academic Press.
- KURATA, K.T., GRATTAN, K.T.V., UCHIYAMA, H. & TANAKAT, T. 1990 Water surface measurements in a shallow channel using the transmitted image of a grating. *Rev. Sci. Instrum.* **6**, 736–739.
- LECORDIER, B., DEMARE, D., VERVISCH, L.M.J., RÉVEILLON, J. & TRINITÉ, M. 2001 Estimation of the accuracy of piv treatments for turbulent flow studies by direct numerical simulation of multi-phase flow. *Meas. Sci. Tech.* **12**, 1382–1391.
- LIGHTHILL, J. 1978 *Waves in Fluids*. Cambridge Univ. Press.

- LOEWEN, S., AHLBORN, B. & FILUK, A.B. 1986 Statistics of surface flow structures on decaying grid turbulence. *Phys. Fluids* **29**, 2388–2397.
- LOURENCO, L. & KROTHAPALLI, A. 2000 True resolution piv, a mesh free second order accurate algorithm. In *Proc. 8th Int. Symp. Appl. Laser Tech. Fluid Mech.*, p. 13.5. Lisbon, Portugal.
- LUFF, J.D., DROUILLARD, T., ROMPAGE, A.M., LINNE, M.A. & J.R. HERTZBERG 1999 Experimental uncertainties associated with particle image velocimetry (piv) based vorticity algorithms. *Exp. in Fluids* **26**, 36–54.
- MAASSEN, S.R. 2000 Self-organization of confined two-dimensional flows. PhD thesis, Eindhoven University of Technology.
- MAGNAUDET, J. 2003 High-reynolds-number turbulence in a shear-free boundary layer: Revisiting the hunt-graham theory. *J. Fluid Mech.* **484**, 167–196.
- MAKITA, H. 1991 Realization of a large scale turbulence field in a small wind tunnel. *Fluid Dyn. Res.* **8**, 53–64.
- VAN MANEN, A.D. SCHWARZ 1992 Coherent structures over grooved surfaces. PhD thesis, Eindhoven University of Technology.
- MCWILLIAMS, J.C. 1984 The emergence of isolated coherent vortices in turbulent flow. *J. Fluid Mech.* **146**, 21–43.
- MOHAMED, S.M. & LARUE, J.C. 1990 The decay power law in grid-generated turbulence. *J. Fluid Mech.* **291**, 195–214.
- MONIN, A. & YAGLOM, A.M. 1975 *Statistical Fluid Mechanics VOL II*. MIT Press.
- MYDLARSKI, L. & WARHAFT, Z. 1990 On the onset of high-reynolds-number grid-generated wind tunnel turbulence. *J. Fluid Mech.* **320**, 331–368.
- NAGAOSA, R. 1999 Direct numerical simulation of vortex structures and turbulent scalar transfer across a free surface in a fully developed turbulence. *Phys. Fluids* **11**, 1581–1595.
- NAGAOSA, R. & HANDLER, R.A. 2003 Statistical analysis of coherent vortices near a free surface in a fully developed turbulence. *Phys. Fluids* **15**, 375–394.
- PAN, Y. & BANERJEE, S. 1995 A numerical study of free-surface turbulence in channel flow. *Phys. Fluids* **7**, 1288–1290.
- PEARSON, B.R., KROGSTAD, P.-Å. & VAN DE WATER, W. 2002 Measurements of the turbulent energy dissipation rate. *Phys. Fluids* **14**, 1288–1290.



- PEROT, B. & MOIN, P. 1995 Shear-free turbulent boundary layers. part 1. physical insights into near-wall turbulence. *J. Fluid Mech.* **295**, 199–227.
- PHILLIPS, O.M. 1957 On the generation of waves by turbulent wind. *J. Fluid Mech.* **4**, 417–445.
- PHILLIPS, O. M. 1980 *The Dynamics of the Upper Ocean, 2nd edition*. Cambridge Univ. Press.
- POORTE, R.E.G. 1998 On the motion of bubbles in active grid generated turbulent flows. PhD thesis, University Twente.
- POORTE, R.E.G. & BIESHEUVEL, A. 2002 Experiments on the motion of gas bubbles in turbulence generated by an active grid. *J. Fluid Mech.* **461**, 127–154.
- POPE, S.B. 2000 *Turbulent Flows*. Cambridge Univ. Press.
- PULLES, C.J.A. 1988 Drag reduction of turbulent boundary layers by means of grooved surfaces. PhD thesis, Eindhoven University of Technology.
- RAFFEL, M., WILLERT, C.E. & KOMPENHANS, J. 1998 *Particle Image Velocimetry, A Practical Guide*. Springer-Verlag.
- RASHIDI, M. & BANERJEE, S. 1988 Turbulence structure in open channel flows. *Phys. Fluids* **31**, 2491–2503.
- ROOD, E.P. & KATZ, J., ed. 1994 *Free-Surface Turbulence*, American Society of Mechanical Engineers, Fluids Engineering Division. FED-Vol. 181.
- ROSHKO, A. 1952 On the development of turbulent wakes from vortex sheets. PhD thesis, California Institute of Technology.
- SAJJADI, S.G. 2002 Vorticity generated by pure capillary waves. *JFM* **459**, 277–288.
- SARPKAYA, T. 1996 Vorticity, free surface, and surfactants. *Annu. Rev. Fluid Mech.* pp. 83–128.
- SARPKAYA, T. & SUTHON, P. 1991 Interaction of a vortex couple with a free surface. *Exp. in Fluids* **11**, 205–217.
- SCARANO, F. & RIETHMULLER, M.L. 1999 Iterative multi-grid approach in piv image processing with discrete window offset. *Exp. in Fluids* **26**, 513–523.
- SENET, C.M., SEEMANN, J. & ZIEMER, J. 2001 The near-surface current velocity determined from images sequences of the sea surface. *IEEE Trans. Geosci. Remote Sensing* **39**, 492–505.

- SETTLES, G.S. 2001 *Schlieren and Shadowgraph Techniques, Visualizing Phenomena in Transparent Media*. Springer-Verlag.
- SHEN, L., ZHANG, X., YUE, D.K.P. & TRIANTAFYLLOU, G.S. 1999 The surface layer for free-surface turbulent flows. *J. Fluid Mech.* **386**, 167–212.
- SONG, M., BERNAL, L.P. & TRYGGVASON, G. 1992 Head-on collision of a large vortex ring with a free surface. *Phys. Fluids A*, **4**, 1457–1466.
- STAMMER, D. 1997 Global characteristics of ocean variability from regional topex/poseidon altimeter measurements. *J. Phys. Oceanogr.* pp. 1743–1769.
- TEIXEIRA, M.A.C. 2000 Interaction of turbulence with a free surface. PhD thesis, University of Reading.
- TEIXEIRA, M.A.C. & BELCHER, S.E. 2000 Dissipation of shear-free turbulence near boundaries. *J. Fluid Mech.* **422**, 167–191.
- TITOV, V., RABINOVICH, B., MOFJELD, H.O., THOMSON, R.E. & GONZÁLEZ, F.I. 2005 The global reach of the 26 december sumatra tsunami. *Science* **309**, 2045–2048.
- TSAI, W.-T. 1998 A numerical study of the evolution and structure of a turbulent shear layer under a free surface. *J. Fluid Mech.* **354**, 239–276.
- TSAI, W.-T. & YUE, D.K.P. 1996 Computation of non-linear free-surface flows. *Annu. Rev. Fluid Mech.* **28**, 249–278.
- WALKER, D.T., CHEN, C.-Y. & WILLMARTH, W.W. 1995 Turbulent structure in free-surface jet flows. *J. Fluid Mech.* **291**, 223–261.
- WALKER, D.T., LEIGHTON, R.I. & GARZA-RIOS, L.O. 1996 Shear-free turbulence near a flat free surface. *J. Fluid Mech.* **320**, 19–51.
- WEHOUSEN, J.V. & LAITONE, J.C. 1960 Surface waves. In *Encyclopedia of Physics, band IX* (ed. S. Flügge & C. Truesdell), pp. 446–778. Springer Verlag.
- WEIGAND, A. 1996 Simultaneous mapping of the velocity and deformation field at a free surface. *Exp. in Fluids* **20**, 358–364.
- WESTERWEEL, J. 1993 Digital particle image velocimetry, theory and application. PhD thesis, Delft University of Technology.
- WESTERWEEL, J. 1994 Efficient detection of spurious vectors in particle image velocimetry data. *Exp. in Fluids* **16**, 236–247.

- WESTERWEEL, J., DABIRI, D. & GHARIB, M. 1997 The effect of a discrete window offset on the accuracy of cross-correlation analysis of digital piv recordings. *Exp. in Fluids* **23**, 20–28.
- WESTRA, M.-T., BINKS, D. J. & VAN DE WATER, W. 2003 Patterns of Faraday waves. *J. Fluid Mech.* **496**, 1–32.
- WILLERT, C.E. & GHARIB, M. 1991 Digital particle image velocimetry. *Exp. in Fluids* **10**, 181–193.
- WILLERT, C.E. & GHARIB, M. 1997 The interaction of spatially modulated vortex pairs with free surfaces. *J. Fluid Mech.* **345**, 227–250.
- ZHANG, C., SHEN, L. & YUE, D.K.P 1999 The mechanism of vortex connection at a free surface. *J. Fluid Mech.* **384**, 207–241.
- ZHANG, X. 1995 Capillary-gravity and capillary waves generated in a wind wave tank: observations and theories. *J. Fluid Mech.* **289**, 51–82.
- ZHANG, X. & COX, C.S. 1994 Measuring the two-dimensional structure of a wavy water surface optically: A surface gradient detector. *Exp. in Fluids* **17**, 225–237.

## SUMMARY

Surprisingly little is known about the statistical nature of the shape of a free surface above turbulence and about how this shape depends on the properties of the turbulence.

The main focus of this thesis is on experiments in which the statistical properties of both the surface and the turbulence are measured with a number of different techniques. The experiments are done in a free-surface water-channel, in which turbulence is generated with an active grid. This active grid consists of an array of horizontal and vertical rods through the channel, with small wings attached to them. The rods are individually driven by electric motors, according to a certain forcing protocol, thereby adding energy to the turbulence. A major advantage of an active grid is that, by changing this protocol, the properties, such as the intensity and the isotropy, of the generated turbulence can be changed. These properties were measured by means of Laser-Doppler Velocimetry. The turbulence behind the active grid is much more intense than turbulence generated by a more common static grid. The maximum Taylor-based Reynolds number reached with the active grid (at 40 times the mesh size behind the grid) was  $Re_\lambda = 256$ , compared to  $Re_\lambda = 70$  with a similarly dimensioned static grid. Consequently, the active-grid-generated turbulence shows clear Kolmogorov scaling behaviour over a relatively wide range of scales. The stronger turbulence also leads to stronger surface deformations.

In order to characterise the shape of the surface, it is essential to measure the surface shape with a high resolution both in space and time. In order to achieve this, a novel technique has been developed, based on refraction of a laser beam that shines through the surface. The deflection of the beam due to the local surface slope is measured by means of an optical position sensing device. The beam is swept along a line by means of a rapidly oscillating mirror (with a frequency of close to 2 kHz). This allows measurements of the surface slope at multiple points along the line as a function of time. This surface scanning technique can be combined with Particle Image Velocimetry (PIV), which provides snapshots of the velocity field and the vertical component of vorticity in horizontal planes just below the surface. This combination allows us to simultaneously measure the velocity field and the surface deformations above it. PIV is based on the cross-correlation of the intensity distributions in images

of particles suspended in the flow, that are illuminated by a thin laser light sheet. When applying PIV to turbulence, it is important to realise that the velocity field that can be obtained with PIV is a spatially averaged representation of the actual velocity field. The effect this averaging has on measured turbulence properties is investigated by means of kinematic simulations, in which realistic turbulent velocity fields, with a prescribed energy spectrum, are generated. Synthetic particle images derived from these fields are evaluated by means of a PIV algorithm and the velocity spectrum is calculated. Comparing this to the prescribed spectrum clearly shows the averaging, and allows us to predict its influence on other measured turbulence properties.

The turbulence generated by our grid is not strong enough to lead to very large deformations of the surface. The measured changes in elevation are less than 1 mm. In that case, somewhat naively, one would expect the surface deformations to be primarily associated with sub-surface vortices. In the core of a vortex the magnitude of the vorticity is high, while the pressure is low. This low pressure causes a dimple in the surface above the vortex. This effect can, for instance, be seen when stirring a cup of tea or in the wake behind bridge pillars in a river. Consequently, in simultaneous measurements of the surface shape and the sub-surface velocity field one would expect to find a relatively large correlation between the vertical component of vorticity and the surface elevation. Indeed, our measurements show that relatively strong vortices in the turbulence do deform the surface. However, the measured correlation coefficients are low ( $< 0.1$ ). Spectra of the surface slope in space and time show that, instead of being connected directly to sub-surface structures, much of the surface actually consists of gravity-capillary waves, i.e. regular surface waves. For surface waves, there is a clear relation between their wavelength and their frequency. This relation can be identified in our spectra. The presence of these waves is somewhat surprising, since resonant wave growth can only be expected to occur if the fluctuation velocities in the turbulence are larger than the minimum phase velocity of the waves ( $\approx 0.23$  m/s), while the measured fluctuation velocities in our turbulence are an order of magnitude smaller. A remarkable feature of the waves above the turbulence is that they travel in all directions across the surface. In fact, provided that the turbulence far below the surface is isotropic, the surface shape itself is isotropic as well. In other words, statistically, the waves on the surface are the same in every direction. We can change this by changing the forcing protocol of the active grid such that the turbulence becomes anisotropic. In that case the surface shape becomes anisotropic as well. This is a clear indication that the surface waves are excited locally by the turbulence. We have found evidence to suggest that the waves are excited by the largest structures in the turbulence. As a consequence of this, the surface shape does not reflect the wide range of scales in the sub-surface turbulence, but instead exhibits waves primarily with wavelenghts close to the integral scale of the turbulence.

## SAMENVATTING

Er is verbazingwekkend weinig bekend over hoe de statistische eigenschappen van de vorm van een vrij oppervlak boven turbulentie afhangen van de turbulentie zelf. Het zwaartepunt van dit proefschrift ligt bij experimenten, waarin de eigenschappen van het oppervlak en van de turbulentie worden gemeten met een aantal verschillende technieken. De experimenten zijn gedaan in een waterkanaal, waarin turbulentie wordt opgewekt met behulp van een actief rooster. Dit rooster bestaat uit horizontale en verticale assen die door het kanaal steken. Aan deze assen zijn vaantjes bevestigd. De individuele assen kunnen onafhankelijk van elkaar worden bewogen met behulp van electro-motoren die volgens een bepaald forcerings-protocol worden aangestuurd. Door dit roeren wordt de turbulentie sterker en door het aanpassen van het protocol kunnen de eigenschappen van de turbulentie, zoals de intensiteit en isotropie, worden beïnvloed. De eigenschappen van de turbulentie zijn gemeten met behulp van Laser-Doppler snelheidsmetingen. Dat de turbulentie achter het actieve rooster intenser is dan die achter een regulier statisch rooster blijkt onder andere uit het gemeten Reynolds-getal gebaseerd op de Taylor lengte-schaal van de turbulentie. De maximum waarde voor het actieve rooster (op 40 keer de maasgrootte achter het rooster) is  $Re_\lambda = 256$ , terwijl voor een statisch rooster van dezelfde afmetingen  $Re_\lambda = 70$  werd gemeten. De sterkere turbulentie vertoont duidelijk schalingsgedrag over een relatief groot schaal-bereik en leidt tot sterkere vervormingen van het oppervlak.

Om te begrijpen wat er aan het oppervlak gebeurt is het belangrijk om de vorm van het oppervlak te meten, met een hoge resolutie in zowel de tijd als in de plaats. Hiervoor is een nieuwe techniek ontwikkeld. De lokale helling van het oppervlak wordt bepaald aan de hand van de uitwijking van een laserbundel die wordt gebroken aan het oppervlak. De uitwijking wordt gemeten met behulp van een zogenaamd optisch position sensing device (een plaats-gevoelige detector). Een oscillerend spiegeltje laat de bundel snel heen-en-weer zwiepen (met een frequentie van bijna 2 kHz), zodat de helling als functie van de tijd wordt gemeten in meerdere punten op een lijn. De oppervlakte metingen kunnen worden gecombineerd met Particle-Image Velocimetry (PIV). Met deze techniek kunnen moment-opnamen van het snelheidsveld onder het oppervlak worden gemaakt. Zo kunnen we gelijktijdig de snelheid en de vorm van het opper-

vlak meten. PIV werkt aan de hand van het correleren van digitale foto's van de deeltjes-verdeling in de stroming, waarbij de deeltjes worden verlicht met een dun laser-lichtvlak. Wanneer PIV wordt toegepast op turbulentie is het van belang dat een met PIV gemeten snelheidsveld een ruimtelijk gemiddelde weergave is van het echte snelheidsveld. Deze middelling heeft gevolgen voor de gemeten eigenschappen van de turbulentie. Dit is nader onderzocht aan de hand van kinematische simulaties. Hierin worden realistische snelheidsvelden met een voorgeschreven energiespectrum berekend. Deze vormen de basis voor synthetische afbeeldingen van de deeltjes-verdeling in de stroming. Deze kunnen worden verwerkt met een PIV-algoritme en vervolgens kan het energie spectrum worden berekend. Een vergelijking hiervan met het oorspronkelijke spectrum laat de middelling duidelijk zien en maakt het mogelijk de invloed van de middelling op andere eigenschappen van de turbulentie te voorspellen. De turbulentie in ons kanaal is niet sterk genoeg om het oppervlak sterk te vervormen. De gemeten variaties in de hoogte zijn minder dan 1 mm. Enigszins naïef valt in dat geval te verwachten dat vervormingen van het oppervlak vooral ontstaan als gevolg van wervels onder het oppervlak. In een wervel is de vorticeiteit groot en de druk laag. Die lage druk kan ervoor zorgen dat er in het oppervlak boven een wervel een deukje ontstaat. Op grond hiervan verwacht je een vrij sterke correlatie tussen de verticale component van de vorticeiteit en de hoogte van het oppervlak. Onze metingen laten inderdaad zien dat sterke wervels het oppervlak vervormen, maar de gemeten correlatie-coëfficiënten zijn klein ( $< 0.1$ ). Er is dus meer aan de hand. Spectra van de helling van het oppervlak in plaats en tijd laten zien dat de vorm van het oppervlak niet direct gekoppeld is aan de turbulentie, maar voor een groot deel bestaat uit capillaire zwaartekrachts-golven. Voor dit soort normale oppervlakte-golven is er een duidelijk verband tussen de golflengte en de frequentie. Deze relatie is terug te zien in de gemeten spectra van het oppervlak. Dat er golven ontstaan is enigszins onverwacht. Een voorwaarde voor het resonant groeien van golven is dat de snelheidsfluctuaties in de turbulentie groter zijn dan de minimum fase-snelheid van de golven ( $\approx 0.23$  m/s). De door ons gemeten fluctuaties zijn echter een orde van grootte kleiner. Heel bijzonder is dat de golven in alle richtingen over het oppervlak reizen. Sterker nog, wanneer de turbulentie ver onder het oppervlak isotroop is, dan is het oppervlak zelf ook isotroop. Dat wil zeggen, de statistische eigenschappen van de golven zijn in alle richtingen hetzelfde. Door het forcerings-protocol van het actieve rooster zodanig te veranderen dat de turbulentie anisotroop wordt, wordt het oppervlak ook anisotroop. Dit toont aan dat de golven lokaal worden aangeslagen door de turbulentie. We hebben aanwijzingen gevonden dat hierbij vooral de grotere structuren in de stroming een rol spelen. In de vorm van het oppervlak is niets terug te zien van de kleinere schalen in de turbulentie. De vorm wordt gedomineerd door golven met een golflengte die vergelijkbaar is met de integrale lengte-schaal van de stroming.

## DANKWOORD / ACKNOWLEDGEMENTS

Het hier beschreven werk had niet kunnen worden gedaan zonder de hulp van een groot aantal mensen. Hoewel mijn gezondheid me af en toe in de steek liet, lieten onderstaande mensen me niet zakken. In de eerste plaats wil ik Willem van de Water bedanken. Zonder Willems drive, duwtjes in de rug, “hands-on approach”, soms wilde maar meestal zinnige ideeën en natuurlijk zijn vermaarde “Fortran-programmes of everything” zou dit werk nooit gelukt zijn. Onze soms heftige discussies, met veel handgebaren, vage krijttekeningen op het bord en vooral ook veel misverstanden waren toch vaak verhelderend en ik zal ze in de toekomst dan ook enorm missen. GertJan van Heijst wil ik vooral bedanken voor het vertrouwen dat hij me gegeven heeft en voor de goede raad en hulp op die hij me gaf op de momenten dat ik zelf het vertrouwen dreigde kwijt te raken. Hoewel het door alle experimentele complicaties er niet van is gekomen om numerieke simulaties aan free-surface turbulence te doen en zijn rol in het project hierdoor kleiner is geworden dan hij zelf misschien gewild had, wil ik ook Herman Clercx bedanken. Hij hield de vinger aan de pols en heeft, zeker in het begin van het project, menige hobbel weten glad te strijken.

I owe many thanks to Carl Tipton for his friendship and the many lively discussions that we had about cross-spectral densities, the peculiarities of Dutch English, (the) Dutch in general, and pretty much anything else one could possibly think of. I also want to thank Anders Andersen for his valuable ideas and input in trying to find the models described in chapter 2. I enjoyed our work together.

Een aantal studenten heeft een directe bijdrage geleverd aan het werk in dit proefschrift: Hubert van Luytelaar als afstudeerder en Koos Delescen, Gijs van der Heijden en Jochem Nietsch als stagairs. Ik hoop dat jullie iets van de samenwerking hebben opgestoken. Ik in ieder geval wel van jullie.

Ik heb heel veel hulp gehad van onze onmisbare technici: Gerald Oerlemans voor het actieve rooster, de bevestiging van de LDV opstelling en onderdelen voor PIV, Freek van Uittert, met name voor de aansturing van het actieve rooster, Ad Holten voor de dataverwerking voor LDV en zijn onmisbare hulp bij het ontwikkelen van de oppervlaktetechniek (file-headers!) en Gert van der Plas voor zijn ondersteuning met PIV, LDV en het hele FreeBSD computergebeuren. Hun bijdragen zijn niet zo beperkt of zo strikt gescheiden als het



voorgaande suggereert. Het hele team heeft me op allerlei manieren geholpen, niet alleen door aan te pakken, maar ook door met me mee te denken en (niet in de laatste plaats) door hun grote rol in de goede sfeer in de groep. In dit licht bezien mogen ook Pim Sluyter, Jan Willems, Gerard Trines en Herman Koolmees niet ontbreken. Onze bezoeken aan de Chinees op de Kruisstraat zal ik niet licht vergeten. Verder zijn veel technische klussen opgeknapt door de Centrale Technische Dienst en door de werkplaats van N-laag, onder de bezielende leiding van Marius Bogers.

Zonder het secretariaat, afwisselend bezet door Anita, Brigitte en Marjan, zou ik er regelmatig een zootje van hebben gemaakt. Administratie en regel zijn niet mijn favoriete bezigheden, maar gelukkig kon ik op het secretariaat vertrouwen.

Ik wil ook Ruben Trieling, Bernard Geurts, Rini van Dongen en Mico Hirschberg bedanken. Hoewel ze formeel niet bij mijn project betrokken waren, waren ze in de praktijk maar al te bereid me van goede raad te voorzien. Voor goede raad in meer algemene zin kon ik ook altijd rekenen op Toon Wouters.

Natuurlijk wil ik ook mijn mede-promovendi en veel van de studenten die door de jaren heen bij ons gewerkt hebben bedanken. Met sommigen heb ik natuurlijk meer contact gehad dan met anderen. De gezamenlijke theepauze 's middags was vaak het gezelligste moment van de dag en de daarbij gevoerde gesprekken over "life, the universe, and everything" waren meestal komisch en zondermeer erg levendig. Na zo'n pauze kon ik er weer een aantal uurtjes tegenaan. Ik ga verder geen lange opsomming van namen geven, maar mijn twee kamergenoten mogen niet onvernoemd blijven: Robin Schoemakers en Laurens van Bokhoven (met waarschijnlijk het netste bureau binnen de TU). We hebben heel wat uurtjes samen doorgebracht en ook heel wat afgelachen.

Tja, en waar zou ik zijn zonder mijn vriendenclub? Harm, Thijs, Maarten, Csaba, Karel en Doryan, Maikel en Fenna. Zij wisten iedere keer op donderdagavond bij die andere Chinees op de Kruisstraat (King Hung) de zaken in het juiste perspectief (of toch net het verkeerde?) te plaatsen. Dat was onontbeerlijk voor mijn gezondheid, hoewel die er de ochtend erna soms ook onder te lijden had. Gon Bao Kai met Palm valt niet altijd even goed. Harm, eindelijk heb ik een geschikte gelegenheid: "René, Edith, the bedknobs, they are blinking!" (het nep-accent moet je er zelf bij bedenken). Ik wil Ben bedanken, onder andere voor de onvergetelijke concerten van Peter Gabriel waar we samen naartoe geweest zijn. Daarnaast wil ik ook Antoin bedanken, al toen ik zeven jaar oud was mijn beste vriend.

Tenslotte wil ik mijn ouders en mijn zus bedanken voor hun onvoorwaardelijke liefde. Zonder hun steun zou dit proefschrift er niet zijn gekomen.

# CURRICULUM VITAE

**July 16, 1975**

Born in Kerkrade, The Netherlands

**1987-1993**

St. Antonius Doctor College, Kerkrade (VWO)

**1993-2000**

Student of Applied Physics, Eindhoven University of Technology.

- Traineeship in the group Equilibria and Transport in Plasmas,  
*Diode Laser Absorption of Balmer- $\alpha$  in the Expanding Hydrogen Plasma*
- Masters thesis in the group Vortex Dynamics and Turbulence,  
*The Free-Surface Evolution of Half Vortex Rings*

**2000-2006**

PhD Candidate in the group Vortex Dynamics and Turbulence, Department of Applied Physics, Eindhoven University of Technology,  
*Experiments on Free-Surface Turbulence*

**May 2006**

Postdoctoral Research Fellow, School of Engineering Sciences, University of Southampton, UK

